SCUOLA DI DOTTORATO IN INGEGNERIA AEROSPAZIALE, NAVALE E DELLA QUALITÀ
XXI CICLO

UNIVERSITÀ DEGLI STUDI DI NAPOLI "FEDERICO II"

PhD dissertation

STEREO PIV ANALYSIS
AND APPLICATION TO CYLINDER WAKE

Rosaria Giordano

Tutors Dott. Ing. Tommaso Astarita

Prof. Ing. Giovanni Maria Carlomagno

Coordinator Prof. Ing. Antonio Moccia

Table of contents

Abstract

A theoretical analysis of the spatial resolution of the Stereo Particle Image Velocimetry (PIV) technique has been performed. This has been done in terms of Modulation Transfer Function (MTF) and by applying the technique with and without the correction of the misalignment error between calibration and measurement planes. The results show that some wavelengths of the flow field can be significantly dephased and modulated. The theoretical analysis has been extended to investigate also the effects caused by the laser thickness and the linear dimension of the interrogation window W (i.e. the modulation associated to the Stereo PIV process). As it will be shown in detail in this work, the modulation associated to the last two parameters cannot be corrected, differently from the modulation due to the misalignment. A performance assessment has been conducted with both synthetic and real images and shows a good agreement with the theoretical analysis.

The reconstruction of the three-dimensional displacement field is achieved using both methods proposed by Soloff et al. (1997) and by Willert (1997).

Finally, the Stereo PIV technique has been used to analyse the vortex shedding caused by both finite and infinite cylinders immersed in a uniform flow field. The Reynolds numbers investigated are within the Shear-Layer Transition Regime, indicated by Williamson (1996) for the infinite cylinder. This regime is characterized by the formation of von Kàrmàn vortices. For the finite cylinder, a counter-rotating pair of tip vortices forms at the free end, extends into the wake and interacts in a complex manner with the von Kàrmàn vortex shedding.

To detect the von Kàrmàn vortex shedding a phase averaged method has been chosen. This approach uses the Proper Orthogonal Decomposition (POD) technique and it has been evidenced that it works properly for the infinite cylinder and for some sections near the base of the finite one.

Abbreviations

2C	Two components
2D	Bi-dimensional
3C	Three components
3D	Three-dimensional
AR	Cylinder aspect ratio, H/D
CCD	Charge Coupled Device
CS	3C reconstruction proposed by Soloff et al. (1997) with correction of misalignment error
CW	3C reconstruction proposed by Willert (1997) with correction of misalignment error
DFT	Digital Fourier Transform
FFT	Fast Fourier Transform
IDM	Image Deformation Method
IDWO	Iterative Discrete Window Offset
MTF_{2C}	Modulation transfer function associated to the PIV process
$MTF_{\Delta z}$	Modulation transfer function associated to the misalignment
MTF_{LT}	Modulation transfer function associated to the laser thickness for the 3C displacement
MTF_{LTc}	Modulation transfer function associated to the laser thickness for the camera c
NCS	3C reconstruction proposed by Soloff et al. (1997) without correction of misalignment error
NCW	3C reconstruction proposed by Willert (1997) without correction of misalignment error
PID	Particle Image Distortion
PIV	Particle Image Velocimetry
POD	Proper Orthogonal Decomposition
THMA	Top Hat Moving Average

List of symbols

$a^{(n)}(t_k)$	n-th temporal POD eigenfunction relative to the instant t_k, *dimensionless*
c	Indicates the camera (1, 2), *dimensionless*
C_{PB}	Base pressure coefficient, *dimensionless*
dx	Infinitesimal displacement vector in object space, dx=[*dx, dy, dz*], *mm*
dx, dy, dz	3C infinitesimal displacement in object space, *mm*
dXc	Infinitesimal displacement vector in the image plane relative to camera c, dXc=[*dXc, dYc*], *pixels*
dXc, dYc	2C infinitesimal displacement in the image plane relative to camera c, *pixels*
D	Cylinder diameter, *m*
D_u	Disparity vector, *mm*
f_K	von Kàrmàn vortices frequency, s^{-1}
f_{SL}	Shear layer vortices frequency, s^{-1}
E_{21}	Power spectra of the v component evaluated along the x direction, mm^2
$\underline{F}^{(c)}=[X^{(c)}, Y^{(c)}]$	Vectorial mapping function relative to camera c, $\underline{F}^{(c)}=[X^{(c)}, Y^{(c)}]$, *pixels*/*mm*
H	Cylinder height, *m*
I	Intensity values map of a image, *dimensionless*
$\hat{I}$	Fourier transform of I, *dimensionless*
k	Turbulent kinetic energy, m^2/s^2
$\underline{k} = \lfloor k_x, \quad k_y, \quad k_z \rfloor = \left[\frac{2\pi}{\lambda_x}, \quad \frac{2\pi}{\lambda_y}, \quad \frac{2\pi}{\lambda_z} \right]$	Wavenumber, *rad*/*mm* or *rad*/*pixels*
L_B	Bubble length, *m*
L_d	Shear layer diffusion length, *m*
L_f	Vortices formation length, *m*
p	Turbulent production term, m^2/s^3
P	Point in the measurement plane, *dimensionless*

R_{cl} (R_{cr})	Resolution measured in the left (right) side of the image recorded by the camera *c*, *pixels*/*mm*
RR_{max}	Maximum ratio between the resolutions measured in the same measurement point of the images recorded by the two cameras, *dimensionless*
$R_{II'}$	Cross-correlation function, *dimensionless*
Re	Reynolds number, $Re = \frac{U_\infty D}{\nu}$, *dimensionless*
S	Strain rate tensor, s^{-1}
St	Strouhal number, $St = \frac{f_K D}{U_\infty}$, *dimensionless*
t_c	Phase of the sinusoidal component relative to camera *c* used in 3C reconstruction without correction of the misalignment errors, *mm*
T_K	von Kàrmàn vortices period, *s*
u	Velocity component in *x* direction, *m*/*s*
u'	Velocity fluctuation component in *x* direction, *m*/*s*
$\overline{u}$	Mean velocity component in *x* direction, *m*/*s*
u^*	Velocity component in *x* direction divided by the free stream velocity U_∞, *dimensionless*
$u'u'$	Term (1,1) of the Reynolds stress tensor, m^2/s^2
$u'v'$	Term (1,2) of the Reynolds stress tensor, m^2/s^2
$u'w'$	Term (1,3) of the Reynolds stress tensor, m^2/s^2
U_{SEP}	Velocity near to separation point, *m*/*s*
U_∞	Free stream velocity, *m*/*s*
u, v, w	3C displacement in object space, *mm*
u_c, v_c	2C displacement relative to camera *c*, *mm*
v	Velocity component in *y* direction, *m*/*s*
v'	Velocity fluctuation component in *y* direction, *m*/*s*
v^*	Velocity component in *y* direction divided by the free stream velocity U_∞, *dimensionless*
$v'v'$	Term (2,2) of the Reynolds stress tensor, m^2/s^2
$v'w'$	Term (2,3) of the Reynolds stress tensor, m^2/s^2
w	Velocity component in *z* direction, *m*/*s*
w^*	Velocity component in *z* direction divided by the free stream velocity

	U_∞, *dimensionless*
W	Linear dimension of the interrogation window, *pixels*
W_x	x component of the vorticity, s^{-1}
W_y	y component of the vorticity, s^{-1}
W_z	z component of the vorticity, s^{-1}
x, y, z	Coordinates in object space, *mm*
x_c	Location of transition point in the shear layer, *m*
X_c, Y_c	Coordinates relative to camera c in the image plane, *pixels*
X_{ij}	Matrix which defines the points where the flow field velocity components are known, *dimensionless*
$X^{(c)}$	Mapping function of the image coordinates X_c, *pixels*/*mm*
$Y^{(c)}$	Mapping function of the image coordinates Y_c, *pixels*/*mm*

Greek symbols

$\alpha(t_k)$	Vortex shedding phase of the instantaneous (in the instant t_k) flow field, *rad*
α_c	Angle between the viewing ray and the plane *yz* measured in the *xz* plane, *rad*
β_c	Angle between the viewing ray and the plane *xz* measured in the *yz* plane, *rad*
δ_{BL}	Boundary layer thickness, *m*
Δz	Local misalignment between calibration and measurement planes, *mm*
θ	Scheimpflug angle, *rad*
θ_{SL}	Shear layer momentum thickness, *m*
λ_n	n-th POD eigenvalue, m^2/s^2
λ_{SL}	Shear layer vortices wavelength, *m*
λ_{SL3}	Spanwise wavelength of the longitudinal vortices developed in the shear layer, *m*
φ	Phase in measured sinusoidal component caused by misalignment, *rad*
$\Phi^{(n)}(X)$	n-th POD mode, *m*/*s*
$\underline{\xi}_c$	Vector obtained by intersecting the optical axis of camera c and the laser sheet, *mm*
ν	Kinematical viscosity, m/s^2

1 Introduction

The Stereo Particle Image Velocimetry technique has been developed in the last ten years. It is a technique that allows capturing the three components planar velocity of an instantaneous flow fields. This is obtained by using two bi-dimensional Particle Image Velocimetry (PIV) flow fields.

The PIV technique is older than the Stereo PIV and in the past various works have been performed to study the frequency response of the technique. This allowed detecting quantitatively spatial structures in unsteady flows, which is not possible with other techniques. Nevertheless, the drawback of the PIV is the impossibility to measure the out-of-plane velocity component.

The aim of this work is to analyse the frequency response of the Stereo PIV technique, since no work is present in the literature on this topic.

Nowadays, there are different methods to implement the Stereo PIV technique; Prasad (2000) subdivided these methods into geometric and calibration-based approaches. At the moment, the former is not used because the latter is more accurate. It is possible to categorise the calibration-based approach in further approaches: the first is based on the procedure introduced by Soloff et al. (1997) and the second is that proposed by Willert (1997). In the former approach a mathematical relation, which computes the three-component (3C) reconstruction in a single step, is proposed. On the other hand, in the Willert's approach, the reconstruction of the three-dimensional displacement field is done by means of geometrical considerations, i.e. local viewing angles of each camera in every point of the measurement plane. Actually, it is known in the Stereo PIV community that the two approaches are almost equivalent (see Sect. 3.2.3).

In order to compute the viewing angles used in the Willert's approach, various methods have been proposed in the past: Willert (1997) proposed to evaluate them by measuring the distances between the measurement points and the cameras and then by using trigonometric relations, whereas Fei and Merzkirch (2004) and Scarano et al. (2005) computed the viewing angles by correlating calibration images recorded in two different z (coordinate orthogonal to the calibration plane). In this work new formulas are proposed, which permit to compute the viewing angles without the necessity to measure any geometrical parameter of the experimental set-up (see Sect. 4.1).

In all calibration-based approaches an accurate calibration, which allows correcting the error in perspective and the possible distortion caused by the lenses, is essential to obtain good results in the measurement of the velocity components (see Sect. 3.2.1). Typically, calibration is obtained setting a calibration pattern, which contains a grid of marks regularly spaced along two orthogonal directions, in one or more positions along the z direction; ideally, $z = 0$ is the position of the light sheet, i.e. the measurement plane. In the calibration procedure, a mapping function is computed, which allows transforming the object coordinates (x, y, z) into the image coordinates (X_1,Y_1) and (X_2,Y_2) of the two cameras; coefficients of the mapping function are normally calculated with the least squares method.

A drawback of the Stereo PIV technique is the impossibility to set the laser sheet exactly in the $z = 0$ position. Many authors have proposed an adjusting procedure based on a cross-correlation between the images of the two cameras, recorded in the same instant. Some authors have proposed a procedure, which corrects only the position error, like Willert (1997) and Coudert and Schon (2001); really this is enough if the misalignment is quite small. Others have suggested procedures with correction of both errors: Scarano et al. (2005) and Wieneke (2005). Also in the present work an adjusting procedure, quite similar to the Wieneke's one, which corrects both errors, is proposed (see Sect. 3.2.2).

Results present in the literature have shown that the correction of misalignment errors isn't needed for a uniform displacement field; for this reason non-uniform ones are herein simulated. They consist of a single one-dimensional sinusoidal shear displacement, with various wavelengths. The Stereo PIV technique applied to the latter displacement type shows that a decrease of the wavelength produces a decrease of the measured sine wave amplitude. For this purpose, the spatial resolution in terms of Modulation Transfer Function (MTF) is investigated by varying the wavelength of the sinusoidal component (see Sect. 4.4). The MTF analysis is extended to investigate also the effects caused by the laser thickness (see Sect. 4.2) and the linear dimension of the interrogation window W (i.e. the modulation associated to the Stereo PIV process, see Sect. 4.3). As it will be shown in detail below, the modulation associated to the last two parameters cannot be corrected, differently from the modulation due to the misalignment.

All the above described analyses has been first investigated theoretically and then supported by a performance assessment, obtained by using three different procedures. The new formulas proposed to compute the viewing angles have been tested by using an experimental apparatus, which is made up of an angular stereoscopic system and a PIV-calibration pattern, whereas the MTF of the Stereo PIV technique has been investigated by

using both synthetic images and real ones relative to the measurement of a finite cylinder wake.

After having performed the analysis of the Stereo PIV technique and its MTF, this technique has been applied to study both infinite and finite cylinders wake (see Sect. 5). Actually, the infinite cylinder vortex dynamic has been widely investigated in the past, while the literature on the finite cylinder is significantly less extensive. Bluff body wakes are complex and they are characterised by a periodic forcing, which can be undesirable since the effects can be distructive. Consequently, it is important for engineers to account for the possible effects of vortex shedding when designing a wide range of structures, e.g. chimneys, submarine periscopes and bridge piers.

The Reynolds numbers investigated are within the Shear-Layer Transition Regime, indicated by Williamson (1996) for the infinite cylinder. In this regime, the separation of the shear layers from the sides of the body causes, by increasing the Reynolds number, the reduction of both the Strouhal number (*St*) and the formation length of the mean recirculation region. Furthermore, for an increase of *Re*, the turbulent transition point moves upstream in the separating shear layers and the 2D Reynolds stresses magnitude increases. The latter effect is caused by the Kelvin-Helmholtz instability. Furthermore, the Shear-Layer Transition Regime is characterized by the formation of von Kàrmàn vortices (see Sect. 2.1).

Although strictly speaking any type of cylinder wake has 3D flow characteristics, really for a 2D cylinder the flow is practically bi-dimensional. Three dimensional features of the flow arise when the cylinder aspect ratio is small as well as when the cylinder is finite, i.e. with a free end; the latter causes changes in the vortex formation length as well as the vortex shedding pattern (see Sect. 2.2).

In the present work, since the frequency used for the image acquisition is lower than the von Kàrmàn vortices one, a phase averaging method has to be used to reconstruct the vortices evolution. In the literature various approaches are present for the phase averaging. Ben Chiekh et al. (2004) proposed to use the first two principal modes obtained with the Proper Orthogonal Decomposition (POD) technique, in order to reconstruct the vortices evolution. By applying this approach to detect the vortex shedding, it has been evidenced that it works properly for the infinite cylinder and for some sections near the base of the finite one.

2 Flow field past a circular cylinder: state of the art

The flow behind an infinite circular cylinder has been widely investigated in the past. Although the infinite cylinder is a very simple geometry, it is greatly used for modelling bluff bodies. The flow field behind a bluff body is an important phenomenology for many engineering and physical fields, because the alternate shedding of vortices, which develops in the near wake, causes pressure forces, which generate structural vibration, acoustic noise and resonance phenomena.

An interesting study in depth of this problem is the analysis of the finite cylinder, since the flow around the base and over the tip of the cylinder causes a strong three-dimensionality of the flow field.

In this chapter the most important results present in the literature regarding both infinite and finite circular cylinders will be shown.

2.1 Infinite cylinder

Williamson (1996) made an interesting overview on the vortex dynamics phenomena in the wake of a cylinder, by varying the Reynolds number, defined as:

$$Re = \frac{U_\infty D}{\nu} \qquad (2.1)$$

where U_∞ is the free stream velocity, D is the cylinder diameter and ν is the kinematical viscosity of the working fluid.

The wake of a cylinder is very sensitive to the Reynolds number. There is a range of *Re* in which the flow is practically laminar. Over this range, the wake always becomes turbulent and the point of turbulence onset moves upstream by increasing the Reynolds number. The fully development of turbulence motion, i.e. when all traces of periodicity is lost, happens at very high *Re*.

The first appearance of a periodic wake happens at $Re \approx 50$: it is stable and detected as far as 100 diameters downstream. By moving downstream, viscous dissipation causes the vortices decay. This phenomenon is detectable till $Re \approx$ 140-194. By increasing the Reynolds number, an irregular burst of the wake velocity appears and the shedding frequency becomes difficult to be measured. This situation is connected to the birth of 3D instability. For higher

Reynolds numbers until the critical value ($\approx 3 \cdot 10^5$), a precise shedding frequency returns, but contrary from the above mentioned laminar vortex shedding, in this case the wake becomes turbulent about 40 diameters downstream, where all periodicity disappear.

Williamson (1996) concluded that by increasing the Reynolds number the flow passes throw three instability sources:

- Wake transition;
- Shear layer transition;
- Boundary layer transition.

He schematised the whole cylinder wake behaviour in 8 different vortex shedding regimes. All these regimes can be found in Fig. 2.1, where the base suction coefficient ($-C_{PB}$, C_{PB} is the base pressure coefficient, i.e. the pressure measured at 180° from the front stagnation point) is plotted as a function of the Reynolds number:

- *Laminar Steady Regime (Re < 49)* – (Up to *A* in Fig. 2.1) the wake is symmetric and steady and its length grows by increasing the Reynolds number;
- *Laminar Vortex Shedding Regime (Re = 49 to 140-194)* – (A-B in Fig. 2.1) in this regime it has been shown the onset of the wake instability with the development of a laminar shedding vortices and the vortex formation length increases as the Reynolds number increases;
- *3D Wake Transition Regime (Re = 190 to 260)* – (B-C in Fig. 2.1) at *Re* = 180-194 the birth of the vortex loops can be seen in the wake formation, which distort the primary vortices with a spanwise wavelength between 3 and 4 diameters (*Mode A*). By increasing the Reynolds number to about 250, a transition from *Mode A* (vortex loops) to *Mode B* (streamwise vortex pair) was observed. The latter vortex shedding mode is characterised by a shorter spanwise wavelength of about one diameter;
- *Increasing Disorder in the Fine Scale Three Dimensionalities (Re = 260 to 10^3)* – (C-D in Fig. 2.1) at *Re* = 300 the primary wake instability becomes again similar to the laminar shedding mode (see Fig. 2.2), with the exception of the presence of fine scale streamwise vortex structure, whose three dimensional disorder increases by increasing the Reynolds number;
- *Shear Layer Transition Regime (Re = 10^3 to $2 \cdot 10^5$)* – (D-E in Fig. 2.1) in this regime the instability of the separating shear layer from the cylinder sides develops (see Fig. 2.2) and, by increasing the Reynolds number, the transition point in the separating shear layers moves upstream and the formation length decreases;

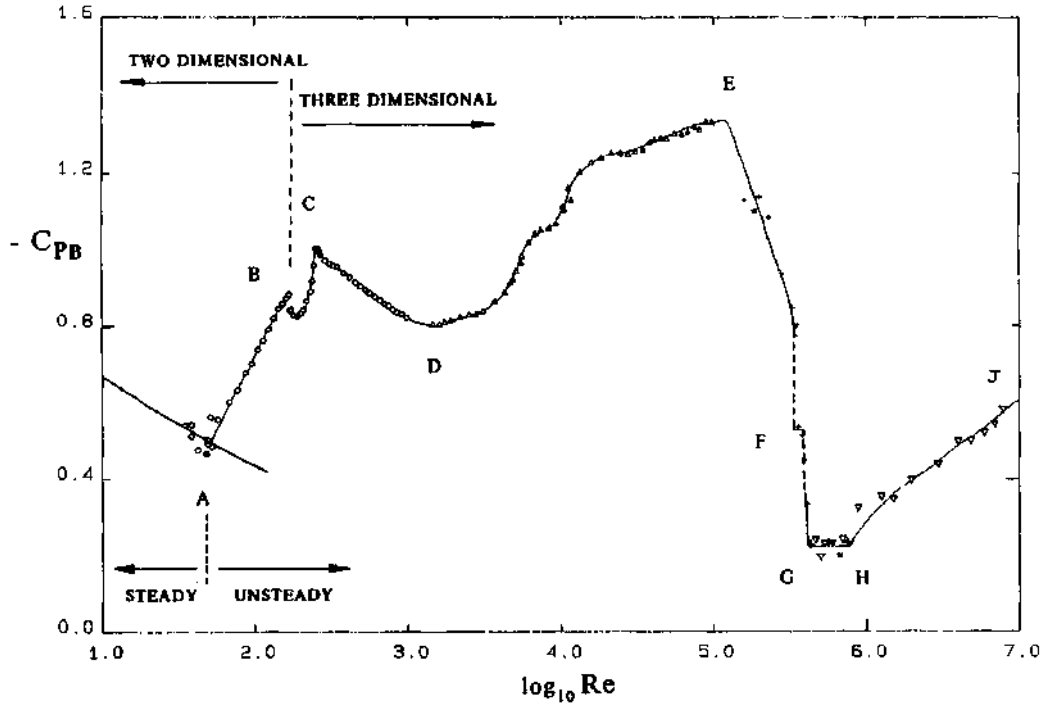

Fig. 2.1 Plot of base suction coefficients versus the Reynolds numbers (Williamson 1996).

- *Critical Transition Regime* – (E-G in Fig. 2.1) in this regime the base suction decreases drastically and the boundary layer separates much further downstream; in point F of Fig. 2.1 a separation reattachment bubble on only one side of the cylinder has been discovered;
- *Supercritical Regime* – (G-H in Fig. 2.1) in this regime the flow becomes symmetric and also some fluctuations are detected;
- *Post-Critical Regime* – (H-J in Fig. 2.1) in this regime the turbulent transition point moves further upstream and the downstream wake becomes fully turbulent.

The choice to correlate the various regimes to the base suction coefficient ($-C_{PB}$) is right because this parameter is very sensible to the flow instabilities changes and it has been found that it is inversely proportional to the *vortex formation length* (L_f). In the literature there are different definitions of this length: some authors (e.g. Bloor 1964 and Bearman 1965) have defined it as that point downstream of the body where the velocity fluctuation level has grown to a maximum and thereafter decays downstream. Bearman (1965) showed that by increasing the formation length L_f both the Reynolds stress maximum level and the base suction coefficient decrease. Other authors (e.g. Roshko 1993) have defined the *mean recirculation region* as the symmetric and closed wake obtained by averaging over a large time the periodic wake. Roshko (1993) derived a relation between the bubble length L_B and both the base suction and the Reynolds stresses. The comparison between these two lengths allows to conclude that they are very similar.

The regime of interest for the measurements made in the present work is the *Shear Layer Transition Regime*, and in the following only this regime will be analysed.

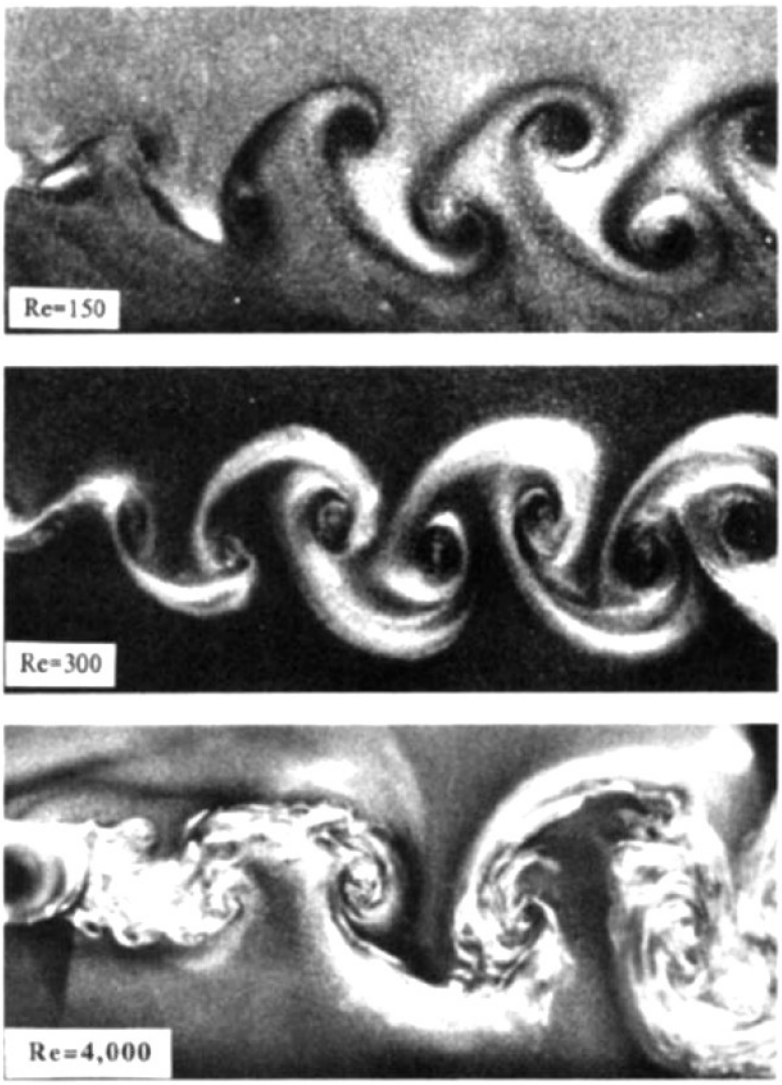

Fig. 2.2 Visualization of laminar and turbulent vortex street (Williamson 1996).

2.1.1 Shear layer instability

As already mentioned, in the *Shear Layer Transition Regime* the shear layer instability develops as *Re* increases.

The shear layer instability causes the increase of the base suction coefficient and of the 2D Reynolds stress level as well as the decrease of the formation length L_f and of the Strouhal number, defined as:

$$St = \frac{f_K D}{U_\infty} \qquad 2.2$$

where f_K is the frequency of the von Kàrmàn vortices.

Furthermore, according to Bloor (1964), the point of turbulence onset moves upstream by increasing the Reynolds number and reaches the separation point on the cylinder at the critical Reynolds number ($\approx 3 \cdot 10^5$). Schiller and Linke (1933) found that the normalised distance between the separation point and the transition point decreases from 1.4 to 0.7, by increasing the Reynolds number from $3.5 \cdot 10^3$ to $8.5 \cdot 10^3$. More recently, Saad et al. (2007) found a relationship which links the normalised location of the transition point with the Reynolds number:

$$\frac{x_c}{D} = 182.5\, Re^{-0.664} \qquad 2.3$$

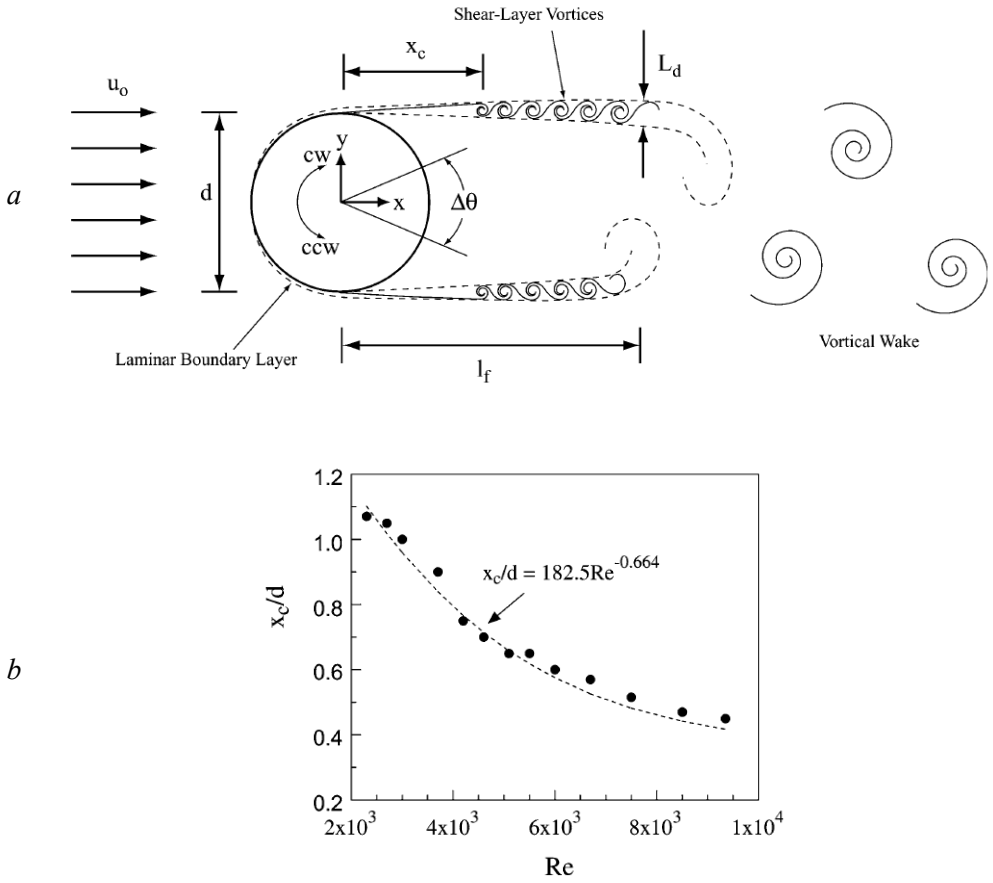

Fig. 2.3 *a*-Definition of x_c, L_d and L_f; *b*- x_c/D as a function of *Re*. Saad et al. (2007)

The location x_c is determined from the appearance of the first packet of high frequency in the hot wire time traces downstream along the shear layer for x/D = 0-3 and y/D = 0.65 (see Fig. 2.3-*a* for the reference frame). This characteristic of the shear layer instability is

considered the cause of the transition. According to both Bloor (1964) and Schiller and Linke (1933), Saad et al. (2007) found a decrease of x_c/D as Re increases. It's interesting to note that for $Re < 5 \cdot 10^3$ x_c/D is a strong function of Re, whereas a weaker decrease is observed for $Re > 5 \cdot 10^3$. This is connected to the stabilisation of the vortex formation process.

According to Williamson (1996), the Kelvin-Helmholtz instability of the shear layer is two-dimensional, whereas three-dimensional structures on the scale of both shear layer (small scale) and von Kàrmàn (large scale) vortices develop in this regime. The small-scale vortical structures are also known in the literature as Bloor-Gerrard vortices.[1]

Although the birth of shear layer vortices was already known, Bloor (1964) was the first to measure the frequency of the shear layer instability waves. He found by means of hot-wire measurements that the ratio between the frequency of the shear layer vortices and the one of von Kàrmàn vortices is proportional to $Re^{1/2}$ for $Re > 3 \cdot 10^3$. Bloor (1964) justified this relation with dimensional arguments. According to her, the frequency of transition waves f_{SL} should be proportional to the velocity near the separation point U_{SEP} divided by the shear layer momentum thickness θ_{SL}. The latter should be proportional to the thickness of the laminar boundary layer, so that:

$$\theta_{SL} \propto \left(\frac{vD}{U_\infty} \right)^{1/2} \qquad (2.4)$$

whereas, since the base pressure coefficient is almost constant for the considered Reynolds number, the velocity near the separation point would be:

$$U_{SEP} = U_\infty \left(1 - C_{PB}\right)^{1/2} = const \qquad (2.5)$$

Then:

$$f_{SL} \propto \frac{U_{SEP}}{\theta_{SL}} \propto \frac{{U_\infty}^{3/2}}{\left(vD\right)^{1/2}} \qquad (2.6)$$

Since for all Reynolds numbers under consideration the Strouhal number (referred to the von Kàrmàn vortices frequency f_K) is almost constant:

$$f_K \propto \frac{U_\infty}{D} \qquad (2.7)$$

[1] Bloor-Gerrard vortices are also identified in the literature as the Kelvin-Helmotz instability, shear layer instability, secondary vortices as well as transition waves.

Then:

$$\frac{f_{SL}}{f_K} \propto \frac{U_\infty^{3/2}}{(vD)^{1/2}} \frac{D}{U_\infty} = \frac{(U_\infty D)^{1/2}}{(v)^{1/2}} = Re^{1/2} \qquad (2.8)$$

After Bloor (1964), Wei and Smith (1986), by using a vortex counting technique in conjunction with the flow field visualisation, found:

$$\frac{f_{SL}}{f_K} = 0.0047\, Re^{0.87} \qquad (2.9)$$

whereas, accordingly with Bloor (1964) Kourta et al. (1987), by means of hot wire measurements, found:

$$\frac{f_{SL}}{f_K} = 0.095\, Re^{1/2} \qquad (2.10)$$

More recently Thompson and Hourigan (2005) have reinterpreted all these results and have concluded that the interpretation of the phenomenon suggested by Bloor (1964) is the most appropriated. In the same year, Rajagopalan and Antonia (2005) measured the frequencies ratio and compared their measurement with the ones present in the literature (see Fig. 2.4). They concluded that the best fit to all the data yields an exponent equal to 0.65, whereas the $Re^{0.5}$ distribution also shown in Fig. 2.4 is clearly not adequate.

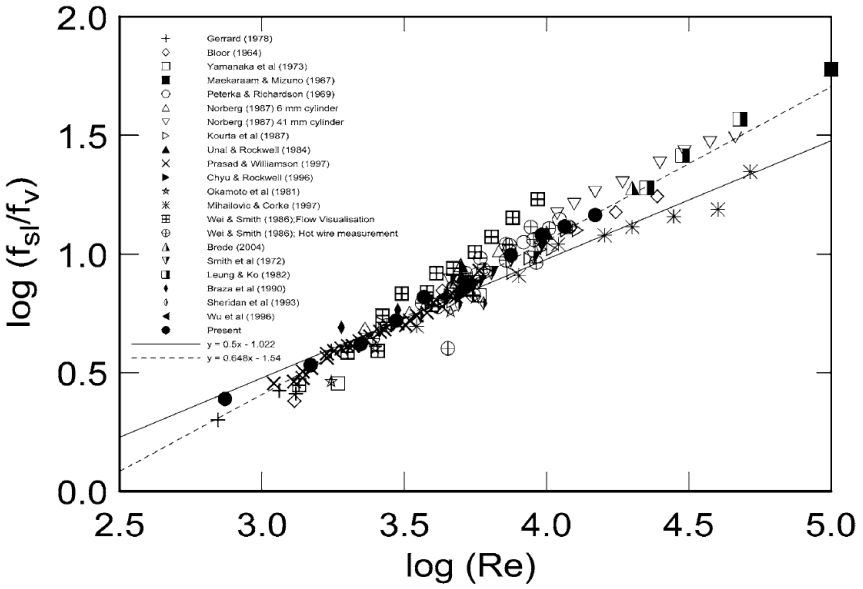

Fig. 2.4 Variation of f_{SL}/f_K with the Reynolds number (Rajagopalan and Antonia 2005).

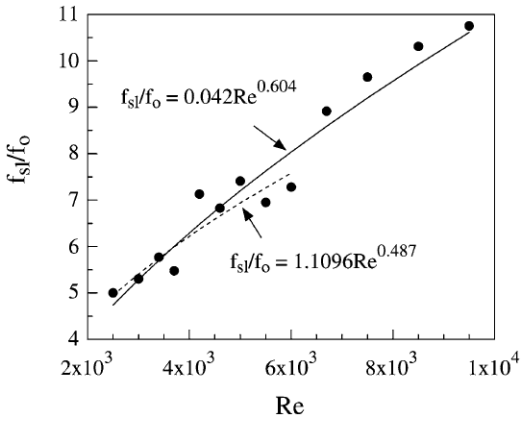

Fig. 2.5 f_{SL}/f_K as a function of *Re* (Saad et al. 2007)

Later on, Saad et al. (2007) have measured the ratio f_{SL}/f_K for $2\cdot10^3<Re<10^4$ (see Fig. 2.5) and obtained:

$$\frac{f_{SL}}{f_K} = 0.1096\, Re^{0.487} \qquad (2.11)$$

for $2\cdot10^3<Re<6.5\cdot10^3$ with a correlation factor of 0.985, while:

$$\frac{f_{SL}}{f_K} = 0.042\, Re^{0.604} \qquad (2.12)$$

for the whole range of interrogation, obviously with a lower correlation factor.

In conclusion, according to Norberg (1994), a single power law may not represent the variation of the normalised shear layer frequency. He observed that the *Re* dependence of f_{SL}/f_K can be divided in two ranges, with a larger exponent for $Re<5\cdot10^3$ and a smaller one for $5\cdot10^3<Re<10^5$. Based on this and other observations, he suggested that the flow undergoes a basic changes at $Re=5\cdot10^3$.

According to Williamson (1996), the shear layer vortices wavelength (in the streamwise direction) is given by:

$$\frac{\lambda_{SL}}{D} \approx \frac{37}{Re^{1/2}} \qquad (2.13)$$

which, if it is combined with:

$$\frac{L_f}{D} \approx 2 \qquad (2.14)$$

valid for $Re \approx 10^3$, produces:

$$\lambda_{SL} < L_f \qquad (2.15)$$

for $Re > 360$. A similar relation has been found by Wu et al. (1996):

$$\frac{\lambda_{SL}}{D} \approx \frac{34}{Re^{1/2}} \qquad (2.16)$$

Obviously, to see the instability wake, it isn't enough that the wavelength λ_{SL} should be smaller than the vortex formation length L_f, but also that the amplification of the shear layer instability should be important. For this reason, Roshko (1993) concluded that the shear layer vortices are detectable only for $Re > 1.2 \cdot 10^3$. In Fig. 2.2 the shear layer vortices amalgamated with the von Kàrmàn ones are shown for $Re = 4 \cdot 10^3$. A similar configuration is also found in the flow visualisation of Lin et al. (1995a). In the latter (see Fig. 2.6) it can be seen that near the point situated at 180° from the front stagnation point the streamlines pattern is ill-defined, especially at $Re = 5 \cdot 10^3$. This distortion is caused by the Bloor-Gerrard vortices in the separating shear layer which are added to the very low intensity of the streamline pattern. For $Re = 10^4$ more than for $Re = 5 \cdot 10^3$ the small scale vortices embedded within the large scale ones are very well visible.

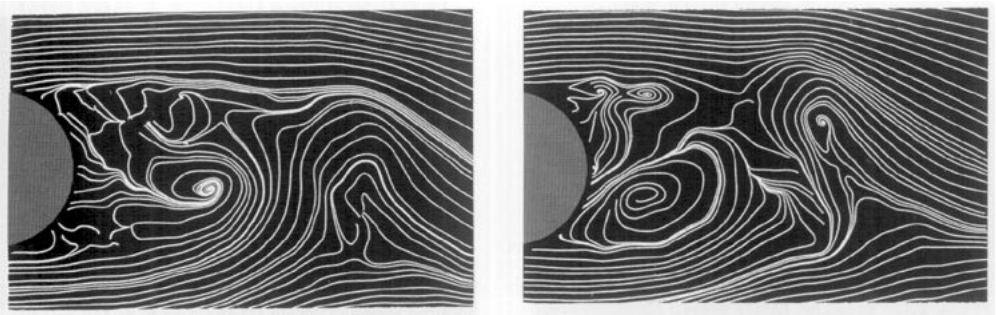

$Re = 5 \cdot 10^3$ $Re = 10^4$

Fig. 2.6 Instantaneous streamlines (Lin et al. 1995a).

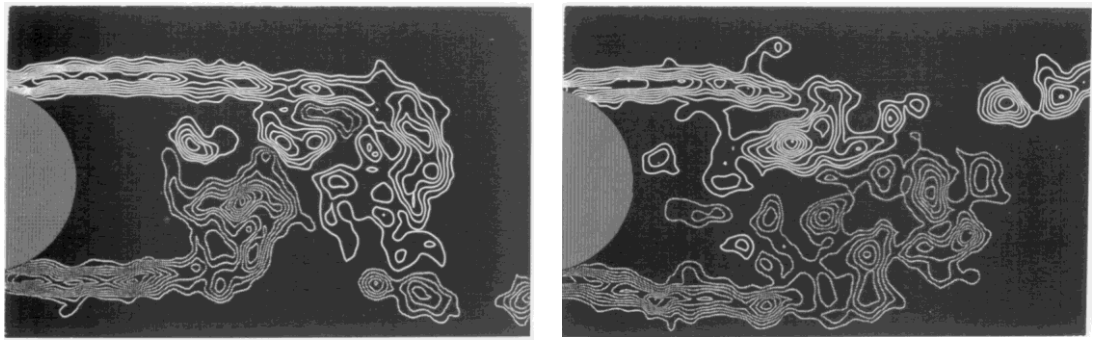

a *b*

$Re = 5 \cdot 10^3$

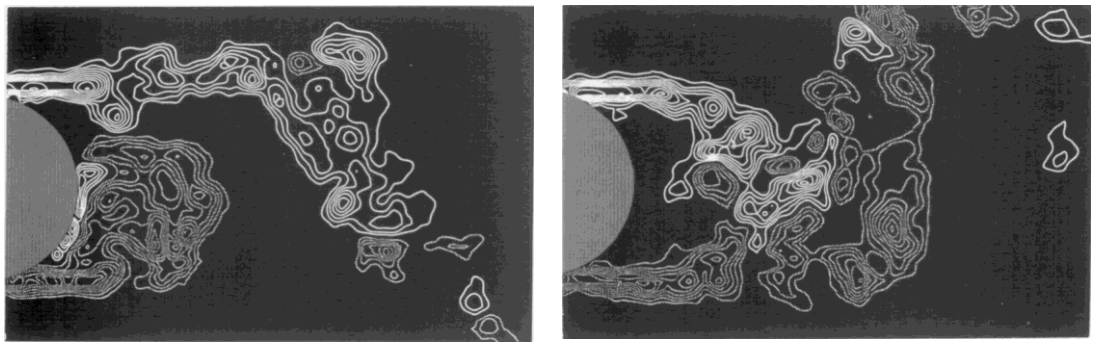

c *d*

$Re = 10^4$

Fig. 2.7 Instantaneous states of near-wake structure represented by contours of constant positive (grey) and negative (white) vorticity (Lin et al. 1995a).

In Fig. 2.7 the instantaneous vorticity patterns of the near wake structure are shown for $Re = 5 \cdot 10^3$ and $Re = 10^4$. Fig. 2.7-*a* shows the predominantly occurring pattern for $Re = 5 \cdot 10^3$. There are small scale vortices amalgamated in both well defined von Kàrmàn vortices (in the lower side of the cylinder) and a shear layer region. Also Fig. 2.7–*b* is referred to the same Reynolds number, but in this case the near wake pattern is almost symmetric.

According to Lin et al. (1995a) this means that the periodic phenomenon of vortex shedding is occasionally interrupted, by producing a quasi-symmetric pattern. Also at $Re = 10^4$ there is a predominant pattern (Fig. 2.7-*c*) of the vortex shedding occasionally interrupted by an approximately symmetric pattern (Fig. 2.7-*d*). The substantial difference between the patterns relative to the two Reynolds numbers is that, for the higher *Re*, there are well formed small-scale structures nearer to the shear layer separation point. Lin et al. (1995a) hypothesized that this abrupt development of the small scale structures at $Re = 10^4$ leads to increased Reynolds stresses and consequently the shear layer amalgamate earlier in the von

Kàrmàn vortices. Accordingly, the vortex formation process is shown closer to the cylinder. This consideration is also supported by Chyu et al. (1995), who demonstrated, by enhancing small scale vortices with external excitation, that the von Kàrmàn vortices development is accelerated by the small scale ones. Later on, Saad et al. (2007) asserted that the two parameters, which play an important role in the formation of the vortex shedding, are the shear layer diffusion length L_d and the vortices formation length L_f (see Sect. 2.1.2).

2.1.2 Von Kàrmàn vortices development

In 1912 von Kàrmàn (see Fig. 2.8) interpreted the cylinder wake oscillations as an intrinsic phenomenon and to support this consideration, he studied the stability of a vortices street. He found that two rows of opposite-signed vortices are unstable in both symmetric and asymmetric configurations, except for a particular asymmetric geometry. Since the experimental configuration obtained in the cylinder wake was very similar to the one obtained by von Kàrmàn, that analysis had a great success. However, the von Kàrmàn analysis demonstrated only the stability of an infinite vortices street and it isn't well understood how this vortices street is related to a bluff body. In other words, that analysis didn't explain how the bluff body can generate the vortices street, but assured that, if such a configuration develops, it can be stable and it is visible for a long distance downstream.

Only several decades after there was a descriptive understanding of the vortex development. Gerrard (1966) suggested that a developing vortex drags the opposite sign shear layer from the other side of the wake, eventually cutting off the supply of vorticity to the growing vortex. Perry et al. (1982) interpreted the vortex formation process in terms of instantaneous streamlines (see Fig. 2.9): initially, the cylinder wake is symmetric; when the wake begin to shed, a cavity opens and a "alleyways" of fluid moves to fill the cavity. According to Fig. 2.9, the vortex A grows following the configurations from (a) to (d) until a saddle point S forms in (e). The formation of a saddle point is the result of the detaching of a vortex from the cylinder and, when it forms a new vortex (anticlockwise in (e) in the low side of the cylinder) is born.

Fig. 2.8 Theodore von Kàrmàn (original Hungarian name Szőllőskislaki Kármán Tódor). May 11, 1881 – May 6, 1963

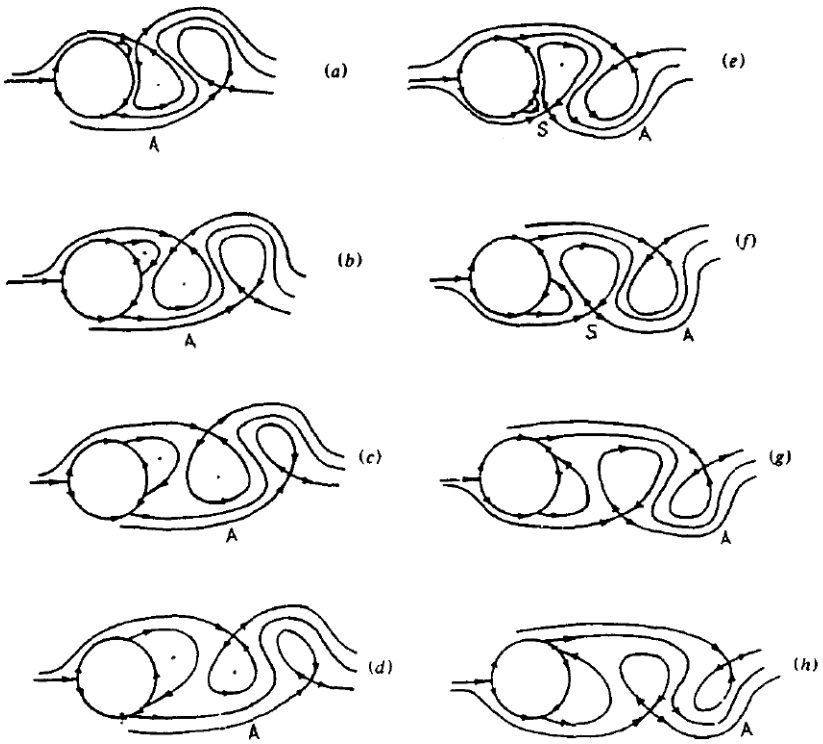

Fig. 2.9 Vortex shedding model using topology of instantaneous streamlines (Perry et al. 1982).

As already said, Chyu et al. (1995) demonstrated, by enhancing small scale vortices with external excitation, that the von Kàrmàn vortices development is accelerated by the small scale ones, i.e. the vortex formation length L_f decreases. Accordingly with these considerations, Saad et al. (2007) asserted that the two parameters, which play an important role in the formation of the vortex shedding, are the shear layer diffusion length and the vortices formation length (L_d and L_f respectively, see Fig. 2.3-*a*). Both L_d/D and L_f/D are plotted as a function of the Reynolds number in Fig. 2.10.

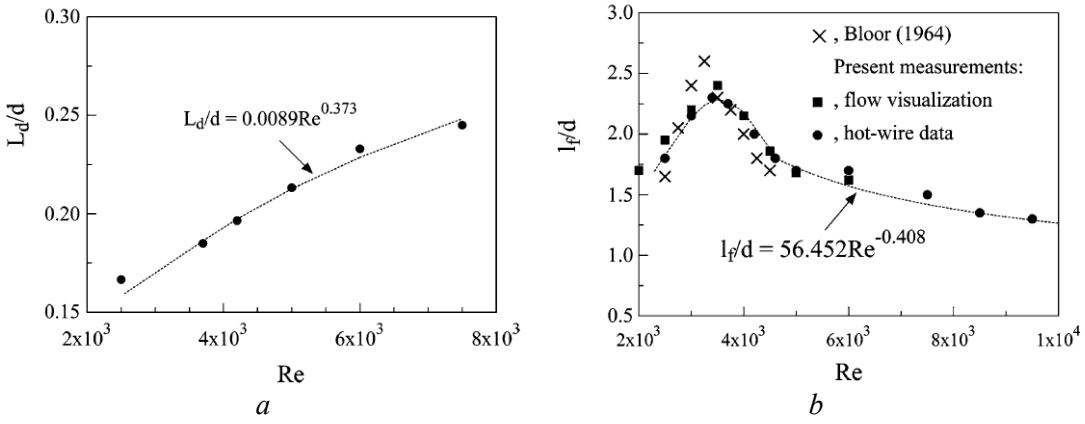

Fig. 2.10 Normalised shear layer diffusion length (*a*) and vortices formation length (*b*) as a function of *Re* (Saad et al. 2007).

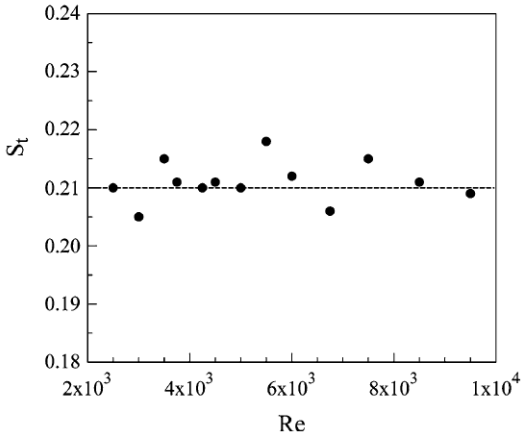

Fig. 2.11 Strouhal number as a function of *Re* (Saad et al. 2007).

According to Gerrard (1966) and Saad et al. (2007), the increase of L_d/D is due to fact that by increasing *Re* the transition point moves upstream in the shear layer (see Fig. 2.3-*b*) and as a consequence the turbulent length of the shear layer grows. Consistently, more fluid can entrain in the shear layer, making it thicker and more diffused. This phenomenon causes a longer time to initiate the vortex shedding, since it's needed to reach a sufficient concentration of vorticity. On the other hand, as *Re* increases, L_f decreases and consequently the interaction of the two shear layer is facilitated when they come close together. Then, the shortening of L_f tends to decrease the vortex formation periodic time. As a result of these considerations, the actions of the two lengths (L_d and L_f) are in antithesis, producing an almost constant Strouhal number (see Fig. 2.11) for a wide range of *Re* number.

2.1.3 Vortex formation length

Bloor (1964) investigated how the length of vortices formation region depends on the Reynolds number. She considered that length as the distance between the centre of the cylinder and the point downstream of the body where the velocity fluctuation level has grown to a maximum and thereafter decays downstream. This means that the end of the formation region is where fluid from outside the wake first crosses the axis. Bloor found that the vortices formation length L_f increases from 2 to 2.5 diameters by varying the Reynolds number from about 300 to $3 \cdot 10^3$. Afterwards, there is a steady fall of L_f by increasing Re.

This decrease of the formation length can be represented in terms of the streamwise variation of a characteristic velocity fluctuation, as described by Bloor and Gerrard (1966) and Szepessy and Bearman (1992). It is also shown in the qualitative flow visualization of Unal and Rockwell (1988) and Lin et al. (1995a).

Saad et al. (2007) investigated a wider Re range and obtained the results shown in Fig. 2.10-*b*, where also Bloor's data are reported. They found that L_f increases from $1.5D$ to $2.3D$ by varying the Reynolds number from $2.5 \cdot 10^3$ to $3.4 \cdot 10^3$. Above this, L_f decreases as the Reynolds number increases until 10^4. For the latter range, a relation which fits well with the experimental points is:

$$\frac{L_f}{D} = 56.452\, Re^{-0.408} \qquad 2.17$$

The decrease of L_f by increasing Re could be caused by the upstream motion of the transition point (see Fig. 2.3-*b*). As explained before, this phenomenon causes the thickening of the shear layer (see Fig. 2.10-*a*) and consequently the formation vortex develops and sheds into the wake earlier.

2.1.4 Mean flow field

Braza et al. (2006) measured the mean flow field at $Re=1.4 \cdot 10^5$ by means of 2C and 3C Particle Image Velocimetry (PIV) technique. Since it is obtained by averaging the alternating vortices, the mean streamlines pattern (see Fig. 2.12) has two-symmetric eddies. It's a result of the symmetric pattern of u and asymmetric one for v (see Fig. 2.13). According to Braza et al. (2006) the normalised vortices formation length L_f/D is about 1.28 and 1.23 if measured by 2C and 3C PIV respectively. Fig. 2.14 shows the iso-contours of the strain rate tensor component:

$$S_{12} = \frac{1}{2}\left(\frac{\partial u}{\partial y} + \frac{\partial v}{\partial x}\right) \qquad 2.18$$

and the rotation rate tensor component (vorticity):

$$W_z = \frac{1}{2}\left(\frac{\partial v}{\partial x} - \frac{\partial u}{\partial y}\right) \qquad 2.19$$

The strain and rotation rate tensors were computed with a central difference scheme. The components of these two tensors reported in Fig. 2.14 have a two-lobes asymmetric configuration and the same order of magnitude.

Fig. 2.15 and Fig. 2.16 show the iso-contours of the Reynolds stress components $u'u'$, $v'v'$, $w'w'$ and $u'v$. The remaining components $u'w'$ and $v'w'$ are very small, confirming the two-dimensionality of the mean flow.

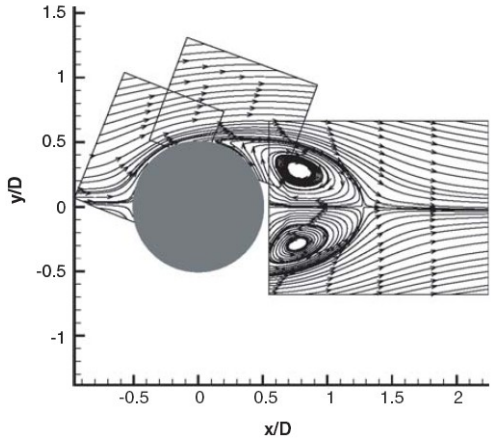

Fig. 2.12 Streamlines of mean flow field at Re=1.4·10^5 (Braza et al. 2006).

Both the turbulent kinetic energy k and turbulent production term p are shown in Fig. 2.17 and computed as below:

$$k = u'u' + v'v' + w'w' \qquad 2.20$$

$$p = u'u'\frac{\partial u}{\partial x} + v'u'\frac{\partial v}{\partial x} + w'u'\frac{\partial w}{\partial x} + u'v'\frac{\partial u}{\partial y} + v'v'\frac{\partial v}{\partial y} + w'v'\frac{\partial w}{\partial y} \qquad 2.21$$

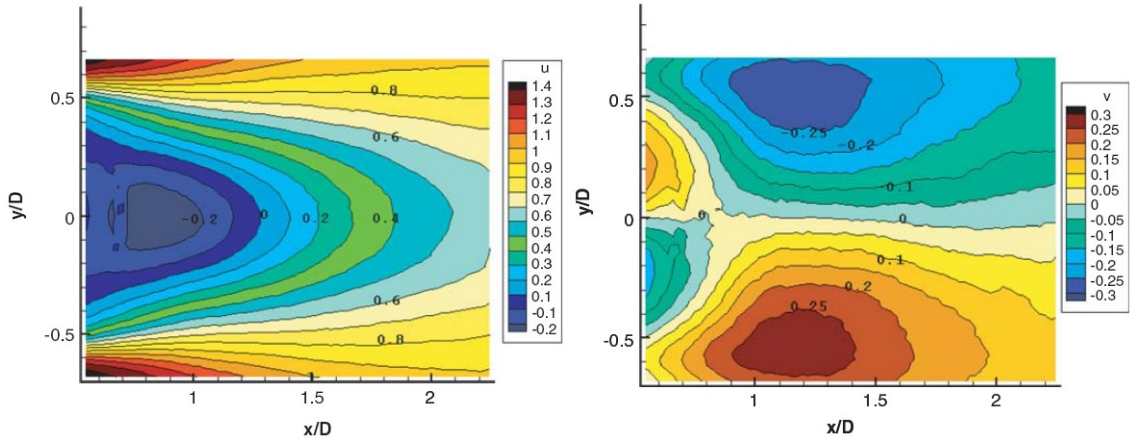

Fig. 2.13 *u* and *v* iso-contours of mean flow field at Re=1.4·10^5 (Braza et al. 2006).

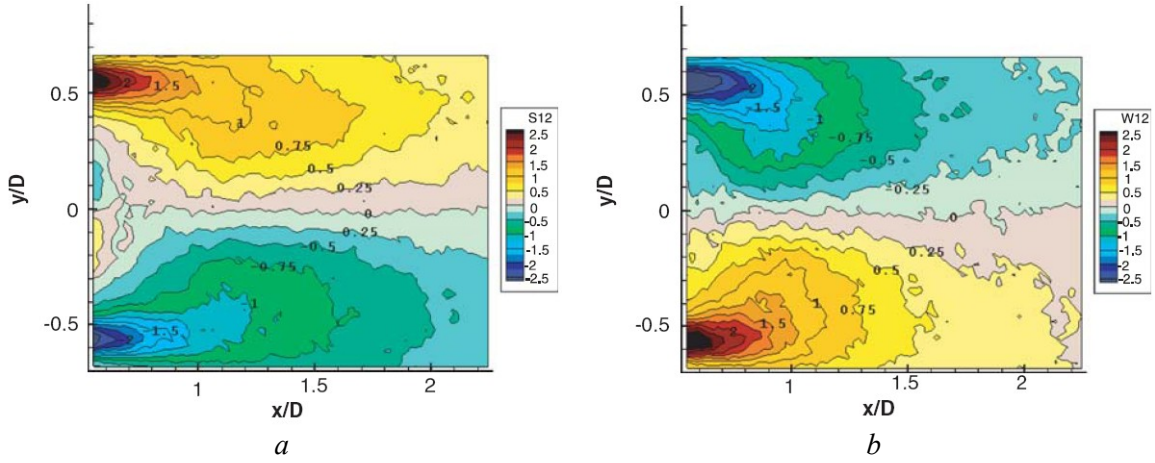

Fig. 2.14 Mean strain rate (*a*) and mean rotation rate (*b*) at Re=1.4·10^5 (Braza et al. 2006).

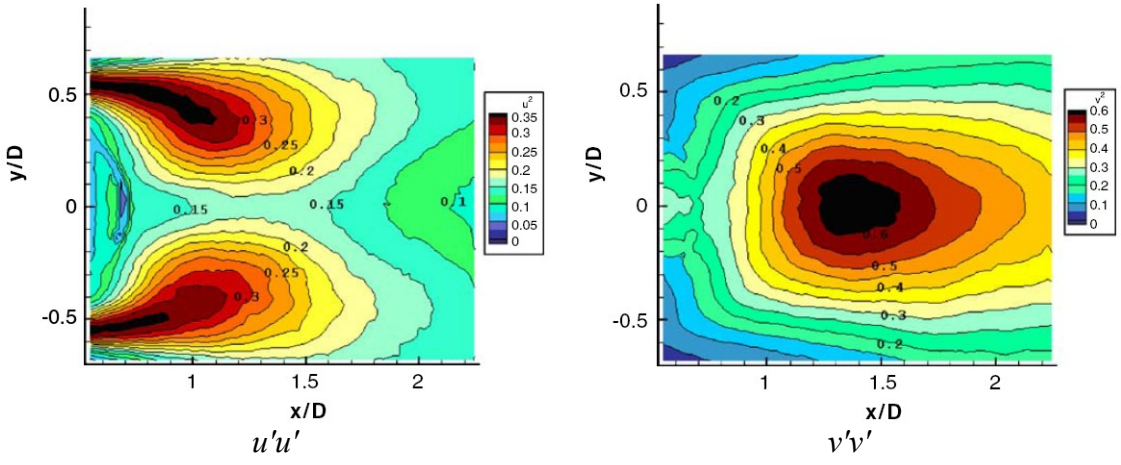

Fig. 2.15 Mean Reynolds stresses at Re=1.4·10^5 (Braza et al. 2006).

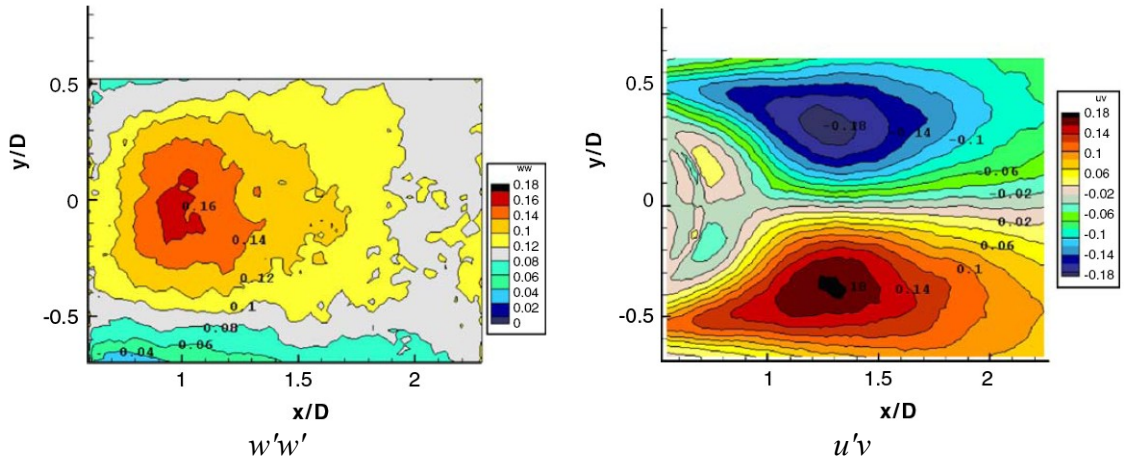

Fig. 2.16 Mean Reynolds stresses at Re=1.4·10^5 (Braza et al. 2006).

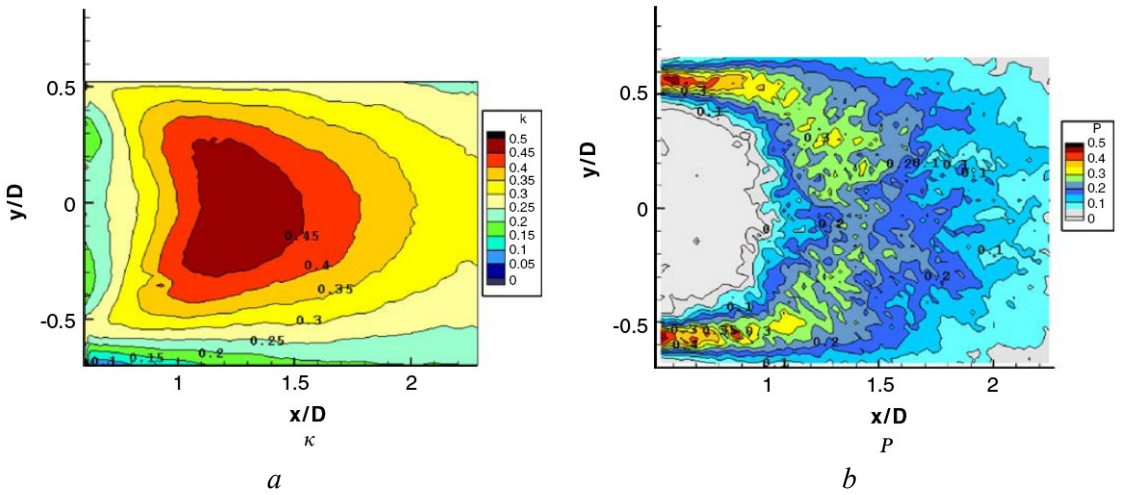

Fig. 2.17 Mean turbulent kinetic energy k (*a*) and production p (*b*) at Re=1.4·10^5 (Braza et al. 2006)

According to Braza et al. (2006), all the components of the Reynolds stress tensor have their maximum value near the vortices formation region and this explains why the turbulent kinetic energy has a one-lobe structure with the maximum located at x/D=1.25 on the rear axes.

2.1.5 Phase averaged flow fields

Braza et al. (2006) also measured the phase averaged flow field. Triggering the PIV images acquisition with a pressure signal did the phase averaging. The periodic vortex shedding is clearly shown in Fig. 2.18, where the streamlines of the phase averaged flow at phase angles 0, π/2, π and 3π/2 are shown. The vortex centres have been identified with the

Q-criterion (Jeong and Hussain 1995) and shown in Fig. 2.19. Accordingly with Cantwell and Coles (1983), the trajectories seem to be nearly parallel to the rear axis after x/D=2. The longitudinal mean velocity of the vortices has been measured and found to reach the value $0.7U_\infty$ at x/D=2.

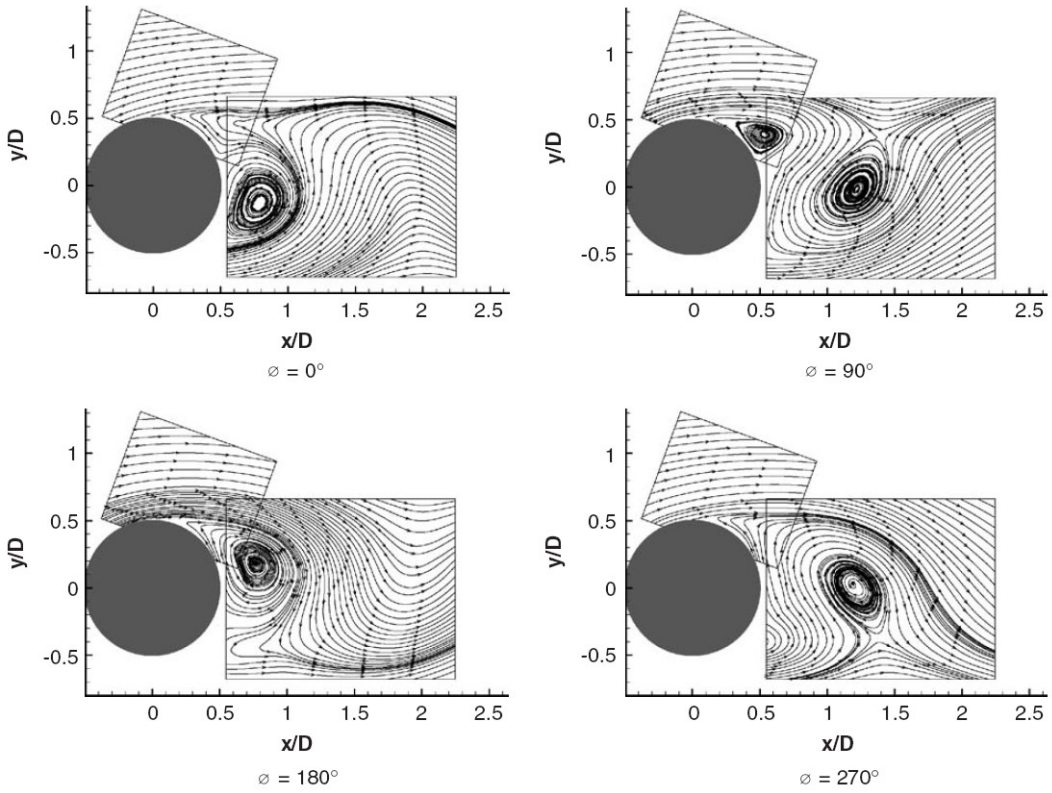

Fig. 2.18 Streamlines of phase averaged flow fields at Re=1.4·10^5 (Braza et al. 2006).

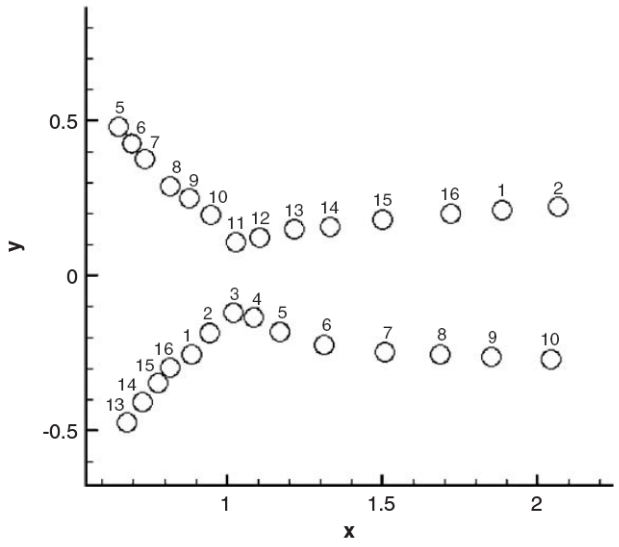

Fig. 2.19 Trajectories of the alternating vortices. Circles indicate the centres of the vortices and number indicates the phase (1:φ=0; …; n: 2π-2π/n). Braza et al. (2006).

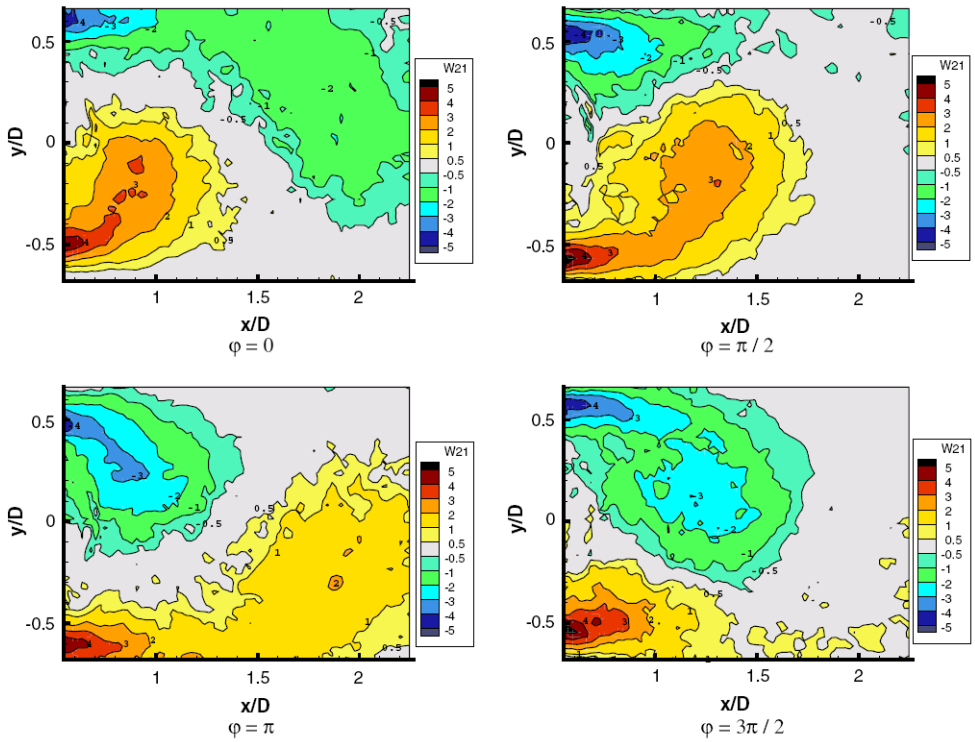

Fig. 2.20 Vorticity of phase averaged flow fields at Re=1.4·10^5 (Perrin et al. 2007a).

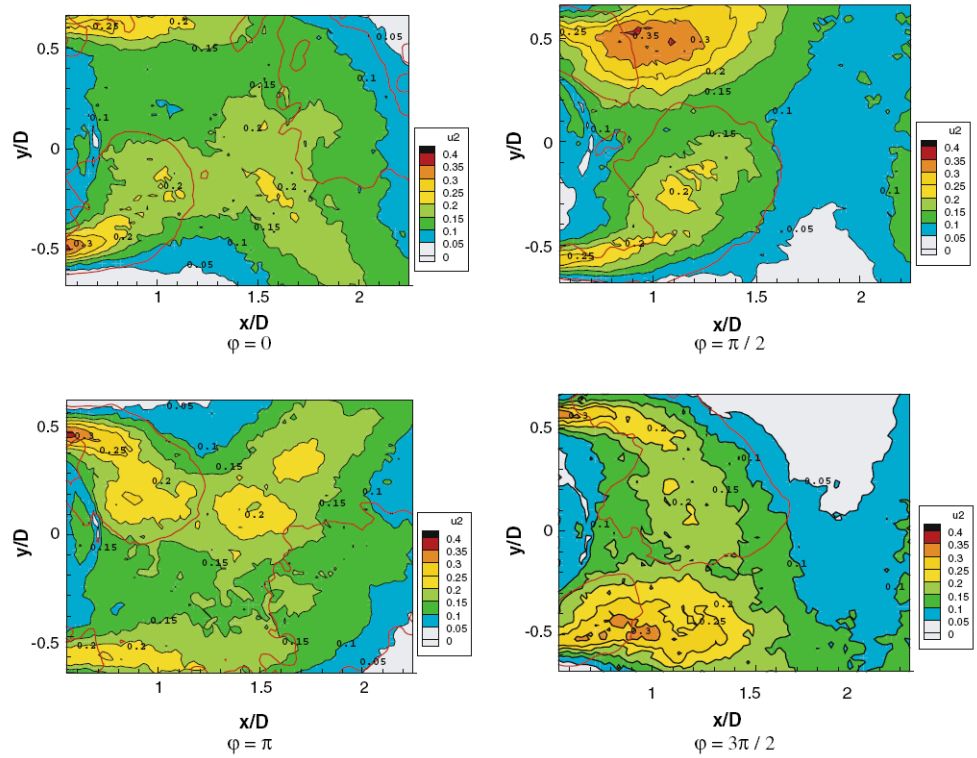

Fig. 2.21 Reynolds stress component $u'u'$ of phase averaged flow fields at Re=1.4·10^5 (Perrin et al. 2007a).

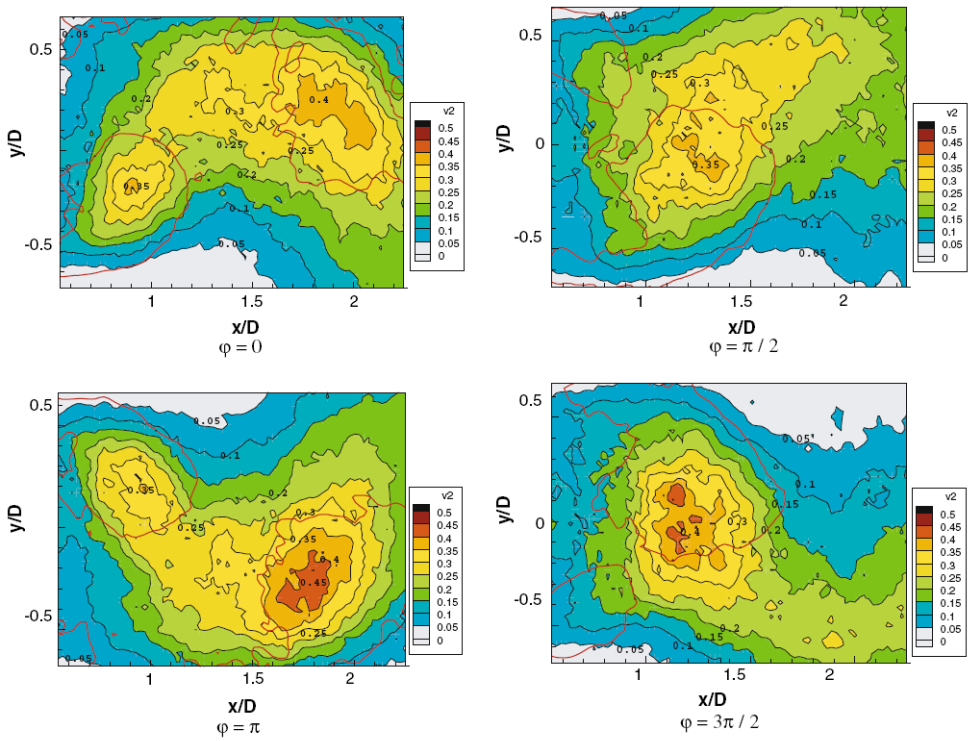

Fig. 2.22 Reynolds stress component $v'v'$ of phase averaged flow fields at Re=1.4·10^5 (Perrin et al. 2007a).

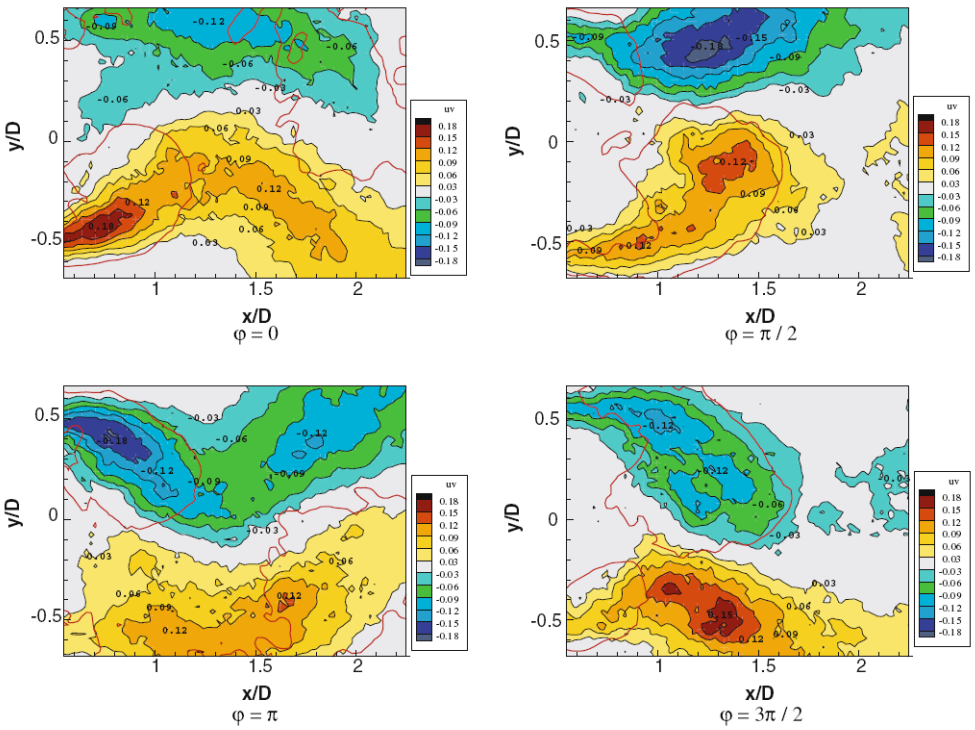

Fig. 2.23 Reynolds stress component $u'v'$ of phase averaged flow fields at Re=1.4·10^5 (Perrin et al. 2007a).

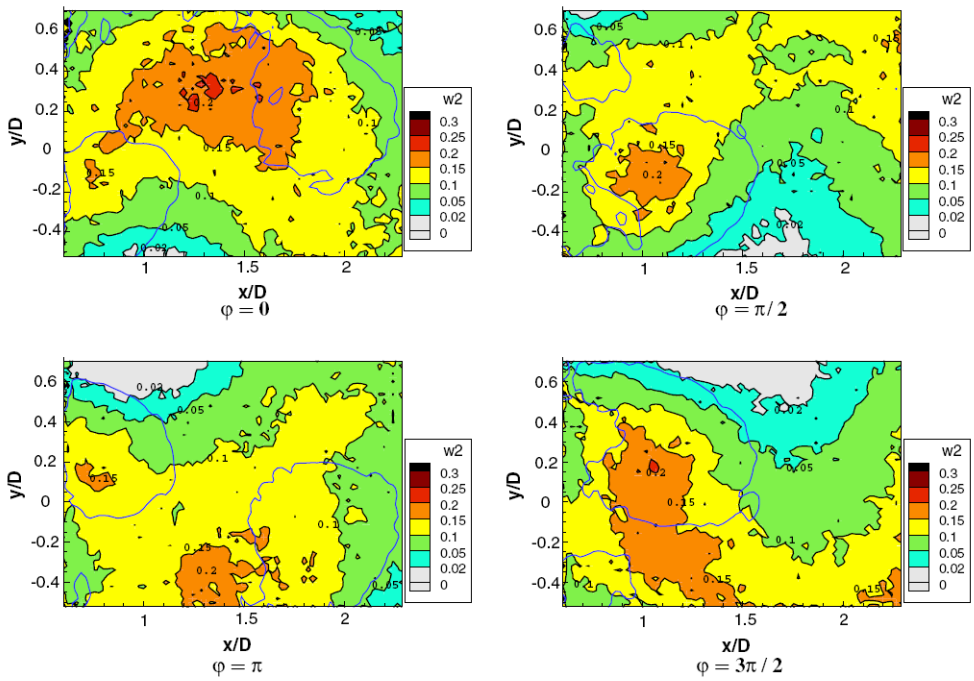

Fig. 2.24 Reynolds stress component $w'w'$ of phase averaged flow fields at Re=1.4·10^5 (Perrin et al. 2007a).

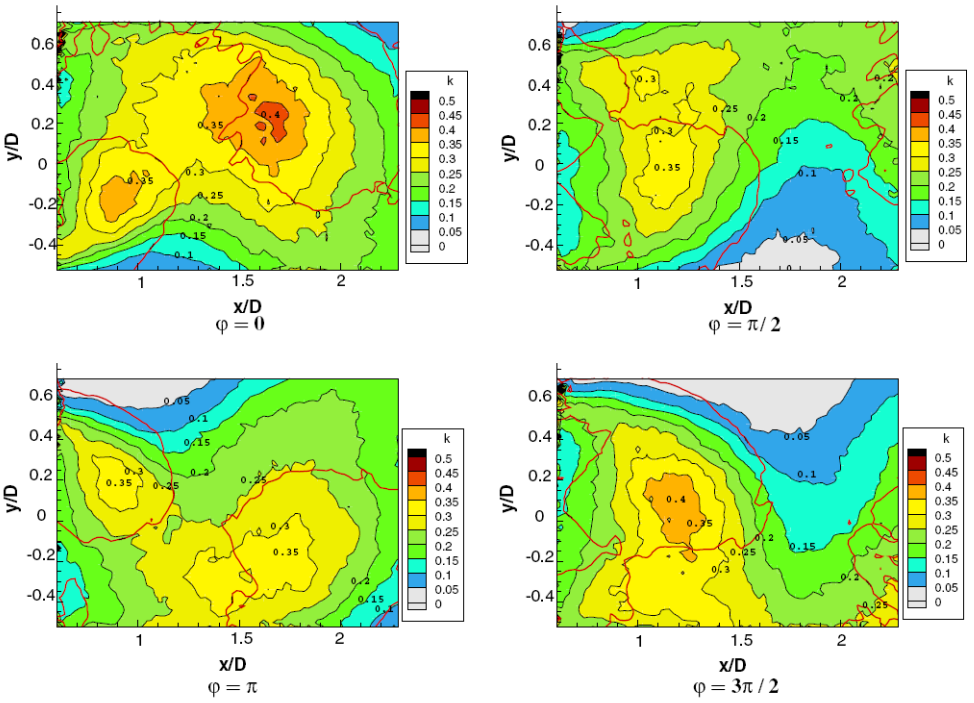

Fig. 2.25 Turbulent kinetic energy of phase averaged flow fields at Re=1.4·10^5 (Perrin et al. 2007a).

Relatively to the same experimental apparatus and measurements, Perrin et al. (2007a) evaluated the dimensionless vorticity at 4 constant phases (see Fig. 2.20). It can be seen that the absolute value of vorticity peak at the vortex centre decreases from 3 to 1 when the vortex moves downstream from x/D=0.6 to x/D=2.

The Reynolds stresses at constant phase are shown in Fig. 2.21, Fig. 2.22 and Fig. 2.23 for components $u'u'$, $v'v'$ and $u'v'$, respectively. Also in this case, the results are in agreement with that shown by Cantwell and Coles (1983):

- downstream of the formation region, the normal stresses have high values near the vortex centres, while the maxima of the shear stress are located around the vortices;
- in the formation region, significant values of $u'u'$ and $u'v'$ are found in the shear layer.

The component $w'w'$ is shown in Fig. 2.24, while the quantities w, $u'w'$ and $v'w'$ are found to be smaller than the measurement uncertainties. The spanwise normal stress $w'w'$ shows the maxima near the vortices and also significant values are collocated between them, e.g. at $\varphi=0$ and $\varphi=\pi$. According to Perrin et al. (2007a), this is due to the longitudinal vortices which connect the primary ones (see Sect. 2.1.6).

Finally, the turbulent kinetic energy is shown in Fig. 2.25. According to the topology of the normal stresses, the maxima are located near the centre of the vortices.

In all the normal and shear stress maps as well as in the turbulent kinetic energy one, the red (or blue, in Fig. 2.24) lines indicates the iso-lines Q=0.5 of the Q-criteria which identifies the vortices (Jeong and Hussain 1995).

2.1.6 Longitudinal vortices

Wu et al. (1994) investigated the longitudinal vortices past a circular cylinder at Re=525 and deduced that the maximum vorticity and circulation of the longitudinal vortices were respectively larger and smaller than those of the spanwise vortices. This phenomenon was connected to a mechanism of stretching of the longitudinal vortices.

In the hydrogen-bubble visualization of Wu et al. (1994) (Fig. 2.26-*a*) it can be seen the mushroom type structures (indicated by the arrow) which develop in the near wake. These imply the existence of the counter-rotating longitudinal vortices in the cylinder wake. Fig. 2.26-*b* and *c* show an instantaneous velocity distribution measured in a reference frame moving with the eddy convection velocity equal to 60% of U_∞. According to Wu et al. (1994), the spiralling of the streamline patterns near the vortices centre is indicative of the flow three-dimensionality. To show the spanwise variation caused by the existence of the longitudinal vortices, Wu et al. (1994) measured a typical instantaneous velocity profile through the centre of longitudinal vortices, as shown in Fig. 2.27. In the figure, u is the streamwise velocity and z is the spanwise axis (parallel to the cylinder axis).

In the same year, also Lin et al. (1995b) investigated longitudinal vortices, by using the Particle Image Velocimetry technique. They provided an interesting 3D representation of

them, shown in Fig. 2.28. The lower left end of the rectangular box represents the *y-z* plane at *x*/*D*=1. The three-dimensional vorticity pattern shows a sinusoidal undulation due to successive formation of the von Kàrmàn vortices.

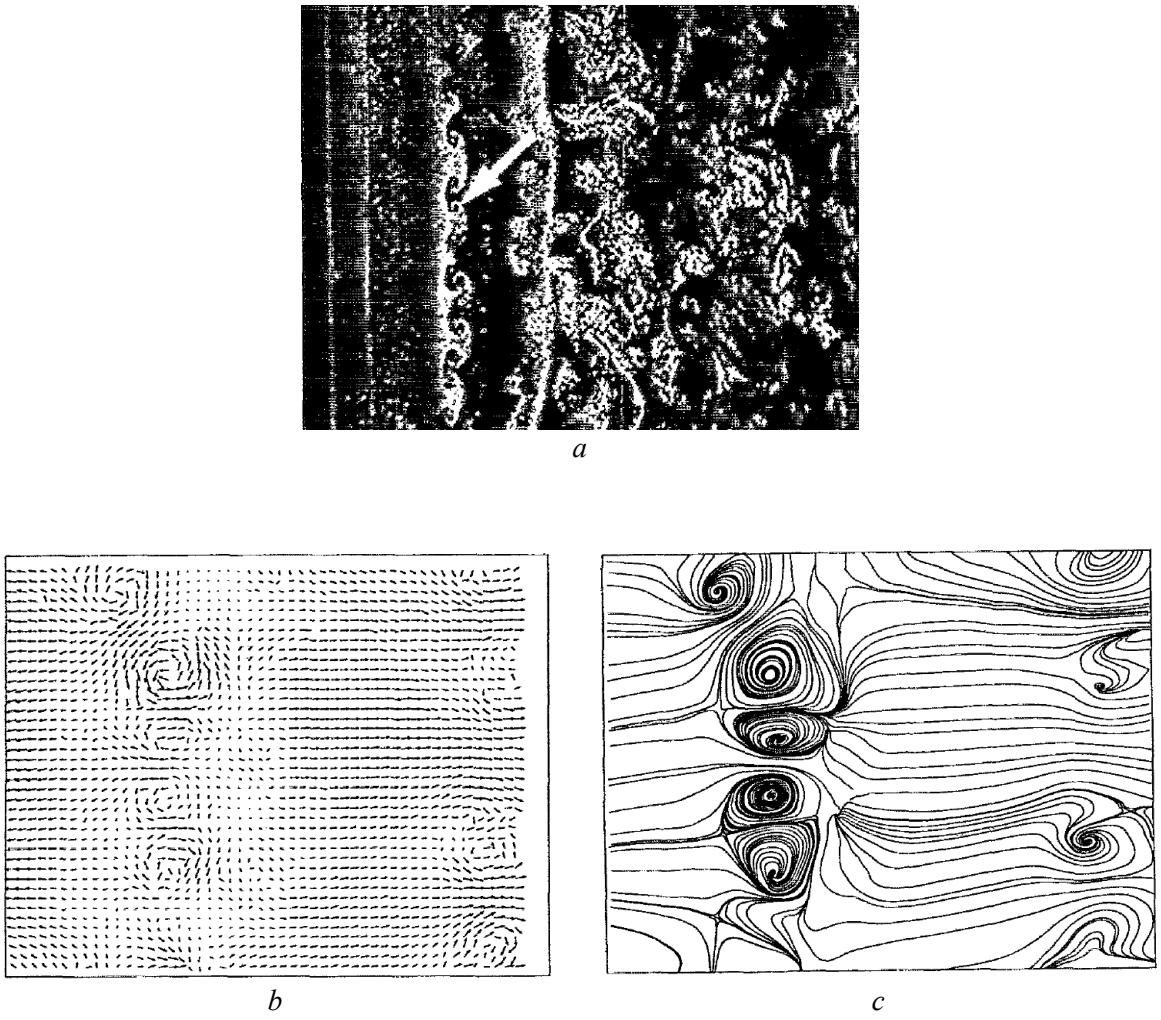

a

b *c*

Fig. 2.26 Flow field in the *x-z* plane. The cylinder is located on the left. *a*- Hydrogen-bubble flow visualization. *b*- Velocity vectors seen in a frame of reference moving at 60% of U_∞. *c*- Sectional streamlines seen in the moving frame of reference. *Re*= 525 (Wu et al. 1994).

Each vorticity volume originating at the left end of the box retains its identity for at least 1.5 cycle of the von Kàrmàn vortices formation. This time scale is an order of magnitude larger than that of shear layer vortices. In Fig. 2.28 is also noticeable that the vorticity volumes exhibit a pattern of alternating sense. The characteristic spanwise wavelength vorticity volume with the same sign is of the order of the cylinder diameter.

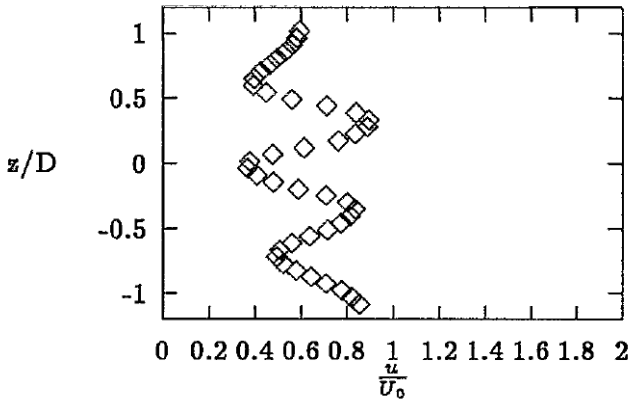

Fig. 2.27 Spanwise variation of *u*: an instantaneous velocity profile sliced through the centre of the longitudinal vortices. *Re*= 525 (Wu et al. 1994).

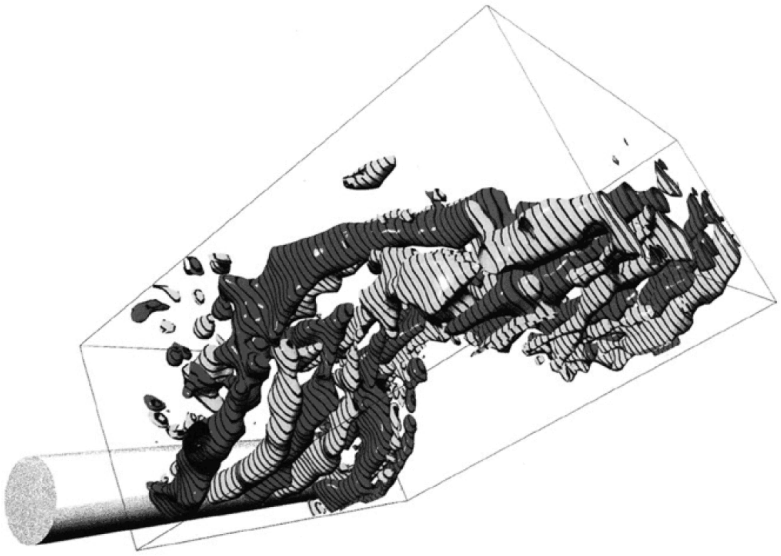

Fig. 2.28 Space-time representation of streamwise vorticity over a time interval corresponding to period of von Kàrmàn vortices formation – $Re=10^4$ (Lin et al. 1995b).

Wu et al. (1996) measured both the wavelengths of the longitudinal vortices developed in the shear layer vortices as well as in the von Kàrmàn ones. They noticed that the ratio between the spanwise wavelength of the longitudinal vortices λ_{SL3} developed in the shear layer and streamwise of the shear layer vortices λ_{SL} is:

$$\frac{\lambda_{SL3}}{\lambda_{SL}} = 0.67 \qquad (2.22)$$

Substituting the Eq. 2.16 in Eq. 2.22 gives:

$$\frac{\lambda_{SL3}}{D} = \frac{23}{Re^{1/2}} \qquad (2.23)$$

The spanwise wavelength of the longitudinal vortices developed in the von Kàrmàn ones were measured, in the Reynolds number range 250-$1.8 \cdot 10^3$, directly from the images. The two spanwise wavelengths are reported in Fig. 2.29. It can be seen that for $Re > 2 \cdot 10^3$ the two structures have quite different spanwise length scales. This observation suggests that they might be effectively decoupled.

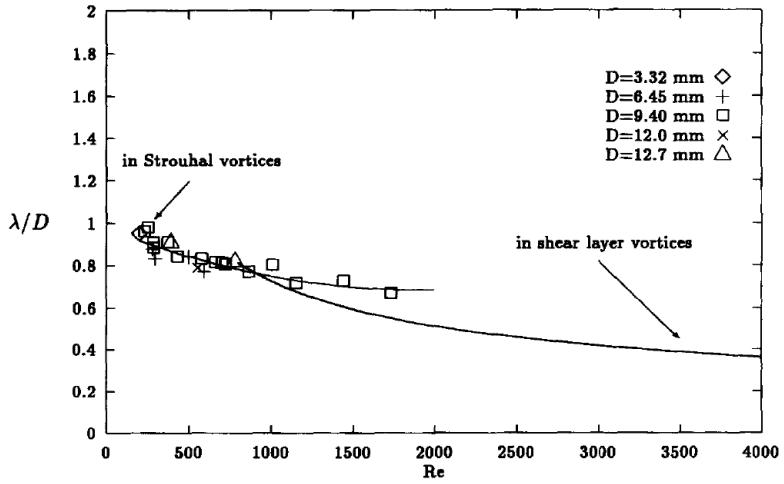

Fig. 2.29 A comparison of spanwise wavelength: streamwise vortices in the separating shear layer and in the von Kàrmàn vortices (Wu et al. 1996).

More recently, Scarano et al. (2006) performed tomo-PIV measurements of the cylinder wake. The visualisation of the wake instantaneous structure in a volume behind the cylinder permitted to obtain the separate contribution of the von Kàrmàn vortices and the interconnecting structures between them. A value of spanwise wavelength equal to 1.2*D* has been found, in good agreement with Lin et al. (1995b). Furthermore, Scarano et al. (2006) found that the vortices organisation into pairs is similar to the instability *Mode B* occurring in lower Reynolds number (*3D Wake Transition Regime* mentioned before).

2.2 Finite cylinder

For a finite circular cylinder there are different flow pattern changes along the cylinder height. In particular, a counter-rotating pair of tip vortices forms at the free end and extends into the wake. These vortex structures interact in a complex manner with von Kàrmàn vortices shedding. By reducing the aspect ratio AR=*H*/*D* in the range 2<AR<6, the regular alternating vortex shedding is replaced by symmetrical shed vortices. For smaller AR, the vortex shedding disappears, as shown by Fig. 2.30.

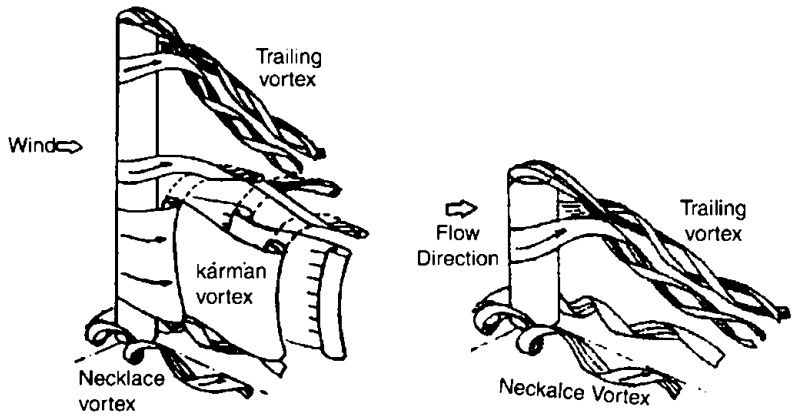

Fig. 2.30 Sketches of the flow field around a finite cylinder with length longer (left) and shorter than the critical length for vortex shedding (Kawamura et al. 1984).

In particular, for high aspect ratios, the vortex shedding frequency may vary in a cellular manner along the cylinder height and each cell has a different frequency (or Strouhal number), whereas the vortex shedding is suppressed near the free end and the cylinder base. These cellular structures disappear when AR≈6-7 and below, and a singular cell with a uniform shedding frequency along the whole cylinder height forms. For smaller aspect ratios, the flow around the cylinder tip suppress the von Kàrmàn vortices along the entire cylinder height and a symmetric arch vortex shedding at a definite frequency forms (see Fig. 2.31). In the last case, the dominant features of the time-averaged flow are: the horseshoe vortex, which forms near the cylinder base when the upstream flow separates due to the adverse pressure gradient; the vortex system on the free end, inside the separated flow; the arch vortex in the rear recirculation region; the trailing vortices downstream of the reattachment.

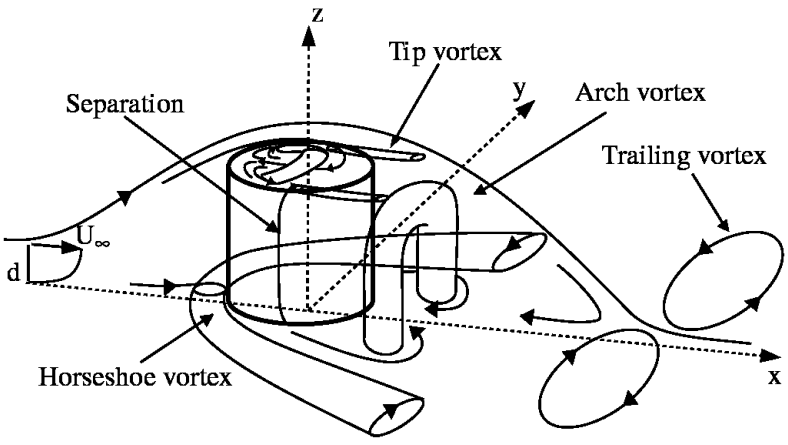

Fig. 2.31 Sketch of the flow around a finite cylinder with small aspect ratio (Pattenden et al. 2005).

Actually, the critical AR, under which the vortex shedding vanishes, varies from 1 to 7, depending on the experimental configuration parameters, e.g. the boundary layer thickness. As shown before, for infinite cylinder the fundamental parameter that determines the flow field regime is the Reynolds number, whereas for the finite one there is the influence of other parameters, as the cylinder aspect ratio AR and the ratio δ_{BL}/L between the boundary layer thickness and the cylinder height.

Some authors have investigated the effect of the aspect ratio on the vortex shedding. Okamoto and Yagita (1973) showed that the vortex shedding pattern does not exist for AR≤6. as the effects of the free end reach the base. Sakamoto and Arie (1983) investigated the effects on the vortex shedding frequency of both aspect ratio and boundary layer thickness. They found that the relation between this frequency and the aspect ratio follows a power law. Furthermore, they noticed that at AR=2.5, the shedding changes from von Kàrmàn type to symmetric arch one. This change was also observed by Okamoto and Sunabashiri (1992) at AR=4. A similar investigation was done by Sumner et al. (2004) who compared the results relative to finite cylinders with an aspect ratio equal to 3, 5 and 9. They found a different vortex shedding pattern at AR=3. By concluding, different critical ARs, under which the vortex shedding vanishes, have been found in the literature and probably this is due to different experimental configurations adopted by the authors mentioned above (e.g. δ_{BL}/L).

Other authors have investigated the mean flow field in the wake of a finite cylinder with various aspect ratios, e.g Tanaka and Murata (1999), Fröhlich and Rodi (2004), Adaramola et al. (2006), Afgan et al. (2007) and Said et al. (2008). Some authors among these have investigated the flow field with a non-negligible boundary layer thickness (see Tab. 2.1, last column).

Since the fundamental difference between the flow field past a finite and infinite cylinders is due to the free end, some authors have concentrated their investigations on the flow over the free end surface, e.g. Roh and Park (2003) and Pattenden et al. (2005).

Results obtained by most of the above mentioned authors will be shown more in details below. Almost all authors use the reference frame showed in Fig. 2.31. When this isn't true, it will be expressly said.

Author(s)	Year	AR	$Re \cdot 10^{-3}$	*BL*
Okamoto and Yagita (1973)	1973	1 -> 12.5	13	
Sakamoto and Arie (1983)	1983	1 -> 8	0.27 -> 0.92	X
Kawamura et al. (1984)	1984	1 -> 8	32	X
Okamoto and Sunabashiri (1992)	1992	0.5 -> 24	25 -> 47	
Tanaka and Murata (1999)	1999	1.25 -> 10	37	
Park and Lee (2000)	2000	6 -> 13	20	
Roh and Park (2003)	2003	1.25 -> 4.25	5.92 -> 148	
Fröhlich and Rodi (2004)	2004	2.5	43	
Sumner et al. (2004)	2004	3 -> 9	60	X
Pattenden et al. (2005)	2005	1	200	
Adaramola et al. (2006)	2006	3 -> 9	60	X
Afgan et al. (2007)	2007	6 -> 10	20	
Hain et al. (2007)	2007	2 -> 2.167	100	
Said et al. (2008)	2008	2.56	8.5 -> 64	

Tab. 2.1 Summary of previous experiments on finite cylinder.

2.2.1 Free end flow

In the past, only few authors paid attention to the flow pattern around the free end surface. At first, Etzold and Fiedler (1976) showed that a pair of vortices originates from the edge of the free end surface. Kawamura et al. (1984) confirmed the presence of these vortices and identified them as *trailing side tip vortices*. They also showed the presence of a pair of *swirl-like flow* spots on the free end surface in addition of the former pair of vortices.

Roh and Park (2003) investigated the formation development and topological features of the combination of swirl-like vortex pair and trailing side tip vortices. By changing the oil mixture ratio, they showed the streak lines on the free end surface (Fig. 2.32). Especially in Fig. 2.32-b, it can be seen a pair of eye-like spots located in the fore region. The authors affirmed that during the experiment they had observed a counter-rotation of the oil particles in the two eye-like spots, i.e. a clockwise rotation of the particles in the right eye and counter-clockwise rotation of the particles in the left one. According to Roh and Park (2003), it can be concluded that a saddle point (A in Fig. 2.32-b) should exist between these spiral nodes.

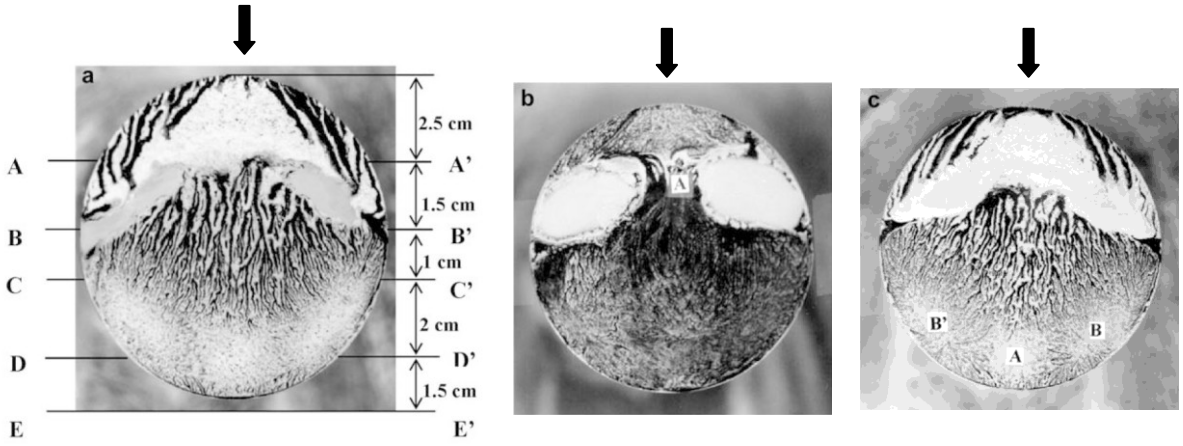

Fig. 2.32 Oil streak lines on the free end surface region for different oil mixture ratios. Flow from top to bottom, Re=1.48·10^5 and AR=1.25 (Roh and Park 2003).

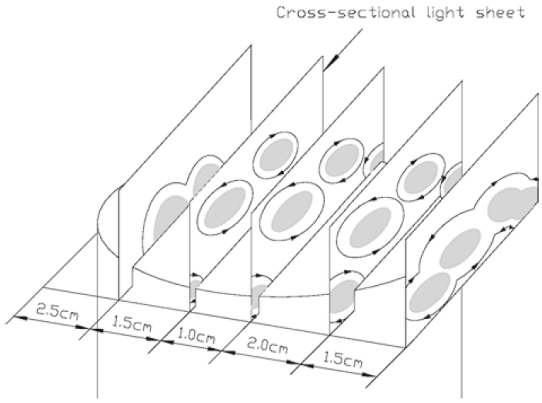

Fig. 2.33 Evolutionary vortical flow over the free end surface (Roh and Park 2003).

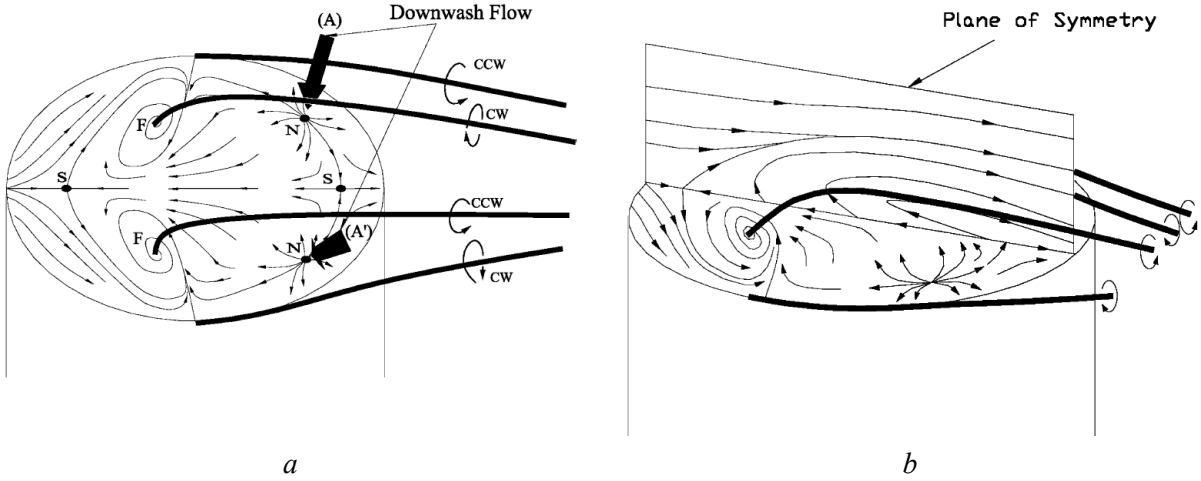

a *b*

Fig. 2.34 Topological flow pattern over the free end surface (*a*) and flow pattern in the symmetry plane (*b*) (Roh and Park 2003).

In Fig. 2.32-c three relevant points can be seen. During the experiment, the particles near the point B and B′ were observed to spread out in all directions. Furthermore, the particles leaving these points toward A were observed to accumulate at point A. According to the authors, this means that the spots B and B′ are attachment nodal points and the spot A is a separation saddle point. By choosing 5 position along the streamwise cylinder diameter (as shown in Fig. 2.32-a by AA′, BB′ and so on), Roh and Park (2003) performed 5 laser light sheet visualisation. As a result of this inquiry, the sketch in Fig. 2.33 has been drawn. This shows the evolutionary sequence of the tornado-like vortices and the side tip vortices over the free end surface and permitted the authors to sketch an overall topological flow pattern (Fig. 2.34). This sketch shows the tornado-like vortices evolving from the two spiral nodes and the side tip vortices. It can be seen both the counter rotating vortices and the three critical spots in the rear zone of the surface. As illustrated in the sketch, both tornado and side tip vortices induce a downwash flow towards the two nodes. Roh and Park (2003) also demonstrated that the vortical flow pattern shown in Fig. 2.34 doesn't undergo substantial changes by varying the Reynolds number from $5.92 \cdot 10^3$ to $1.48 \cdot 10^5$ and the aspect ratio from 1.25 to 4.25.

A similar investigation has been done by Pattenden et al. (2005) for a cylinder with a small aspect ratio, and found that the flow pattern is like the one shown in Fig. 2.31. They investigated both the free end flow and the horseshoe vortex.

With regard to the free end flow, the measurements obtained by Pattenden et al. (2005) are shown in Fig. 2.35. In agreement with Roh and Park (2003), also Pattenden et al. (2005) found the two foci (F_T), the saddle point (S_T) and the reattachment point (R_T). According to the authors, in the fore zone the separated flow forms a small vortex near the leading edge and the reverse flow moves towards the cylinder sides.

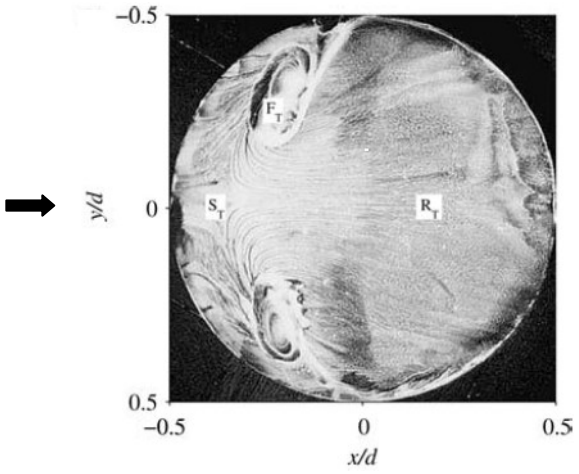

Fig. 2.35 Free end surface flow visualisation. Flow from left to right. *Re*=$2 \cdot 10^5$ and AR=1 (Pattenden et al. 2005).

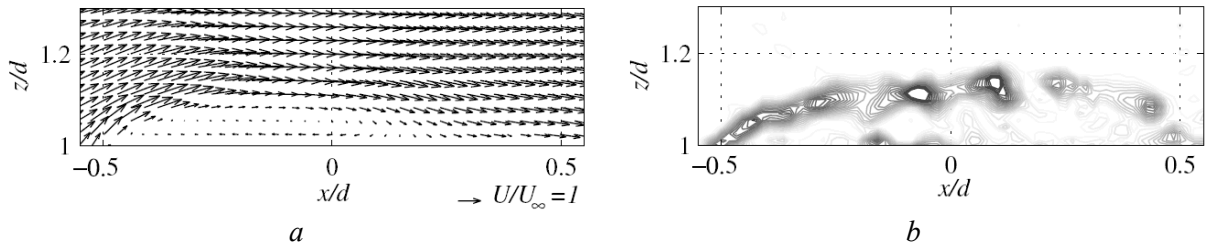

Fig. 2.36 Flow in the symmetry plane (y/D=0). *a*-Velocity vectors of the time-averaged flow. *b*-Vorticity contours of a instantaneous flow. Re=2·10^5 and AR=1 (Pattenden et al. 2005).

To allow a better understanding, Pattenden et al. (2005) performed also PIV measurements on the region above the free end cylinder. The mean flow field in the streamwise symmetry plane (see Fig. 2.36-*a*) shows the region of circulating flow and the reattachment zone. The instantaneous vorticity map (see Fig. 2.36-*b*) shows the shear layer over the top of the cylinder, maintaining almost constant for the first 0.2D and becoming turbulent afterward.

The tip vortices formed by the flow up over the edge of the free end are visible in the secondary mean flow field map measured immediately behind the trailing edge of the cylinder (see Fig. 2.37).

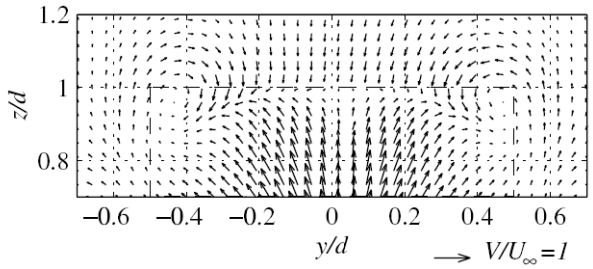

Fig. 2.37 Time-averaged velocity vectors at x/D=0.5. Re=2·10^5 and AR=1 (Pattenden et al. 2005).

Also Hain et al. (2007) performed measurements on the free end flow, by using tomographic PIV. They used a finite cylinder with AR=2.167 and the Reynolds number was about 10^5. Fig. 2.38-*a* shows the vector plane located at 0.13D over the top of the cylinder. In this average field the two foci are visible at x/D=0.4 and y/D=±0.43 as well as the centre of the tip vortices, highlighted by the region where the velocity in the x direction is very small (x/D=0.8 and y/D=±0.4). The tip vortices are also visible in the normalised u iso-contours (Fig. 2.38-*b*). The separation on the top of the cylinder causes a wake which leads to a region with decelerated flow, as it can be seen in both Fig. 2.38-*a* and *b* at x/D=1.0 and -0.1 ≤ y/D ≤

0.1. By using the λ_2-criterion to identify the vortices, Hain et al. (2007) performed the iso-surfaces shown in Fig. 2.39-*a*. According to these iso-surfaces, the tip vortices begin at $x/D \approx 0.5$ and $y/D \approx \pm 0.5$. In addition, weak vortical structures are observed between these tip vortices. Finally, Hain et al. (2007) have also reported an instantaneous flow field (see Fig. 2.39-*b*), which demonstrates that the flow field is very unsteady. In fact, many small vortices are observed and a well defined tip vortex isn't observed.

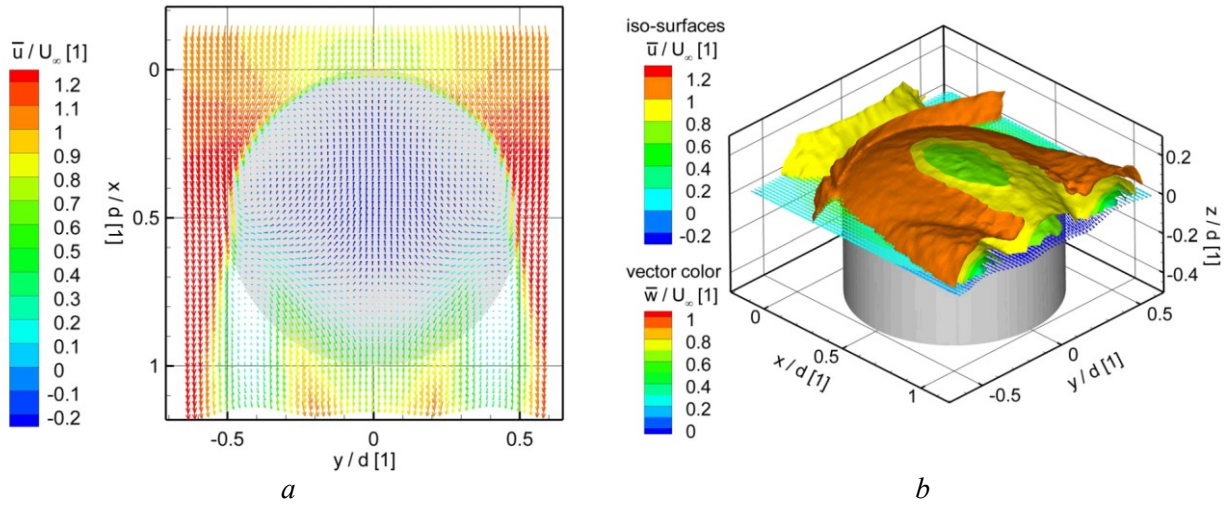

a *b*

Fig. 2.38 *a*- Bottom vector plane located at 0.13*D* over the top of the cylinder. b- Iso-surfaces of the normalised *u* component of the velocity. Measurements for AR=2.167 and $Re \approx 10^5$ (Hain et al. 2007).

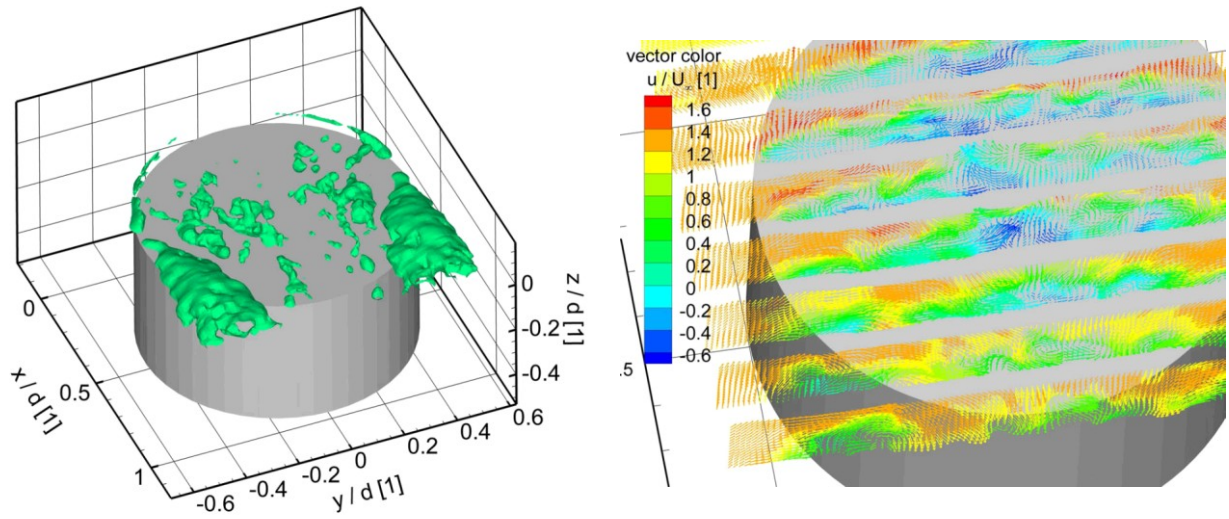

a *b*

Fig. 2.39 *a*- Iso-surfaces of λ_2-criterion calculated with the normalised *v* and *w* components. *b*- Instantaneous velocity field. Measurements for AR=2.167 and $Re \approx 10^5$ (Hain et al. 2007).

2.2.2 Horseshoe vortex

As already mentioned, the horseshoe vortex forms near the cylinder base when the upstream flow separates due to the adverse pressure gradient (see Fig. 2.31). Pattenden et al. (2005) investigated this phenomenon. Fig. 2.40-*a* shows the signature of this vortex on the ground. It can be seen the primary separation point (S_1) and the line of converging streamlines at the upstream edge of the primary vortex (line C). According to the authors, the latter has a thickness of about 0.04*D*, i.e. almost the width of the vortex 1′ sketched in Fig. 2.41. This means that the separation point S_2 and the attachment point A_1 are at downstream and upstream edges of this line, respectively. In Fig. 2.40-*a* it can be seen another line of diverging streamlines (D), which extends from the leading edge of the cylinder. According to Pattenden et al. (2005), this line is the inner edge of the horseshoe, which moves downstream and the inward facing streamlines are due to the small vortex (0) drawn in Fig. 2.41. Fig. 2.40-*c* shows the frontal view, where it can be seen the upwash near the free end and the downwash near the ground.

Furthermore, by means of instantaneous flow field measurements in this region, Pattenden et al. (2005) also demonstrated that the dominant vortex (1) sketched in Fig. 2.41 isn't stationary and that the location of the vortex centre varies from the position x=-0.8D to x=-0.6D.

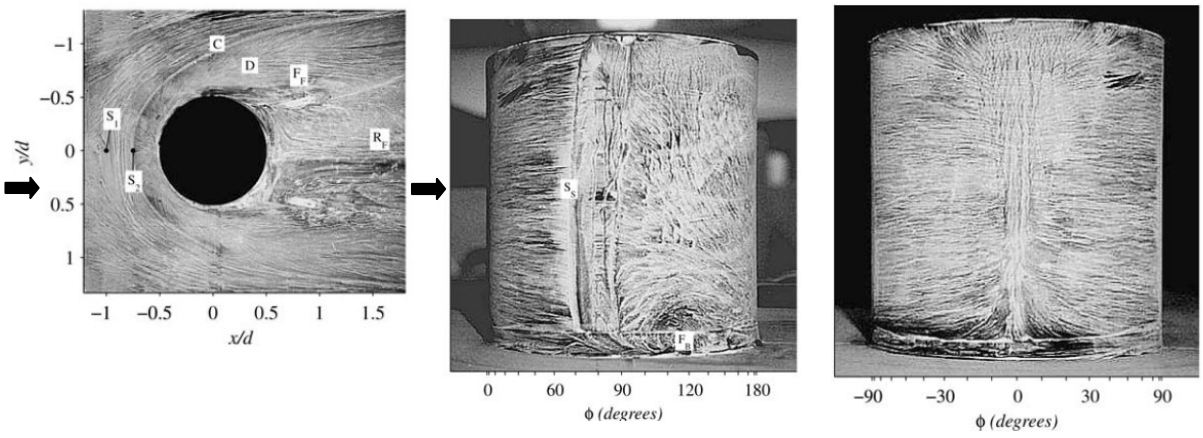

a - flow from left to right *b - flow from left to right* *c – flow into page*

Fig. 2.40 Surface flow visualisation images. *a*-Floor of tunnel. *b*-Side of cylinder. *c*-Front of cylinder. Re=2·10^5 and AR=1 (Pattenden et al. 2005).

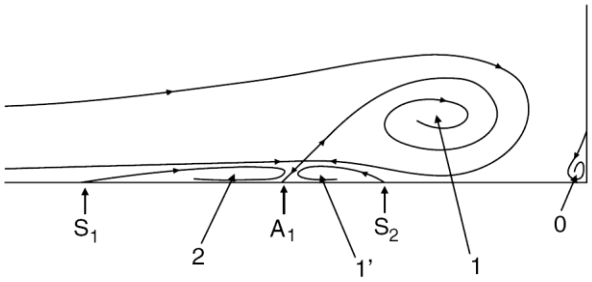

Fig. 2.41 Topology of horseshoe vortex system (Pattenden et al. 2005).

2.2.3 Mean flow field

Tanaka and Murata (1999) investigated 4 cylinders with AR equal to 1.25, 2.5, 5 and 10 for Re=3.7·10^4. For all measurement setups, they plotted the mean flow field in planes *yz*, *xz* and *xy* (see Fig. 2.42, Fig. 2.43 and Fig. 2.44, respectively). In all velocity maps, also the vorticity is shown with a solid or broken line if it is positive or negative, respectively.

In the plane *yz* located at x/D=5 it can be seen a downwash flow, which reaches the ground plate only for the cylinder with the smallest aspect ratio. For all cylinders, two vortical structures are present at the cylinder sides and for the cylinder with the highest AR there is another couple of vortical structures with opposite rotation sense near the ground plate. By decreasing the aspect ratio, the centres of the vortical structures move downward, whereas by increasing the distance of the *yz* plane from the cylinder, the vortical structure becomes smaller and weaker.

Also the velocity and vorticity maps relative to the *xz* plane at y/D=0 show the downwash flow, more remarkable for cylinders with small aspect ratios than for cylinder with AR=10 (see Fig. 2.43). For the last cylinder, the downwash extends until 5-6D downward and after that, the flow field is almost bi-dimensional. It's interesting to note that the vorticity component W_y is positive everywhere. According to Tanaka and Murata (1999), similar velocity and vorticity maps can be seen in the planes at y/D=±0.75.

The velocity and vorticity maps measured in the *xy* planes located at mid spans for all cylinders have been also considered by Tanaka and Murata (1999) and shown in Fig. 2.44. They used a rotating yaw-meter system. According to the authors, for the cylinder with AR=10 the recirculation region is bigger than that of the infinite cylinder. An interesting consideration has been pointed out concerning the cylinders with AR=1.25 and 2.5: in the centre of the wake, highlighted by the shadow effect, there are vortical regions where vorticity values are opposite in sign to those around them.

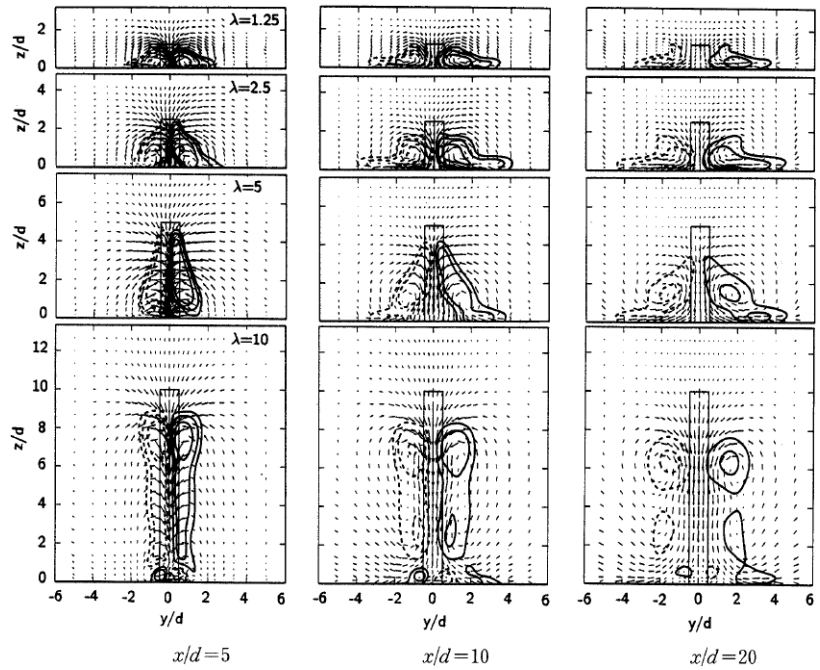

Fig. 2.42 Velocity vectors and vorticity W_x in three *yz* planes for AR=1.25, 2.5, 5 and 10 and $Re=37\cdot10^3$ (Tanaka and Murata 1999).

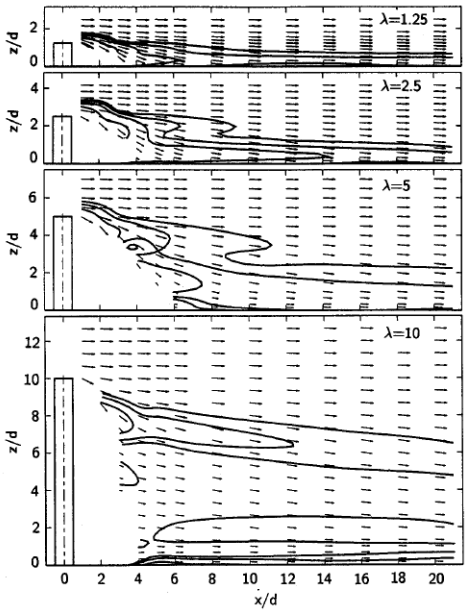

Fig. 2.43 Velocity vectors and vorticity W_y in the *xz* plane at $y/D=0$ for AR=1.25, 2.5, 5 and 10 and $Re=37\cdot10^3$ (Tanaka and Murata 1999).

This phenomenon has been called *inverse wake* by Tanaka and Murata (1999) and has been found also in the wake of the cylinder with AR=10 at $z/D=6$ and $x/D>20$. It is a known phenomenon in the bluff body community, as it is caused by the downwash flow.

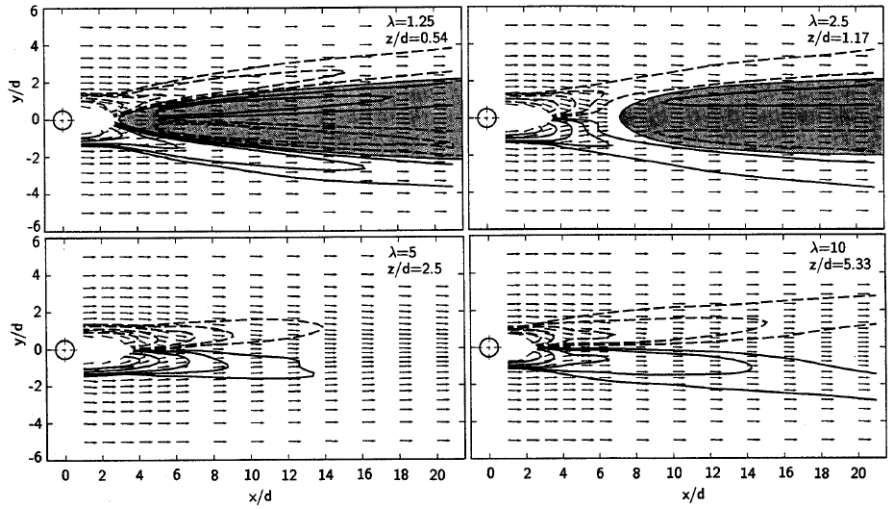

Fig. 2.44 Velocity vectors and vorticity W_z in a *xy* plane for AR=1.25, 2.5, 5 and 10 and $Re=37\cdot10^3$ (Tanaka and Murata 1999).

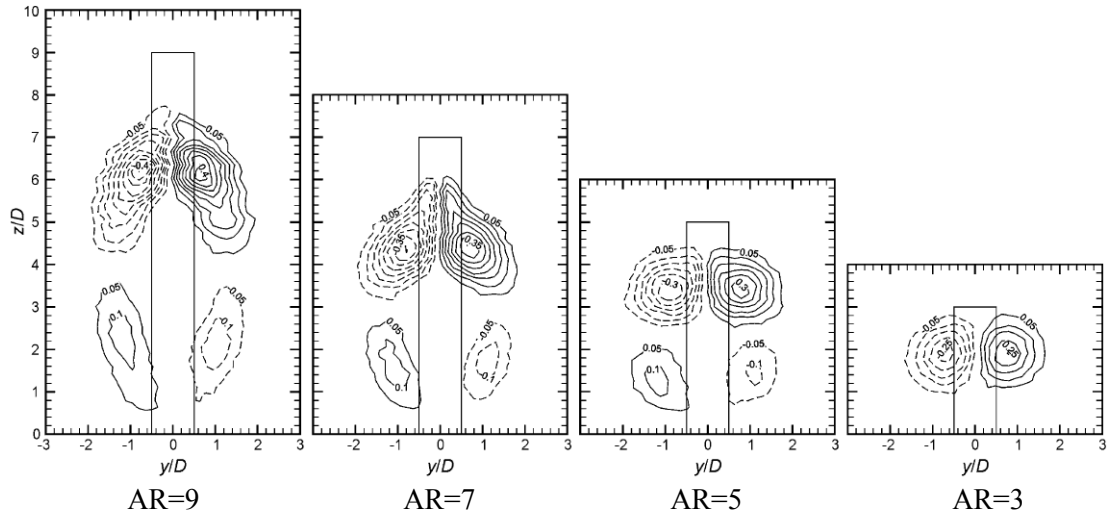

Fig. 2.45 Mean streamwise non-dimensional vorticity field in the *yz* plane at $x/D=6$ for $Re=60\cdot10^3$ (Sumner et al. 2004).

The mean vortical field in the *yz* plane has been investigated with a seven-hole pressure probe by Sumner et al. (2004) for $Re=6.0\cdot10^4$ and AR equal to 3, 5, 7 and 9 (see Fig. 2.45). However, differently from Tanaka and Murata (1999), Sumner et al. (2004) considered the effect of the boundary layer thickness ($\delta_{BL}/D=2.6$). They found for all cylinders, except for the one with AR=3, the couple of counter-rotating vortical structures along each side of the cylinder, similar to those shown by Tanaka and Murata (1999) for AR=10 (Fig. 2.42). Since in both works the aspect ratio equal to 5 has been investigated and only Sumner et al. (2004) found that type of vortical structures, it could be concluded that by increasing δ_{BL}/D or *Re*, or both of them, the counter-rotating vortical structures form. Since in this regime the flow is

qualitatively insensitive to the Reynolds number (Zdravkovich 1997), probably the above explained change is due to the boundary layer thickness.

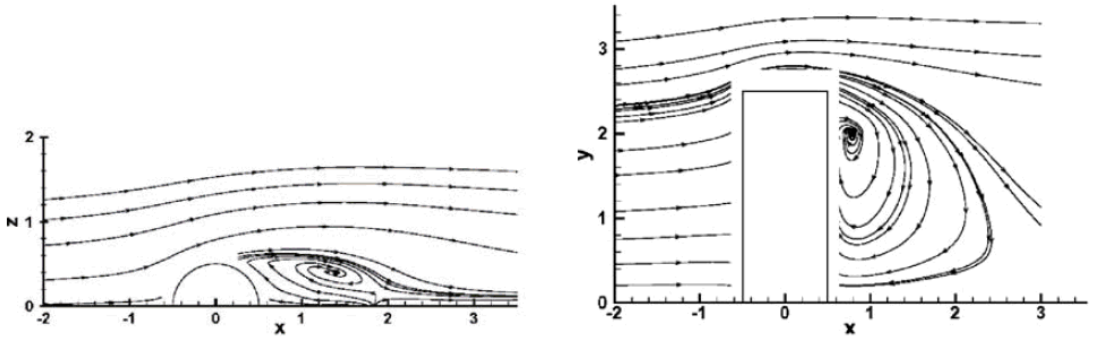

xy plane at z/D=1.5 *xz* plane at y/D=0

Fig. 2.46 Average streamlines for Re=43·10^3 and AR=2.5 (Fröhlich and Rodi 2004)[2].

Fröhlich and Rodi (2004) investigated, by means of the Large Eddy Simulation, a finite cylinder wake for Re=4.3·10^4 and AR=2.5. In this case, the comparison with results obtained by Tanaka and Murata (1999) could be done (as the latter authors investigated a cylinder with AR=2.5 and Re=3.7·10^4). Unfortunately, as regard the mean flow fields in the planes *xy* and *xz*, it has been investigated until x/D≈3.5 and the velocity maps (see Fig. 2.46) show the vortical structures that haven't been shown by Tanaka and Murata (1999), because in this region they didn't compute measurements (see Fig. 2.43 and Fig. 2.44). Also the mean flow field in the *yz* plane can't be compared with the one obtained by Tanaka and Murata (1999), because these authors investigated the planes located at x/D=5, 10 and 20, whereas Fröhlich and Rodi (2004) made measurements in the planes located at x/D=1, 2 and 3.5 (see Fig. 2.47). As already shown (see Fig. 2.42), by moving the *yz* plane from x/D=5 to 20, the vortical structures tend to get squashed on the ground. On the other hand, measurements made by Fröhlich and Rodi (2004) show that by moving the *yz* plane from x/D=1 to 3.5, the centre of the vortical structure moves along the cylinder height, first toward the ground and then toward the cylinder tip.

Fröhlich and Rodi (2004) found alternating vortex shedding in the rear region of the cylinder from the base until y/D≈1.5; above this height, perturbations with only small scales have been found. These considerations allow to conclude that the above mentioned critical aspect ratio for the vortex shedding is lower than 2.5 (see Fig. 2.30).

[2] Reference frame different from the traditional one sketched in Fig. 2.31. Switch *y* with *z* to obtain the traditional reference frame.

Fröhlich and Rodi (2004) computed also normal and shear stresses in *xy* planes located at z/*D*=1 and *z*/*D*=2. It can be seen (Fig. 2.48) that the *u*-fluctuations dominate in the separated shear layer, while *v*- and *w*-fluctuations are maximal near the symmetry plane. By comparing the two *xy* planes, it can be concluded that near the top, the recirculation is much shorter and all fluctuations are smaller because the shedding is absent.

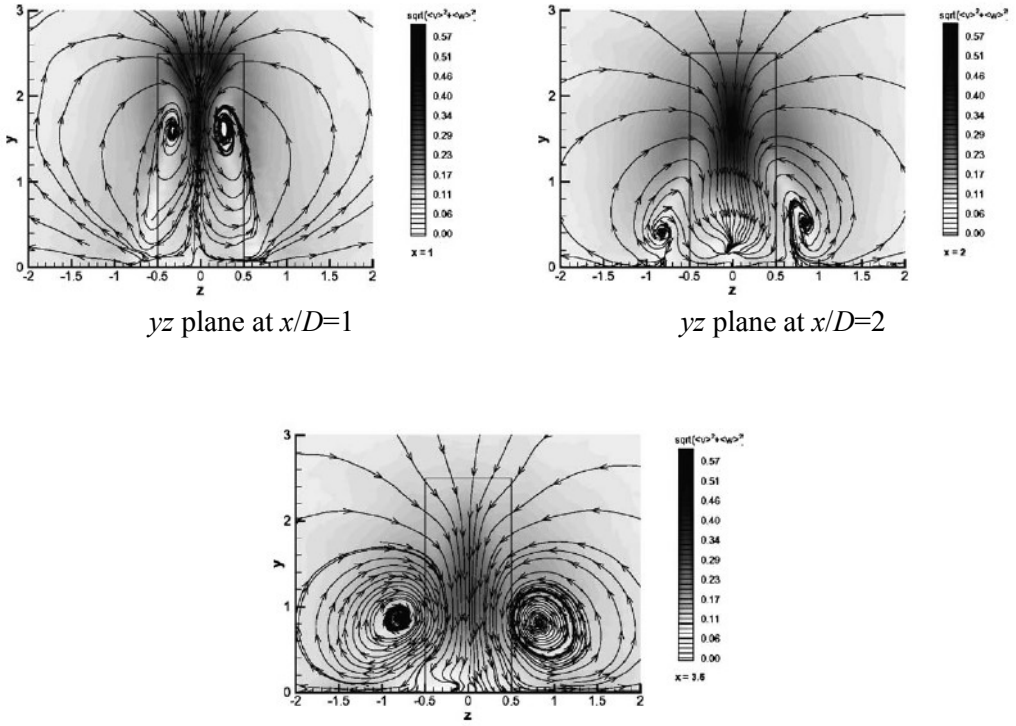

yz plane at *x*/*D*=1 *yz* plane at *x*/*D*=2

yz plane at *x*/*D*=3.5

Fig. 2.47 Average flow structures and magnitude of the secondary flow ($\sqrt{\overline{v}^2 + \overline{w}^2}$) represented by grey scale (values from 0 to 0.6). *Re*=43·10^3 and AR=2.5 (Fröhlich and Rodi 2004) [2].

Also Pattenden et al. (2005) made measurements of the mean flow fields in the *yz* planes moving along the *x* axes (see Fig. 2.49). In this case the cylinder has a very small aspect ratio (AR=1) and *Re*=2·10^5. In this measurements, it can be seen the couple of tip vortices which form because the shear layers at the sides and over the top interact (see Fig. 2.49). At the first measurement plane (*x*/*D*=0.5), two counter-rotating tip vortices can be seen at the free end of the cylinder. The vortices remain at the same position until *x*/*D*=1.0, where they start to expand and move downward. According to Pattenden et al. (2005), this is caused by the downwash behind the cylinder. At *x*/*D*=0.5 is also visible the inside edge of the horseshoe vortex: it extends to *y*/*D*=±1 in this plane and it can be seen at the outside lower corners, where the vectors are pointing downwards and outwards. At *x*/*D*=1.5 the flow coming from the sides of the cylinder combines with the downwash flow. As a result, the flow

converges on the centreline and impinges on the ground plane. At this point, the flow is forced outwards, increasing vorticity and forming the two trailing vortices shown at x/D=2.5.

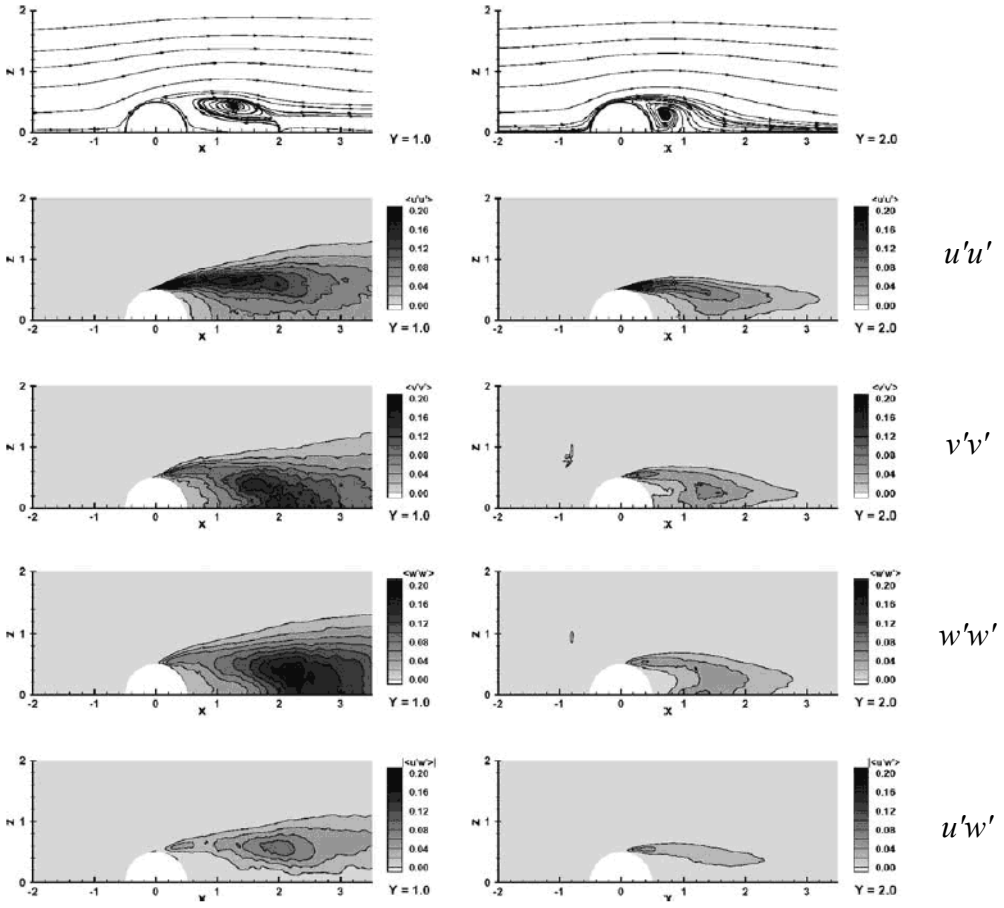

xy plane at z/D=1 *xy* plane at z/D=2

Fig. 2.48 Streamlines and stresses. The grey scale ranges from 0 to 0.2. Re=43·10^3 and AR=2.5 (Fröhlich and Rodi 2004) [2].

Afgan et al. (2007) investigated two different cylinders with AR=6 and 10 and a Reynolds number equal to 2.0·10^4. In the mean flow fields, measured in the wake at different *xy* planes, they found an almost symmetrical pattern, with a pair of narrow recirculation bubbles, similar to the one obtained by Fröhlich and Rodi (2004) (e.g. see Fig. 2.48).

Finally, Said et al. (2008) investigated a cylinder with AR=2.56 and a Reynolds numbers equal to 8.5·10^3 and 6.4·10^4. Since, as mentioned before, in this regime the flow field doesn't change significatively with the Reynolds number, this investigation is very similar to the one made by Fröhlich and Rodi (2004).

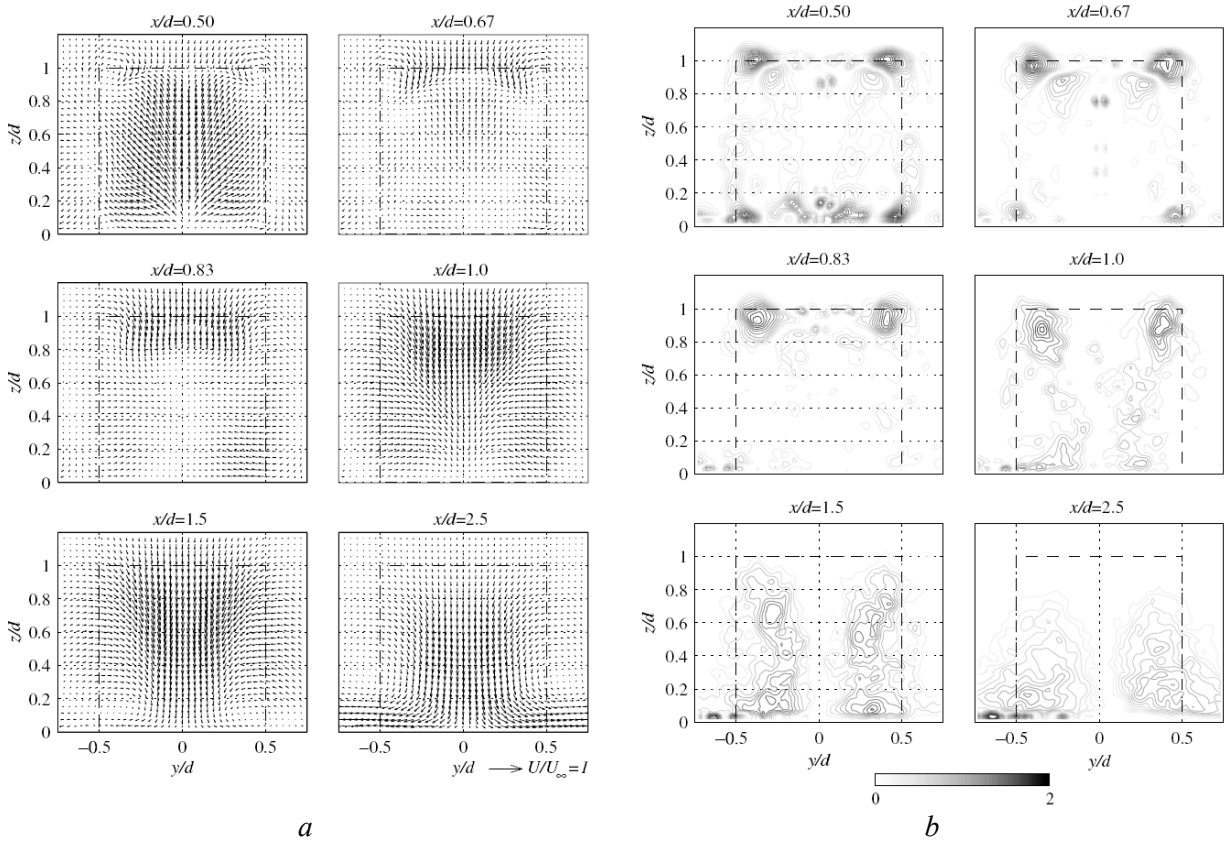

Fig. 2.49 Streamwise evolution of the flow in the *yz* plane, showing mean velocity vectors (*a*) and contours of mean non-dimensional vorticity magnitude (*b*). Re=2·10^5 and AR=1 (Pattenden et al. 2005).

2.2.4 Vortex formation length

Some authors have measured the vortex formation length relative to finite cylinders.

For example, by means of the hot wire technique Park and Lee (2004) measured this length as suggested by Bloor (1964), by varying the *xy* plane along the cylinder height. They investigated the flow field for Re=2.0·10^4 and three different cylinder with AR=6, 10 and 13, comparing the results to the ones relative to the infinite cylinder.

In Fig. 2.50-*a* it can be seen that the vortex formation length increases by decreasing the aspect ratio. It's interesting to note that for the smaller aspect ratios AR=6 and 10 this length is almost twice the length relative to the infinite cylinder. Furthermore, by decreasing the aspect ratio, the magnitude of the turbulence intensity decreases and the peak becomes blunt. Fig. 2.50-*b* shows the turbulence intensity for the cylinder with AR=10 by varying the position *z*/*L* where the measurement is taken. As the free end is approached, both turbulence intensity and vortex formation region decrease. According to Afgan et al. (2007), this is due to the downwash flow, in fact they measured the flow field in the *xz* centre-plane, obtaining

the mean streamlines pattern shown in Fig. 2.51. A dense cluster of lines generated just before the free end of the cylinder later highlights the strong arc shaped downstream, which almost reaches the ground plane. The location of this arc determines the size of the recirculation vortex pair.

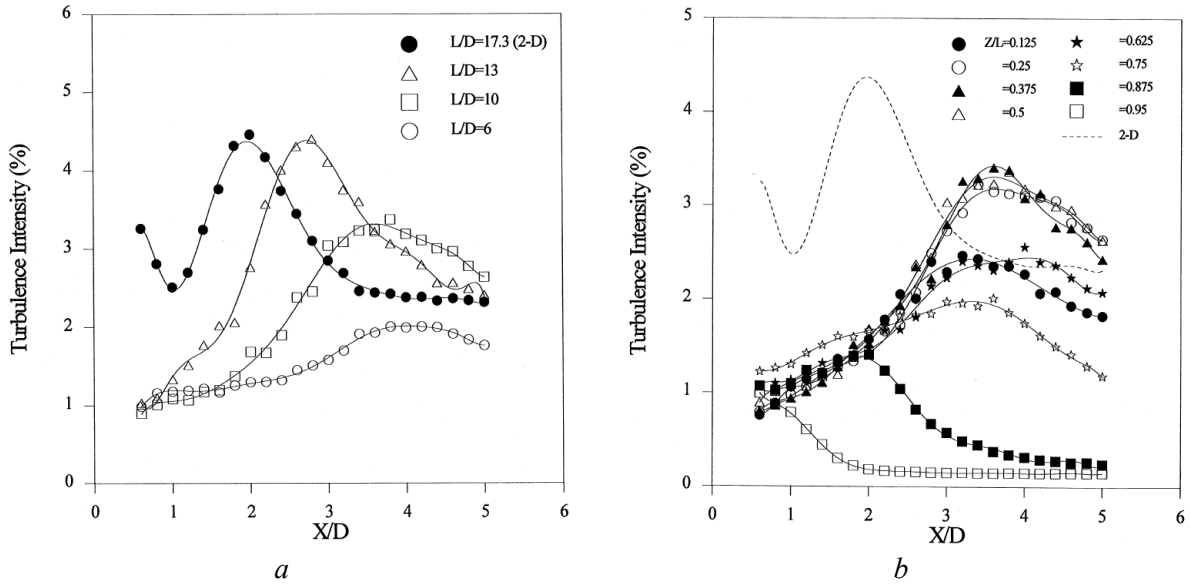

Fig. 2.50 Comparison of the vortex formation region measured at y=0 and: *a*- at z/L=0.5 by varying the aspect ratio; *b*- for AR=10 by varying the position z/L. Re=$2.0 \cdot 10^4$ (Park and Lee 2004).

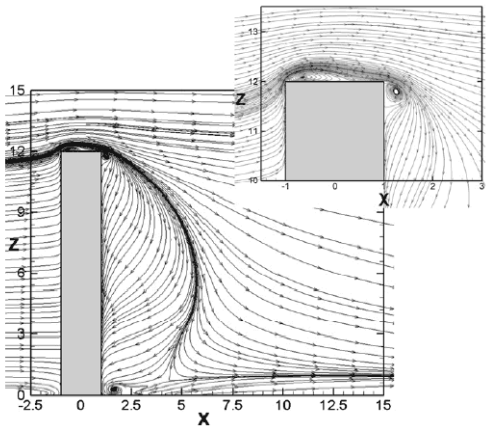

Fig. 2.51 Mean streamlines in the *xz* centre-plane. AR=6 and Re=$2.0 \cdot 10^4$ (Afgan et al. 2007).

3 Stereo Particle Image Velocimetry technique: working principles

The Stereo Particle Image Velocimetry is an evolution of a more developed technique: the Particle Image Velocimetry (PIV). The latter permits to obtain two components of the instantaneous displacement field in a cross-section of a flow, whereas with the former also the component orthogonal to the measurement plane can be measured. Most of the working principles are common to the two techniques and this is the reason why hereafter first the PIV technique will be shown and then the extension to the Stereo PIV will be done.

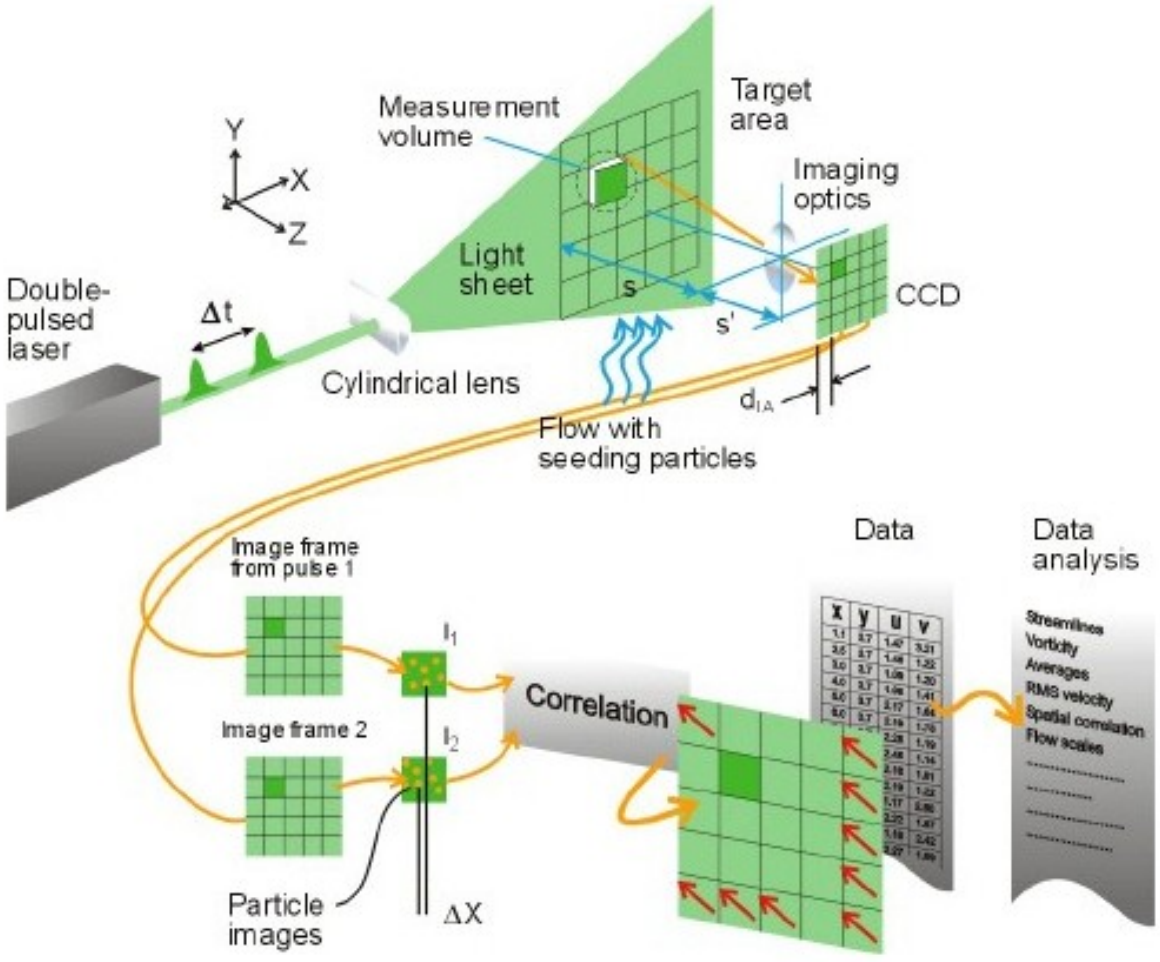

Fig. 3.1 Sketch of the Particle Image Velocimetry technique (by Dantec Dynamics website).

3.1 Particle Image Velocimetry technique

The experimental configuration of a PIV system is made up of tracer particles, a light source and a camera. In Fig. 3.1 a sketch of a typical PIV system is shown. The tracer particles have to be added to the flow and illuminated in a plane of the flow by means of the light source. The camera has to record at least two images of the illuminated tracer particles in two very close instants. Once obtained a couple of PIV images, they are divided in small sub-areas called *interrogation window*. The local displacement vector for the images of the two instants is determined for each interrogation window by means of a statistical method. Then, it is assumed that all particles in each interrogation window have moved homogeneously between the two illuminations.

3.1.1 Tracer particles

The role played by the tracer particles is very important since the PIV technique measures the velocity of these particles instead of the flow one. For this reason, fluid mechanical properties of the tracer particles are very important and the choice of the particles determines the goodness of the measurements.

The most important features are density and dimension. The former determines the influence of gravitational force that can be neglected if the densities of the tracer particle and working fluid are very similar. The latter determines the light scattering behaviour of the particles. Both the features have also a strong influence on the capability of the particles to correctly follow the main flow. Further information about these aspects can be found in Raffel et al. (2007) Sect. 2.1.

In air flows, the seeding particles are typically oil drops in the range 1 μm to 5 μm. For water applications, the seeding is typically polystyrene, polyamide or hollow glass spheres in the range 5 μm to 100 μm. Any particle that follows the flow satisfactorily and scatters enough light to be captured by the camera can be used.

The number of particles in the flow is of some importance in obtaining a good signal peak in the cross-correlation. As a rule of thumb, 10 to 25 particle images should be seen in each interrogation area.

3.1.2 Light source

Nowadays the most common light source used in PIV applications is the Nd:YAG laser. Generally, PIV lasers are designed as double oscillator system, so that it’s possible to obtain

two illuminations of the tracer particles at a very short time distance. Since the laser light comes out of the laser cavity as a beam, an optical system has to be used in order to realize a light sheet (cylindrical lens in Fig. 3.1). Further information about light source as well as light sheet optics can be found in Raffel et al. (2007) Sect. 2.3-2.4.

3.1.3 Image recording

The most important features of the camera used in PIV measurements are the number of sensible elements dimensions and sampling rate. The former determines the spatial resolution and the latter the temporal one. Typically the CCD dimension used in PIV applications is about of $10^6 pixels$ and the sampling rate is about of $10 Hz$.

The camera acquisition has to be synchronized with the laser light pulses in order to obtain two particle images relative to the two particles illuminations. For this purpose, generally synchronization software is used. Further information about the imaging as well as the characteristic of CCD or CMOS for PIV applications can be found in Raffel et al. (2007) Sect. 2.8, 2.9 and 4.

3.1.4 Classical PIV images evaluation

In order to compute the displacement field from PIV images an interrogation procedure is required.

This procedure consists in a repartition of the PIV images in many interrogation windows and cross-correlation of the corresponding interrogation windows relative to the two PIV images (see Fig. 3.1). After the cross-correlation has been done, the mean displacement of each interrogation window is known, i.e. the particles displacement in each interrogation window is assumed to be homogeneous.

Strictly speaking, this cross-correlation can be computed directly, i.e. by means of the discrete cross-correlation function:

$$R_{II'}(x,y) = \sum_{i=-K}^{K} \sum_{j=-L}^{L} I(i,j) I'(i+x, j+y) \qquad 3.1$$

where I and I' are the intensity values maps of the two images. Alternatively, the cross-correlation can be computed by taking into account the correlation theorem. According to this theorem, the cross-correlation of two functions is equivalent to anti-Fourier transform of the complex conjugate multiplication of their Fourier transform:

$$R_{II'} \Leftrightarrow \hat{I} \cdot \hat{I}' \qquad 3.2$$

where $\hat{I}$ and $\hat{I}'$ are the Fourier transforms of I and I', respectively. In order to reduce the computational effort, the Digital Fourier Transform (DFT) is implemented by means of the Fast Fourier Transform (FFT).

Since in theory the DFT is a sum of infinite data and in practice it is computed over finite domain, an artefact is needed:

- *Zero padding*

This method consists in to extend the sample size to four times the original size by filling in zeros. Unfortunately, this artefact performs poorly, because the image sample generally consists of a nonzero background and then the discontinuity caused by the zero padding contaminates the spectra of the data with high frequency noise which in turn deteriorates the cross-correlation signal.

- *Periodicity of data.*

Another method can be to assume the periodicity of data, i.e. the image sample is assumed to repeats itself in all directions. This condition leads to use an artefact (e.g. windowing) that implies systematic errors in the cross-correlation computation:

  - *Aliasing:* the data periodicity implies that also the correlation data are periodic. The aliasing is a phenomenon that happens when the sampling criterion is violated. In particular, if the linear length of the image sample is N and the displacement exceeds half the sample size $dx>N/2$, the measured displacement will be equal to dx-N and the correlation peak will be folded back into the correlation plane to appear on the opposite side (because of the signal periodicity).
  - *Bias error:* by increasing the displacement, less data are correlated with each other, since the periodically continued data makes no contribution to the right correlation value. This means that values on the edge of the correlation plane are computed from only the overlapping half of the data and consequently the estimated displacement is biased to a lower value (see Fig. 3.2). To correct this error, an opportune weighting function has to be used.

Since the standard cross-correlation function yields different maximum correlation values for the same degree of matching, a normalization of the function is useful. For this purpose, first the mean is subtracted from each interrogation window, then the cross

correlation is computed as before shown and finally the cross-correlation is divided by the two standard deviations of the original interrogation windows.

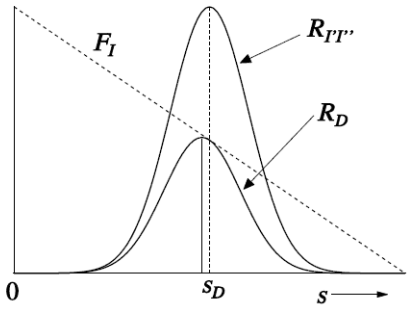

Fig. 3.2 Bias error introduced in the calculation of the cross-correlation using FFT (Westerweel 1997).

Furthermore, since the correlation signal is strongly affected by variations in image intensity, caused for example by the particles brightness and the non uniform illumination, in such case an image pre-processing is suitable. For this purpose, different methods are present in literature, e.g. background subtraction, intensity capping, etc. (see Raffel et al. 2007 Sect. 5.4.2).

In the past, various authors worked on an efficient approach to the analysis of PIV images and, in the first years, the classical cross-correlation approach was proposed, e.g. the works of Utami et al. (1991), Willert and Gharib (1991) and Westerweel (1993). By using the classical approach, the *loss of pairs* (Keane and Adrian 1993) due to in-plane motion causes both a decrease of the signal-to-noise ratio and a significant increase of the total error, which is more evident for smaller particles. For this reason, in the following years, different advanced PIV images evaluations have been proposed.

3.1.5 Advanced PIV images evaluation

One of the advanced evaluations, which is a solution of the problem mentioned above, is to displace the interrogation windows by a discrete offset. This permits to follow the particles between the two frames. This method is known as *Iterative Discrete Window Offset* (IDWO) approach and has been proposed by many authors, e.g. Soria (1996), Westerweel et al. (1997), Scarano and Retihmuller (1999) and Hart (2000). The scheme of IDWO is shown in Fig. 3.3 and is made up of the following step:

- The standard DFT interrogation is performed;
- A validation criterion is used in order to find the outliers, which are consequently corrected;

- The displacement estimated is used to adjust the interrogation window offset locally to the nearest integer;
- The linear dimension of the interrogation window *W* is decreased in order to increment the resolution and then the interrogation is iterated until the integer offset vectors converge to unity.

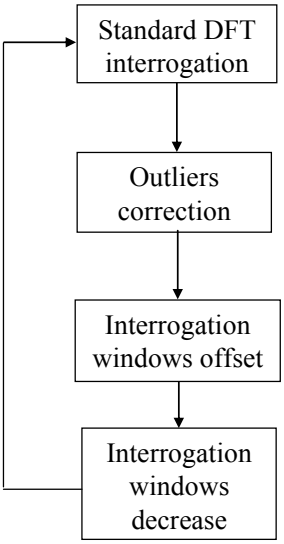

Fig. 3.3 Scheme of Iterative Discrete Window Offset technique.

Wereley and Meinhart (2001) demonstrated that a symmetric offset of the interrogation windows with respect of the interrogation point works better than an asymmetric offset. This is justified by the fact that the symmetric offset corresponds to a central difference interrogation, which is second-order accurate in time. As improvement to this approach, Lecordier et al. (2001) proposed a sub-pixel offset of the interrogation window.

A significant evolution of the IDWO technique was proposed by Huang et al. (1993), which took into account the deformation and rotation of the interrogation windows caused by the flow field. They proposed the *Particle Image Distortion* (PID) technique, whose main idea was to maximize the correlation coefficient in the presence of large velocity gradient. Jambunathan et al. (1995) developed a different algorithm to evaluate the deformation of the interrogation windows. They proposed to interpolate on each pixel of the first image the displacement field obtained in the previous step and to use it to evaluate the distortion of the second image.

In the last years, the *Image Deformation Method* (IDM) has been widely used. It requires the evaluation of the image intensity, with a sub-pixel interpolation. Unfortunately, depending on the choice of interpolating function, significant bias errors may be introduced.

Astarita and Cardone (2005) made a comparison of various advanced image interpolating functions, whereas Astarita (2006) analysed the effect of the interpolator choice on the accuracy and the spatial resolution.

3.2 Stereo Particle Image Velocimetry technique

Stereo PIV is based on the same fundamental principle as human eye-sight: stereo vision. Our two eyes see slightly different images of the world surrounding us, and comparing these images, the brain is able to make a 3-dimensional interpretation. With only one eye you will be perfectly able to recognise motion up, down or sideways, but you may have difficulties judging distances and motion towards or away from yourself.

As with PIV measurements, Stereo PIV measures displacements rather than actual velocities, and here cameras play the role of "eyes". The most accurate determination of the out-of-plane displacement (i.e. velocity) is accomplished when there is 90° between the two cameras. In case of restricted optical access, smaller angles can be used at the cost of a somewhat reduced accuracy. In Fig. 3.4 a sketch of the Stereo PIV technique has been drawn.

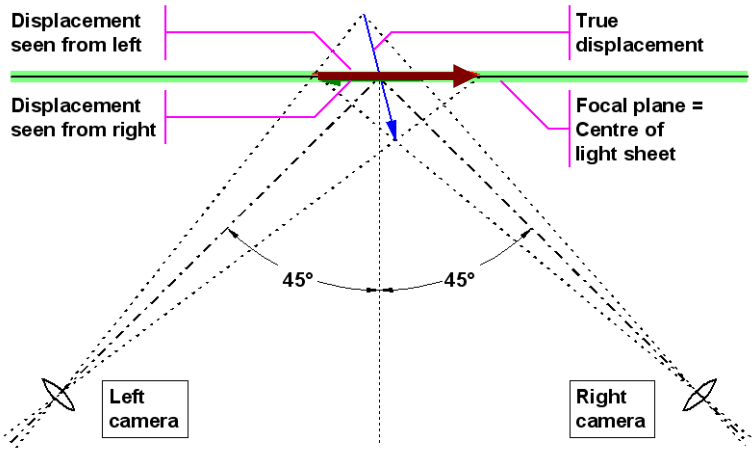

Fig. 3.4 Sketch of the Stereo PIV technique (by Dantec Dynamics website).

When viewing the light sheet at an angle, the camera must be tilted in order to properly focus the camera's entire field of view. It can be shown that the image (i.e. CCD), lens and object planes must cross each other along a common line in space for the images to be properly focused in the entire field of view. This is referred to as the Scheimpflug condition, and is used in most Stereo PIV systems (see Fig. 3.5).

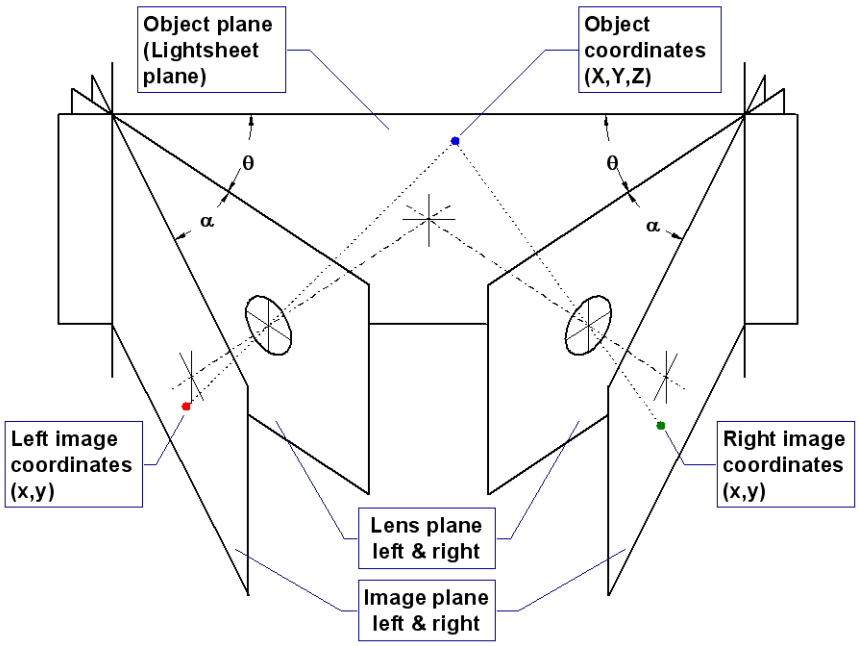

Fig. 3.5 Sketch of the Scheimpflug condition: θ is the Scheimpflug angle (by Dantec Dynamics website).

Nowadays, there are different methods to implement the Stereo PIV technique; Prasad (2000) subdivided these methods into geometric and calibration-based approaches. The latter is the most accurate one and it is possible to categorise it in further approaches: the first is based on the procedure introduced by Soloff et al. (1997) and the second is that proposed by Willert (1997). In the former approach a mathematical relation, which computes the three-component (3C) reconstruction in a single step, is proposed. On the other hand, in the Willert's approach, the reconstruction of the three-dimensional displacement field is done by means of geometrical considerations, i.e. local viewing angles of each camera in every point of the measurement plane.

In all calibration-based approaches an accurate calibration, which permits to correct the error in perspective and the possible distortion caused by the lenses, is essential to obtain good results in the measurement of the velocity components. Typically, calibration is obtained setting a calibration pattern, which contains a grid of marks regularly spaced along two orthogonal directions, in one or more positions along the z direction (orthogonal to the plane); ideally, the position $z = 0$ is the position of the light sheet, i.e. the measurement plane.

A drawback of the Stereo PIV technique is the impossibility to set the laser sheet exactly in the $z = 0$ position. By neglecting this misalignment, one commits the following errors:

- Position error: 3C displacement reconstruction is made using two-components (2C) vectors relative to two different positions.

- 3C-reconstruction error: in the 3C reconstruction proposed by Soloff et al. (1997), the local gradient matrix is computed in a wrong point, and this, in turn, causes a wrong displacement vector (see Sect. 3.2.3); in the 3C reconstruction proposed by Willert (1997), the local viewing angles are calculated in an erroneous position, so they cause a mistake in the evaluation of 3C displacement vectors (see Sect. 3.2.3).

An adjusting procedure based on a cross-correlation between the images of the two cameras, recorded in the same instant, has been proposed by many authors (e.g. Willert 1997, Coudert and Schon 2001, Scarano et al. 2005 and Wieneke 2005.

The common procedure of the methods proposed by Soloff et al. (1997) and Willert (1997) consists in the following steps:

- Calibration is achieved to correct errors in perspective and distortions caused by lenses: a mapping function which transforms the object coordinates (x, y, z) into the image coordinates (X_1, Y_1) of camera 1 and (X_2, Y_2) of camera 2 is computed.
- The misalignment between calibration and measurement planes is evaluated.
- The 3C displacement field is computed.

The scheme is drown in Fig. 3.6.

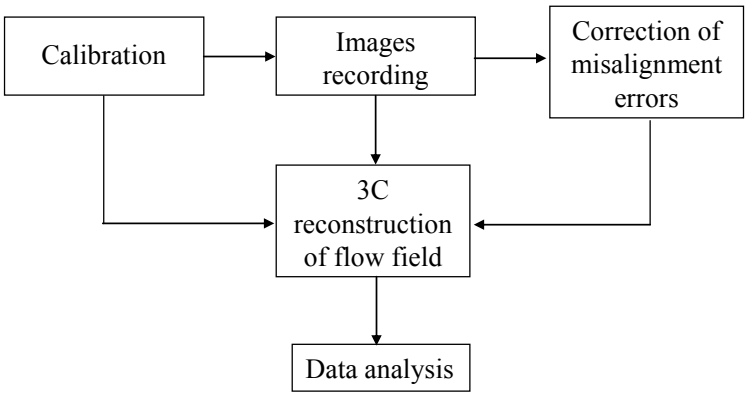

Fig. 3.6 Scheme of Stereo PIV procedure.

3.2.1 Calibration

As described before, the calibration is obtained by setting a calibration pattern, which contains a grid of marks regularly spaced along two orthogonal directions, in one or more positions along the z direction (see Fig. 3.7). In the calibration procedure, a mapping function is computed, which allows to transform the object coordinates (x, y, z) into the image coordinates (X_1,Y_1) and (X_2,Y_2) of the two cameras:

$$\begin{bmatrix} X_c \\ Y_c \end{bmatrix} = \begin{bmatrix} X^{(c)}(x,y,z) \\ Y^{(c)}(x,y,z) \end{bmatrix} \qquad 3.3$$

$$\underline{X}_c = \underline{F}^{(c)}(\underline{x})$$

where *c* indicates the camera[3]. Coefficients of the mapping function are normally calculated with the least squares method.

Nowadays, different calibration models are used: camera pinhole model and interpolating function-based ones.

The camera pinhole model, proposed by Tsai (1987), is made up of 6 extrinsic and 6 intrinsic parameters. The former describe the position of the camera pinhole in object space by means of a translation vector and a rotation matrix. Intrinsic parameters are specific to the camera: pixel aspect ratio; radial distortion factors (first and second order) which describe the distortion caused by the lenses; focal length; intersection of the optical axis with the image plane.

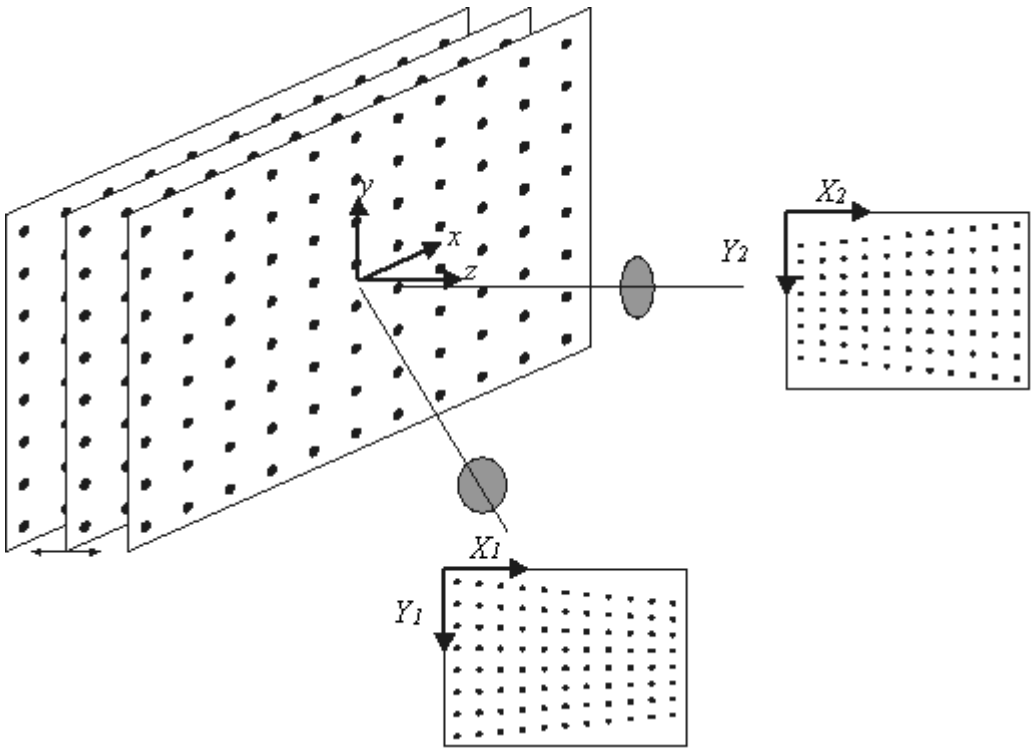

Fig. 3.7 Set up of the calibration target.

[3] Some authors (e.g. van Oord 1997 and Willert 1997) compute the inverse function:

$$\underline{x} = \underline{F}^{(c)}(\underline{X}_c)$$

For the interpolating function-based approach, a generic interpolating function can be chosen. In the literature there are a lot of examples, which can be subdivided in:

- Bi-dimensional (2D) calibration model: second order polynomial function in X_c and Y_c (van Oord 1997); first and second order rational-polynomial function in X_c and Y_c (Willert 1997);
- Three-dimensional (3D) calibration model: polynomial function of third order in x and y and second order in z (Soloff et al.1997); bicubic splines (Lawson and Wu 1997).

Obviously, for the bi-dimensional interpolating functions, only one position of the calibration pattern is required, whereas more than one position along the z direction are needed for the 3D ones.

In the past, many studies have been conducted in order to compare the efficiency of different mapping functions. Coudert and Westerweel (2000) showed the equivalence in the accuracy between the second order polynomial and the second order rational-polynomial functions. Willert (2006) compared different calibration types based on the camera pinhole model: simplified (in which only the extrinsic parameters are optimised), full (all parameters optimised) and direct linear transformation (distortion-free imaging system). It's interesting to note that the last method is equivalent to the first order rational-polynomial function in x, y and z. The result of this comparison shows a little influence of the choice of the camera model on the determination of the pinhole position for the configuration chosen by the author.

3.2.2 Correction of misalignment between calibration and measurement planes

As already mentioned, when real Stereo PIV measurements are made, one of the major problems is the unavoidable misalignment that occurs between the calibration plane and the laser sheet, i.e. the measurement plane. Generally, an offset along the z direction and a rotation around the x and y axis form this misalignment.

As mentioned before, a correction procedure based on cross-correlation between the images of the two cameras, recorded in the same instant, has been proposed by many authors. In the following, the procedure adopted in this work will be described. It's very similar to the ones present in literature. The few differences will be explained at the end of the section.

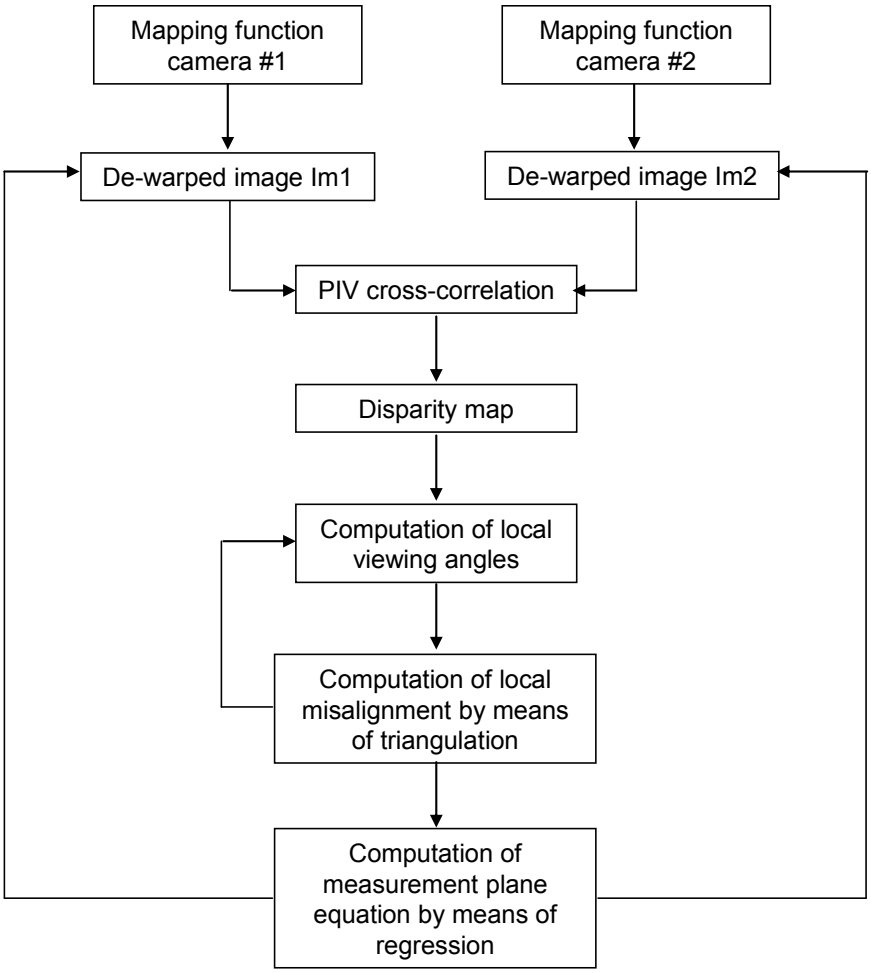

Fig. 3.8 Scheme of the procedure used to correct the misalignment error between calibration and measurement planes.

The scheme of the whole correction procedure is shown in Fig. 3.8. By comparing the two de-warped images recorded in the same instant by the two cameras, with a classical PIV process, the *disparity map* can be computed; naturally, in absence of misalignment, the disparity map shows a null displacement field. But, if a misalignment occurs, a generic point P of the measurement plane is viewed (in the de-warping process) in two different positions P_1 and P_2 by the two cameras (see Fig. 3.9).

Using the disparity vector D_u and the local viewing angles α_c (angle between the viewing ray and the plane yz measured in the xz plane), it is possible to compute the local misalignment, by means of triangulation:

$$\Delta z = z_{meas} - z_{calib} = \frac{D_u}{tan\,\alpha_1 + tan\,\alpha_2} \qquad 3.4$$

So, if the disparity map is known, the local misalignment in each point of the measurement plane can be calculated. Since the local viewing angles α_1 and α_2 are unknown

when the local misalignment isn't known (see Fig. 3.9), it is possible to apply the Eq. 3.4 only with an approximated value of the angles (e.g. the angles computed in the point P_1, or P_2, or in the middle of them). For this reason, an iterative algorithm is used to compute the correct local misalignment: it stops when the difference between the local z-position computed in two successive iterations is smaller than a prefixed precision.

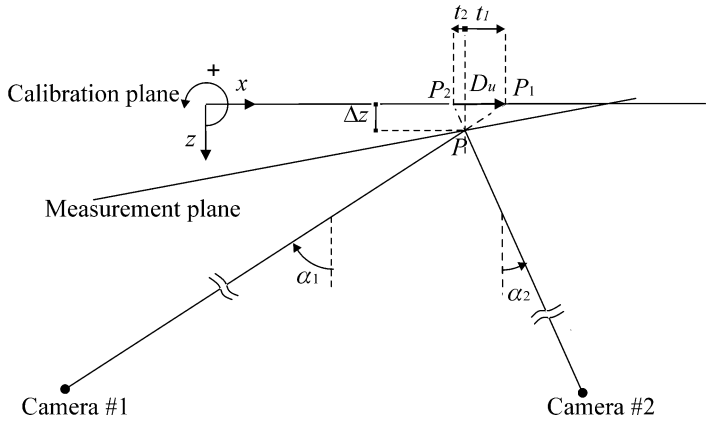

Fig. 3.9 Sketch of a generic misalignment error between calibration and measurement planes.

Finally, the equation of the measurement plane in the object space is computed by means of a regression method. The whole procedure is iterated in order to obtain a better accuracy in the determination of the measurement plane equation. Typically, three iterations are enough. After the first iteration, the images are de-warped taking into account the measurement plane equation computed in the previous step. For this reason, herein a 3D calibration is used; obviously, in order to avoid extrapolation in the de-warping process, the mapping volume has to contain the measurement plane. Alternatively, it's also possible to re-compute the mapping function (Wieneke 2005); in this way, the measurement plane has always the equation $z = 0$.

With the procedure just described, both types of errors are corrected: this is possible because after the computation of the measurement plane equation, the "right" correspondence between the image coordinates (X_1, Y_1) and (X_2, Y_2) and the object coordinates (x, y, z) is known. So, the position error is corrected by de-warping the images in the right positions, whereas the 3C reconstruction error is corrected by computing the local viewing angles (Willert's procedure) or the local gradient-matrix (Soloff's procedure) in the right position.

Coudert and Schon (2001) proposed a different procedure in which the correction was made by modifying the grid on which the 2C-vectors were computed. Also in this case, like in the Willert's work (1997), only the correction of the 2C-vectors' origin is computed. On the contrary, Scarano et al. (2005) corrected both types of errors associated with misalignment:

the position error was corrected by de-warping the images in the right position and the 3C reconstruction one was corrected by correcting the viewing angles.

3.2.3 3C reconstruction of flow field

With the approach proposed by Soloff et al. (1997) first the 2C displacement fields are evaluated for the two cameras with a standard PIV algorithm applied to the warped images; then, the 3C displacement field is computed with a procedure that includes in one step the images de-warping and the 3C reconstruction.

Since the displacement of a particle in the image plane is:

$$d\underline{X}_c = \underline{F}^{(c)}(\underline{x}+d\underline{x}) - \underline{F}^{(c)}(\underline{x}) \tag{3.5}$$

if by computing a Taylor series expansion and a volume averaging over the interrogation window, one obtains:

$$\overline{d\underline{X}_c} = \nabla \underline{F}^{(c)} \cdot \overline{d\underline{x}} \tag{3.6}$$

Since two cameras are used in Stereo PIV technique, the two systems (with the same unknown) can be combined. The resulting system is linear with three unknowns and four equations:

$$\begin{bmatrix} \overline{dX}_1 \\ \overline{dY}_1 \\ \overline{dX}_2 \\ \overline{dY}_2 \end{bmatrix} = \begin{bmatrix} X_x^{(1)} & X_y^{(1)} & X_z^{(1)} \\ Y_x^{(1)} & Y_y^{(1)} & Y_z^{(1)} \\ X_x^{(2)} & X_y^{(2)} & X_z^{(2)} \\ Y_x^{(2)} & Y_y^{(2)} & Y_z^{(2)} \end{bmatrix} \cdot \begin{bmatrix} \overline{dx} \\ \overline{dy} \\ \overline{dz} \end{bmatrix} \tag{3.7}$$

$$\overline{d\underline{X}}_{1,2} = \nabla \underline{F}^{(1,2)} \cdot \overline{d\underline{x}}$$

Only with an ideal measurement, two of the equations are dependent. In the real measurement, a least squares solution can be used to minimize the squared Euclidean norm of the residual. The scheme of the whole procedure proposed by Soloff et al. (1997) is drown in Fig. 3.10 and is made up of the following steps:

- Calibration is performed so that the mapping function is computed;
- Images are recorded;
- Misalignment between measurement and calibration planes is corrected. This correction is made by means of the PIV images and by using the mapping function;
- PIV interrogation is computed on the warped images;

- The 3C reconstruction is computed by using both the mapping function and the correct position of the measurement plane. The former is used because the gradient of mapping function has to be computed. Furthermore, this gradient has to be computed in the correct position and this is the reason why also the coefficients obtained in the misalignment correction step are used.

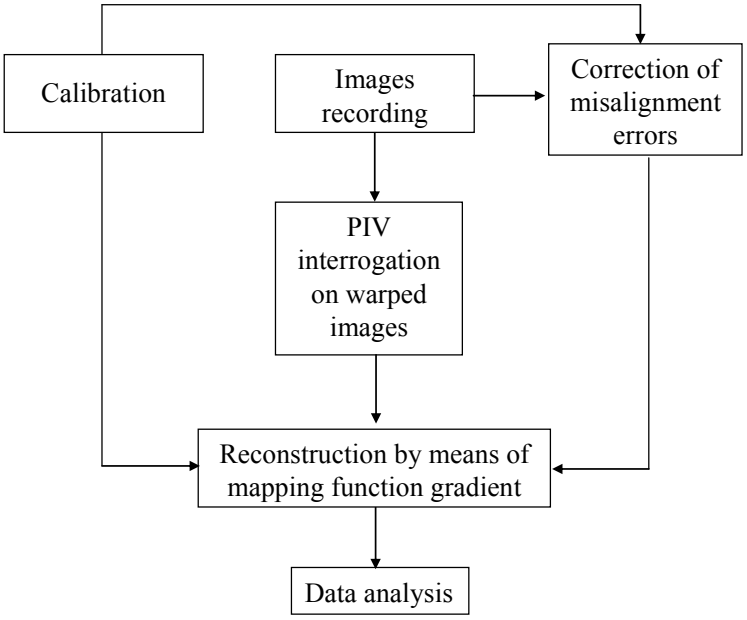

Fig. 3.10 Scheme of the 3C reconstruction procedure proposed by Soloff et al. (1997).

With regard to the 3C reconstruction method proposed by Willert (1997), as showed by Coudert and Schon (2001), it can be applied in the following two approaches: *mapping* and *warping*.

The scheme of the former approach is shown in Fig. 3.11 and is made up of the following steps:

- Calibration is performed so that the mapping function is computed;
- Images are recorded;
- Misalignment between measurement and calibration planes is corrected. This correction is made by means of the PIV images and by using the mapping function;
- Dewarping of images is made by using the mapping function and the coefficients obtained in the misalignment correction (so that the dewarping is computed in the correct position);
- PIV interrogation is performed on dewarped images;
- The 3C reconstruction is made by means of formulas 3.8, 3.9 and 3.10.

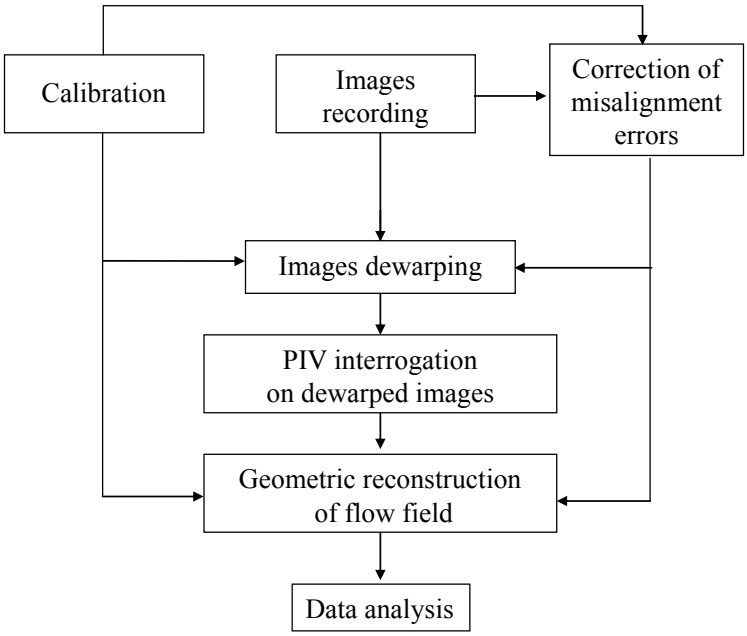

Fig. 3.11 Scheme of the 3C reconstruction procedure proposed by Willert (1997) – mapping approach.

The scheme of the warping approach is shown in Fig. 3.12 and is made up of the following steps:

- Calibration is performed so that the mapping function is computed;
- Images are recorded;
- Misalignment between measurement and calibration planes is corrected. This correction is made by means of the PIV images and by using the mapping function;
- PIV interrogation is made on warped images;
- Dewarping of the 2C displacement field obtained with images recorded by both cameras is computed. For this step the mapping function is required to dewarp the displacement field and the coefficients obtained in the misalignment correction are needed because the dewarping has to be made in the correct position. In this step also an interpolation is required because the two 2C displacement field are available on different grids;
- The 3C reconstruction is made by means of formulas 3.8, 3.9 and 3.10.

Concluding, the advantage of the warping method is the smaller computational time with respect to the mapping one. However, with the warping approach, the 2C vectors field is smoothed, as it is obtained interpolating the vector maps on a common regular grid, and the spatial resolution is non-uniform and non-isotropic, as the cross-correlation is done on warped images. The disadvantage of the mapping method, instead, is the need of image re-sampling, and consequently the loss of image quality.

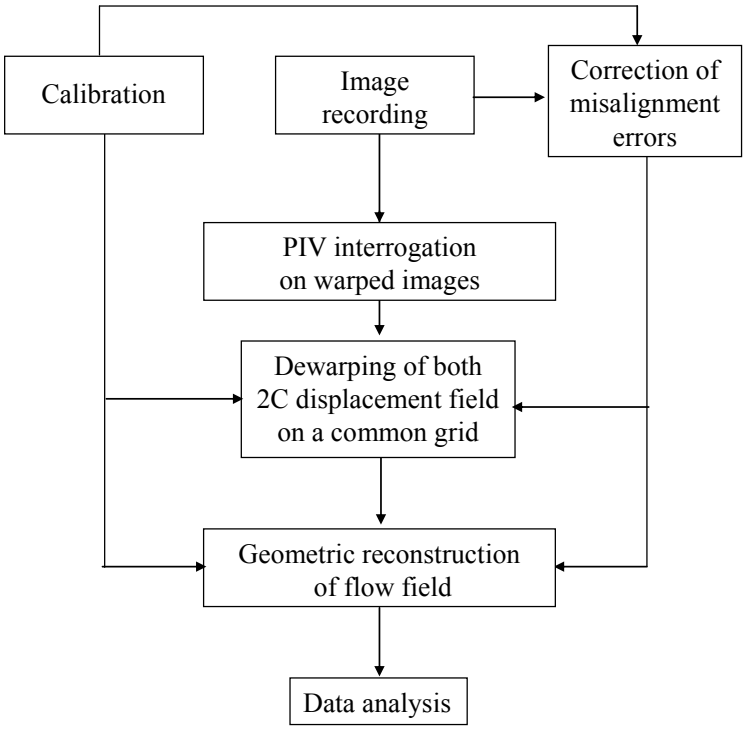

Fig. 3.12 Scheme of the 3C reconstruction procedure proposed by Willert (1997) – warping approach.

In this work, the mapping approach is adopted with a further precaution, in order to reduce the loss of image quality and, then, of the 3C displacement field: images de-warping is made inside the iterative deformation PIV process, according to Scarano et al. (2005) and Wieneke (2005).

In both 3C reconstruction approaches proposed by Willert (1997), geometric reconstruction of the three-dimensional displacement field is obtained by means of the two 2C-vector fields (related to the two cameras) and of the local viewing angles α_1, α_2, β_1 and β_2 (see Fig. 3.13, β_c is the angle between the viewing ray and the plane xz measured in the yz plane). The three components of the particles displacement (u, v, w) are calculated from the two–dimensional displacements u_1, v_1, u_2, v_2 by means of the formulas proposed by Willert (1997):

$$u = \frac{u_1 tan\alpha_2 - u_2 tan\alpha_1}{tan\alpha_2 - tan\alpha_1} \qquad 3.8$$

$$w = \frac{u_1 - u_2}{tan\alpha_2 - tan\alpha_1} \qquad 3.9$$

$$v = \frac{v_1 tan\beta_2 - v_2 tan\beta_1}{tan\beta_2 - tan\beta_1} = \frac{v_1 + v_2}{2} + \frac{w}{2}\left(tan\beta_1 + tan\beta_2\right) \qquad 3.10$$

where the viewing angles, in the original work by Willert, were evaluated by measuring the relative distances between the measurement point and the cameras. The formulas (2-4) are almost identical with Eq. 7.3-7.7 in Raffel et al. (2007); they differ because the viewing angles are defined in a different way.

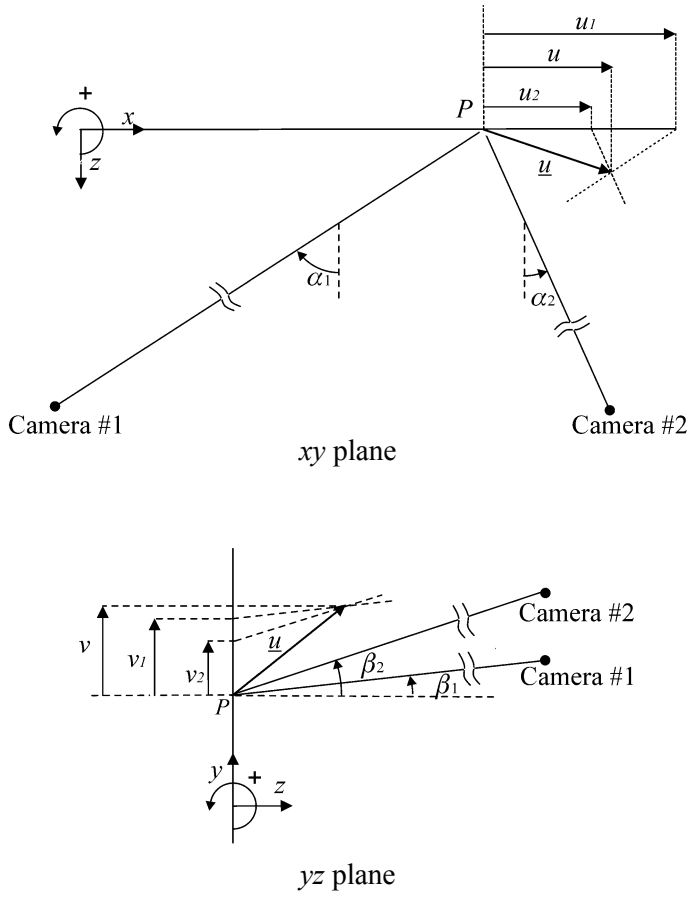

Fig. 3.13 Geometric reconstruction used by Willert (1997).

More recently, Fei and Merzkirch (2004) suggested a new method for the evaluation of α_1 and α_2 angles, whereas the terms with β_1 and β_2 are neglected. This method requires the correlation of two calibration images recorded in two different z positions. A similar method has been used by Scarano et al. (2005). In this work new formulas are proposed, which permit to compute the viewing angles without the necessity to measure any geometrical parameter of the experimental set-up and without further computations in addition to the unavoidable calibration of the stereoscopic configuration (see Sect. 4.1).

4 Stereo Particle Image Velocimetry technique: new developments and performance assessment

In the first part of this section, new formulas to compute the viewing angles will be obtained and the performance assessment will be computed.

After that, the Modulation Transfer Function (MTF) of the Stereo PIV technique will be analysed through investigation of the effects caused by three different parameters: the laser thickness, the linear dimension of the interrogation window W (i.e. the modulation associated to the Stereo PIV process) and the misalignment between measurement and calibration planes. As it will be shown in detail below, the modulation associated to the first two parameters cannot be corrected, differently from the modulation due to the misalignment. The main results of this section can be found in Giordano and Astarita (2009).

4.1 New formulas to compute the viewing angles

4.1.1 Theoretical analysis

In order to determine the local viewing angle, one can imagine an infinitesimal displacement vector $d\underline{x}$ along the viewing ray of the camera c (see Fig. 4.1). Obviously, the correspondent displacement $d\underline{X}_c$ in the image plane is null. Consequently, if one consider the Taylor series expansion of the mapping function:

$$d\underline{X}_c = \nabla \underline{F}^{(c)} \cdot d\underline{x}$$

$$\begin{bmatrix} dX_c \\ dY_c \end{bmatrix} = \begin{bmatrix} X_x^{(c)} & X_y^{(c)} & X_z^{(c)} \\ Y_x^{(c)} & Y_y^{(c)} & Y_z^{(c)} \end{bmatrix} \cdot \begin{bmatrix} dx \\ dy \\ dz \end{bmatrix} \qquad 4.1$$

(where $X^{(c)}$ is the mapping function for the image coordinate X_c relative to camera c and the subscript indicates derivation) the projection of Eq. 4.1 along the viewing ray becomes:

$$\begin{bmatrix} X_x^{(c)} & X_y^{(c)} & X_z^{(c)} \\ Y_x^{(c)} & Y_y^{(c)} & Y_z^{(c)} \end{bmatrix} \cdot \begin{bmatrix} dx \\ dy \\ dz \end{bmatrix} = \underline{0} \qquad 4.2$$

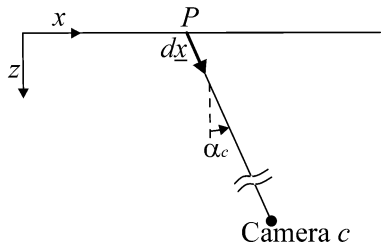

Fig. 4.1 Sketch of a generic displacement along the viewing ray of the camera *c*.

So, the viewing angles α_c and β_c in a generic point *P* are found to be:

$$tan(\alpha_c) = \left.\frac{dx}{dz}\right|_{d\underline{X}_c=\underline{0}} = \frac{Y_z^{(c)} X_y^{(c)} - Y_y^{(c)} X_z^{(c)}}{Y_y^{(c)} X_x^{(c)} - Y_x^{(c)} X_y^{(c)}} \tag{4.3}$$

$$tan(\beta_c) = \left.\frac{dy}{dz}\right|_{d\underline{X}_c=\underline{0}} = \frac{Y_z^{(c)} X_x^{(c)} - Y_x^{(c)} X_z^{(c)}}{Y_x^{(c)} X_y^{(c)} - Y_y^{(c)} X_x^{(c)}} \tag{4.4}$$

The main advantage of the formulas proposed in this section is that there is no need to measure any additional geometrical parameter of the experimental set-up. Moreover, with these formulas it is possible to compute the viewing angles without any further computations in addition to the unavoidable calibration of the stereoscopic configuration.

Generally, the assumption β=0 is done. In this case, since the terms $X_y^{(c)}$ and $Y_x^{(c)}$ are very small, the eqs 4.3 and 4.4 become:

$$tan(\alpha_c) = \left.\frac{dx}{dz}\right|_{dy=0} = \frac{-X_z^{(c)}}{X_x^{(c)}} \tag{4.5}$$

$$tan(\beta_c) = \left.\frac{dy}{dz}\right|_{dx=\underline{0}} = \frac{-Y_z^{(c)}}{Y_y^{(c)}} \tag{4.6}$$

Obviously, the error made using the latter formulas is as big as the approximations are wrong. For the computation of α_c angles, the approximation:

$$\left.\frac{dx}{dz}\right|_{d\underline{X}=\underline{0}} = \left.\frac{dx}{dz}\right|_{dy=0} \tag{4.7}$$

is acceptable, since the β_c angles are generally small. On the contrary, the approximation:

$$\left.\frac{dy}{dz}\right|_{d\underline{X}=\underline{0}} = \left.\frac{dy}{dz}\right|_{dx=0} \tag{4.8}$$

isn't acceptable, because the α_c angles used are usually very large, typically +/- 45°.

4.1.2 Experimental apparatus

In order to verify the new formulas to compute the viewing angles, the experimental setup described below has been used. Experiments are carried out in an angular stereoscopic PIV system, consisting of: two CCD cameras (PCO Sensicam) with a resolution of 1280x1024 *pixels*, 12 bits to record the images and a 50*mm* focal length; a combined PIV-calibration pattern containing both the regular grid of dots to make the calibration and the random positioned particles to create the particle image (see Fig. 4.2); a translation stage, which allows to shift the pattern in the z direction, with an accuracy of $10\mu m$. In order to obtain uniform focusing, the Scheimpflug condition is fulfilled (Prasad and Jensen 1995).

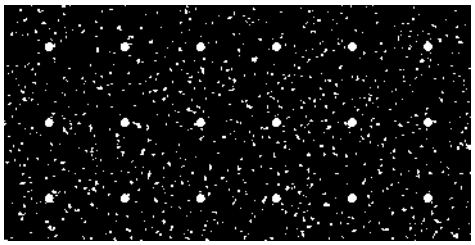

Fig. 4.2 Part of the calibration pattern that contains random positioned particle.

The PIV–calibration pattern is generated by a synthetic PIV pattern generator, as described in Astarita and Cardone (2005) and it also contains dots for calibration spaced of 5*mm* along both the x and the y directions. The advantage of this type of pattern is the possibility to use a single target for the whole simulation process and, thus, to avoid possible position errors associated with the change of the pattern.

4.1.3 Performance assessment

In order to show the capabilities of the new formulas proposed to compute the viewing angles, an uniform displacement field along z equal to 1*mm* has been simulated with no misalignment and the 3C reconstruction proposed by Willert (1997) has been used. The stereoscopic set-up characteristics are reported in Tab. 4.1. The PIV images have been investigated by using the iterative image deformation method (IDM) described by Astarita (2006), where the standard cross correlation and the top hat moving average approach (THMA) have been used. The used square interrogation windows have the linear dimension W equal to 32*pixels*; no overlap has been used.

In Fig. 4.3 the scatter plots of the three components are shown. The measurement points dispersions are practically equal for the three components. The mean errors committed in the

evaluation of the *u*, *v* and *w* components are equal to 4.23*μm*, 1.87*μm* and 1.45*μm* respectively and even smaller than the accuracy of the translation stage. All these results are comparable to the ones obtained by Scarano et al. (2005).

Mean viewing angles	+/- 45°
Mean distance between cameras and measurement plane	700*mm*
Focal length	50*mm*
Mean resolution along *x*	7.9*pixel*/*mm*
Mean resolution along *y*	11.4*pixel*/*mm*
Interrogation windows linear dimension *W*	32*pixel*
Laser thickness (*LT*)	0*mm*
Misalignment: translation	0*mm*
Misalignment: rotation (*x*/*y*)	0/0°
Size of calibration volume	2*mm*

Tab. 4.1 Stereoscopic set-up used with the simulated displacement.

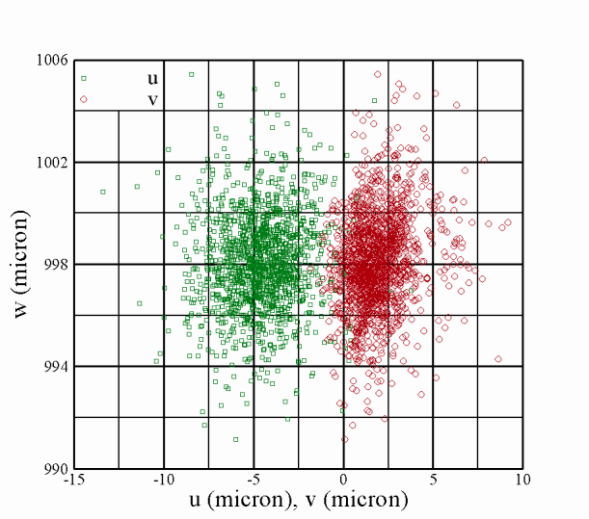

Fig. 4.3 Scatter plot of *u*, *v* and *w* components obtained with the formulas proposed for computing the viewing angles for the Willert's 3C reconstruction.

The displacement simulated in this section allows us to investigate also the goodness of the formulas 4.3-4.4 (second order) in comparison to the simplified formulas 4.5-4.6 (first order). In fact, the *u* and *w* component maps show no remarkable differences between results obtained with formulas of the first and second order, whereas improvements are obtained in the evaluation of the *v* component. The results obtained with first order formulas (Fig. 4.4-*a*) show a trend along the *y* direction: the value of *v* component varies in the interval [-0.020, 0.020]*mm*, in spite of the predictor value equal to 0*mm*. This trend is corrected by using the second order formulas (Fig. 4.4-*b*).

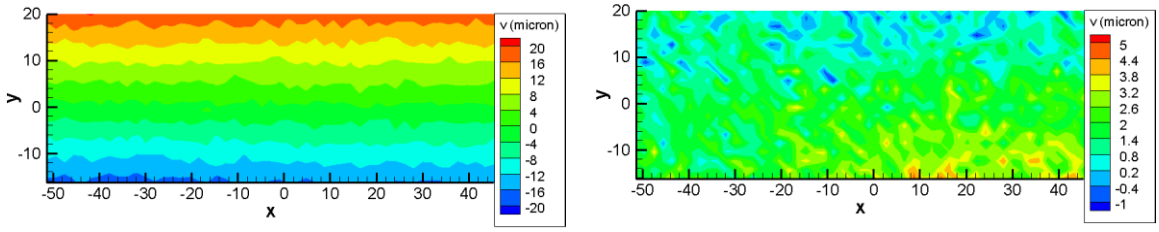

a *b*

Fig. 4.4 *v* component (*mm*) of 3C displacement field obtained with formulas used to compute viewing angles of: *a*-first order; *b*-second order.

4.2 Modulation dependence on the laser thickness

4.2.1 Theoretical analysis

As far as the laser thickness is concerned, the modulation happens in the image recording and then it can't be corrected. By considering a gradient in a generic direction with wavenumber $\underline{k}$:

$$\underline{k} = \left[k_x, \quad k_y, \quad k_z\right] = \left[\frac{2\pi}{\lambda_x}, \quad \frac{2\pi}{\lambda_y}, \quad \frac{2\pi}{\lambda_z}\right] \tag{4.9}$$

the modulation depends on the local vector $\underline{\xi}_c$ obtained by intersecting the optical axis of camera *c* and the laser sheet (see Fig. 4.5). Really, the displacement "seen" by camera *c* is an average of the displacement along the viewing ray.

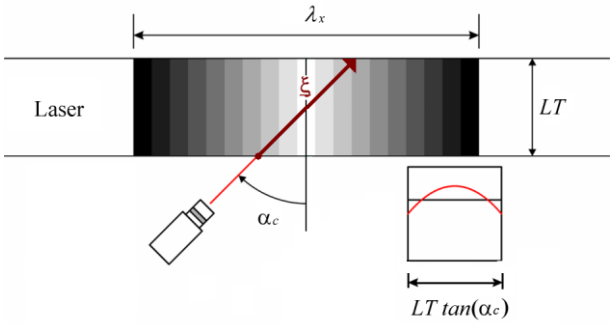

Fig. 4.5 Sketch of the modulation associated to the laser thickness for a gradient in the *x* direction.

Therefore, the modulation transfer function turns out to be:

$$\mathrm{MTF}_{\mathrm{LTc}} = \mathrm{sinc}\left(\frac{\left|\underline{\xi}_c \cdot \underline{k}\right|}{2\pi}\right) \tag{4.10}$$

For example, if the gradient is in the x direction (as sketched in Fig. 4.5), the modulation is:

$$\mathrm{MTF}_{\mathrm{LTc}} = \mathrm{sinc}\left(\frac{\left|\underline{\xi}_c \cdot \underline{k}\right|}{2\pi}\right) = \mathrm{sinc}\left(\frac{\left|\dfrac{LT}{\cos\alpha_c}\dfrac{2\pi}{\lambda_x}\sin\alpha_c\right|}{2\pi}\right) = \mathrm{sinc}\left(\frac{LT}{\lambda_x}\tan\left|\alpha_c\right|\right) \qquad 4.11$$

whereas, if the gradient is in the z direction:

$$\mathrm{MTF}_{\mathrm{LTc}} = \mathrm{sinc}\left(\frac{\left|\underline{\xi}_c \cdot \underline{k}\right|}{2\pi}\right) = \mathrm{sinc}\left(\frac{\left|\dfrac{LT}{\cos\alpha_c}\dfrac{2\pi}{\lambda_z}\cos\alpha_c\right|}{2\pi}\right) = \mathrm{sinc}\left(\frac{LT}{\lambda_z}\right) \qquad 4.12$$

If the gradient is in the viewing direction, the camera c can't appreciate it, $\mathrm{MTF}_{\mathrm{LTc}}$ being null. Obviously in this case, if the viewing angles of the two cameras form a 90° angle, the other camera measures the gradient without any modulation. In any case the resulting modulation due to laser thickness $\mathrm{MTF}_{\mathrm{LT}}$ can be evaluated by using the 3C reconstruction formulas (3.8-3.10); e.g. for the u component:

$$\mathrm{MTF}_{\mathrm{LT}} \cdot u = \frac{\mathrm{MTF}_{\mathrm{LT1}} \cdot u_1 \cdot \tan\alpha_2 - \mathrm{MTF}_{\mathrm{LT2}} \cdot u_2 \cdot \tan\alpha_1}{\tan\alpha_2 - \tan\alpha_1} \qquad 4.13$$

4.2.2 Synthetic image generator

A synthetic image generator has been used to validate the theoretical analysis of the MTF relative to the laser thickness. For this purpose, a sinusoidal displacement has been simulated for different values of the laser thickness.

The images are generated including the effect of perspective and distortion caused by the viewing angle of the cameras, set in an angular stereoscopic configuration. The geometrical and optical configurations are simulated by using the camera pinhole model proposed by Tsai (1987). Obviously, both calibration and PIV images are generated with the same configuration parameters.

The light sheet has a Gaussian shape. The particle diameter distribution is Gaussian and the position distribution of the particles is uniform in the whole volume. On average, the particles have a size of 2-3 *pixels* in the image. Their shape is supposed to be Gaussian and, then, the intensity level is computed by integrating the particle light distribution on each image pixel; really if two or more particles overlap, the intensity level of each pixel is the sum

of the intensity of each particle. The pixels have a maximum level of 4095 and a unit fill factor. The dimension of the images is 1280x1024 *pixels*.

4.2.3 Performance assessment

In order to validate Eq. 4.10, a displacement field with the v component sinusoidal along x direction with amplitude 0.1*mm* and wavelength equal to 12*mm* has been simulated, whereas the laser thickness ranges from 0*mm* to 18*mm*. Obviously, this range includes thickness too large physically speaking; this choice is done only to verify the Eq. 4.10. The stereoscopic set-up is described in Tab. 4.1.

Mean viewing angles	+/- 45°
Mean distance between cameras and measurement plane	520*mm*
Focal length	50*mm*
Mean resolution along x	10.2*pixel*/*mm*
Mean resolution along y	14.6*pixel*/*mm*
Interrogation windows linear dimension W	16*pixel*
Amplitude of sinusoidal component	0.10*mm*
Wavelength of sinusoidal component	12*mm*
Laser thickness range (LT)	0-18*mm*
Size of calibration volume	2*mm*

Tab. 4.2 Stereoscopic set-up no. 1 used with synthetic images.

Since the sinusoidal displacement is along the x direction, we want to validate the Eq. 4.11; furthermore, since the stereoscopic setup is symmetric, the modulation due to the laser thickness is practically equal for the two cameras:

$$\alpha_1 = \alpha_2 = \alpha \quad \Rightarrow \quad \mathrm{MTF}_{\mathrm{LT}1} = \mathrm{MTF}_{\mathrm{LT}2} = \mathrm{sinc}\left(\frac{LT}{\lambda_x} \tan|\alpha| \right) \tag{4.14}$$

Then, by using Eq. 3.10, one obtains:

$$\mathrm{MTF}_{\mathrm{LT}} \cdot v = \frac{\mathrm{MTF}_{\mathrm{LT1}} \cdot v_1 + \mathrm{MTF}_{\mathrm{LT}2} \cdot v_2}{2} \quad \Rightarrow \quad \mathrm{MTF}_{\mathrm{LT}} = \mathrm{MTF}_{\mathrm{LT1}} = \mathrm{MTF}_{\mathrm{LT}2} \tag{4.15}$$

Fig. 4.6 shows the theoretical curve (solid line) and the ones obtained with both Soloff and Willert approaches (circle and triangle symbols, respectively): these are nearly coincident with the theoretical one and substantially coincident with each other.

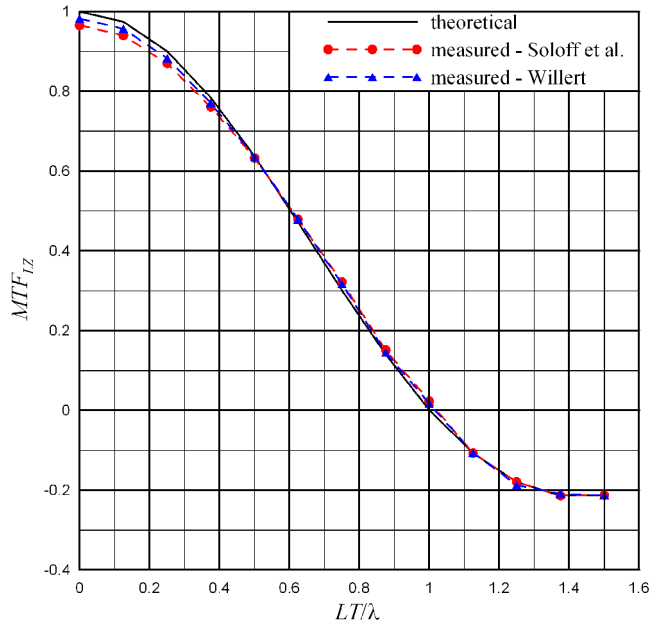

Fig. 4.6 MTF_{LT} as a function of LT/λ for the stereoscopic set-up used with a wavelength $\lambda_x = 12mm$.

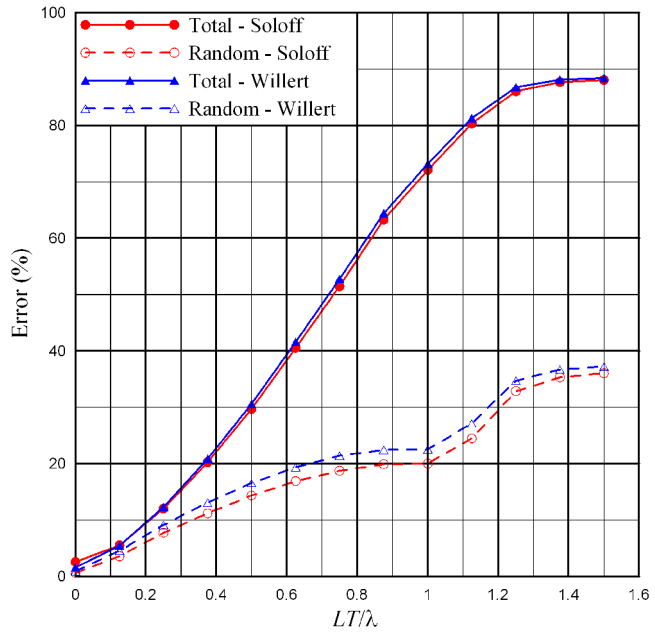

Fig. 4.7 Total and random errors as a function of LT/λ for the stereoscopic set-up used with a wavelength $\lambda_x = 12mm$.

Fig. 4.7 shows the total and random errors for both approaches: the total error is the quadratic mean of the error committed in the evaluation of the sinusoidal component in each point of the measurement plane; whereas, the random error indicates only the error made with respect to the modulated sinusoidal component. The difference between them is the error associated with the modulation. The good overlapping of the curves relative to the two approaches for both total and random errors is a further proof that this kind of modulation is

associated to the image recording and, then, it doesn't' depend on the 3C reconstruction approach.

4.3 Modulation dependence on the 3C reconstruction

4.3.1 Theoretical analysis

In order to study the influence of the PIV interrogation window size W on the MTF of the technique, let's consider a displacement field consisting of a single sinusoidal component with several wavelengths and a very small laser thickness, that allows to neglect the above mentioned effect. In this analysis, the PIV images have been investigated by using the iterative image deformation method (IDM) described by Astarita (2006), where the standard cross correlation and the top hat moving average approach (THMA) have been used. On account of the method chosen to evaluate the PIV images, the theoretical MTF of the PIV technique used herein should be practically equal to the one of the top hat moving window filter; the latter, for the typical values of the interrogation window dimensions and of the wavelengths λ used in PIV measurements, is practically coincident with sinc(W/λ), where W is the linear dimension of the square interrogation window.

The additional modulation due to the 3C reconstruction procedure is explained in detail below. As in most cases (i.e. when the experimental configuration is almost symmetric[4]) the 3C reconstructions proposed by Soloff et al. (1997) and Willert (1997) are practically equivalent, the main differences are in the choice whether one uses the warping or mapping approach. Nevertheless, since usually the Soloff and Willert procedures are applied with warping and mapping approaches respectively, here these equivalences are supposed.

Since in the 3C reconstruction proposed by Willert (1997), the PIV interrogation is made on the de-warped images, the MTF of the PIV process is uniform on the two 2C displacement fields:

$$\mathrm{MTF}_{2\mathrm{C}}(X_1,Y_1)=\mathrm{MTF}_{2\mathrm{C}}(X_2,Y_2)\quad\forall(X_c,Y_c) \tag{4.16}$$

By looking at the reconstruction formulas (3.8 - 3.10), it's easy to understand that there is no additional modulation relative to the 3C reconstruction process. For this purpose, let's consider a sinusoidal u component: if in a generic point of the measurement plane we have

[4] For more details about the case in which this equivalence isn't true, see Sect. 4.4.3.

two 2C-vectors with the same modulation MTF_{2C}, the modulation associated with the 3C-vector will be equal to MTF_{2C}:

$$\mathrm{MTF}u = \frac{\mathrm{MTF}_{2C} \cdot u_1 \cdot \tan\alpha_2 - \mathrm{MTF}_{2C} \cdot u_2 \cdot \tan\alpha_1}{\tan\alpha_2 - \tan\alpha_1} = \mathrm{MTF}_{2C} \cdot u \qquad 4.17$$

A similar conclusion can be drawn for the *v* and *w* components. The only reason of an additional modulation could be due to the de-warping process. However, this effect has been neglected here and the results shown in the following prove the correctness of this assumption.

On the contrary, in the 3C reconstruction proposed by Soloff et al. (1997), since the PIV interrogation is made with the warped images, the MTF of the PIV process (depending on the local spatial resolution) isn't uniform on both the 2C displacement fields and then the 2C vectors used in the 3C reconstruction have different modulations. Since, when the spatial resolution and the viewing angles of the two cameras are similar, the two 3C reconstructions are practically equivalent, it is possible to use the Willert reconstruction with unequal dimension of the interrogation windows to explain the MTF of the Soloff approach. For this purpose, let's consider a displacement field with the *u* component sinusoidal along the *y* direction, with a same side symmetric stereoscopic set-up described in Tab. 4.3 and let's suppose to use again the Willert's reconstruction, but with unequal dimension of the interrogation windows.

Mean viewing angles	+/- 45°
Mean distance between cameras and measurement plane	700*mm*
Focal length	25*mm*
Mean resolution along x	7.3*pixel*/*mm*
Mean resolution along y	10.5*pixel*/*mm*
Amplitude of sinusoidal component	0.10*mm*
Wavelength range of sinusoidal component	7-50*mm*
Laser thickness (*LT*)	0.2*mm*
Misalignment: translation	0*mm*
Misalignment: rotation (*x*/*y*)	0/0°
Size of calibration volume	2*mm*

Tab. 4.3 Stereoscopic set-up no. 2 used with synthetic images.

In such a configuration, the modulation in a generic point of the measurement plane can be evaluated by using the formulas (3.8-3.10) and, since the two 2C vectors used in the 3C

reconstruction have different modulations (due to different W), depends on both the local viewing angles and the local $MTF_{2C}(X_c, Y_c)$. Then, the modulation associated to the 3C vectors changes inside the measurement plane giving the possibility to evaluate a maximum, minimum and mean MTF over the measurement plane. Locally the MTF can be computed by substituting in Eq. 4.17 the local values of the viewing angles and $MTF_{2C}(X_c, Y_c)$. By using an interrogation window size equal to 16x16 *pixels* for the first camera and 32x32 *pixels* for the second one, the theoretical minimum, maximum and mean MTF for each wavelength are shown in Fig. 4.8 (cross symbols). In the same figure, also the theoretical MTFs relative to the standard process with W=16*pixels* and W=32*pixels* are reported.

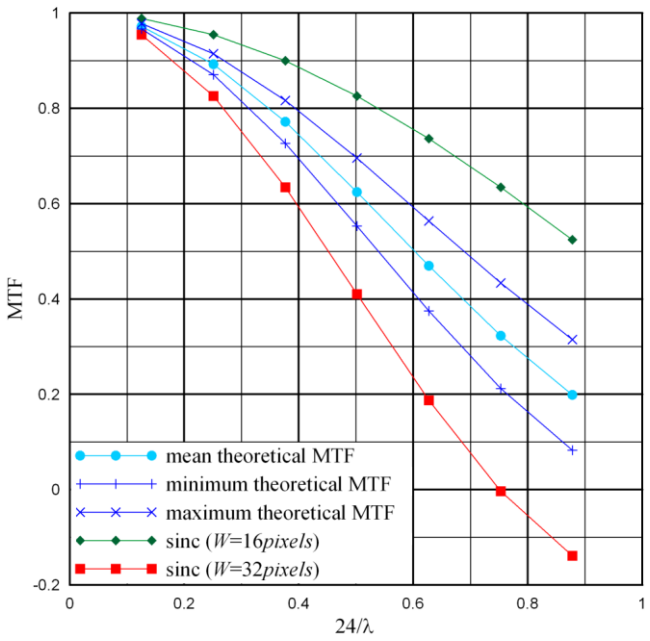

Fig. 4.8 MTF as a function of 24/λ (W=24*pixels*) for the procedure proposed by Willert (1997) applied with two different W on each camera..

In order to demonstrate that the last analysis can explain the modulation associated to the Soloff's 3C reconstruction, let's indicate with R_{cr} and R_{cl} the resolution of the image recorded by the camera c in the right and left sides respectively, if the stereoscopic configuration is such that the maximum resolution ratio:

$$RR_{\max} = \frac{R_{1l}}{R_{1r}} = \frac{R_{2r}}{R_{2l}} = \frac{R_{1l}}{R_{2l}} = \frac{R_{2r}}{R_{1r}} \qquad 4.18$$

is equal to 2 (for the sake of brevity, the considered stereoscopic set up is same side symmetric: $R_{1l} = R_{2r}$ and $R_{1r} = R_{2l}$), the modulation of the reconstruction suggested by Soloff et al. (1997) with W=24*pixels* could be represented by the curve with circles (Fig. 4.8). This

situation isn't so strange since a stereoscopic configuration which presents the ratio of the resolution along x between left and right sides of warped image almost equal to 2 is exactly the one described in Tab. 4.3. Obviously, the above mentioned ratio is so high only at the sides of the images, whereas it is unitary at the centre[5]. In Fig. 4.9 the mean theoretical MTF for the Soloff's procedure applied with W=24*pixels* is shown (cross symbol). In the same figure, also the theoretical MTF relative to the maximum and minimum resolutions are reported (diamond and square symbols respectively). Actually this additional modulation associated to the Soloff's 3C reconstruction can be reduced if a correlation with adapted windows is used (i.e. different correlation window sizes in the image plane during the analysis), so that the resolution preserves almost uniform on the object plane.

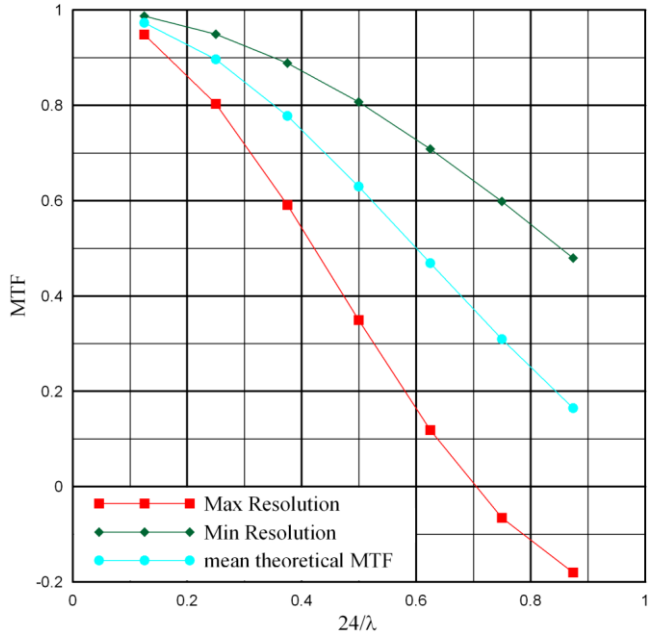

Fig. 4.9 MTF as a function of 24/λ (W=24*pixels*) for the procedure proposed by Soloff et al. (1997).

Theoretically, a different modulation associated to the two 2C-vectors used in the 3C reconstruction can cause the birth of false components of the displacement field. For this reason, let's consider the formulas (3.8 - 3.10): if the modulations of the two 2C vectors (u_1 and u_2) are different, false w and v components can arise[6] and obviously also the arisen

[5] This happens because the stereoscopic setup used here is same side symmetric. For a opposite side symmetric setup, both the local viewing angles and MTF_{2C} relative to the two cameras are equal in the same physical point, but they change inside the image and then, also in this case, the MTF of the 3C vector isn't uniform on the object plane.

[6] An analogous conclusion can't be drawn if the two 2C vectors with different modulations are v_1 and v_2, as the formulas (2-4) suggest.

components *v* and *w* are sinusoidal. This is what happens in the above described analysis in which the Willert's reconstruction has been applied with two different interrogation windows for the images recorded by the two cameras. In Fig. 4.10 the ratio between the amplitude of the measured *w* component and the exact *u* component (*w*/*u*) is shown as a function of W/λ (square symbol): for $W/\lambda \approx 0.8$ the MTF is almost equal to 0.3 and the ratio *w*/*u* is almost equal to 0.33; this means that the measured *u* and *w* have roughly the same amplitude. The same figure shows the maximum *w*/*u* (which is obtained where the resolution ratio is maximum, i.e. in the left and right sides of the measurement plane) for the Soloff's approach applied in the same stereoscopic set-up (circle symbol). It's encouraging to note that the two curves are quite coincident. A similar analysis can be done for the false *v* component: in this case the ratio *v*/*u* is never higher than 6%.

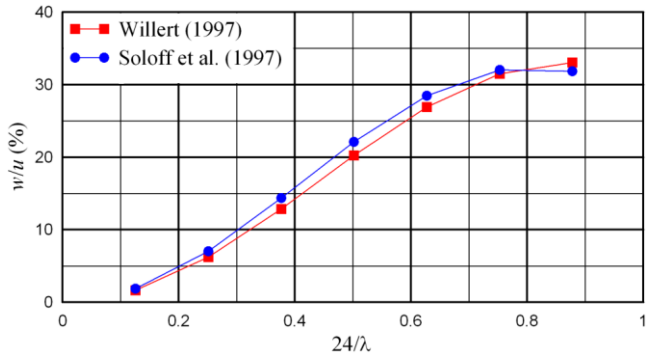

Fig. 4.10 *w*/*u* (%) as a function of 24/λ (*W*=24*pixels*) for the Willert's approach applied with two different *W* and for the Soloff's one (maximum value).

4.3.2 Synthetic images

In order to validate the theoretical analysis, the synthetic image generator (described in Sect. 4.2.2) is used to simulate images with sinusoidal displacements at various wavelengths. This choice is in accord with the test case A4 setup by Scarano and Wieneke for the PIV technique and the test case D1 setup by Stanislas for the Stereo PIV technique in the third PIV challenge (Stanislas et al. 2008).

4.3.3 Performance assessment

Fig. 4.11 shows the MTF measured for both procedures investigated (dashed lines) applied with the same side standard symmetric configuration described in Tab. 4.4 (without misalignment) and the relative theoretical curves. Since the Modulation Transfer Function depends on the resolution and this is a little different for the two procedures, there is a little

difference between the two theoretical MTF (relative to the two approaches), so they both have been drawn in the figure (solid lines). The measured MTFs relative to both procedures (circles and diamonds for Soloff and Willert procedures, respectively) are very similar; the measured MTF of the Soloff's procedure being slightly below the other one.

Mean viewing angles	+/- 45°
Mean distance between cameras and measurement plane	520*mm*
Focal length	50*mm*
Mean resolution along *x*	10.2*pixel*/*mm*
Mean resolution along *y*	14.6*pixel*/*mm*
Interrogation windows linear dimension *W*	16*pixel*
Amplitude of sinusoidal component	0.10*mm*
Wavelength range of sinusoidal component	1.6-12*mm*
Laser thickness (*LT*)	0.2*mm*
Size of calibration volume	2*mm*

Tab. 4.4 Stereoscopic set-up no. 3 used with synthetic images.

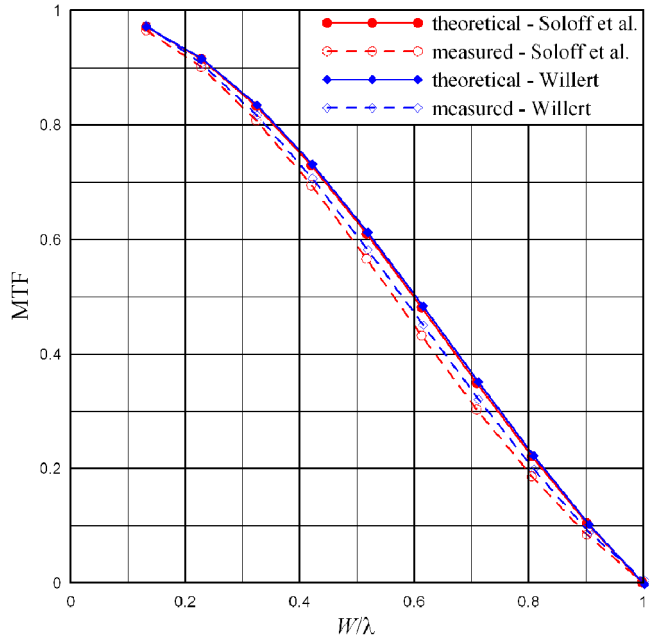

Fig. 4.11 MTF as a function of W/λ: closed symbols refer to theoretical values while open symbols to measured ones. Circles and diamonds are relative to the procedures proposed by Soloff et al. (1997) and Willert (1997) respectively.

In Fig. 4.12 the errors committed in both approaches are shown. As mentioned before, the total error is the quadratic mean of the error committed in the evaluation of the sinusoidal component in each point of the measurement plane; whereas, the random error indicates only the error made with respect to the modulated sinusoidal component. The difference between them is the error associated with the modulation. The figure shows quite similar total and

random errors relative to both procedures, Willert's procedure error curves being slightly above the other ones.

In conclusion, according to the theoretical analysis, the performance assessment showed that the modulation relative to the 3C reconstruction for both approaches could be neglected for common configurations.

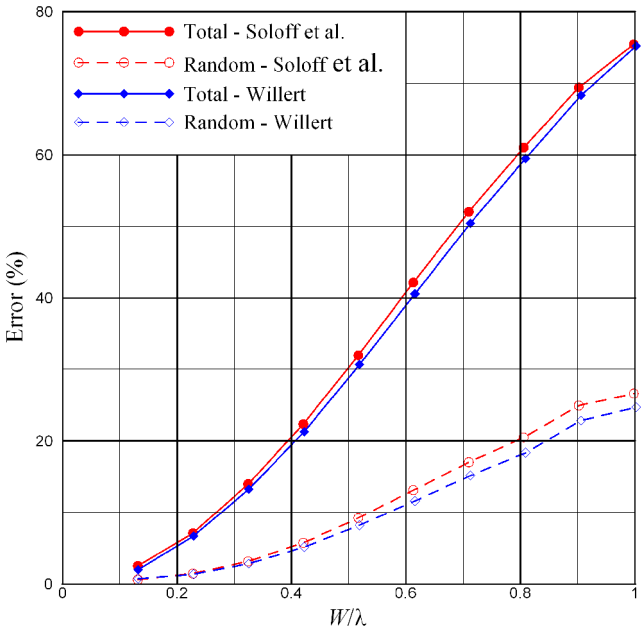

Fig. 4.12 Errors as a function of W/λ: closed symbols refer to total errors while open symbols to random ones. Circles and diamonds are relative to the procedures proposed by Soloff et al. (1997) and Willert (1997) respectively.

4.4 Modulation dependence on the misalignment

4.4.1 Theoretical analysis

In order to extend the theoretical analysis of the MTF relative to the Stereo PIV technique with a misalignment between the calibration and measurement planes, let's consider a misalignment consisting of a translation along z equal to $1mm$. For a displacement field consisting of a sinusoidal component along the y direction, the misalignment above described doesn't bring any appreciable error. This happens because the position error (see Sect. 3.2) implies the use of two 2C-vector in the 3C reconstruction translated along x and practically coincident, since the sinusoidal component recurs unchanged along the x direction. Actually, the two 2C-vectors are translated also along the y direction, but this translation is equal to $\Delta z \cdot tan\beta$ and then it is very small. On the other hand, the 3C reconstruction error is negligible for the misalignment contemplated herein.

For the aforesaid reason, it is chosen to simulate a displacement field that consists of a *v* component sinusoidal along the *x* direction, for which the position error is relevant. A similar analysis can be done for a *u* or *w* sinusoidal component. The characteristics of the stereoscopic set-up are the ones reported in Tab. 4.4.

For this displacement field the position error implies the combination of two dephased sinusoidal components in the 3C reconstruction and so a further modulation. For this purpose, let's consider the reconstruction formulas for the *v*-component (Eq. 3.9) used in 3C reconstruction proposed by Willert (1997); for the displacement field simulated, it becomes ($w = 0$):

$$v = \frac{v_1 + v_2}{2} \tag{4.19}$$

So, if in a generic point a misalignment Δz occurs between calibration and measurement planes, two dephased sinusoidal component are used in the reconstruction, instead of the correct component $sin(k_x x)$, where $k_x = 2\pi/\lambda_x$ is the wavenumber:

$$v = \frac{\sin\left[k_x\left(x + t_1\right)\right] + \sin\left[k_x\left(x + t_2\right)\right]}{2} \tag{4.20}$$

The two phases t_1 and t_2 are:

$$t_c = -\Delta z \cdot \tan\left(\alpha_c\right) \quad c = 1,2 \tag{4.21}$$

where Δz is the local misalignment and α_c is the viewing angle of camera *c* (see Fig. 3.9).

By manipulating Eq. 4.20, it is possible to find:

$$\begin{aligned} v &= \frac{1}{2}\left[\cos\left(k_x t_1\right) + \cos\left(k_x t_2\right)\right]\sin\left(k_x x\right) + \frac{1}{2}\left[\sin\left(k_x t_1\right) + \sin\left(k_x t_2\right)\right]\cos\left(k_x x\right) \\ &= \mathrm{MTF}_{\Delta z}\sin\left[k_x x + \varphi\right] \end{aligned} \tag{4.22}$$

where:

$$\mathrm{MTF}_{\Delta z} = \begin{cases} abs\left\{\cos\left[k_x\left(t_1 - t_2\right)/2\right]\right\} & for \quad \cos\left(k_x t_1\right) + \cos\left(k_x t_2\right) \geq 0 \\ -abs\left\{\cos\left[k_x\left(t_1 - t_2\right)/2\right]\right\} & for \quad \cos\left(k_x t_1\right) + \cos\left(k_x t_2\right) < 0 \end{cases} \tag{4.23}$$

$$\varphi = \arctan\left\{\tan\left[k_x\left(t_1 + t_2\right)/2\right]\right\} \quad , \quad \varphi \in \left]-\frac{\pi}{2}, \frac{\pi}{2}\right[\tag{4.24}$$

So, instead of the correct component $sin(k_x x)$, one measures a modulated and dephased sinusoidal component, with a modulation factor $\mathrm{MTF}_{\Delta z}$ and phase φ. Since both the

modulation factor and the phase depend on t_1 and t_2 (see Eqs. 4.23 and 4.24) and in turn these depend on the local viewing angles and misalignment, the Eqs. 4.22, 4.23 and 4.24 are general and can be applied with any stereoscopic setup in order to determine the local modulation.

If the two viewing angles have almost the same absolute value and opposite signs (i.e. same side standard symmetric configuration with little variation of the viewing angles on the whole measurement plane), the two phases t_1 and t_2 have the same absolute value and opposite signs (see Eq. 4.21). In this case, the phase φ becomes null and the measured sinusoidal component is only modulated respect to the exact one.

In Fig. 4.13 the $MTF_{\Delta z}$ as a function of W/λ is shown, for the stereoscopic set-up described in Tab. 4.4 and with a misalignment consisting of a translation along z equal to $1mm$: it's interesting to note that $MTF_{\Delta z}$ can be even negative for particular values of W/λ. The $MTF_{\Delta z}$ function for this configuration (see Tab. 4.4) doesn't vary in an appreciable manner for the small variation of the difference between the absolute values of the viewing angles $\Delta\alpha = |\alpha_2| - |\alpha_1|$; for this reason only one curve is shown. On the other hand, the phase value is very sensible to the latter difference. For this reason, in Fig. 4.14 φ as a function of W/λ is shown for different values of $\Delta\alpha$. Since the configuration adopted here is symmetric, the maximum value of the latter difference is identical (in absolute value) at the right and left extremities of the image plane.

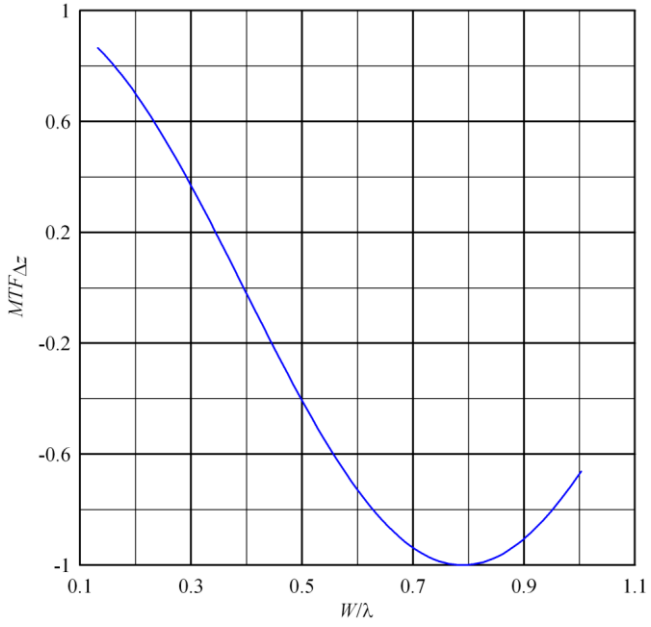

Fig. 4.13 $MTF_{\Delta z}$ as a function of W/λ for the stereoscopic set-up described in Tab. 4.4 with a misalignment $\Delta z=1mm$.

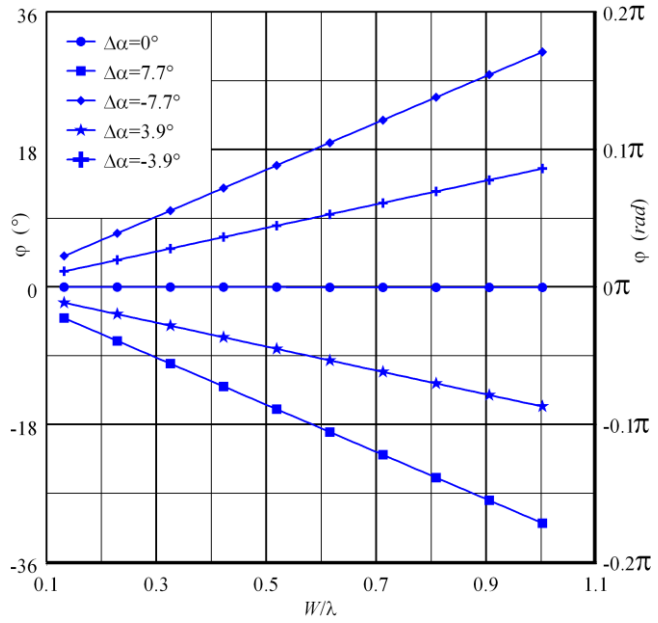

Fig. 4.14 φ as a function of W/λ for various $\Delta\alpha = |\alpha_2| - |\alpha_1|$ and the stereoscopic set-up described in Tab. 4.4 with a misalignment Δz=1*mm*.

4.4.2 Performance assessment with synthetic images

The performance assessment is conducted in order to validate the theoretical analysis computed in the last section. This has been done by using the synthetic images generated as described in Sect. 4.3.2.

Fig. 4.15 shows the MTF for both approaches applied with and without correction of the misalignment errors, in addition to the theoretical curves (green lines without symbol, solid and dashed for approaches applied with and without correction, respectively). The stereoscopic set-up is the same of the last section (Tab. 4.4) with a misalignment consisting of a translation along *z* equal to 1*mm*.

For both approaches applied with and without correction of the misalignment, it can be seen a good agreement with the theoretical curves; also in this case, the Soloff's curves (CS and NCS for results obtained with and without correction of misalignment, respectively) are less in accordance with the theoretical ones respect to the Willert's curves (CW and NCW for results obtained with and without correction of misalignment, respectively).

The error curves associated to both configurations (see Fig. 4.16) show, also in this case, quite similar total and random errors. The curves relative to the procedures applied without correction show normally, as expected, higher errors with respect to the one obtained with correction. With regard to the procedures applied with the correction of the misalignment, the Willert's approach has lower random and total errors; the opposite happens for the curves relative to the procedures applied without correction.

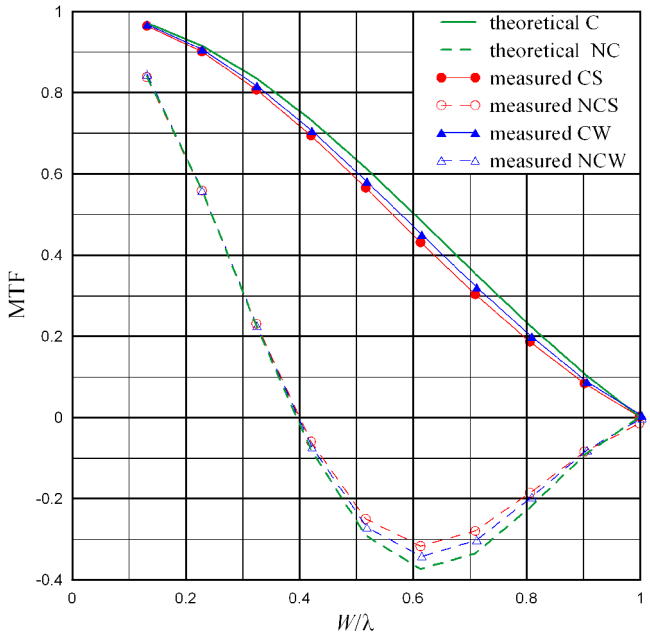

Fig. 4.15 MTF as a function of W/λ: curves without symbols refer to theoretical values. Circles and diamonds are relative to the procedures proposed by Soloff et al. (1997) and Willert (1997) whereas closed and open symbols refer to values measured with and without correction of misalignment error, respectively.

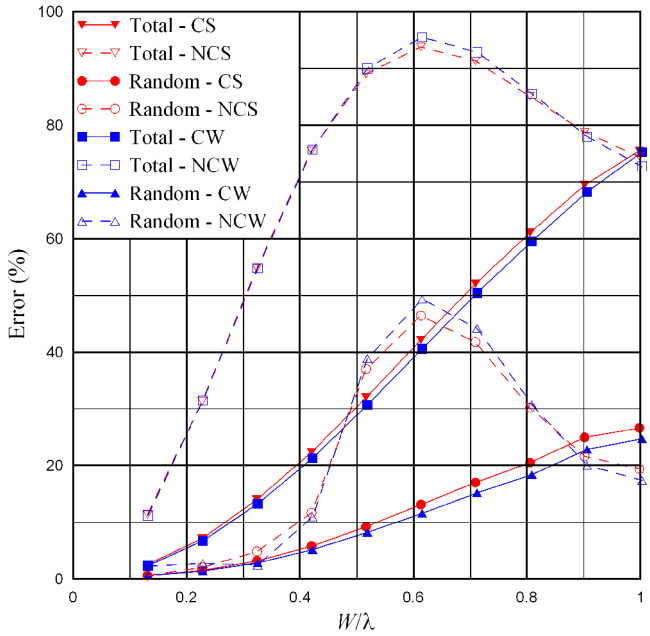

Fig. 4.16 Errors as a function of W/λ. Circles and diamonds are relative to the procedures proposed by Soloff et al. (1997) and Willert (1997) whereas closed and open symbols refer to values measured with and without correction of misalignment error, respectively.

It has to be evidenced that the errors associated to the misalignment of the measuring plane is not a consequence of the normal Stereo PIV modulation, but would be even higher if an higher resolution method was used in PIV process.

In conclusion, as theoretically explained before, in presence of misalignment and depending on the stereoscopic set-up used, some wavelengths of the flow field can be dephased and modulated, even with a negative modulation modulus. The performance assessment conducted in this section is in good agreement with the theoretical analysis.

4.4.3 Performance assessment with real images

In order to validate the theoretical analysis also with real images, the Stereo PIV technique has been applied to measure the wake of a finite cylinder in the experimental configuration described in Sect. 5.1 (see Tab. 4.5). Since the distance between the plane that contains the CCDs and the measurement plane is quite big (620*mm*) and one of the two viewing angles is very small (-8°), in order to appreciate the difference between the MTF of Stereo PIV applied with and without correction of misalignment, a huge misalignment has been simulated. The used calibration volume is from +6*mm* to -1*mm* regarding to reference plane. It contains the laser sheets as its thickness is 1.5*mm* (computed with the procedure described by Wieneke 2005) and the misalignment is 5*mm*. A better reference plane may have been chosen to have less misalignment, as we have many calibration planes (i.e. total number of calibration planes is 8). Also in this case, an iterative image deformation method has been used to interrogate the PIV images, with standard cross correlation and the top hat moving average approach.

Mean viewing angles	- 8°/+52°
Mean distance between cameras and measurement plane	620*mm*
Focal length	50*mm*
Mean resolution along *x*	14.05/6.67*pixel*/*mm*
Mean resolution along *y*	14.20/9.52*pixel*/*mm*
Interrogation windows linear dimension *W*	32-48*pixel*
Laser thickness (*LT*)	1.5*mm*
Misalignment: translation	5*mm*
Misalignment: rotation (*x*/*y*)	0.15/-0.35°
Size of calibration volume	[-6, 1]*mm*

Tab. 4.5 Stereoscopic set-up used with real images.

For the Stereo PIV parameters above described, the $MTF_{\Delta z}$ and φ functions are shown in Fig. 4.17 and Fig. 4.18, of course, they refer to the Willert's approach, since for the

Soloff's one the modulation associated to the misalignment can't be split from the modulation due to the technique.

In this case, differently from what shown in Fig. 4.13, the $MTF_{\Delta z}$ varies significantly by varying the parameter $\Delta\alpha = |\alpha_2| - |\alpha_1|$. This happens because for the configuration adopted here, the variation in the measurement plane of $\Delta\alpha$ is larger than the one relative to the stereoscopic set-up described in Tab. 4.4. The variation is such as to cause a different sign for the $MTF_{\Delta z}$ relative to different points of the measurement plane for some particular wavelengths (e.g. $W/\lambda \approx 0.3$). This is the reason why in Fig. 4.17 the mean $MTF_{\Delta z}$ and the $MTF_{\Delta z}$ relative to minimum and maximum $\Delta\alpha$ are reported (square, triangle and circle symbols, respectively). Fig. 4.18 shows the φ curves by varying the $\Delta\alpha$ (minimum and maximum values, triangle and circle symbols, respectively) and the mean curve (square symbol). In both figures, the vertical dashed line indicates the normalised spatial wavelength in which the mean $MTF_{\Delta z}$ is minimum.

The Stereo PIV images have been evaluated with both procedures proposed by Soloff et al. (1997) and Willert (1997). In this case, the comparison between the two approaches isn't very simple, because the two cameras are set in a strong asymmetric configuration, i.e. the viewing angles and the distance between the camera and the measurement plane are very different for the two cameras. However, in order to allow a comparison, two different W have been chosen for the two approach: W=32*pixels* for the Soloff's approach and W=48*pixels* for the Willert's one.

In Fig. 4.19 the mean flow fields measured with Willert's procedure behind the cylinder with and without correction of the misalignment errors are shown, where the average is made with 500 samples. On the mean flow field, the only errors caused by the uncorrected misalignment that can be detected are the position and the 3C reconstruction ones, while no information about the MTF of the technique can be drawn. The position error committed without correction of misalignment is highlighted by the two vertical dashed lines: the shift along x of the vortices centre is bigger than 3*mm*, whereas variation of the vortex formation length is almost equal to 1*mm*.

In order to analyse the spatial response of the technique applied to this real experiment, the method proposed by Foucaut et al. (2004) has been used. The power spectra E_{21} of v evaluated along the central horizontal line of the contour map are plotted, as a function of the normalised spatial wavelength, in Fig. 4.20. Both the curves relative to the two approaches applied with and without correction of misalignment are shown, as well as the vertical dashed line which indicate the W/λ relative to the minimum mean $MTF_{\Delta z}$. Obviously, the E_{21} curves

relative to the uncorrected measurement are always under the other ones and the difference between the two curves increases in correspondence of the vertical line, in confirmation of the theoretical $MTF_{\Delta z}$ reported in Fig. 4.17.

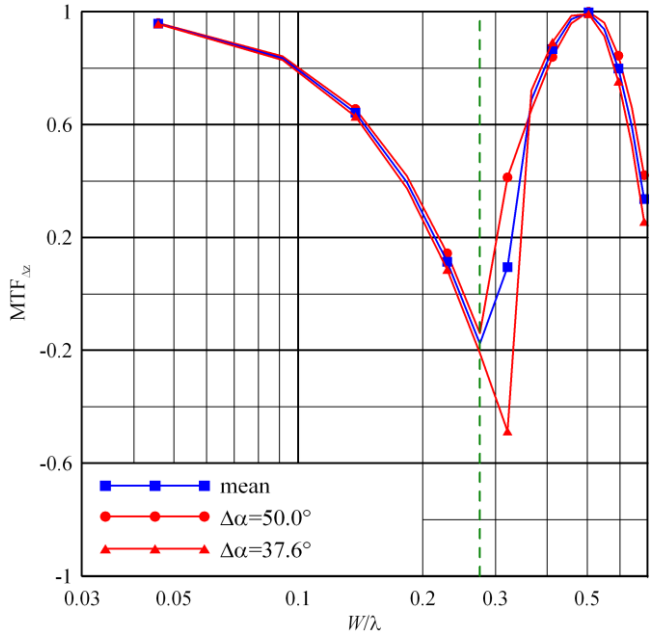

Fig. 4.17 $MTF_{\Delta z}$ as a function of W/λ, for two $\Delta\alpha = |\alpha_2| - |\alpha_1|$ and Δz=5*mm*. The curves with square symbols are relative to mean values. The green dashed line is plotted in correspondence of the $MTF_{\Delta z}$ minimum.

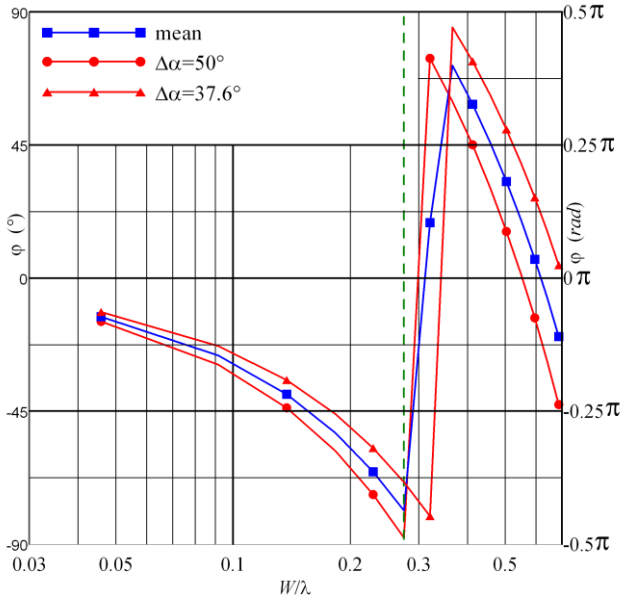

Fig. 4.18 φ□ as a function ofW/λ for two $\Delta\alpha = |\alpha_2| - |\alpha_1|$ and Δz=5*mm*. The curves with square symbols are relative to mean values. The green dashed line is plotted in correspondence of the $MTF_{\Delta z}$ minima.

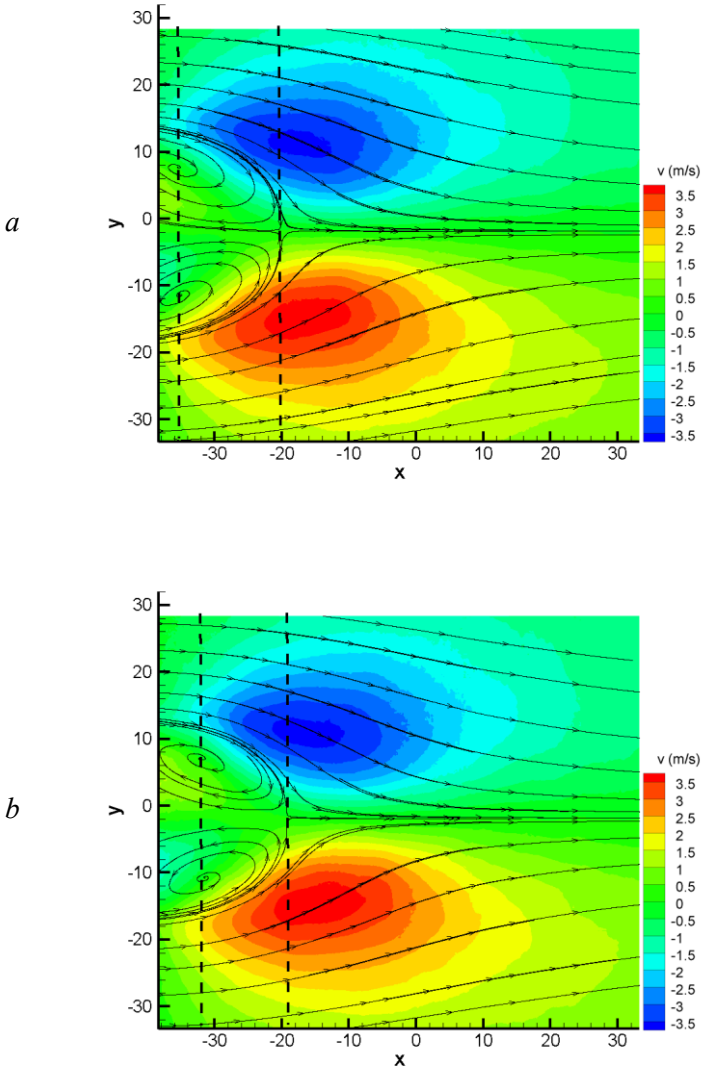

Fig. 4.19 Mean flow field obtained with the Willert's procedure measured behind a finite cylinder (*a*) without correction and (*b*) with correction of misalignment error.

The curves relative to both approaches applied with correction of the misalignment are almost coincident. This has been obtained by choosing two different interrogation window linear dimensions for the two approaches. In order to understand why the curves relative to the two approaches applied without correction of the misalignment are quite different, a brief analysis of the two approaches is requested.

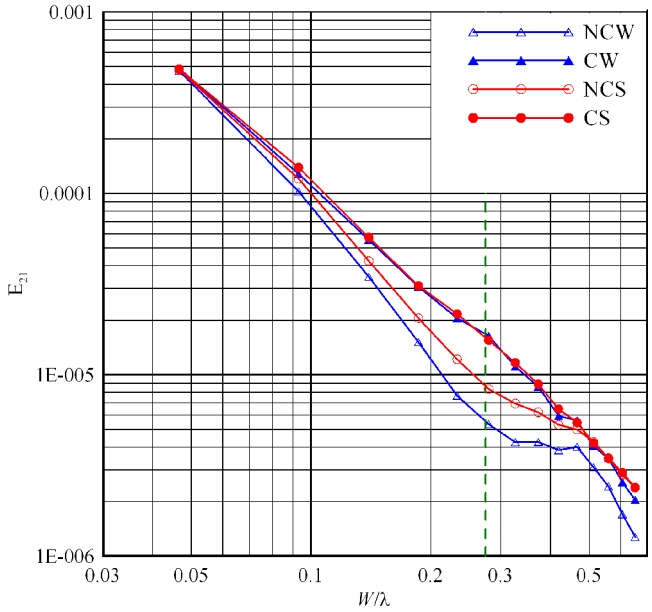

Fig. 4.20 Power spectra of the wake of a finite cylinder for the Stereo PIV procedure applied with and without correction of misalignment error for both Willert and Soloff approach. The green dashed line is plotted in correspondence of the theoretical $MTF_{\Delta z}$ minimum.

The analysis made in Sects. 4.3 and 4.4 is correct if the stereoscopic configuration is symmetric, i.e. the spatial resolutions and then the viewing angles of the two cameras are quite similar. In the case analysed in this section, the stereoscopic setup is strongly asymmetric. The analysis computed for the Willert's approach is correct also here, since with this approach the PIV analysis is done on the de-warped images and then the resolution is made fictitiously equal for the two cameras. On the contrary, for the Soloff's approach, the situation changes. For example, if we consider a displacement field with only the v-component (the other components being null), Eq. 3.7 becomes:

$$\begin{bmatrix} X_x^{(1)} & X_y^{(1)} & X_z^{(1)} \\ Y_x^{(1)} & Y_y^{(1)} & Y_z^{(1)} \\ X_x^{(2)} & X_y^{(2)} & X_z^{(2)} \\ Y_x^{(2)} & Y_y^{(2)} & Y_z^{(2)} \end{bmatrix} \cdot \begin{bmatrix} 0 \\ v \\ 0 \end{bmatrix} = \begin{bmatrix} U_1 \\ V_1 \\ U_2 \\ V_2 \end{bmatrix} \qquad 4.25$$

If we consider the simplified case with $\beta = 0$, also U_1 and U_2 are null:

$$\begin{bmatrix} X_x^{(1)} & X_y^{(1)} & X_z^{(1)} \\ Y_x^{(1)} & Y_y^{(1)} & Y_z^{(1)} \\ X_x^{(2)} & X_y^{(2)} & X_z^{(2)} \\ Y_x^{(2)} & Y_y^{(2)} & Y_z^{(2)} \end{bmatrix} \cdot \begin{bmatrix} 0 \\ v \\ 0 \end{bmatrix} = \begin{bmatrix} 0 \\ V_1 \\ 0 \\ V_2 \end{bmatrix} \Rightarrow \begin{bmatrix} Y_y^{(1)} \\ Y_y^{(2)} \end{bmatrix} \cdot [v] = \begin{bmatrix} V_1 \\ V_2 \end{bmatrix} \qquad 4.26$$

If the Gauss method is used to minimize the Euclidean norm of the residual, the last system becomes:

$$\left[Y_y^{(1)} \quad Y_y^{(2)}\right] \cdot \begin{bmatrix} Y_y^{(1)} \\ Y_y^{(2)} \end{bmatrix} \cdot [v] = \left[Y_y^{(1)} \quad Y_y^{(2)}\right] \cdot \begin{bmatrix} V_1 \\ V_2 \end{bmatrix} \tag{4.27}$$

that is:

$$\left[\left(Y_y^{(1)}\right)^2 + \left(Y_y^{(2)}\right)^2\right] \cdot v = Y_y^{(1)} \cdot V_1 + Y_y^{(2)} \cdot V_2 \quad \Rightarrow \quad v = \frac{Y_y^{(1)} \cdot V_1 + Y_y^{(2)} \cdot V_2}{\left[\left(Y_y^{(1)}\right)^2 + \left(Y_y^{(2)}\right)^2\right]} \tag{4.28}$$

So, if the two terms $Y_y^{(1)}$ and $Y_y^{(2)}$ are similar, i.e. the resolution of the two cameras are similar that happens in a standard symmetric configuration, the last equation becomes:

$$v = \frac{V_1 + V_2}{2 \cdot Y_y^{(c)}} = \frac{Y_y^{(1)} v_1 + Y_y^{(1)} v_2}{2 \cdot Y_y^{(c)}} = \frac{v_1 + v_2}{2} \tag{4.29}$$

which is the Willert's equation 3.10.

But, if the configuration is strongly asymmetric, the two resolutions are very different and then the two terms $Y_y^{(1)}$ and $Y_y^{(2)}$ are also different. For example if $Y_y^{(1)} > Y_y^{(2)}$ the last equation becomes:

$$v = \frac{\left(Y_y^{(1)}\right)^2 \cdot v_1 + \left(Y_y^{(2)}\right)^2 \cdot v_2}{\left[\left(Y_y^{(1)}\right)^2 + \left(Y_y^{(2)}\right)^2\right]} \tag{4.30}$$

where v isn't the mathematical mean between v_1 and v_2, but it is the mean in the least square method sense (i.e. v is more similar to v_1 than to v_2).

5 Flow field past a circular cylinder: experimental results

In this work the experimental measurements of the flow field in the wake of both infinite and finite cylinders have been carried out. Both the mean and the phase-averaged flow fields will be shown in this chapter. The flow fields have been measured with the PIV technique for the infinite cylinder and with both PIV and Stereo PIV techniques for the finite one.

5.1 Experimental apparatus

All the experimental measurements have been conducted by using the equipments available in the Gas Dynamic Laboratory of the Aerospace Engineering Department (DIAS) of the University of Naples "Federico II". A sketch of the experimental apparatus is shown in Fig. 5.1.

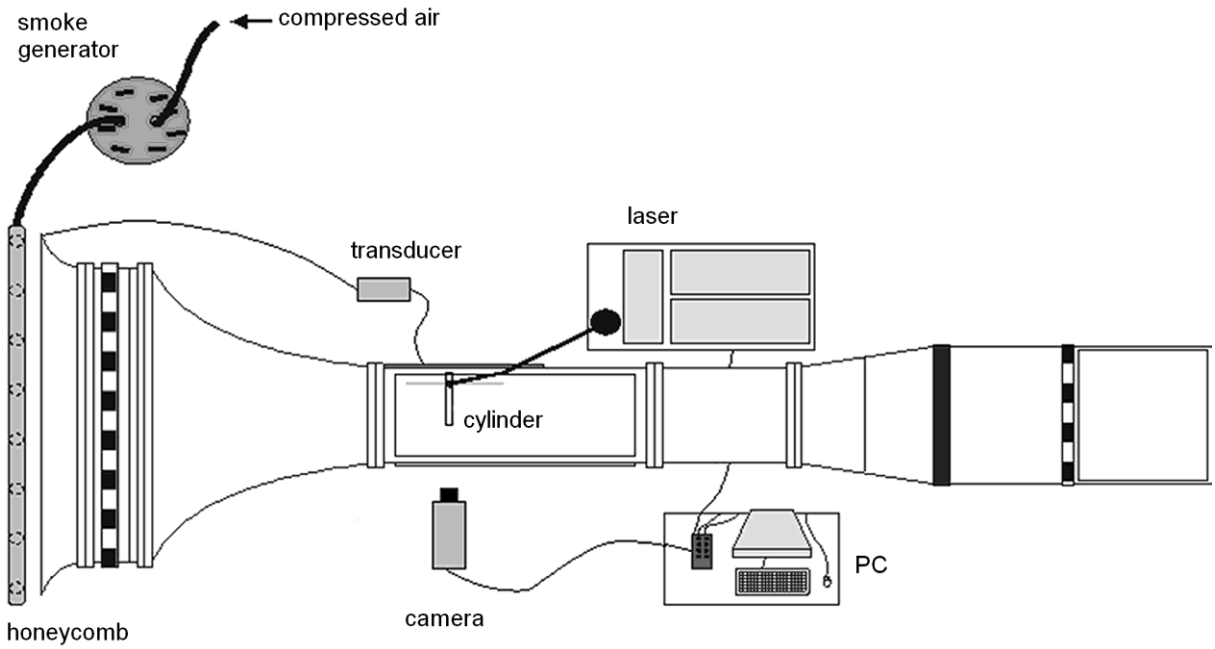

Fig. 5.1 Sketch of the experimental apparatus.

The used experimental set-up is composed of an aspirated subsonic open circuit wind tunnel, which has a low turbulence intensity level (0.1%) and a rectangular test section of $300\times400mm^2$. Three cylinders have been used for the measurements: two finite cylinders and an infinite one. The first has a diameter of $26mm$ and a length of $208mm$ giving an aspect ratio

AR=L/D=8 and a blockage coefficient equal to 0.045; the second has an aspect ratio AR=2 (D=26mm) and the blockage coefficient is equal to 0.011; the last has a diameter of 20mm and spans the width of the test section, giving an aspect ratio L/D=20 and a blockage coefficient D/H=0.067. The free-stream velocity is measured by using a differential pressure transducer and the Reynolds number is based on the cylinder diameter D and the free stream velocity U_∞. For the infinite cylinder, different Reynolds numbers (varying from $4\cdot10^3$ to $20\cdot10^3$) have been investigated, whereas only Re=$16\cdot10^3$ has been examined for the finite ones. For these Reynolds numbers, it has been estimated that the boundary layer thickness varies from 3 to 6mm.

In order to produce the PIV images, seeding has been injected into the flow; it is used in the form of oil droplets produced by a oil smoke generator. This is an aerosol generator composed of 8 Laskin nozzles (see Fig. 5.2). The oil droplets obtained with the vaporization are 1μm in diameter. A bypass circuit is used to adjust the particles density in the flow.

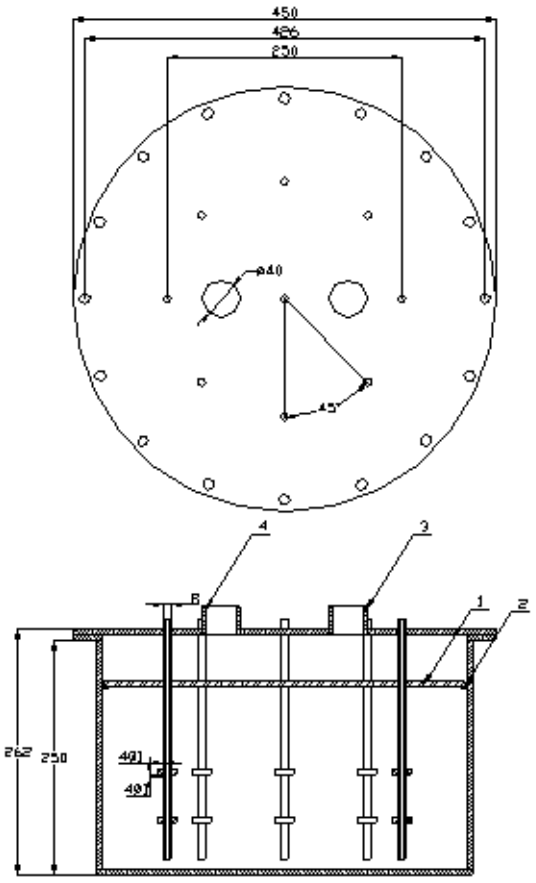

Fig. 5.2 Sketch of the aerosol generator.

The light sheet, which is generated by a double cavity Nd-YAG laser, has a thickness of about 1*mm*, a pulse duration of 6*ns*, a wavelength of 532*nm* and a maximum energy per pulse of about 200*mJ*.

To display, acquire and record digital images for the PIV measurements, the following items are used: a video camera Kodak Megaplus model ES 1.0 with a CCD sensor (1008×1018*pixels*, 256 grey levels) and a PC with a Matrox Genesis frame grabber.

For the Stereo PIV measurements, two PCO-sensicam cameras with CCD sensors (1024×1280 pixels, 4096 grey levels) have been used. These have been mounted on a common mounting with a viewing angle smaller than 90°. Consequently, in order to obtain an uniform focusing of the images, the Scheimpflug condition is fulfilled (Prasad and Jensen 1995).

The PC is also equipped with a counter board, which permits to synchronize the system with the pulsed laser (Fig. 5.3). Once the lasers Q-Switch are known, the counter board has been scheduled so that the right pulses are sent to lasers and camera(s). All parameters of interest can been chosen individually: the interval between the pulses and the acquisition rate.

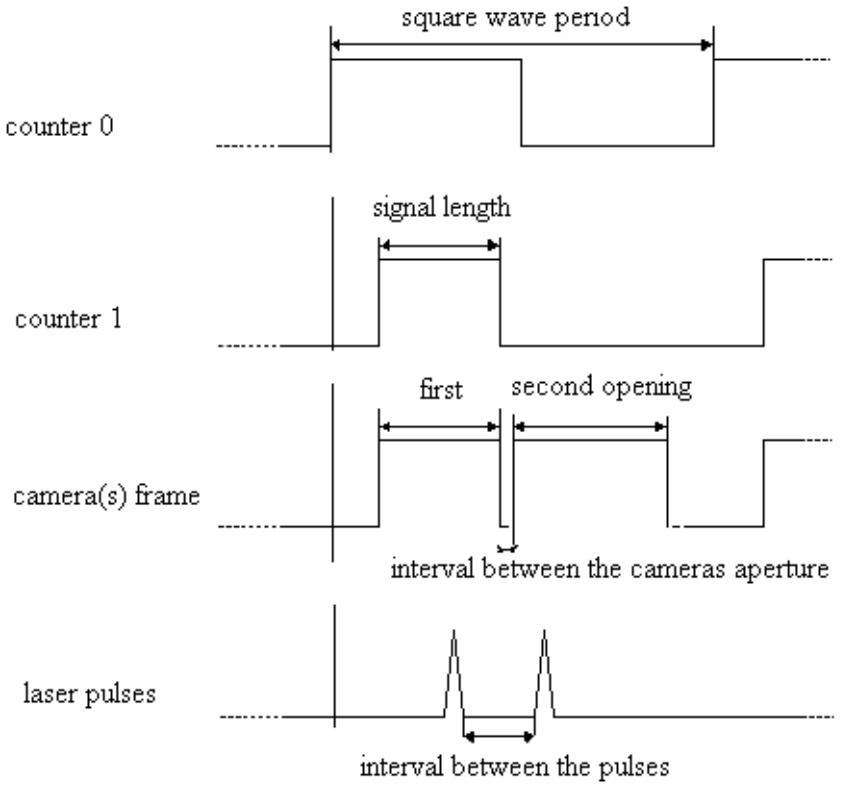

Fig. 5.3 Sketch of the synchronization system.

5.2 Experimental results: analysed physical quantities

For all the experimental measurements performed, different variables of interest have been analysed. All these variables have been reduced so that they are non-dimensional.

As said before, for the infinite cylinder only the PIV technique has been used: in this case the measurement plane is the one orthogonal to the cylinder axis (*xy*-plane) and set in the cylinder height middle (z = 200mm). Viceversa, for the finite cylinders both the techniques have been used to measure the flow field in different *xy*-planes along the cylinder height. In particular, with the Stereo PIV technique, also various *xz*-planes have been chosen, so that the downwash flow could be clearly detected.

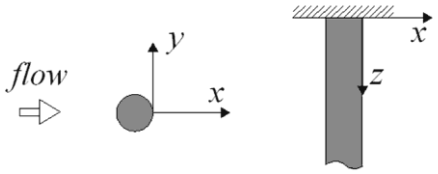

Fig. 5.4 Sketch of reference frame.

Some of the measured variables, of course, are the mean velocity components, i.e. u and v for the PIV measurements and also the w component for the Stereo PIV ones. These velocity components have been divided by the free stream velocity U_∞, so that they are dimensionless and they are indicated as u^* v^* and w^*:

$$u^* = u/U_\infty \tag{5.1}$$

$$v^* = v/U_\infty \tag{5.2}$$

$$w^* = w/U_\infty \tag{5.3}$$

Furthermore, both the vorticity and the Reynolds stress tensor components have been analysed. The first (W) has been computed on a central cross stencil with 4 points and multiplied by (D/U_∞), so that it is dimensionless. Of course, only the component orthogonal to the measurement plane has been measured:

$$W_y = \left[\partial u/\partial z - \partial w/\partial x\right] \cdot D/U_\infty \qquad 5.4$$

$$W_z = \left[\partial v/\partial x - \partial u/\partial y\right] \cdot D/U_\infty \qquad 5.5$$

With regard to the Reynolds stress tensor:

$$\begin{vmatrix} \sigma_x & \tau_{xy} & \tau_{xz} \\ \tau_{yx} & \sigma_y & \tau_{yz} \\ \tau_{zx} & \tau_{zy} & \sigma_z \end{vmatrix} = -\rho \cdot \begin{vmatrix} \overline{u'^2} & \overline{u'v'} & \overline{u'w'} \\ \overline{u'v'} & \overline{v'^2} & \overline{v'w'} \\ \overline{u'w'} & \overline{v'w'} & \overline{w'^2} \end{vmatrix} \qquad 5.6$$

all components are the product between the fluid density and the average of the product of the velocity fluctuations. Hereafter it will be indicated with:

$$u'u' = \overline{u'^2} / U_\infty^2 \qquad 5.7$$

the dimensionless component $\overline{u'^2}$ and in a similar way the other components.

Finally, the mean kinetic turbulent energy *k* and the turbulent production *p* have been computed. The former being:

$$k = \frac{1}{2}\left(u'u' + v'v'\right) \qquad 5.8$$

for the PIV measurements, whereas the complete formula has been used for the Stereo PIV ones:

$$k = \frac{1}{2}\left(u'u' + v'v' + w'w'\right) \qquad 5.9$$

Incomplete formulas to compute the turbulent production (dimensionless) have been used:

$$p = -\left[u'u'\frac{\partial u}{\partial x} + u'v'\frac{\partial v}{\partial x} + u'v'\frac{\partial u}{\partial y} + v'v'\frac{\partial v}{\partial y}\right] \cdot \frac{D}{U_\infty} \qquad 5.10$$

and:

$$p = -\left[u'u'\frac{\partial u}{\partial x} + u'v'\frac{\partial v}{\partial x} + u'w'\frac{\partial w}{\partial x} + u'v'\frac{\partial u}{\partial y} + v'v'\frac{\partial v}{\partial y} + w'v'\frac{\partial w}{\partial y}\right] \cdot \frac{D}{U_\infty} \qquad 5.11$$

respectively for both PIV and Stereo PIV measurements.

All these variables have been measured for the mean flow field as well as for the phase averaged one. The latter has been obtained by using the Proper Orthogonal Decomposition (POD), as it will be explained in the next section.

5.3 Phase averaging method

In the present work, since the image acquisition frequency is almost 10*Hz* (7*Hz* for the Stereo PIV measurements and 10*Hz* for the PIV ones) and the von Kàrmàn vortices have a frequency almost 10 times bigger (it depends on the Reynolds number), a phase averaging method has to be used to reconstruct the vortices evolution. In the literature various approaches are present for the phase averaging. Lin et al. (1995) used the hot wire signal to trigger the sampling of the vortex shedding phases, whereas Braza et al. (2006) used a pressure signal. Ben Chiekh et al. (2004) proposed to use the first two principal modes obtained with the POD technique, in order to reconstruct the vortices evolution, whereas Perrin et al. (2007) compared the phase averaged flow fields obtained with a trigger originated from pressure signal with the POD-based approach. Perrin et al. (2007) found that an enhancement in the averaged velocity fields is obtained with the POD approach, since the phase angles is determined directly from the velocity fields to be averaged. Konstantinidis et al. (2005) proposed an other approach to compute an *a posteriori* phase averaging. It consists in to cross-correlate all the flow fields and to check the ones that correlate well with each other. By this way, various flow field ensembles can be computed, all of them representative of a particular phase of the vortex shedding.

After having investigated both the approaches based on POD and cross-correlation, the former has been chosen. The reason of this choice is in the less computational effort and better phase location of the POD approach.

In the following, first the working principles of the POD technique will be shown and then the phase averaging method will be explained.

5.3.1 Proper Orthogonal Decomposition: working principles

The POD was introduced by Lumley (1967). It consists in finding a set of realisations of the flow field, which maximises the mean square energy. This maximisation leads to a Fredholm integral eigenvalue problem:

$$\sum_{j=1}^{N_c}\int_D \overline{u_i'(X)u_j'(X)}\Phi_j^{(n)}(X')dX' = \lambda^{(n)}\Phi_i^{(n)}(X) \qquad 5.12$$

where: X indicates the space variable (x, y, z); N_c is the number of velocity components used; $\overline{u_i'(X)u_j'(X)}$ is the tensor obtained by time-averaging the two-points spatial correlation tensor of the velocity fluctuations u'; $\Phi^{(n)}(X)$ are the spatial POD eigenfunctions and $\lambda^{(n)}$ are the corresponding eigenvalues. By projecting the instantaneous velocity fields on the POD eigenfunctions, one obtains the POD temporal coefficients $a^{(n)}(t)$.

The described approach to the POD technique is the classical one introduced by Lumely (1967). In this case, the dimension of the spatial correlation tensor is $2n_x \cdot 2n_y$ for the 2D case (i.e. two velocity components in 2D domain) and $3n_x \cdot 3n_y \cdot 3n_z$ if the domain is three-dimensional with three velocity components. For this reason, such POD approach is useful if one disposes few spatial components for a lot of temporal instants, like in the case of Hot Wire measurements.

Viceversa, with PIV measurements, many spatial velocity components in few temporal instants are available (see Fig. 5.5). In this case the snapshot approach proposed by Sirovich (1987) is preferable. In such approach, the velocity correlation tensor is defined by:

$$R_{ij} = \frac{1}{n_x n_y}\sum_{l=1}^{n_x}\sum_{m=1}^{n_y} u'(X_{lm},t_i)u'(X_{lm},t_j) \qquad 5.13$$

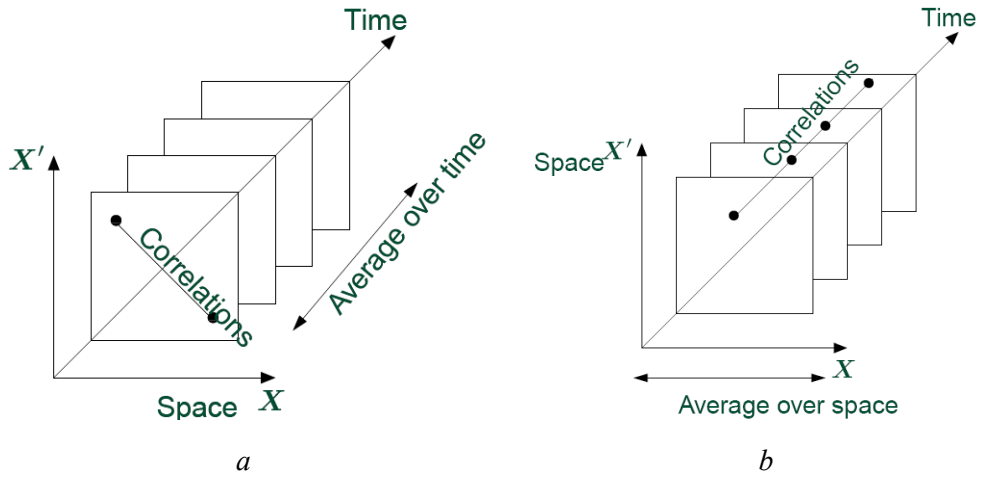

Fig. 5.5 Schematic view of the classical (*a*) and snapshot (*b*) POD (Cordier and Bergmann 2008).

By using this correlation tensor, the Fredholm integral eigenvalue problem allows to obtain temporal POD eigenfunctions $a^{(n)}(t)$. In this case, by projecting the instantaneous velocity fields on the POD eigenfunction $a^{(n)}(t)$, the POD coefficients $\Phi^{(n)}(X)$ are computed.

For both POD approaches, each instantaneous velocity component u can be expressed with the following equation:

$$u(X_{ij},t_k)=\overline{u}(X_{ij},t_k)+\sum_{n=1}^{M}a^{(n)}(t_k)\Phi^{(n)}(X_{ij}) \qquad 5.14$$

where M is the number of POD modes.

In order to apply the above mentioned POD concept to the PIV (or Stereo PIV) measurements obtained in this work, let us consider a time sequence of N_t 2D velocity field[7]:

$$\mathbf{V}(X_{ij},t_k), \quad i=1,2,\ldots n_x, \quad j=1,2,\ldots n_y, \quad k=1,2,\ldots N_t, \qquad 5.15$$

where in each position (X_{ij}, t_k) there are two (or three) velocity components (u, v). If we indicate with:

$$\widetilde{V}(X_{lj},t_k)=\begin{bmatrix}u'(X_{ij},t_k)\\ v'(X_{ij},t_k)\end{bmatrix}, \quad i=1,2,\ldots n_y, \quad l=1,2,\ldots 2\cdot n_y, \quad j=1,2,\ldots n_x, \quad k=1,2,\ldots N_t$$

$$=\begin{bmatrix}u'(X_{11},t_k) & u'(X_{12},t_k) & \cdots & u'(X_{1n_x},t_k)\\ v'(X_{11},t_k) & v'(X_{12},t_k) & \cdots & v'(X_{1n_x},t_k)\\ \vdots & \vdots & \ddots & \vdots\\ u'(X_{n_y1},t_k) & u'(X_{n_y2},t_k) & \cdots & u'(X_{n_yn_x},t_k)\\ v'(X_{n_y1},t_k) & v'(X_{n_y2},t_k) & \cdots & v'(X_{n_yn_x},t_k)\end{bmatrix}, \quad k=1,2,\ldots N_t \qquad 5.16$$

the three dimensional matrix (n_x, $2\cdot n_y$, N_t), which contains both u' and v' velocity fluctuations components, the velocity correlation matrix (5.13) becomes:

$$R_{ij}=\frac{1}{2n_xn_y}\left[\widetilde{V}(t_i),\widetilde{V}(t_j)\right] \qquad 5.17$$

where [.,.] indicates the inner product:

$$\begin{aligned}\left[\widetilde{V}(t_i),\widetilde{V}(t_j)\right]&=\widetilde{V}(X_{11},t_i)\widetilde{V}(X_{11},t_j)+\ldots+\widetilde{V}(X_{2n_xn_y},t_i)\widetilde{V}(X_{2n_xn_y},t_j)\\ &=u'(X_{11},t_i)u'(X_{11},t_j)+\ldots+u'(X_{n_xn_y},t_i)u'(X_{n_xn_y},t_j)+\\ &+v'(X_{11},t_i)v'(X_{11},t_j)+\ldots+v'(X_{n_xn_y},t_i)v'(X_{n_xn_y},t_j)\end{aligned} \qquad 5.18$$

[7] For the sake of brevity, here only the 2D case (i.e. PIV measurements) will be illustrated. The extension to the 3D case is immediate.

By using the correlation matrix (5.17) (which is a symmetric $N_t \cdot N_t$ matrix), the eigenvalue problem provides a discrete series of POD coefficients:

$$RA^{(n)} = \lambda^{(n)} A^{(n)} \tag{5.19}$$

where:

$$A^{(n)} = \left(a^{(n)}(t_1), \cdots, a^{(n)}\left(t_{N_t}\right)\right) \tag{5.20}$$

is the nth POD eigenfunction. Then, the nth POD mode is obtained by the following equation:

$$\Phi^{(n)}\left(X_{ij}\right) = \sum_{k=1}^{N_t} a^{(n)}(t_k)\tilde{V}\left(X_{ij}, t_k\right) \tag{5.21}$$

With this procedure, the normalised POD modes are orthogonal:

$$\left[\Phi^{(m)}\left(X_{ij}\right), \quad \Phi^{(n)}\left(X_{ij}\right)\right] = \delta_{mn} \tag{5.22}$$

while the POD coefficients are uncorrelated in time:

$$\overline{a^{(m)}(t_k)a^{(n)}(t_k)} = \delta_{mn} \cdot \lambda_n \tag{5.23}$$

the sign $\bar{}$ indicating the temporal average.

5.3.2 Proper Orthogonal Decomposition: phase identification

According to many other authors (e.g. Ben Chiekh et al. 2004, van Oudheusden et al. 2005, Perrin et al. 2007b), the first two POD modes (e.g. see Fig. 5.11) are correlated to the convection of the vortices. As suggested by Ben Chiekh et al. (2004), it is possible to compute the vortex shedding phase of each instantaneous flow field with the POD coefficients associated to these first two modes.

Actually, this procedure is applicable only if two principal modes are found with the POD technique, i.e. if the first two modes contain a large part of the flow field energy. By following this approach, only the first two modes are used and each instantaneous flow field can be computed by:

$$u\left(X_{ij}, t_k\right) = \bar{u}\left(X_{ij}, t_k\right) + a^{(1)}(t_k)\Phi^{(1)}\left(X_{ij}\right) + a^{(2)}(t_k)\Phi^{(2)}\left(X_{ij}\right) \tag{5.24}$$

where the two POD coefficients can be expressed by:

$$a^{(1)}(t_k) = \sqrt{2\lambda_1}\sin(\alpha(t_k))$$
$$a^{(2)}(t_k) = \sqrt{2\lambda_2}\cos(\alpha(t_k)) \qquad 5.25$$

$\alpha(t_k)$ being the vortex shedding phase.

The higher order modes neglected contain the higher order harmonics of the coherent motion as well as the random turbulent motion. According to eq. 5.25, the first two POD coefficients form an ellipse in the plane $a^{(1)}(t_k) - a^{(2)}(t_k)$:

$$\frac{\left[a^{(1)}(t_k)\right]^2}{2\lambda_1} + \frac{\left[a^{(2)}(t_k)\right]^2}{2\lambda_2} = 1 \qquad 5.26$$

as shown in Fig. 5.12.

Consequently, the vortex shedding phase can be computed as:

$$\alpha(t_k) = \arctan\left(\frac{\sqrt{\lambda_1}}{\sqrt{\lambda_2}}\frac{a^{(2)}(t_k)}{a^{(1)}(t_k)}\right) \qquad 5.27$$

where λ_1 and λ_2 are the two eigenvalues obtained by the POD relative to the first two temporal POD eigenfunctions (or coefficient) $a^{(1)}(t_k)$ and $a^{(2)}(t_k)$.

5.4 Flow field past an infinite circular cylinder

As already said, with regard to the infinite cylinder, the measurement plane is orthogonal to the cylinder axis (*xy*-plane) and it is set in the middle of the cylinder height (z = 200*mm*). Five Reynolds numbers have been investigated ($4\cdot10^3$, $8\cdot10^3$, $12\cdot10^3$, $16\cdot10^3$ and $20\cdot10^3$), all being within the *Shear Layer Transition Regime* indicated by Williamson (1997).

5.4.1 Mean flow field

The mean flow field has been analysed according to Reynolds averaging decomposition. For the sake of brevity, only the measurements at Re=$4\cdot10^3$ and Re=$20\cdot10^3$ will be shown here.

The comparison between these two Reynolds numbers is interesting because, according to Saad et al. (2007), for Re<$5\cdot10^3$ the transition point location in the shear layer is strongly dependent on the Reynolds number, whereas a weaker decrease is observed for Re>$5\cdot10^3$. This is connected to the vortex formation process stabilisation. Furthermore, the strong

change undergone by the flow at $Re=5\cdot10^3$ is proved also by the variation of the shear layer frequency law at this Reynolds number (Norberg 1994). As a consequence of this abrupt change, by increasing the Reynolds number from $4\cdot10^3$ to $20\cdot10^3$, a strong decrease of the vortex formation length occurs. This is observable in Fig. 5.6, where both the dimensionless u and v velocity components and the streamlines of the mean flow field are shown. As expected, a two-eddies pattern is obtained, due to the averaging of the passage of the alternating vortices, resulting in a symmetric pattern for u^* and in an asymmetric one for v^*.

Fig. 5.7 shows the dimensionless mean Reynolds stress tensor components relative to $Re=4\cdot10^3$ and $Re=20\cdot10^3$. Only the components $u'u'$, $v'v'$ and $u'v'$ are shown since those are the only ones measurable with the PIV technique. It's interesting to note that by changing the Reynolds number, only the vortex formation length changes, the qualitative shape of the contour maps keeping unchanged. According to Braza et al. (2006), both $u'u'$ and $u'v'$ contour maps has a two lobes structure and the $v'v'$ contour map has a one-lobe structure. A quantitative comparison between these results and the Braza ones isn't possible, since the Reynolds numbers investigated are quite different ($Re=140\cdot10^3$ in Braza's work).

The vorticity W_z, the kinetic turbulent energy k and the turbulent production p are shown in Fig. 5.8, all of them dimensionless. The vorticity contour map shows clearly the shear layer region. According to Braza et al. (2006), the kinetic turbulent energy has his maximum located near the vortex formation region. With regard to the turbulent production, a different map shape has been obtained with respect to the Braza one. Nevertheless, the turbulent production is computed by using the formula (5.11) and then is strongly affected even by a small error in u and v components as well as in Reynolds stress tensor components $u'u'$, $v'v'$ and $u'v'$. This is the reason why the turbulent production maps are not well defined as the other ones, for both this and Braza's works.

Since several researches (e.g. Bloor 1964, Park and Lee 2000 and Saad et al. 2007) have measured the vortex formation length as the point that has the maximum value of the turbulence intensity measured along the symmetry section, also herein the kinetic turbulent energy has been computed on the symmetry section as a function of x/D (see Fig. 5.9), in order to investigate the vortex formation length by varying the Reynolds number. According to the considerations previously done, a substantial difference can be seen between the curve relative to $Re=4\cdot10^3$ and the ones relative to the others Reynolds numbers. This is a further proof that at $Re=5\cdot10^3$ the flow undergoes a strong change.

$Re = 4 \cdot 10^3$ $Re = 20 \cdot 10^3$

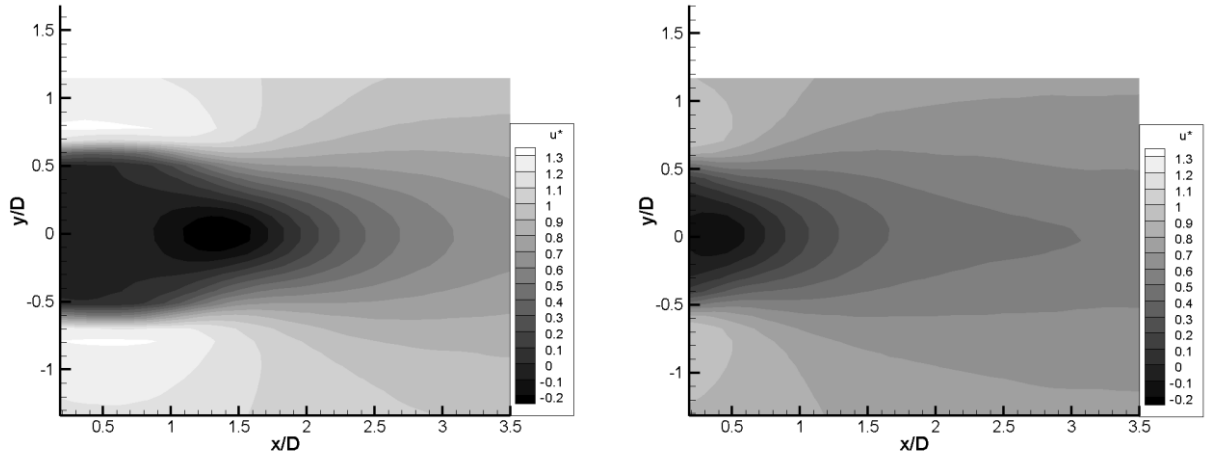

Mean dimensionless velocity component u^*

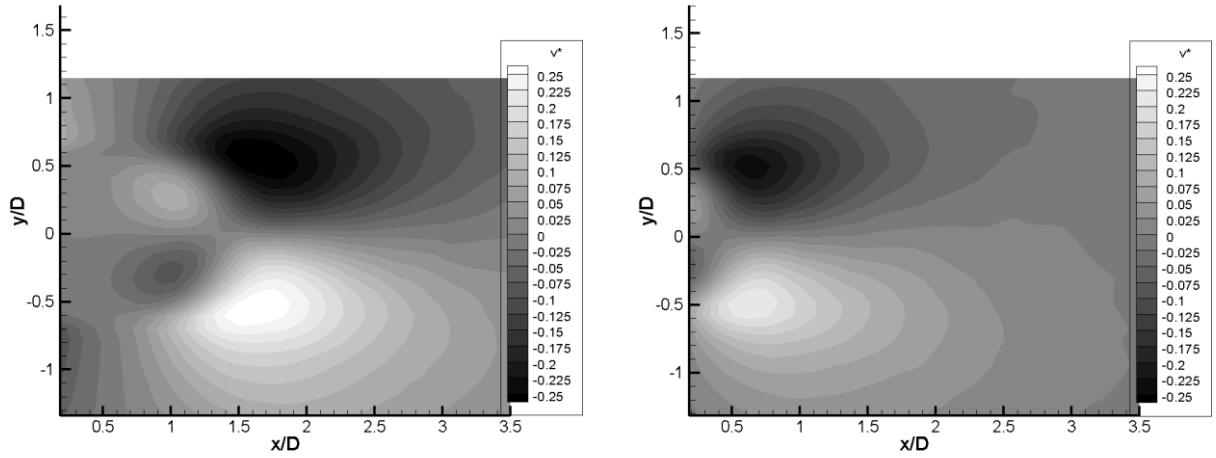

Mean dimensionless velocity component v^*

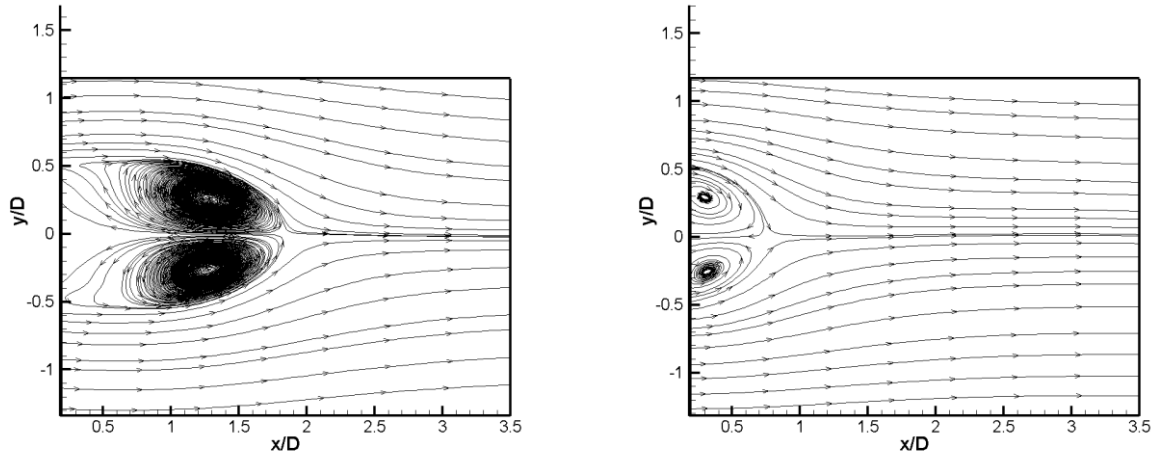

Streamlines of mean flow field

Fig. 5.6 Mean flow field relative to the infinite cylinder.

$Re = 4 \cdot 10^3$ $Re = 20 \cdot 10^3$

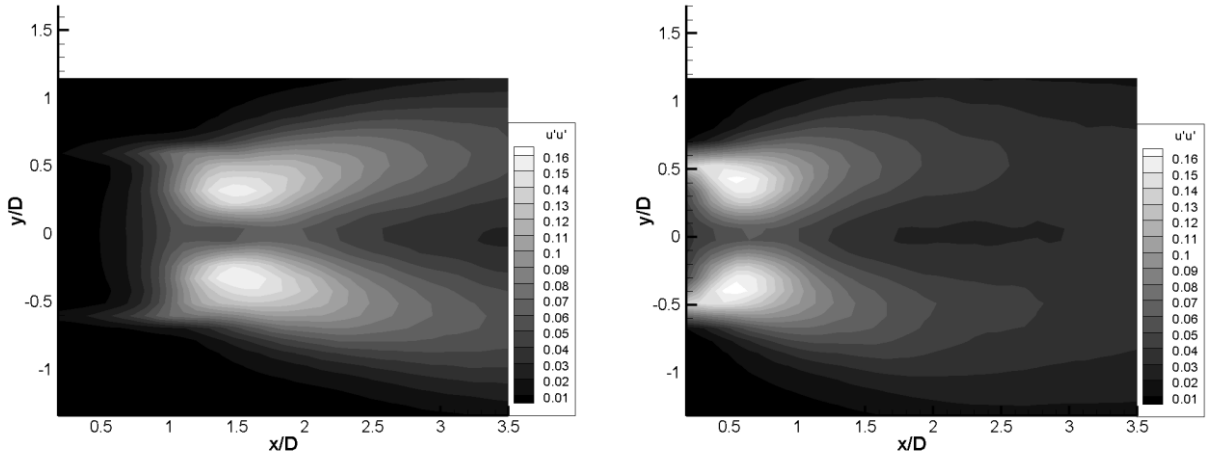

Mean dimensionless Reynolds stress tensor component $u'\,u'$

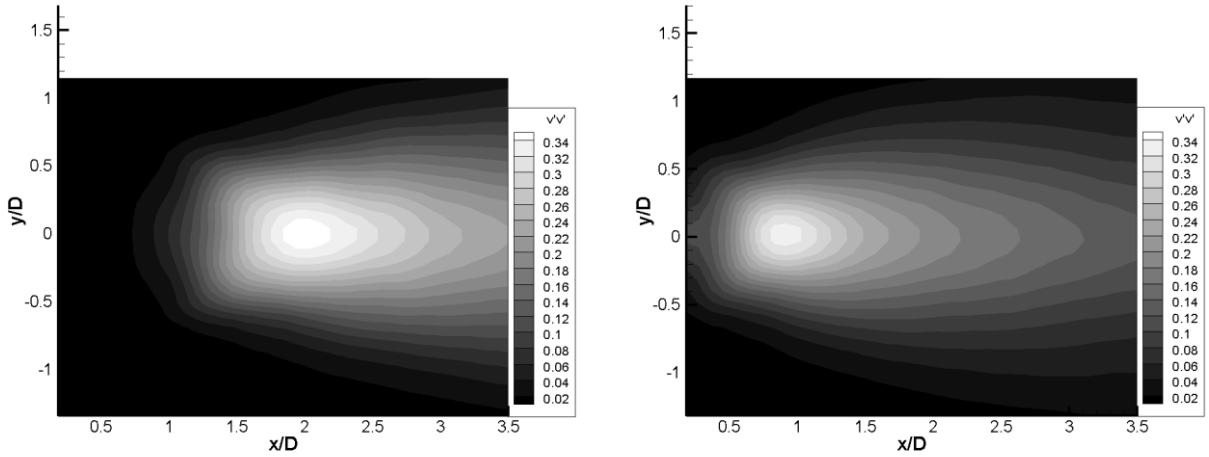

Mean dimensionless Reynolds stress tensor component $v'\,v'$

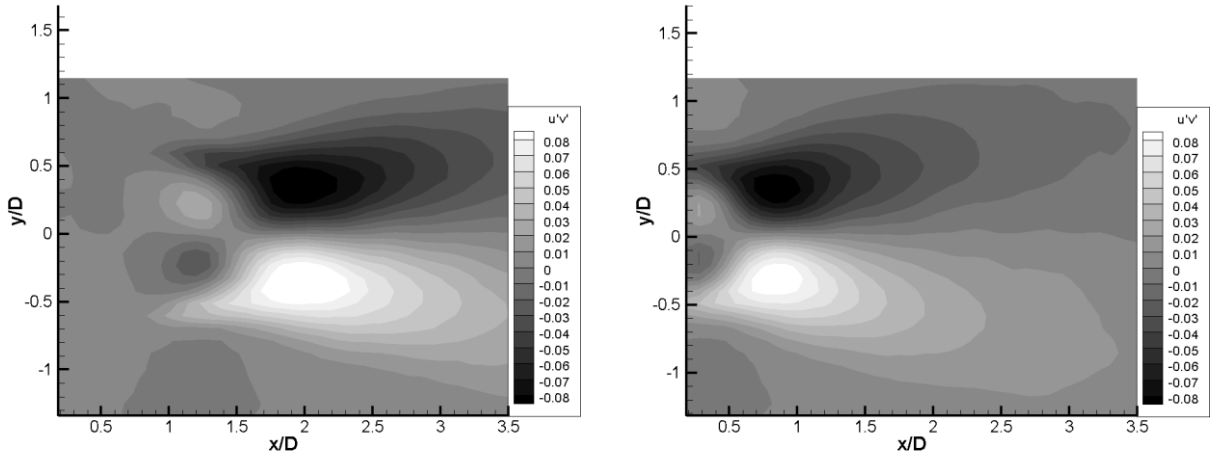

Mean dimensionless Reynolds stress tensor component $u'\,v'$

Fig. 5.7 Mean dimensionless Reynolds stress tensor component relative to the infinite cylinder.

$Re = 4 \cdot 10^3$ $Re = 20 \cdot 10^3$

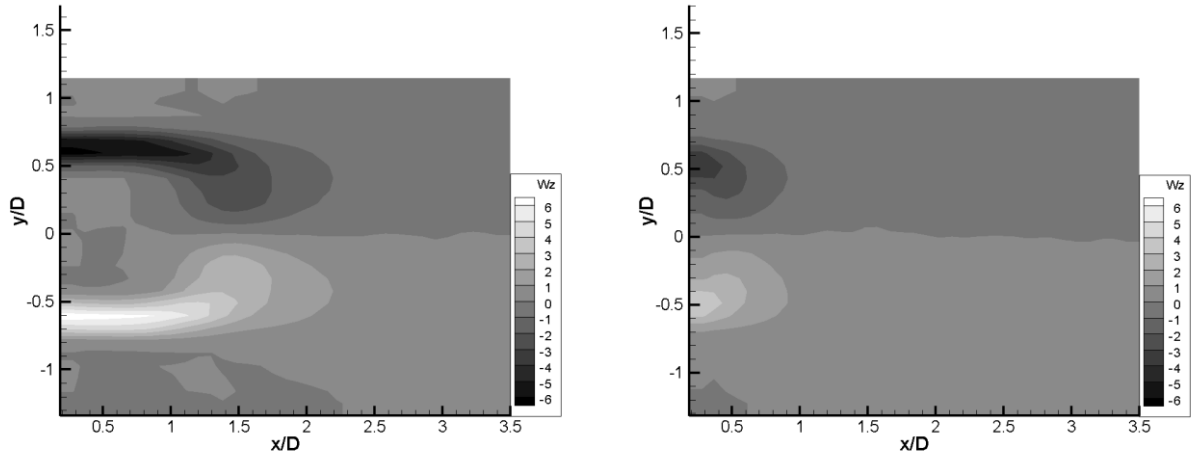

Mean dimensionless vorticity W_z

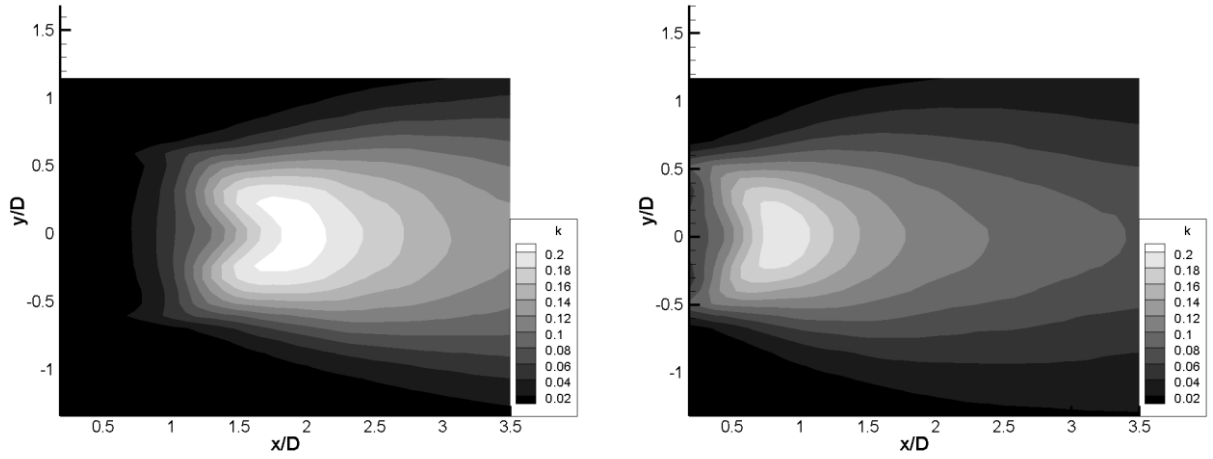

Mean dimensionless kinetic turbulent energy k

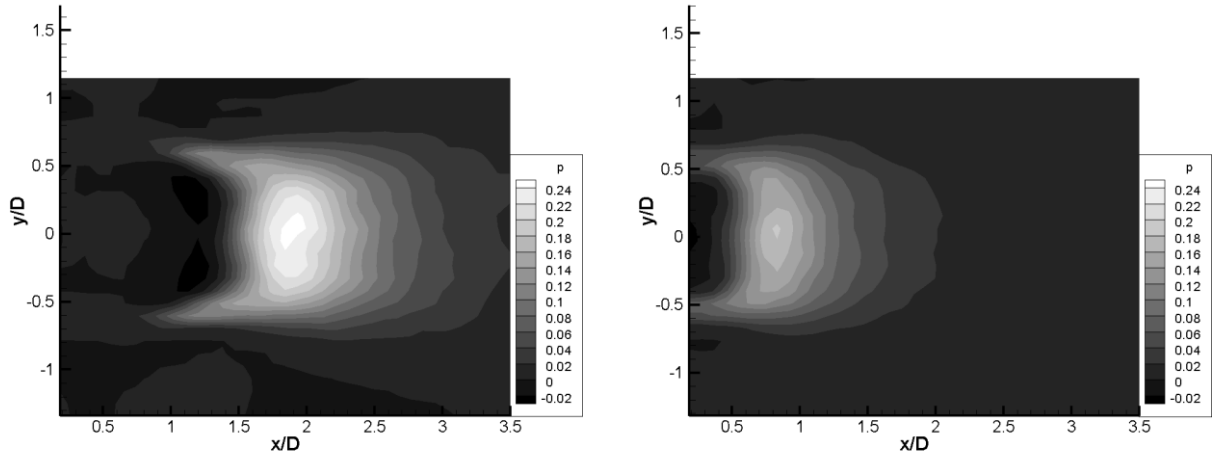

Mean dimensionless turbulent production p

Fig. 5.8 Mean kinetic turbulent energy, production and vorticity relative to the infinite cylinder.

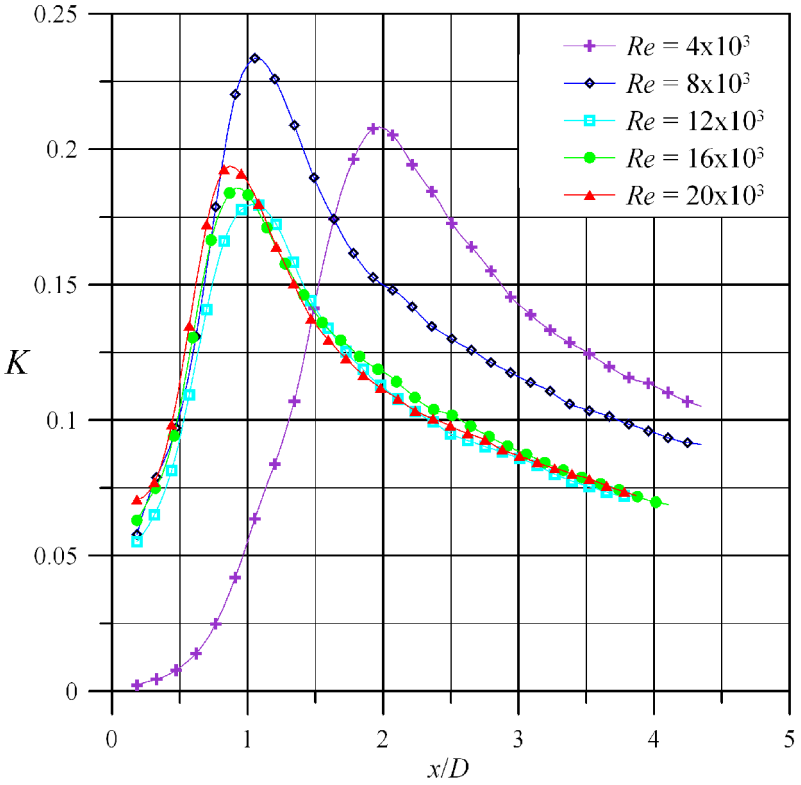

Fig. 5.9 Turbulence intensity distribution on $y/D = 0$ section for all Reynolds numbers investigated.

5.4.2 Phase averaged flow field

As explained in Sect. 5.3.2, the phase identification procedure based on the POD technique is applicable only if two principal modes are found, i.e. if the first two modes contain a large part of the flow field energy. For this purpose, in Fig. 5.10 the energy associated to first 10 modes for all Reynolds numbers investigated are shown. As it can be seen, for all Reynolds numbers, the first two modes contain a large part of overall flow field energy. Also in this case, only the results relative to Re=4·10^3 and Re=20·10^3 have been reported, since they have been considered representative of all the others investigated.

In Fig. 5.11 the first two modes are reported. Those relative to Re=20·10^3 are very similar to the ones present in the literature (Perrin et al. 2007). Instead, one of the first two modes relative to Re=4·10^3 is different, but this could be explained by the already mentioned change in flow field, which occurs at Re=5·10^3.

According to eq. 5.25, the first two POD coefficients form an ellipse in the plane $a^{(1)}(t_k) - a^{(2)}(t_k)$. This has been shown in Fig. 5.12. Actually, the radial distribution of the $a^{(1)}(t_k) - a^{(2)}(t_k)$ coefficients have been found to be Gaussian and in Fig. 5.12 only the point included in –σ/+σ have been shown (since only these points have been used in the vortex shedding phase identification (eq. 5.27)).

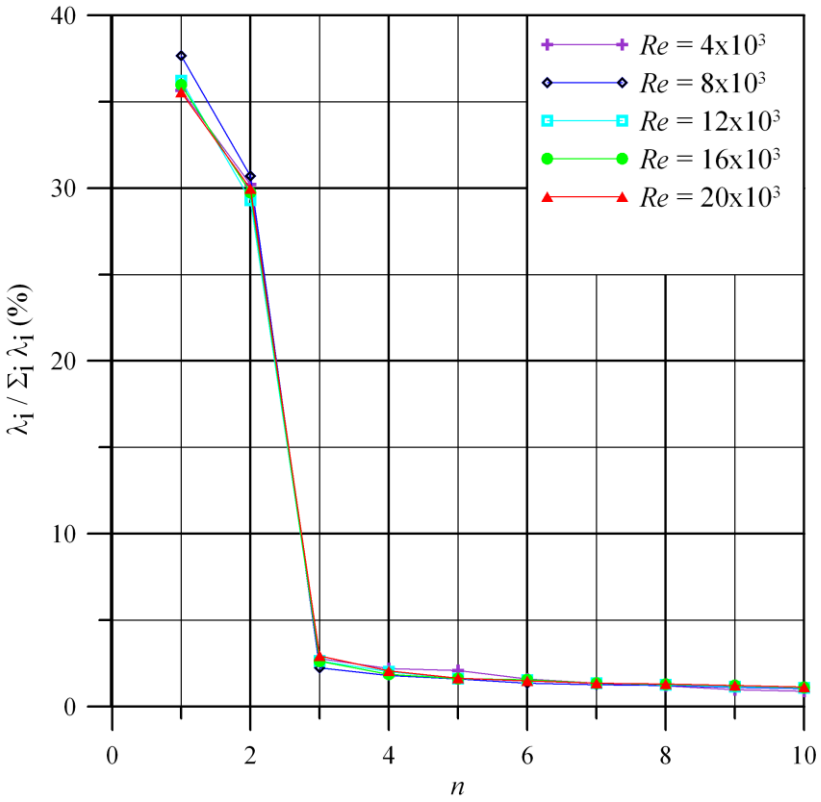

Fig. 5.10 Energy percentage associated to first 10 POD eigenvalues.

In Fig. 5.13 the streamlines of the phase averaged flow fields are shown for the two Reynolds numbers: only four equidistant phases are reported. Also in this case, results relative to Re=20·10^3 are very similar to the ones present in the literature (Braza et al. 2006 and Perrin et al. 2007). Instead those relative to Re=4·10^3 are different, but no results have been found in the literature for this Reynolds number, i.e. under the Reynolds number at which significant change in flow filed occurs (Re=5·10^3). In particular, differently from results found for Re=20·10^3, phase averaged flow fields relative to Re=4·10^3 show the coexistence of two vortices in the same instant. Moreover, also in phase averaged flow fields, it is possible to note the different vortex formation lengths for the Reynolds number shown.

The phase averaged dimensionless vortical maps shown in Fig. 5.14 for Re=20·10^3 prove a good agreement with results present in the literature (Braza et al. 2006 and Perrin et al. 2007). The quantitative comparison cannot be done because in these works the Reynolds number investigated is 1.40·10^5. It's interesting to note that the absolute value of the vorticity peak at the centre of a vortex decreases from 4.7 to 1.8 when the vortex moves downstream from x/D=0.45 to x/D=3. A similar conclusion can be drawn for Re=4·10^3.

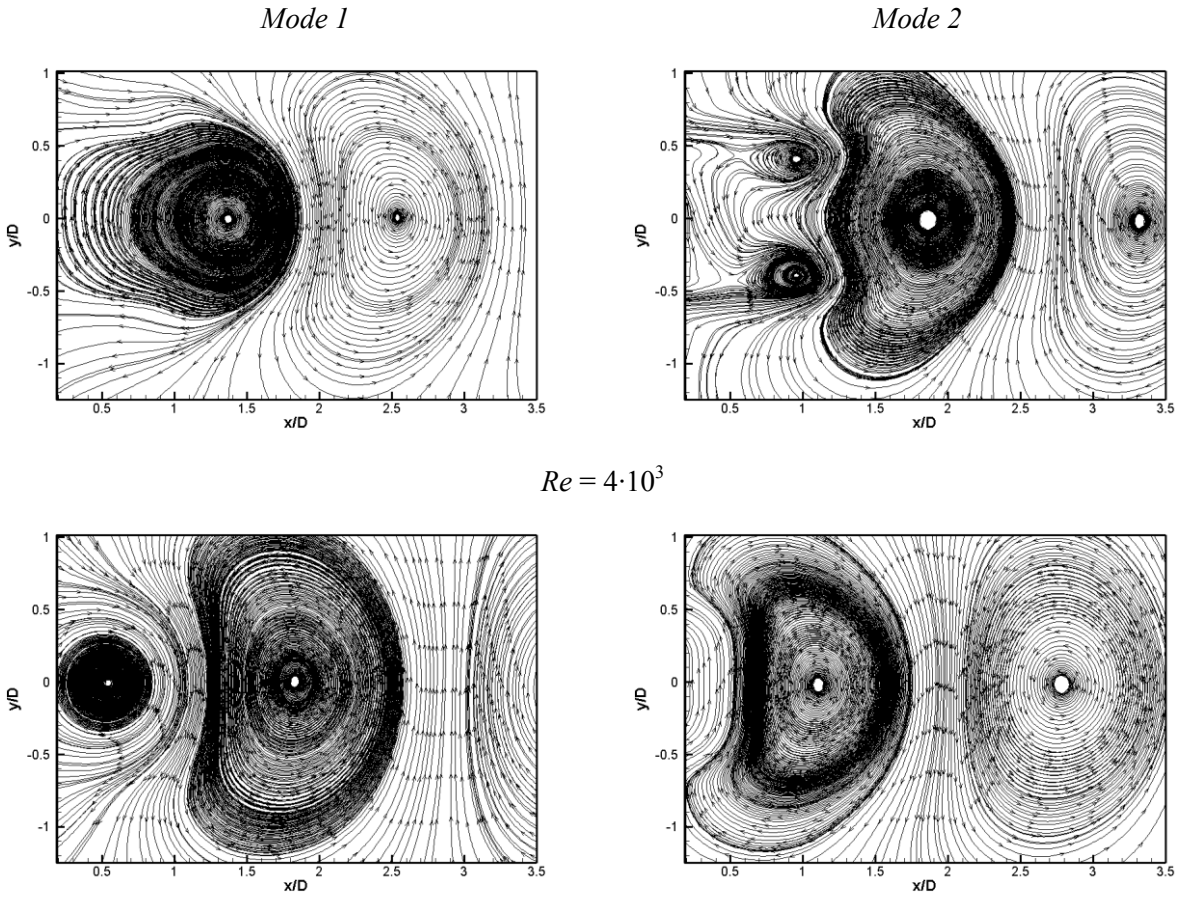

Fig. 5.11 First and second modes obtained for $Re = 4 \cdot 10^3$ and $Re = 20 \cdot 10^3$.

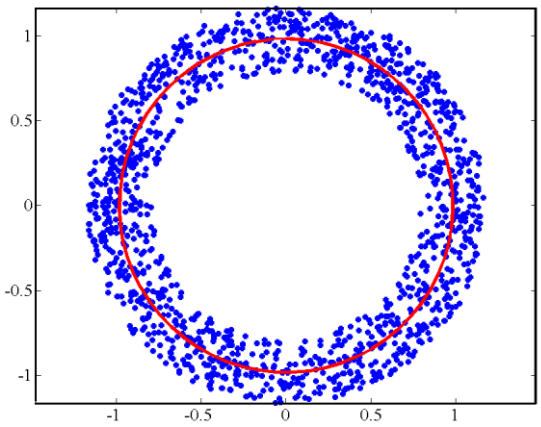

Fig. 5.12 First two POD coefficients.

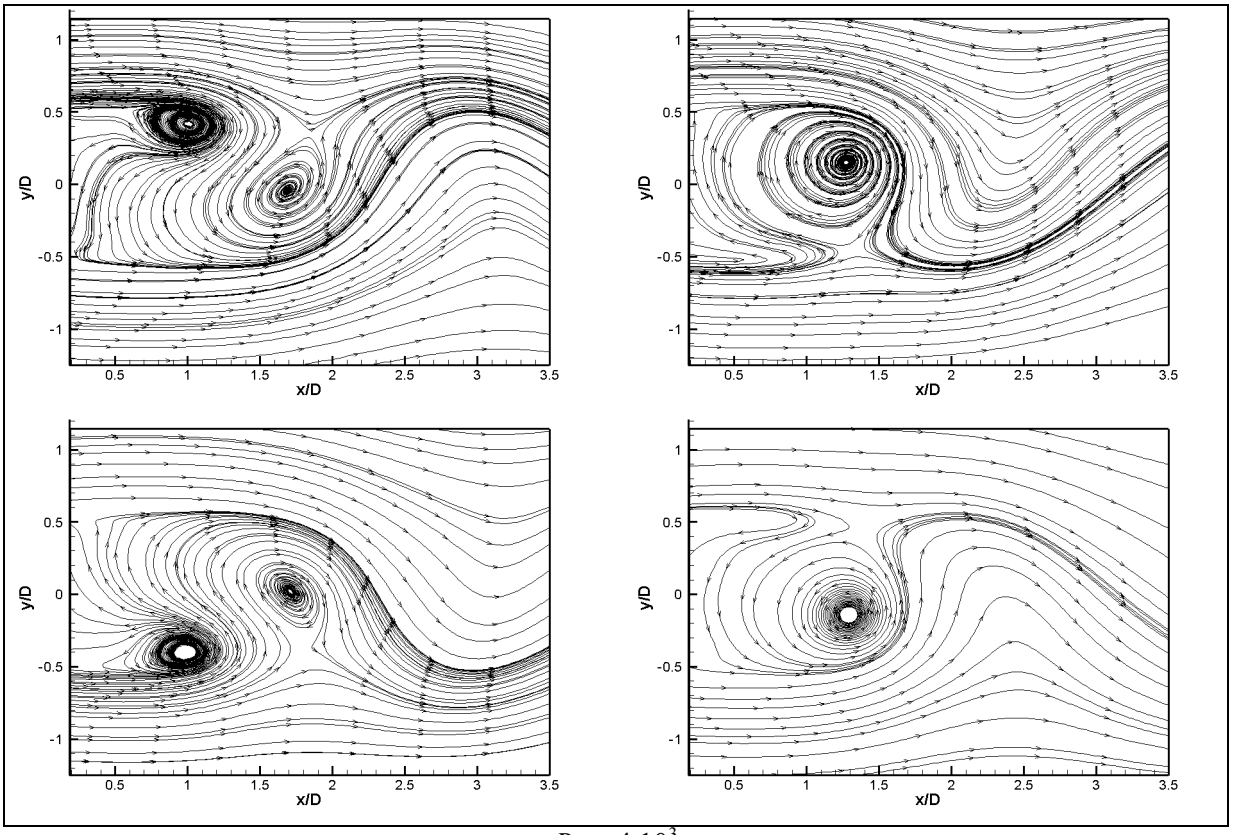

$Re = 4 \cdot 10^3$

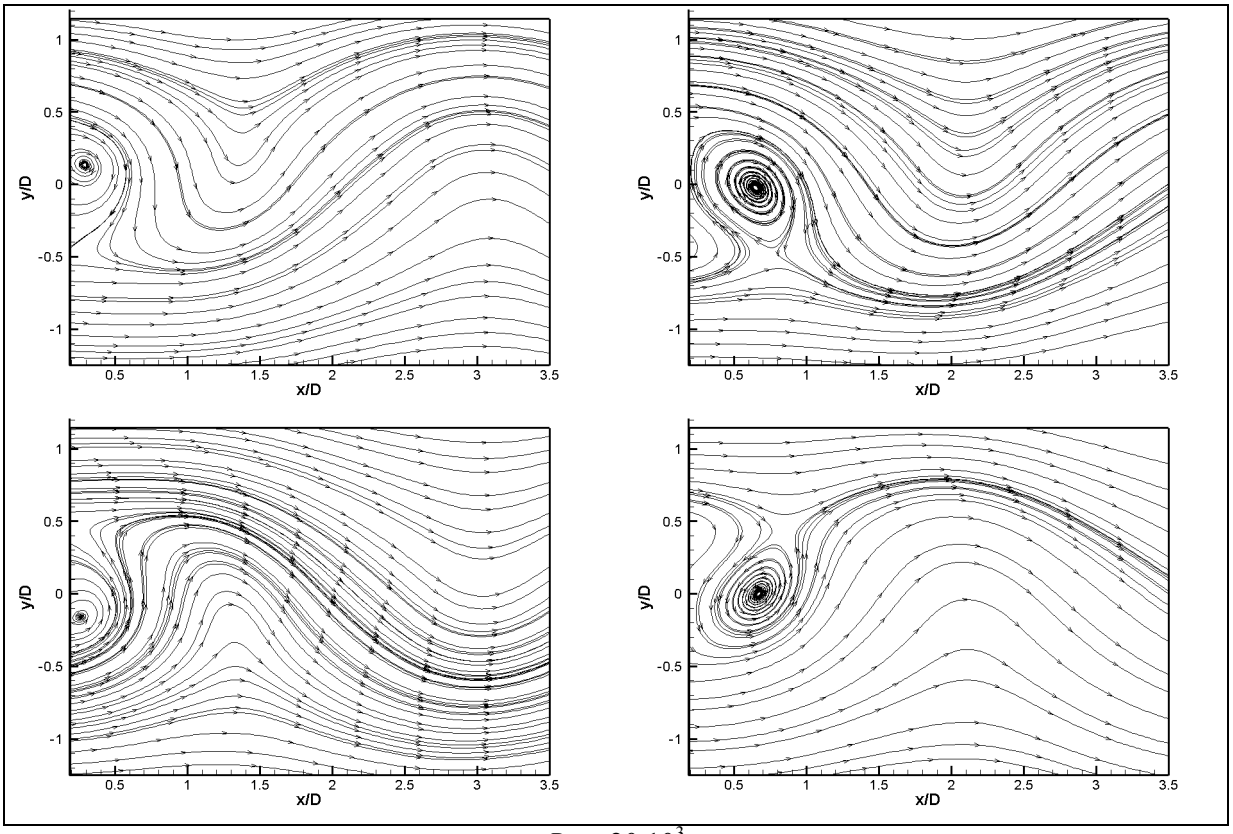

$Re = 20 \cdot 10^3$

Fig. 5.13 Streamlines of phase averaged flow fields relative to $Re = 4 \cdot 10^3$ and $Re = 20 \cdot 10^3$.

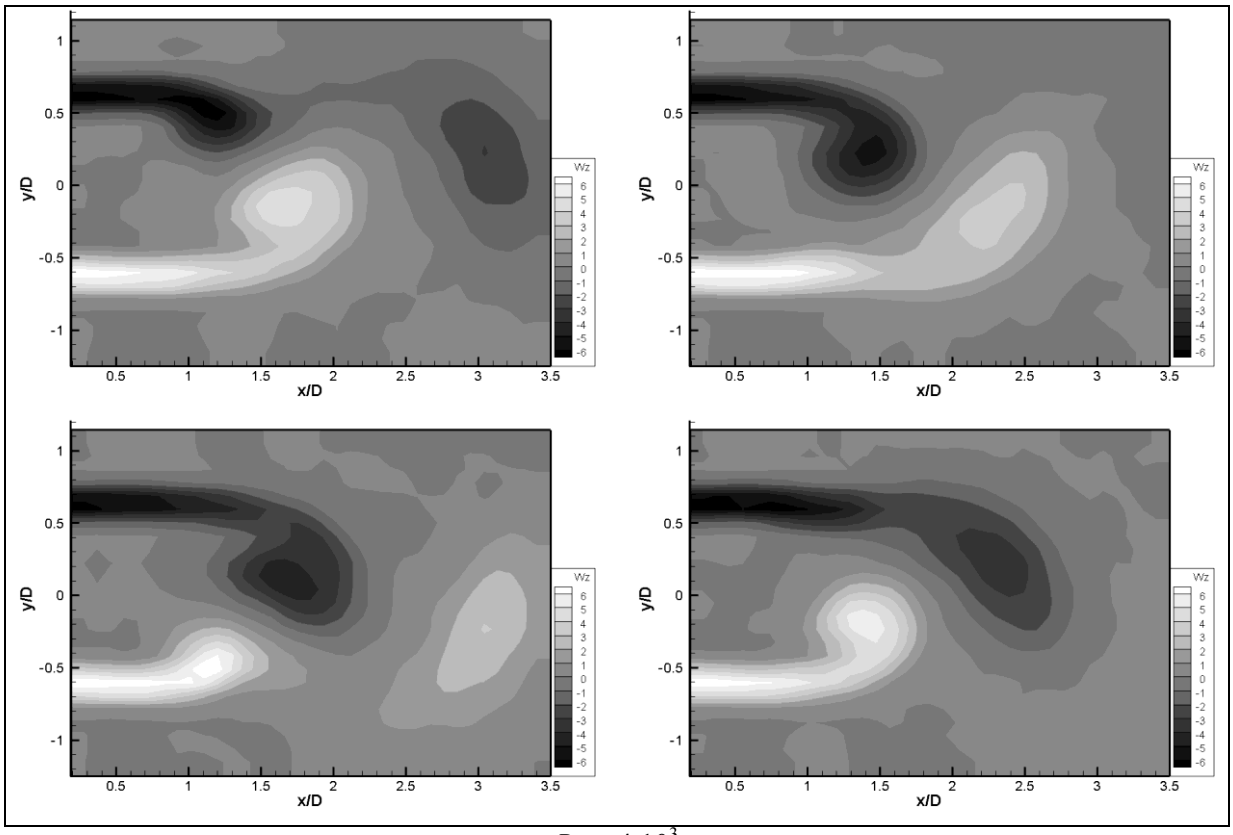

$Re = 4 \cdot 10^3$

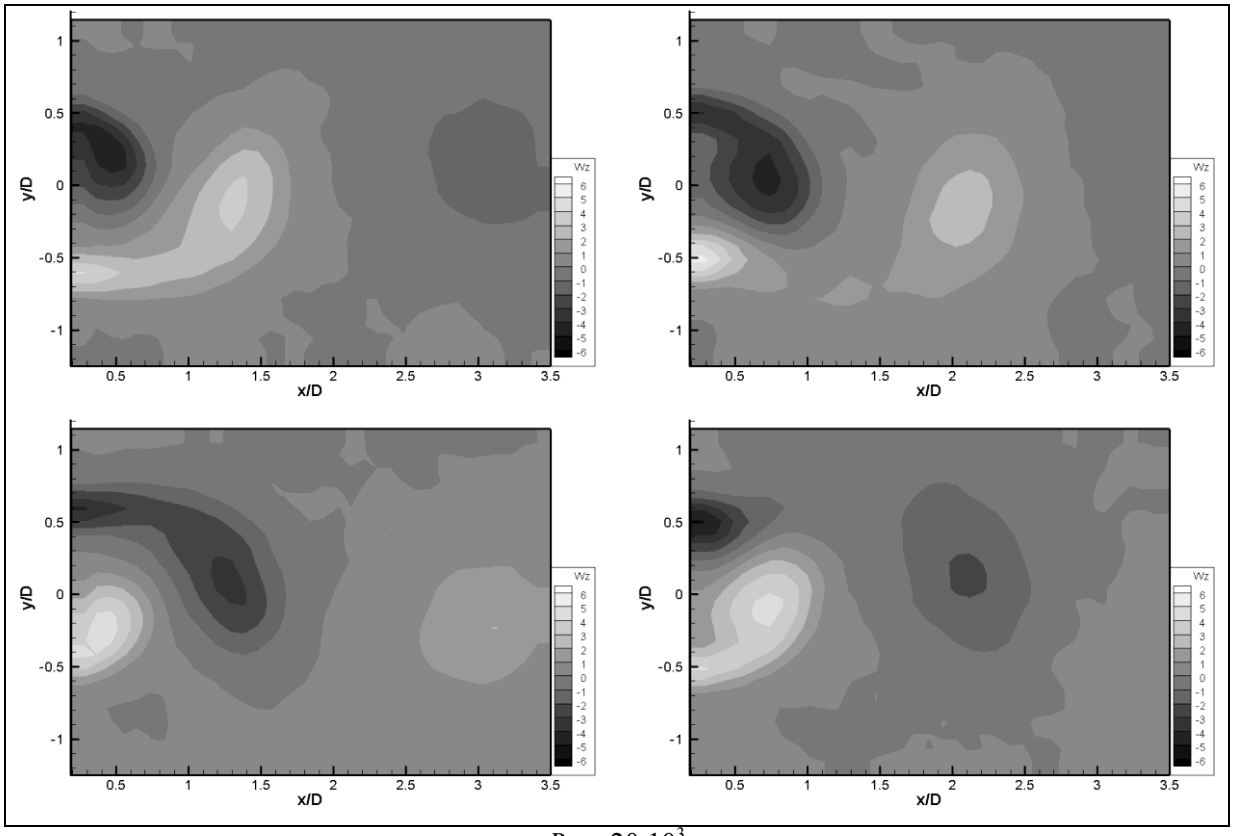

$Re = 20 \cdot 10^3$

Fig. 5.14 Dimensionless vorticity W_z for the phase averaged flow fields relative to $Re = 4 \cdot 10^3$ and $Re = 20 \cdot 10^3$.

5.5 Flow field past a finite circular cylinder: PIV measurements

PIV measurements have been done also for a finite cylinder. The cylinder aspect ratio AR=L/D is equal to 8. Differently from the infinite cylinder, for which the measurement plane was located in the middle of the cylinder height, in this case 9 measurement planes have been investigated to analyse the flow field along the cylinder height, as shown in Tab. 5.1. The Reynolds number investigated is Re=16·10^3.

Plane n.	z (mm)	z/L	z/D
1	30	0.14	1.15
2	60	0.29	2.31
3	90	0.43	3.46
4	120	0.58	4.62
5	140	0.67	5.38
6	160	0.77	6.15
7	180	0.87	6.92
8	200	0.96	7.69
9	210	1.01	8.08

Tab. 5.1 Measurement xy-planes investigated for the finite cylinder with AR=8.

5.5.1 Mean flow field

The mean flow field has been analysed according to Reynolds averaging decomposition. In Fig. 5.15 the mean flow field streamlines for all measurement planes are shown. The map symmetry proves the goodness of the average process. It's interesting to note that by moving from the cylinder base (z/L=0.14) to the tip (z/L=1.01) the vortex formation length decreases. This is reasonable since three dimensional features of the flow arise when the cylinder is finite, i.e. with a free end; the latter causes changes in the vortex formation length as well as the vortex shedding pattern. Consequently, the bigger length of finite cylinder vortex formation length is probably dependent on the downwash flow field, which lengthens this length near the cylinder base. For almost all measurement plane investigated, the vortex formation length of the finite cylinder is bigger than the one relative to the infinite cylinder (2D) for the same Reynolds number (Re=16·10^3).

The dimensionless vorticity W_z maps (Fig. 5.16) show clearly the shear layer region. Also in this case, the comparison between the finite cylinder measurements and infinite one

has been done. The same order of magnitude for the two cylinders proves that shear layer vorticity magnitude doesn't depend on the cylinder geometry.

The dimensionless Reynolds stress tensor components $u'u'$, $v'v'$ and $u'v'$ are shown in Fig. 5.17, Fig. 5.18 and Fig. 5.19 respectively. All these components have the same shape of the one relative to the infinite cylinder (also shown in the figures). The main difference between finite and infinite cylinder maps is in the order of magnitude. In fact, in all maps the order of magnitude of the Reynolds stress tensor components relative to the infinite cylinder is twice the ones of the finite cylinder or even more. With regard to the $v'v'$ map in the measurement plane nearest the cylinder base (z/L=0.14), there is noise along the centreline due to the laser reflections. The same phenomenon can be seen in the turbulent kinetic energy maps (see Fig. 5.20). In this case, the order of magnitude of the infinite cylinder map is even more than twice the one of the finite cylinder. Finally, the turbulent production maps are shown in Fig. 5.21. These have more noise than the others seen until now, because the computation of this variable (see Eq. 5.10) implies the use of the product between a Reynolds stress tensor component and the derivation of a velocity component (e.g. $u'u'\partial u/\partial x$), then if noise is present in the Reynolds stress component maps as well as in the velocity component ones, here this noise is amplified.

Finally, in order to investigate the vortex formation length by varying the measurement plane along the cylinder height, also herein the kinetic turbulent energy has been computed on the symmetry section as a function of x/D (see Fig. 5.22). The comparison with the infinite cylinder has been done. The infinite cylinder turbulence intensity is normally higher than the one relative to the finite one, whereas the vortex formation length is smaller. The latter decreases by approaching the free end of the finite cylinder and assumes about the same value of the 2D cylinder for z/L = 0.87. Probably this is due to the downwash flow along the free end of the finite cylinder. Fig. 5.22 is qualitatively similar to Fig. 2.50b by Park and Lee (2000). Nevertheless, a quantitative comparison cannot be done since in the cited work the Reynolds number is $20 \cdot 10^3$ and the aspect ratio AR = L/D is 10.

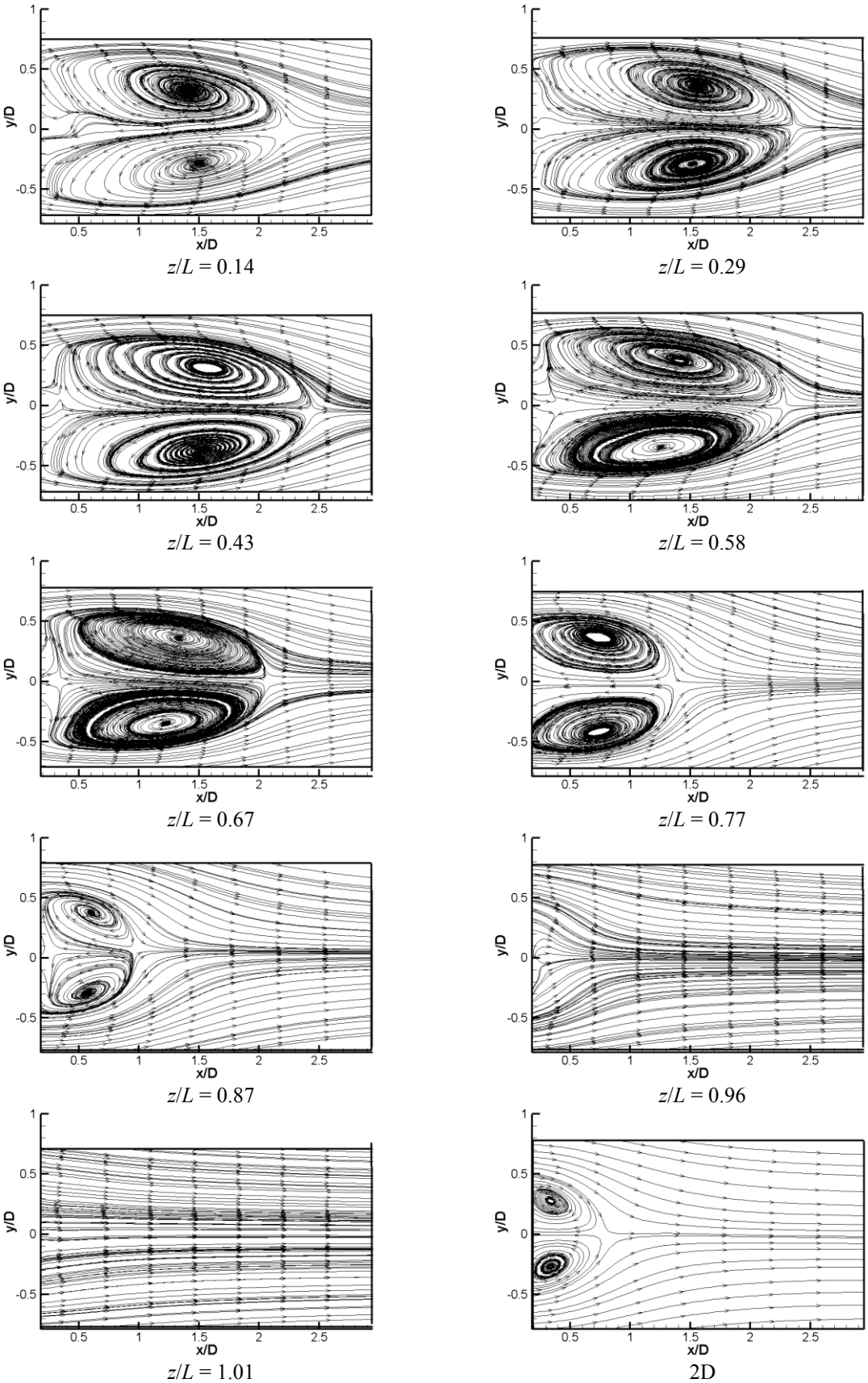

z/*L* = 0.14 *z*/*L* = 0.29

z/*L* = 0.43 *z*/*L* = 0.58

z/*L* = 0.67 *z*/*L* = 0.77

z/*L* = 0.87 *z*/*L* = 0.96

z/*L* = 1.01 2D

Fig. 5.15 Streamlines of the mean flow field in xz-planes relative to finite cylinder with AR=8.

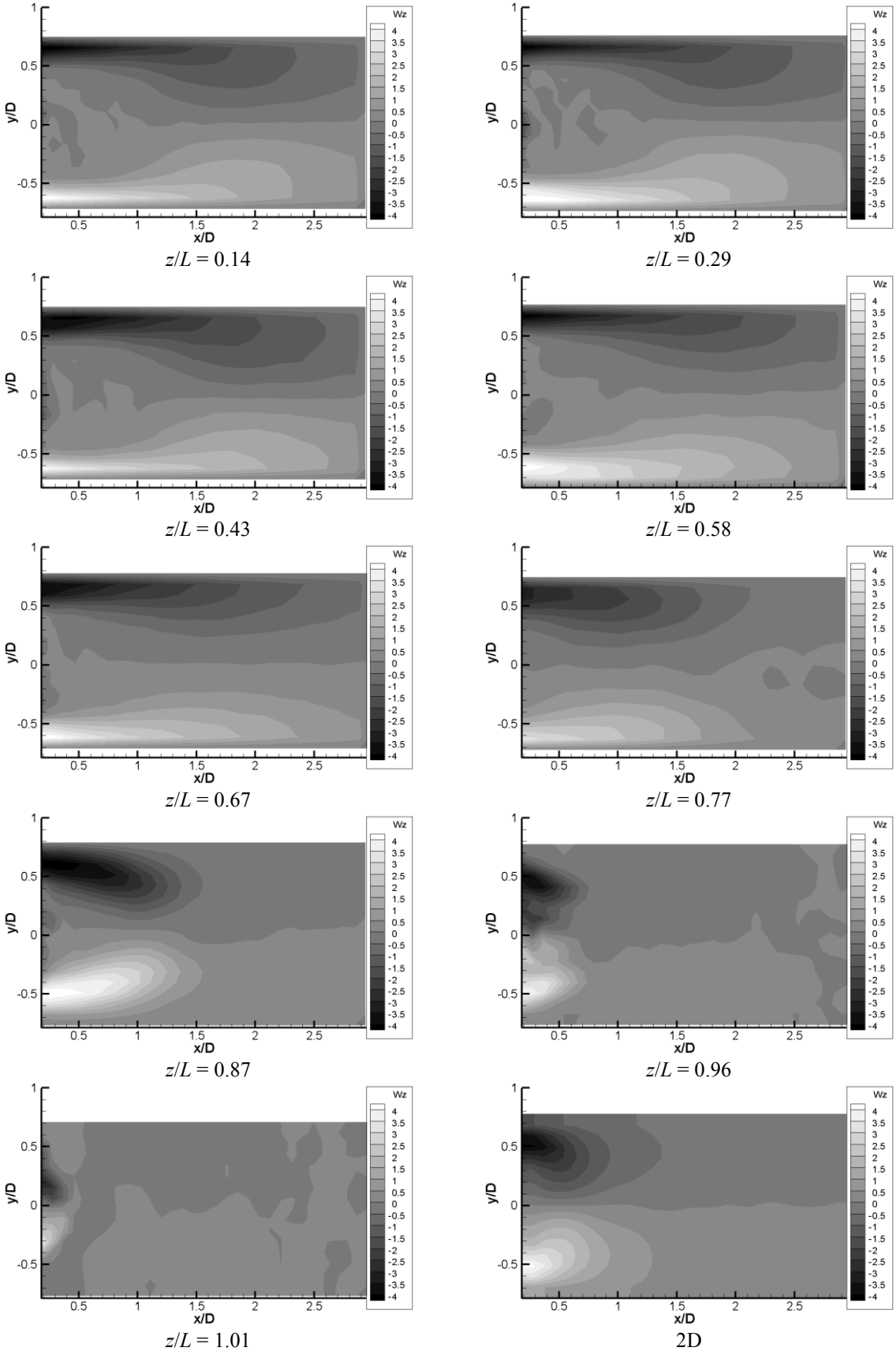

z/*L* = 0.14 *z*/*L* = 0.29

z/*L* = 0.43 *z*/*L* = 0.58

z/*L* = 0.67 *z*/*L* = 0.77

z/*L* = 0.87 *z*/*L* = 0.96

z/*L* = 1.01 2D

Fig. 5.16 Dimensionless vorticity W_z of the mean flow field in xz-planes relative to finite cylinder with AR=8.

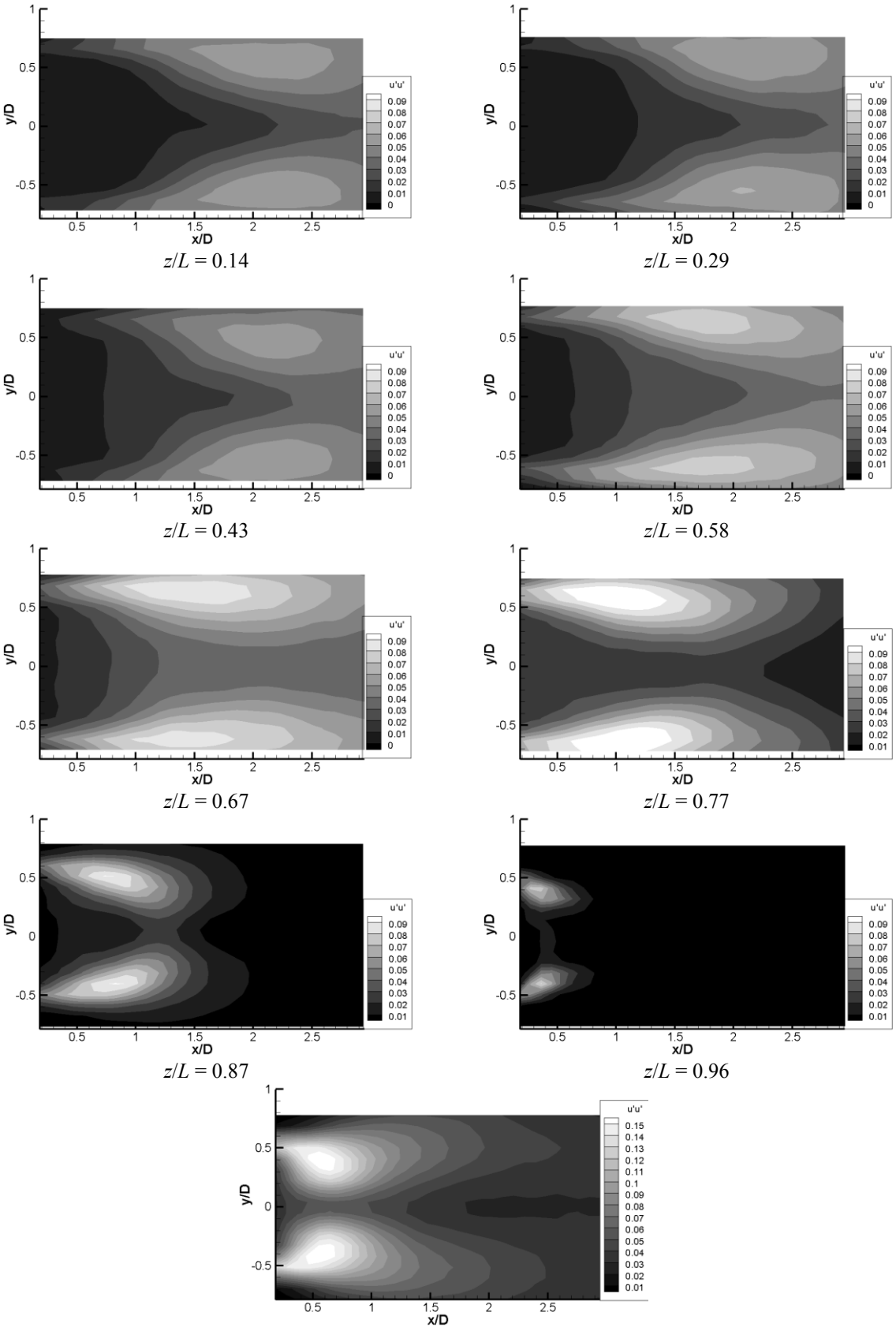

z/L = 0.14 z/L = 0.29

z/L = 0.43 z/L = 0.58

z/L = 0.67 z/L = 0.77

z/L = 0.87 z/L = 0.96

2D

Fig. 5.17 Dimensionless Reynolds stress tensor component $u'u'$ of the mean flow field in xz-planes relative to finite cylinder with AR=8

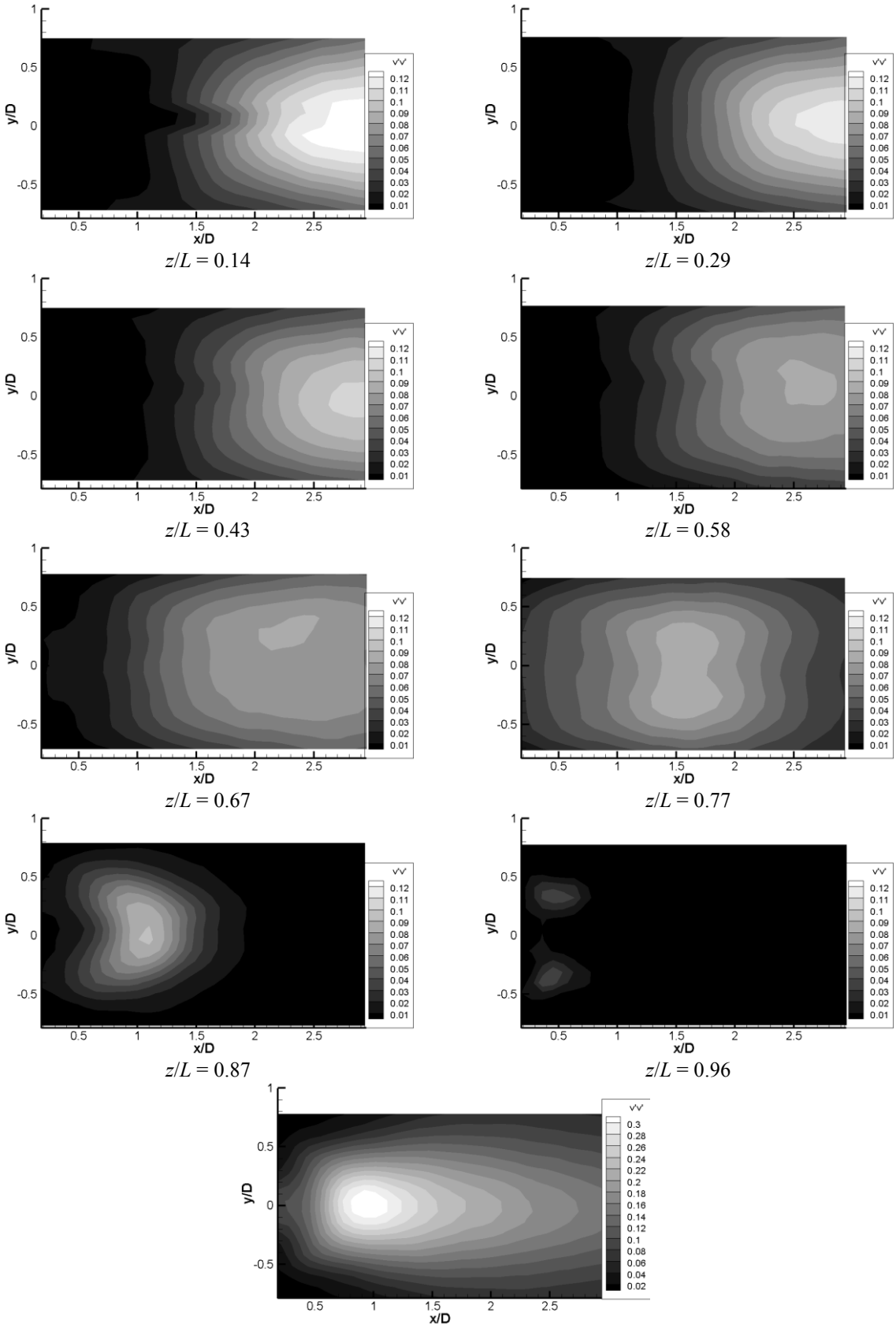

z/L = 0.14 z/L = 0.29

z/L = 0.43 z/L = 0.58

z/L = 0.67 z/L = 0.77

z/L = 0.87 z/L = 0.96

2D

Fig. 5.18 Dimensionless Reynolds stress tensor component $v'v'$ of the mean flow field in xz-planes relative to finite cylinder with AR=8.

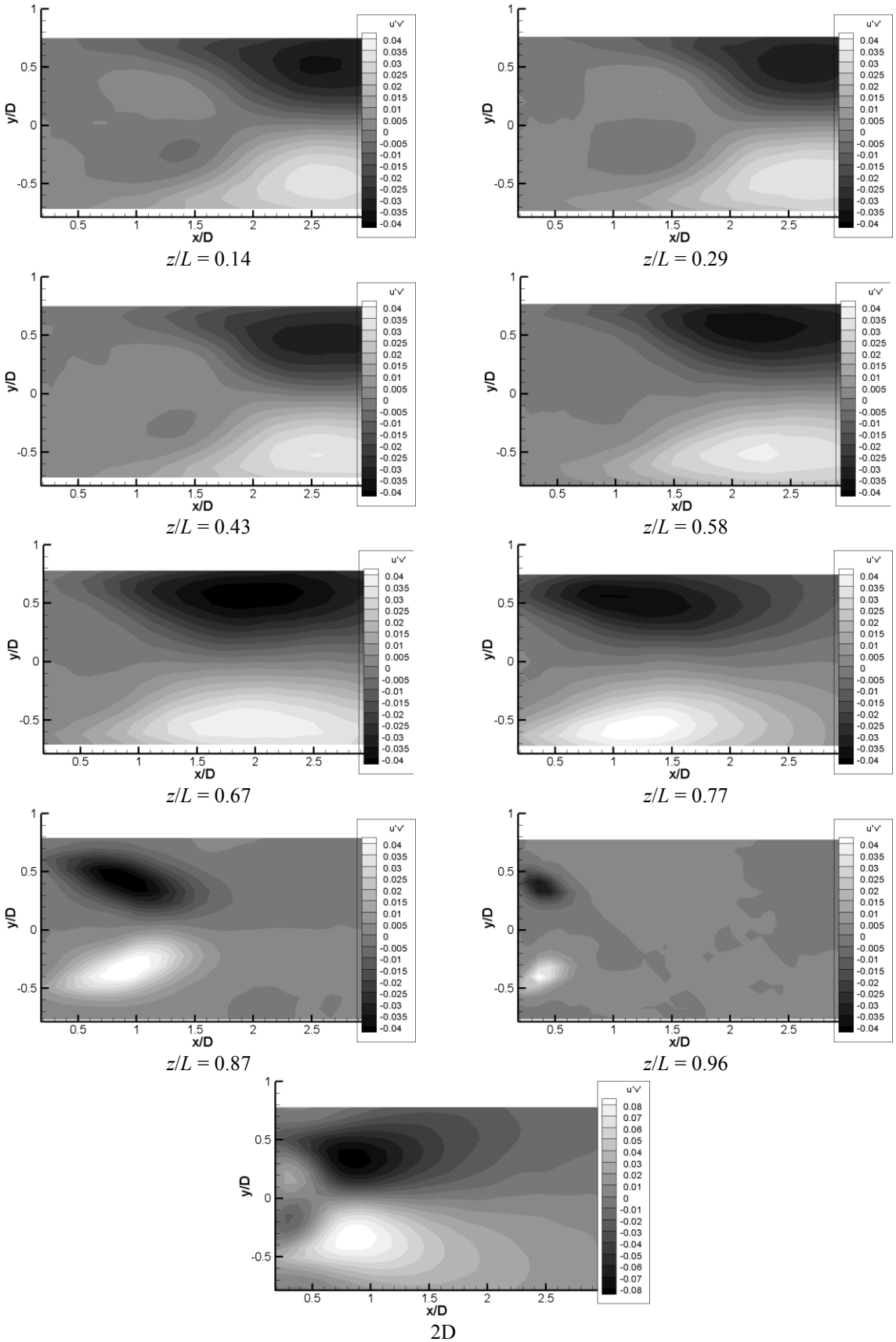

z/L = 0.14 z/L = 0.29

z/L = 0.43 z/L = 0.58

z/L = 0.67 z/L = 0.77

z/L = 0.87 z/L = 0.96

2D

Fig. 5.19 Dimensionless Reynolds stress tensor component $u'v'$ of the mean flow field in xz-planes relative to finite cylinder with AR=8.

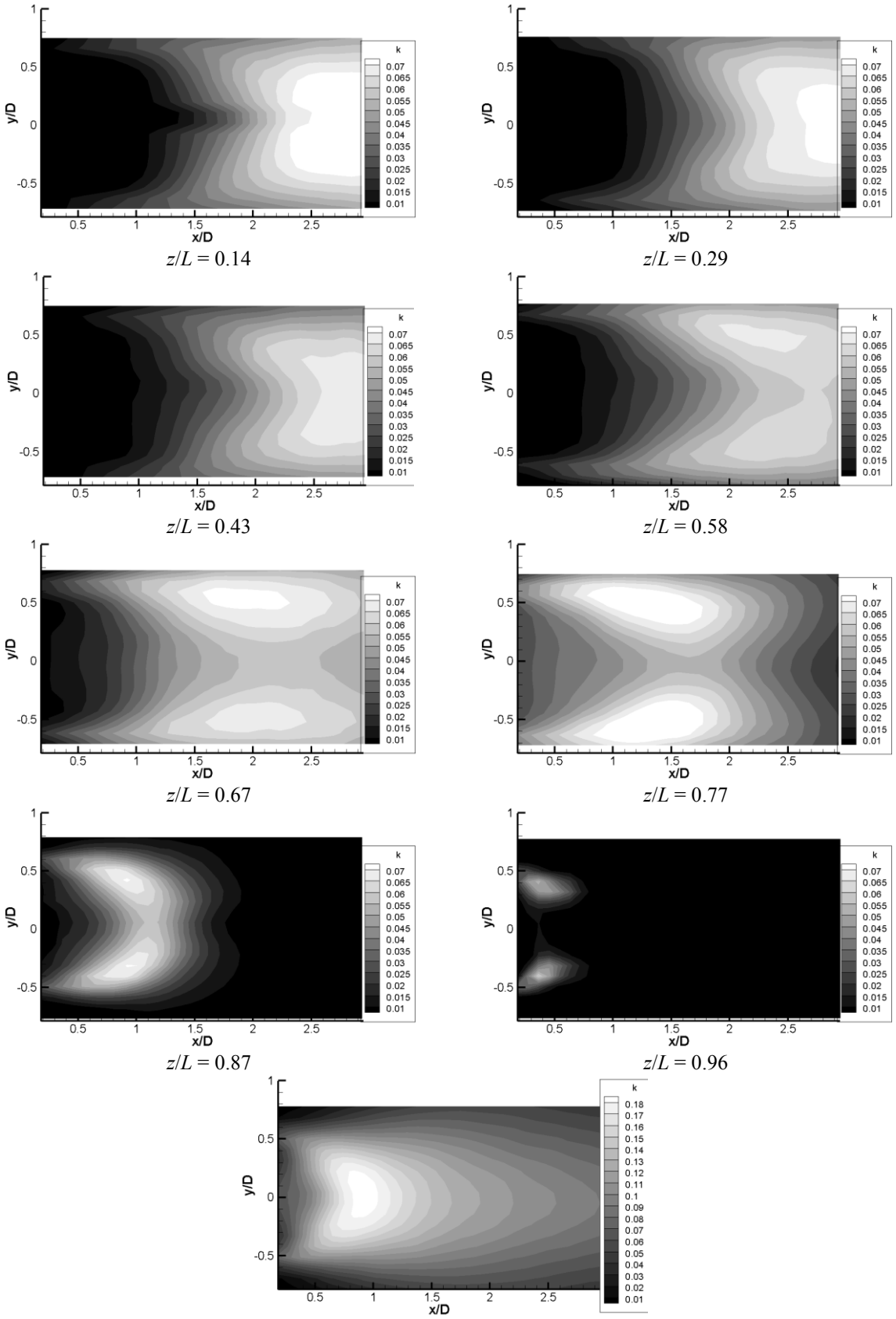

z/L = 0.14 z/L = 0.29

z/L = 0.43 z/L = 0.58

z/L = 0.67 z/L = 0.77

z/L = 0.87 z/L = 0.96

2D

Fig. 5.20 Dimensionless kinetic turbulent energy k of the mean flow field in xz-planes relative to finite cylinder with AR=8.

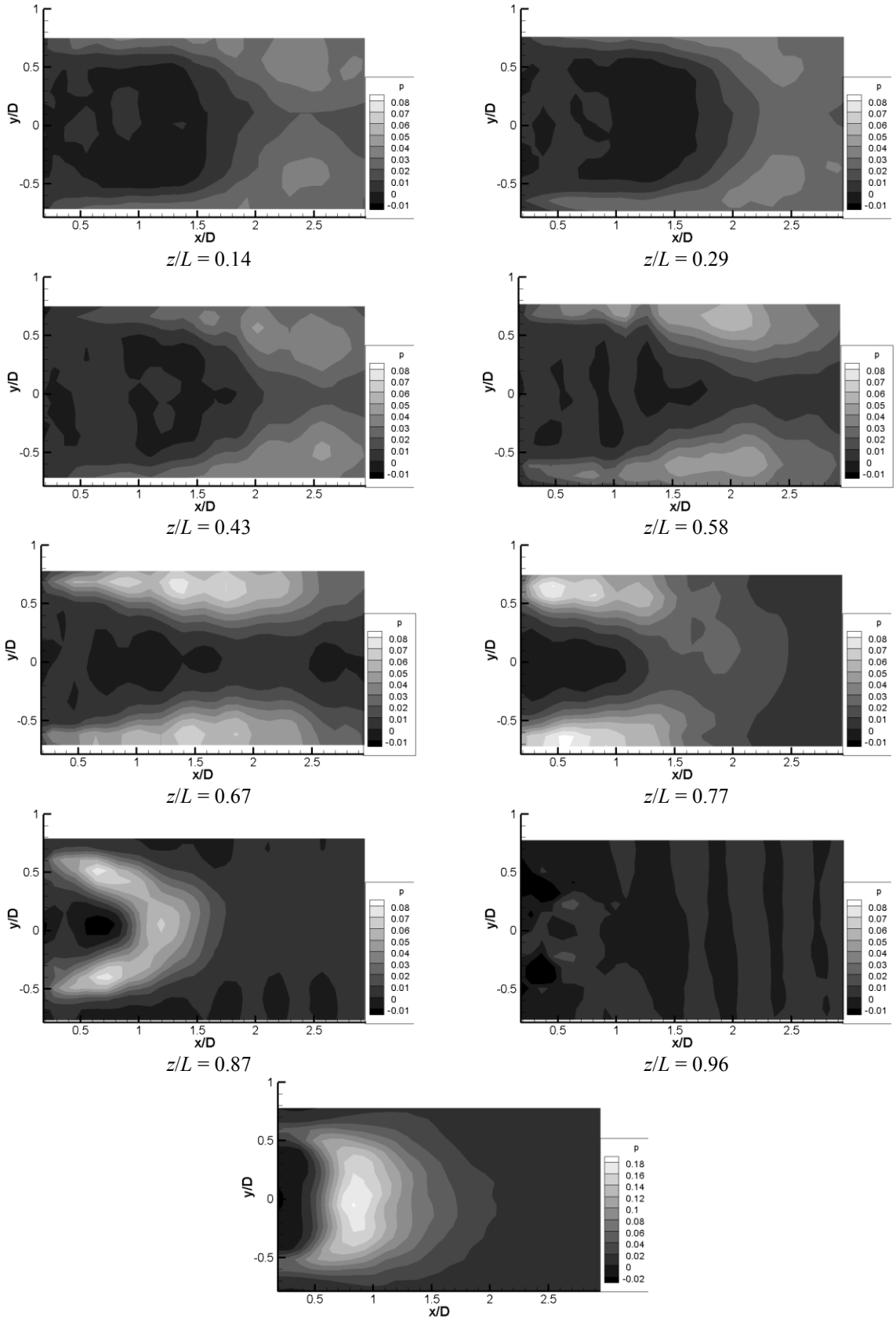

z/L = 0.14 z/L = 0.29

z/L = 0.43 z/L = 0.58

z/L = 0.67 z/L = 0.77

z/L = 0.87 z/L = 0.96

2D

Fig. 5.21 Dimensionless turbulent production p of the mean flow field in xz-planes relative to finite cylinder with AR=8.

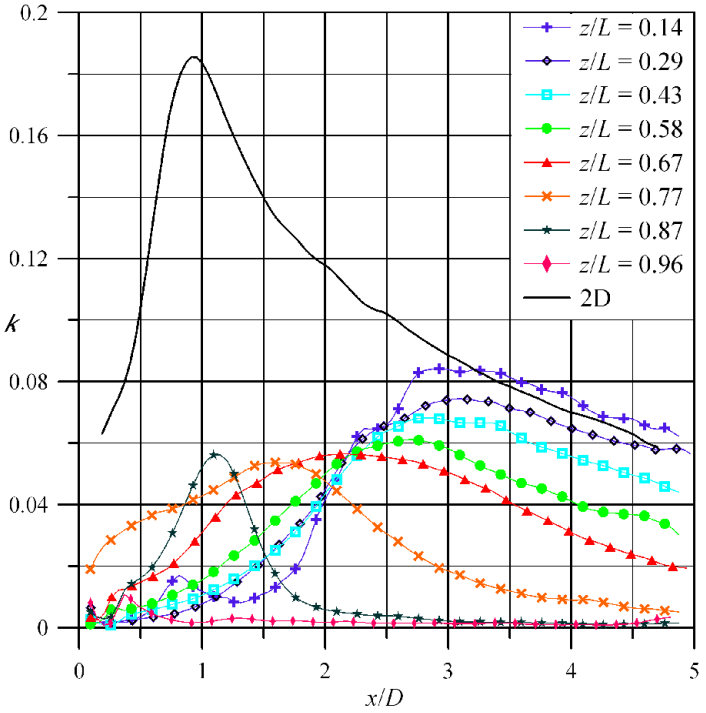

Fig. 5.22 Turbulence intensity distribution on $y/D = 0$ section.

5.5.2 Phase averaged flow field

Also in this case, the procedure based on the Proper Orthogonal Decomposition has been applied to identify the von Kàrmàn vortex shedding.

As explained in Sect. 2, the vortex shedding disappears for an aspect ratio lower than a critical value, which depends on the experimental condition like boundary layer thickness or turbulence intensity. Furthermore, for the aspect ratio used in this work, Kawamura et al. (1984) showed that the von Kàrmàn vortices are present only in a small region in proximity of the cylinder base.

Consequently, one expects that by applying the POD technique to find the vortex shedding in all measurement planes along the cylinder height, the two principal modes are detectable only for few measurement planes near the cylinder base.

Fig. 5.23 shows the percentage energy respect to the overall one, associated to the first 10 eigenvalues, for both finite and infinite cylinders. The curve relative to the 2D cylinder shows the first 2 eigenvalues having more than 30% of the overall energy, whereas all the others have values lower than 3%. As before explained, this is the ideal condition to apply the POD technique to compute phase averaging, since the first two eigenvalues contain almost 65% of the flow field energy. For the finite cylinder, while near the base plane ($z/L = 0.14$) the first two eigenvalues contain almost 65% of the overall energy; by approaching the free end of the cylinder, the situation gets worse. For example for $z/L = 0.29$ almost 57% and for

z/L=0.43 this value decreases to only 48%. It is interesting to note that, contrary to the 2D cylinder, for the three sections of the finite cylinder nearer to the wall, the third eigenvalue owns a relatively high value of percentage energy, whereas the residual ones contain significantly smaller values. Curves relative to other measurement sections suggest the inapplicability of the POD approach.

As a conclusion of these observations and accordingly with Kawamura et al. (1984), it can be affirmed that the region which shows the von Kàrmàn vortex shedding for a finite cylinder with AR=8 extends from about z/L≈0.14 until z/L≈0.43. Unfortunately, it was not possible to make any measurements nearer the cylinder base, because of too much reflections of the laser on the plane on which the cylinder was mounted.

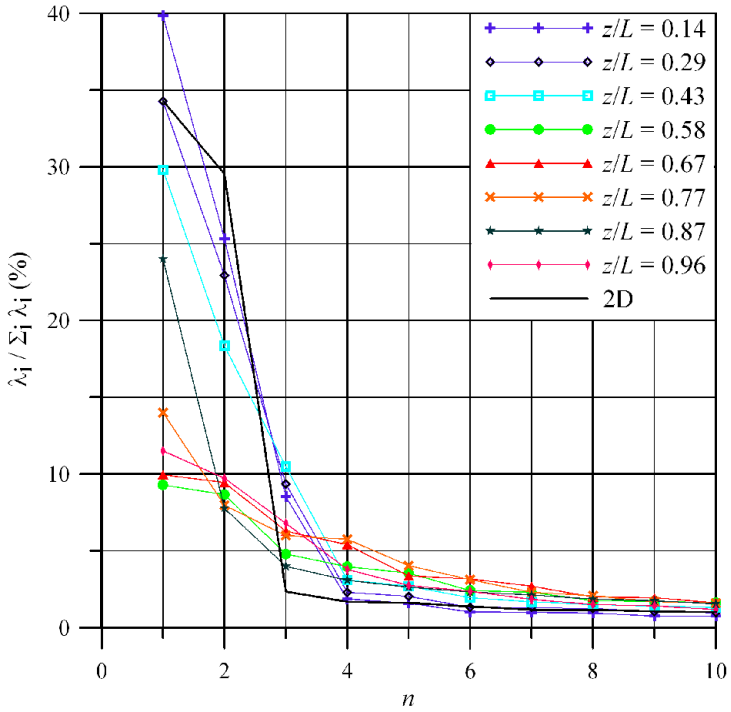

Fig. 5.23 Energy percentage associated to first 10 POD eigenvalues.

Fig. 5.24 shows the first two POD modes relative to the 2D cylinder and the finite one for z/L=0.14, z/L=0.29 and z/L=0.43. The first are very similar to the ones present in the literature (e.g. Perrin et al. 2007), while the ones relative to the finite cylinder, even if different from the 2D modes, are very similar to each other.

In Fig. 5.25 and Fig. 5.26 the streamlines of the phase averaged flow fields are shown. For each section only 4 phases of the von Kàrmàn vortex shedding period are illustrated.

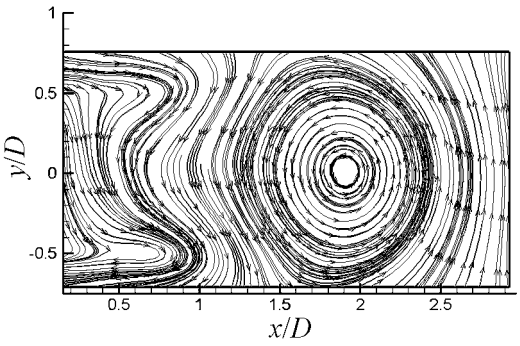

z/*L* = 0.14 - mode 1

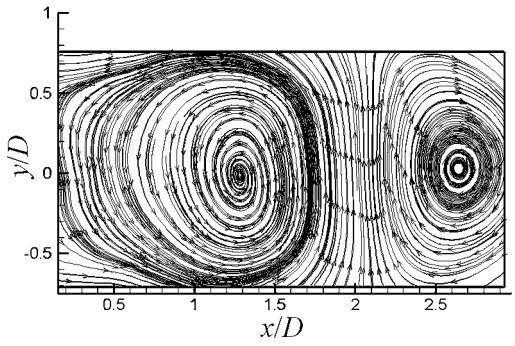

z/*L* = 0.14 - mode 2

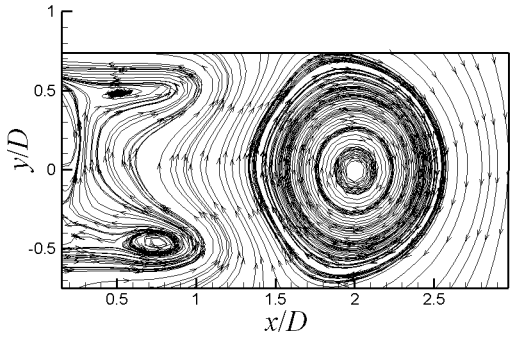

z/*L* = 0.29 - mode 1

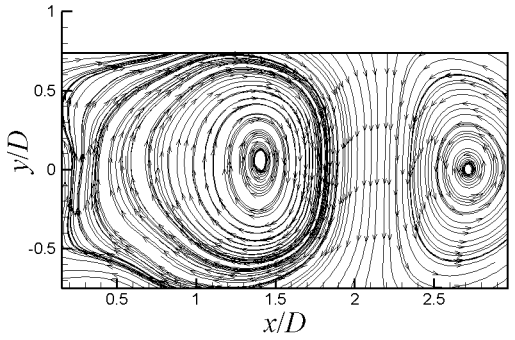

z/*L* = 0.29 - mode 2

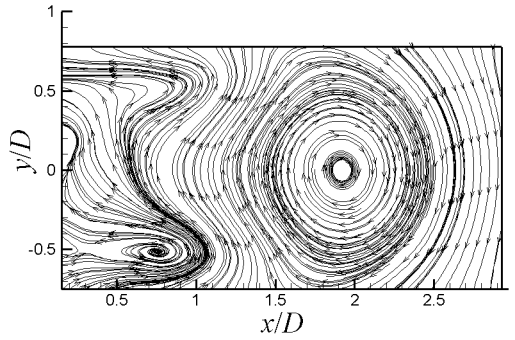

z/*L* = 0.43 - mode 1

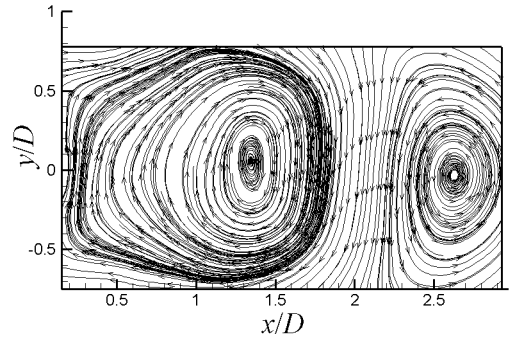

z/*L* = 0.43 - mode 2

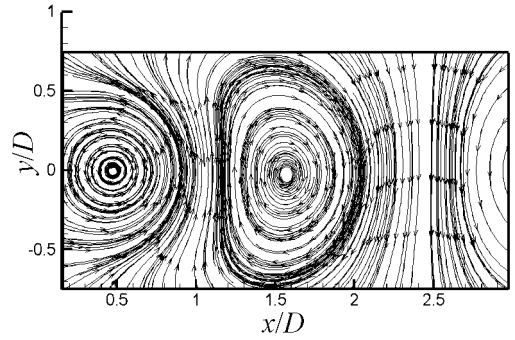

2D - mode 1

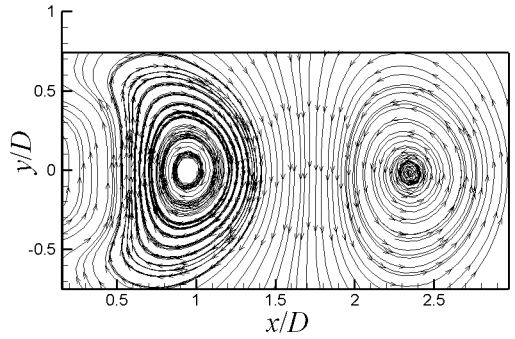

2D - mode 2

Fig. 5.24 First 2 POD modes.

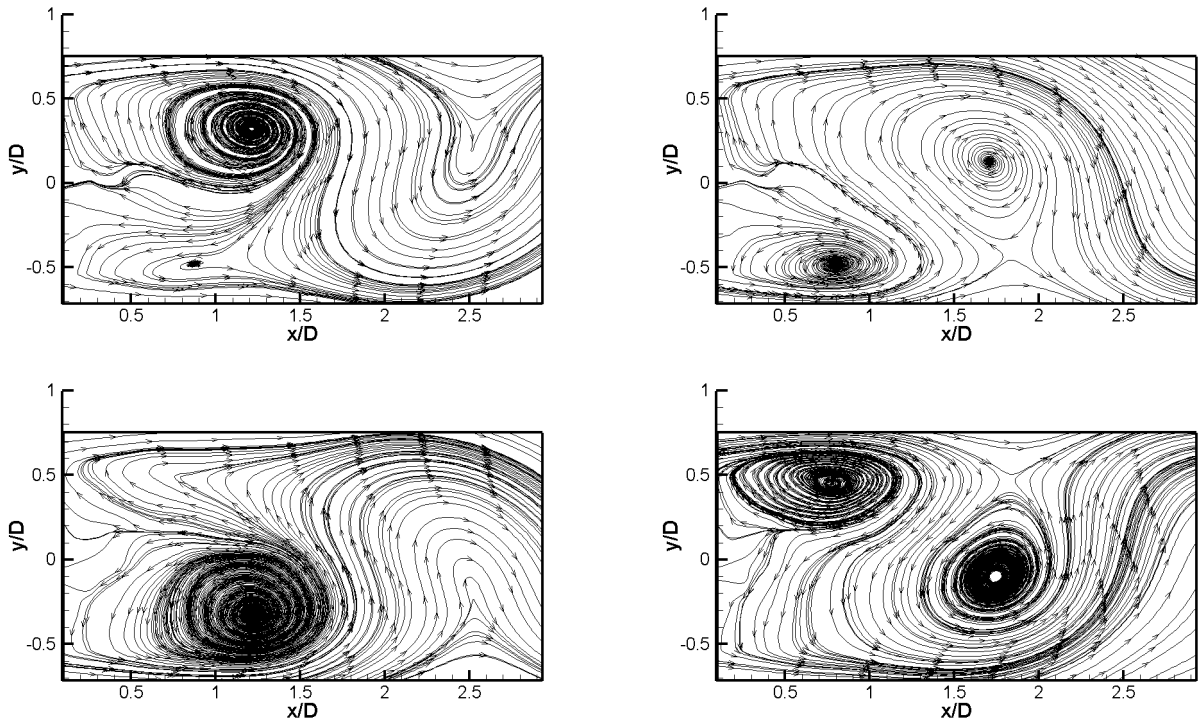

Finite cylinder - $z/L = 0.14$

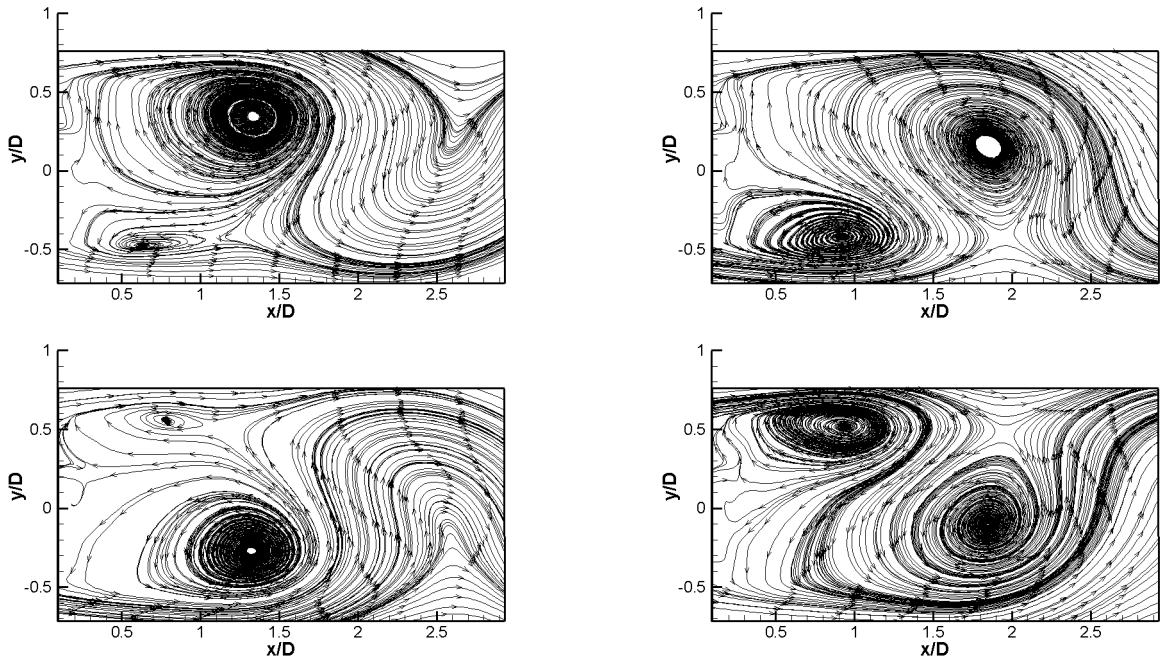

Finite cylinder - $z/L = 0.29$

Fig. 5.25 Streamlines of phase averaged flow field relative to the finite cylinder for the measurement planes set in $z/L = 0.14$ and $z/L = 0.29$ positions.

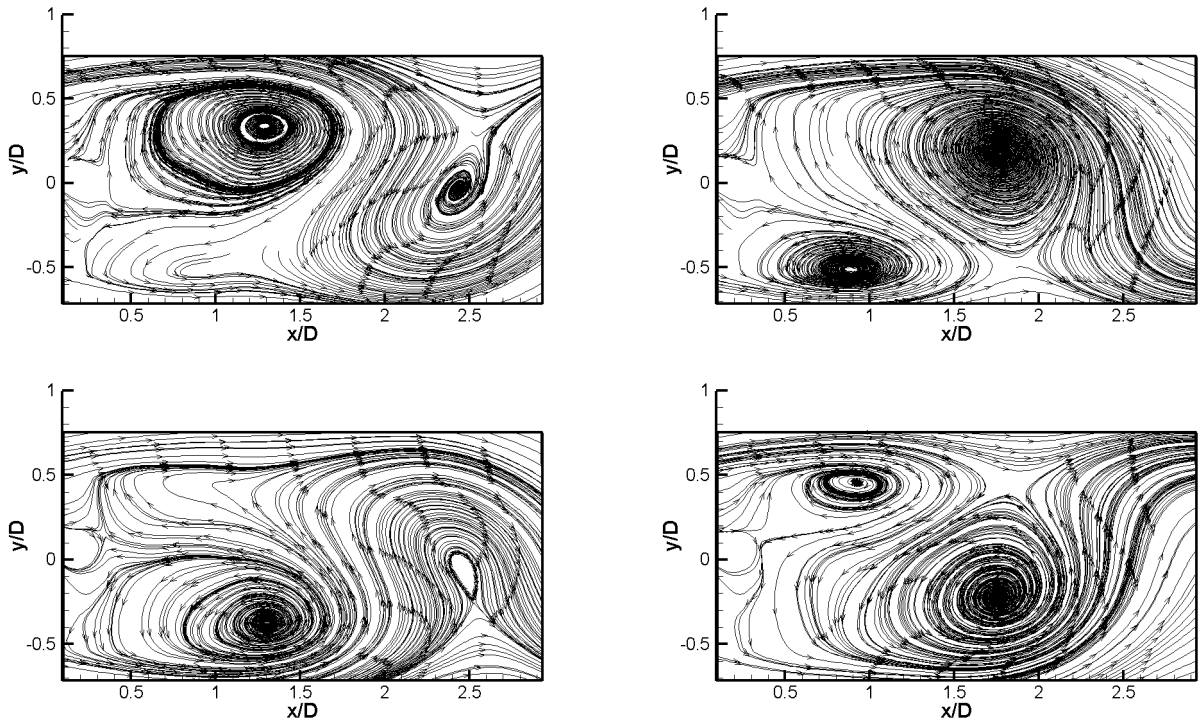

Finite cylinder - $z/L = 0.43$

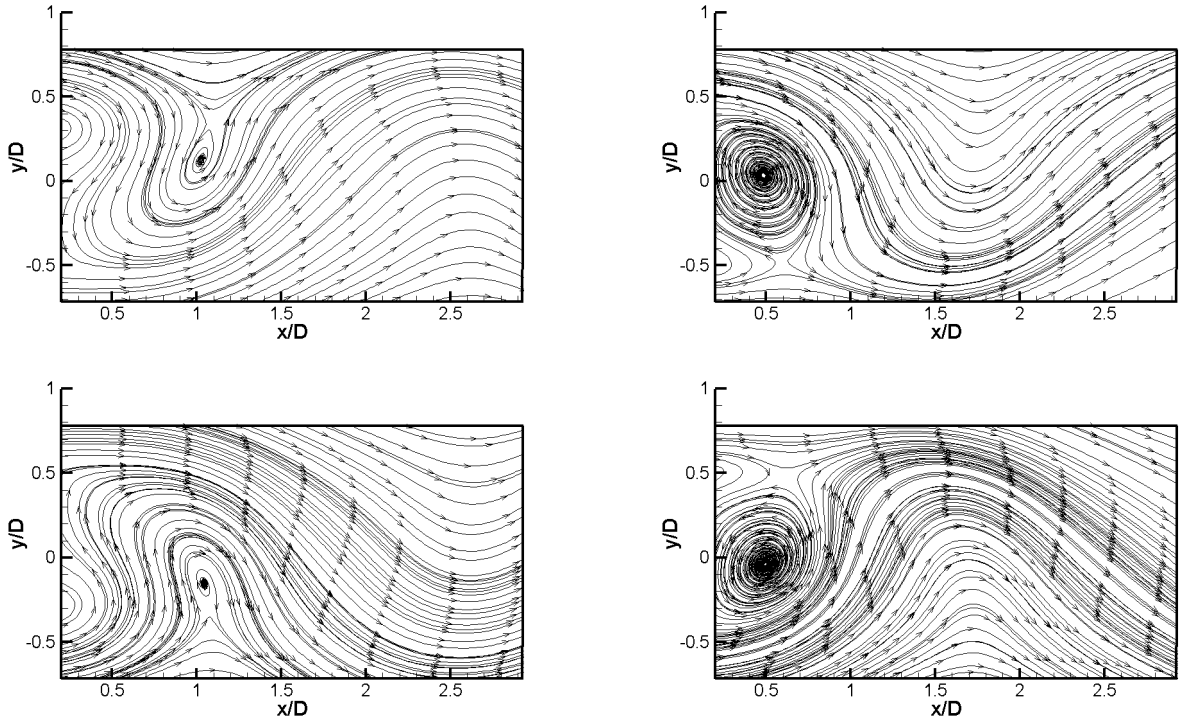

Infinite cylinder – 2D

Fig. 5.26 Streamlines of phase averaged flow field relative to both finite cylinder at $z/L = 0.43$ and infinite one with $Re = 16 \cdot 10^3$.

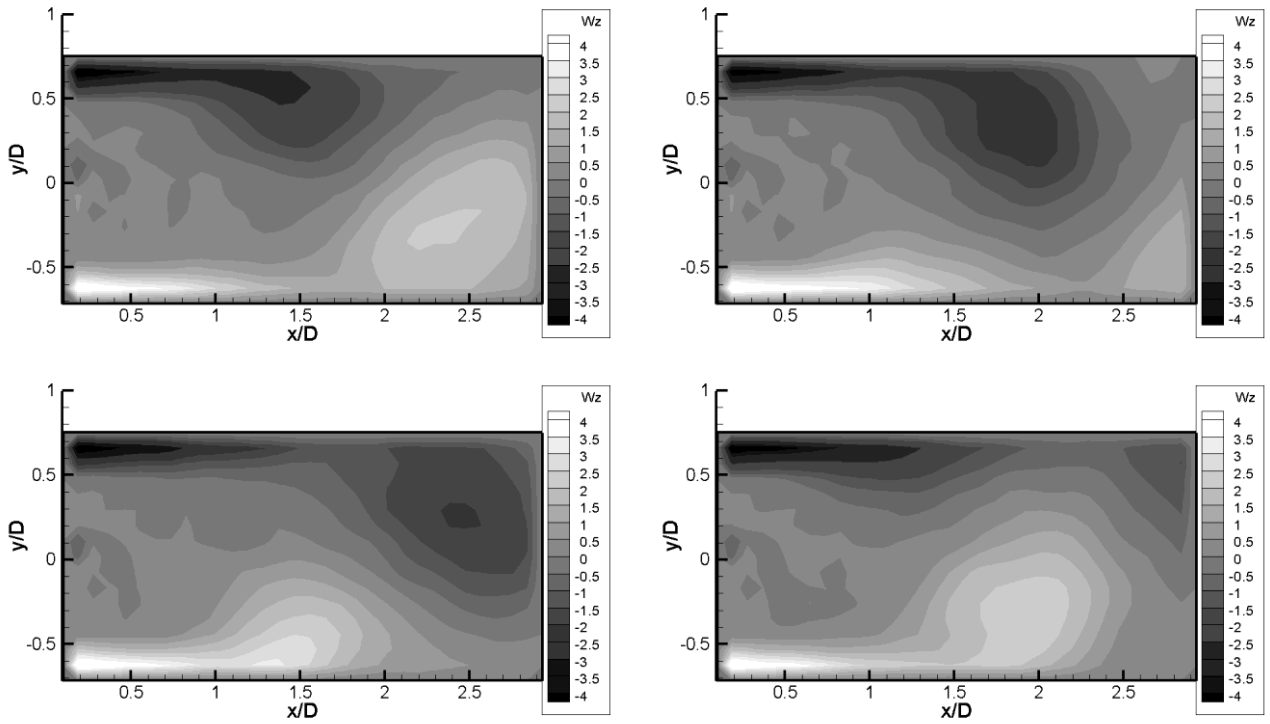

Finite cylinder - $z/L = 0.14$

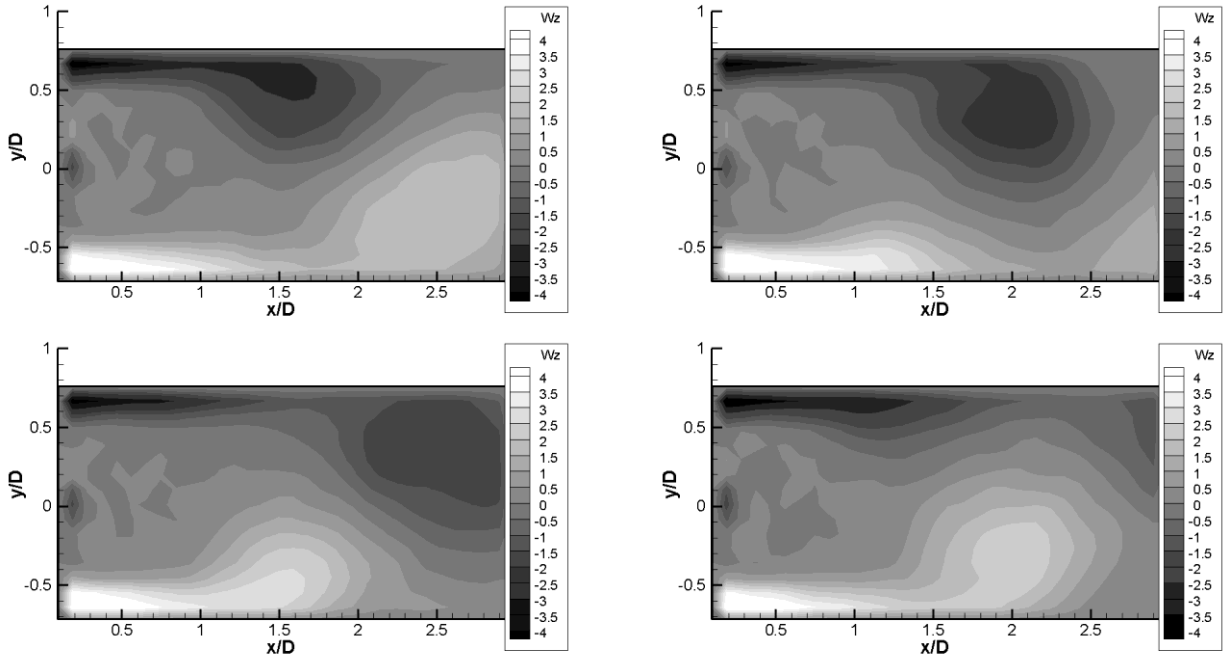

Finite cylinder - $z/L = 0.29$

Fig. 5.27 Dimensionless vorticity W_z for the phase averaged flow field relative to the finite cylinder for the measurement planes set in $z/L = 0.14$ and $z/L = 0.29$ positions.

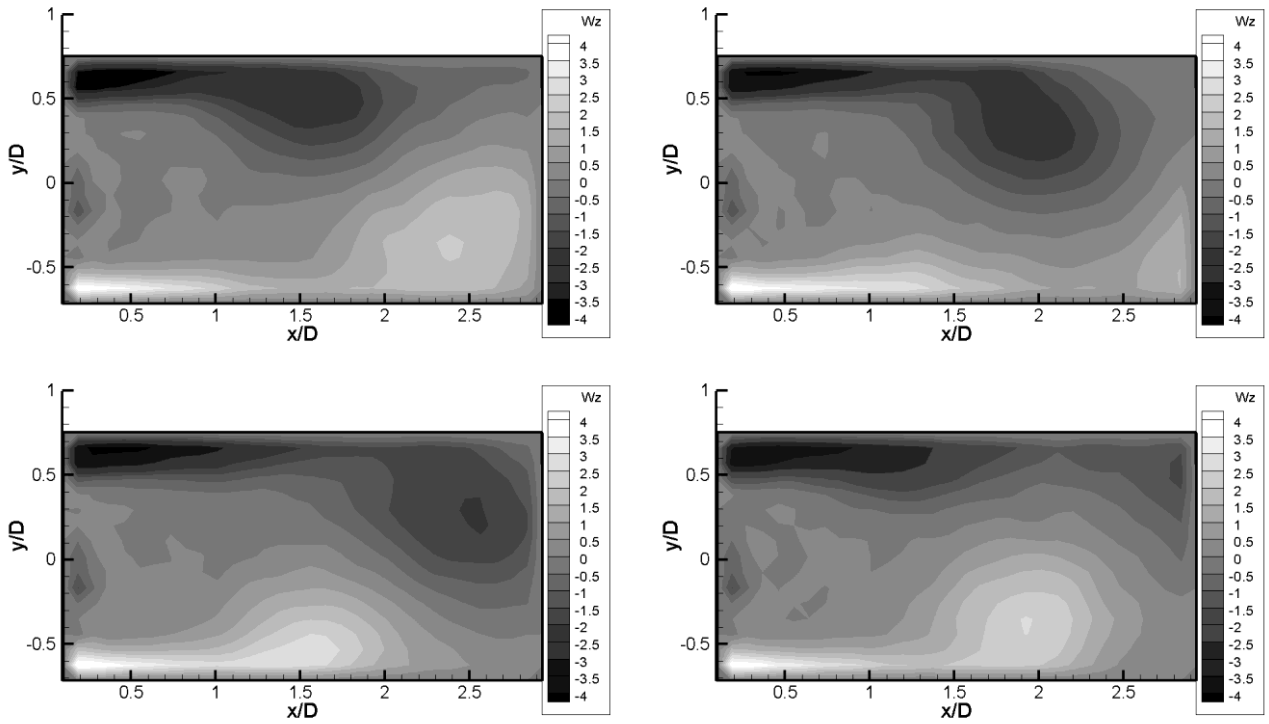

Finite cylinder - $z/L = 0.43$

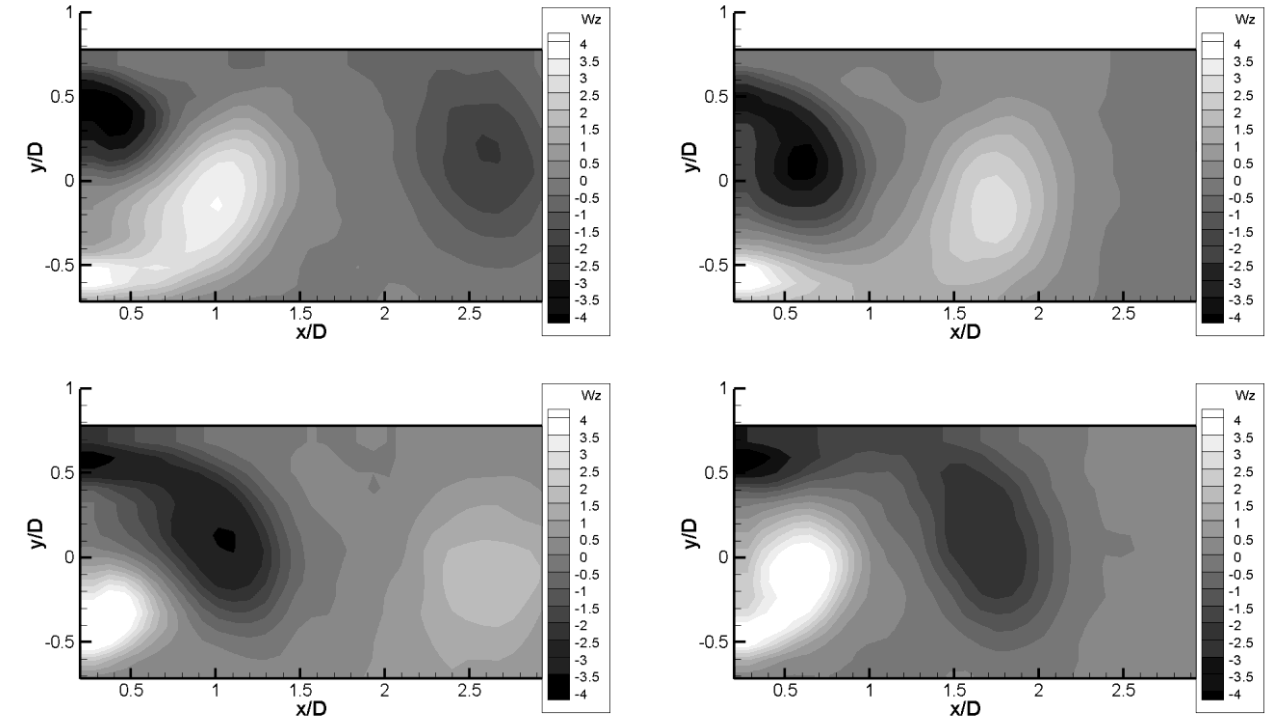

Infinite cylinder – 2D

Fig. 5.28 Dimensionless vorticity W_z for the phase averaged flow field relative to both finite cylinder at $z/L = 0.43$ and infinite one with $Re = 16 \cdot 10^3$.

For all the finite cylinder planes, the first phase averaged flow field shows a single upper vortex and a pair of lower vortices. The first lower vortex is forming just downstream of the cylinder and the second one is in the final part of the measurement zone. The former

vortex grows first in the downstream direction and then starts to move toward the centreline and becomes more symmetrical. For the 2D cylinder, besides the already shown different vortex formation length, the vortices disappear quicker and their evolution is significantly accelerated.

The phase averaged dimensionless vorticity maps are shown in Fig. 5.27 and Fig. 5.28. Also in this case, it's interesting to note that the absolute value of the vorticity peak at the centre of a vortex decreases when the vortex moves downstream.

5.6 Flow field past a finite circular cylinder: Stereo PIV measurements

In the previous section, an accurate analysis of the flow field in the wake of a finite cylinder with AR=8 has been done. In particular, both mean flow fields and Kàrmàn vortex shedding have been investigated.

In order to investigate also the downwash flow, which characterizes the finite cylinder flow field as well, measurements in *xz*-planes have been performed.

Actually the flow fields in such planes are strongly dependent on the cylinder aspect ratio. This is the reason why cylinder with AR=2 (Sect. 5.6.2) is investigated besides the one with AR=8 (Sect. 5.6.1).

5.6.1 Flow field in x-z plane relative to the cylinder with AR=8

In Tab. 5.2 all the measurement planes investigated are described. They are arranged along the positive *y*-axis: the last one is set at y/D=0.577, i.e. just over the cylinder. No measurement plane has been set at negative *y*-coordinate because the mean flow field is symmetric with respect to the *x*-axis.

Actually, each flow field map has been obtained by merging two flow field maps at the same y/D and shifted along *z* (see Fig. 5.29). This allowed obtaining a higher spatial resolution. For each common area point, the variable (e.g. velocity component *u*) has been computed with a weighted average of the two available values.

The mean flow field streamlines maps are shown in Fig. 5.30 and Fig. 5.31.

No. plane	*y* (*mm*)	*y*/*D*

1	0	0
2	2	0.077
3	5	0.192
4	7	0.269
5	9	0.346
6	11	0.423
7	13	0.500
8	15	0.577

Tab. 5.2 Measurement *xz*-planes investigated for the finite cylinder with AR=8.

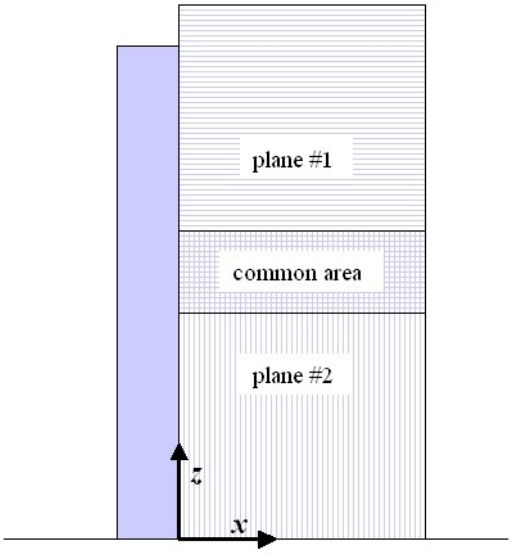

Fig. 5.29 Sketch of the measurement planes setting.

According to Afgan et al. (2007), a dense cluster of lines generated just before the free end of the cylinder later highlights the strong arc shaped downstream, which almost reaches the ground plane. The location of this arc determines the size of the recirculation vortex pair seen in the last section (see Fig. 5.15). By moving the measurement plane from the symmetry plane (y/D=0) to the *xz*-plane over the cylinder (y/D=0.577), this arc flattens itself until it perfectly adheres to the cylinder. The mean flow field streamlines measured in the plane set at y/D=0 are similar to the ones shown by Afgan et al. (2007) (see Fig. 2.51). Their measurements were for AR=6 and Re=$2.0 \cdot 10^4$.

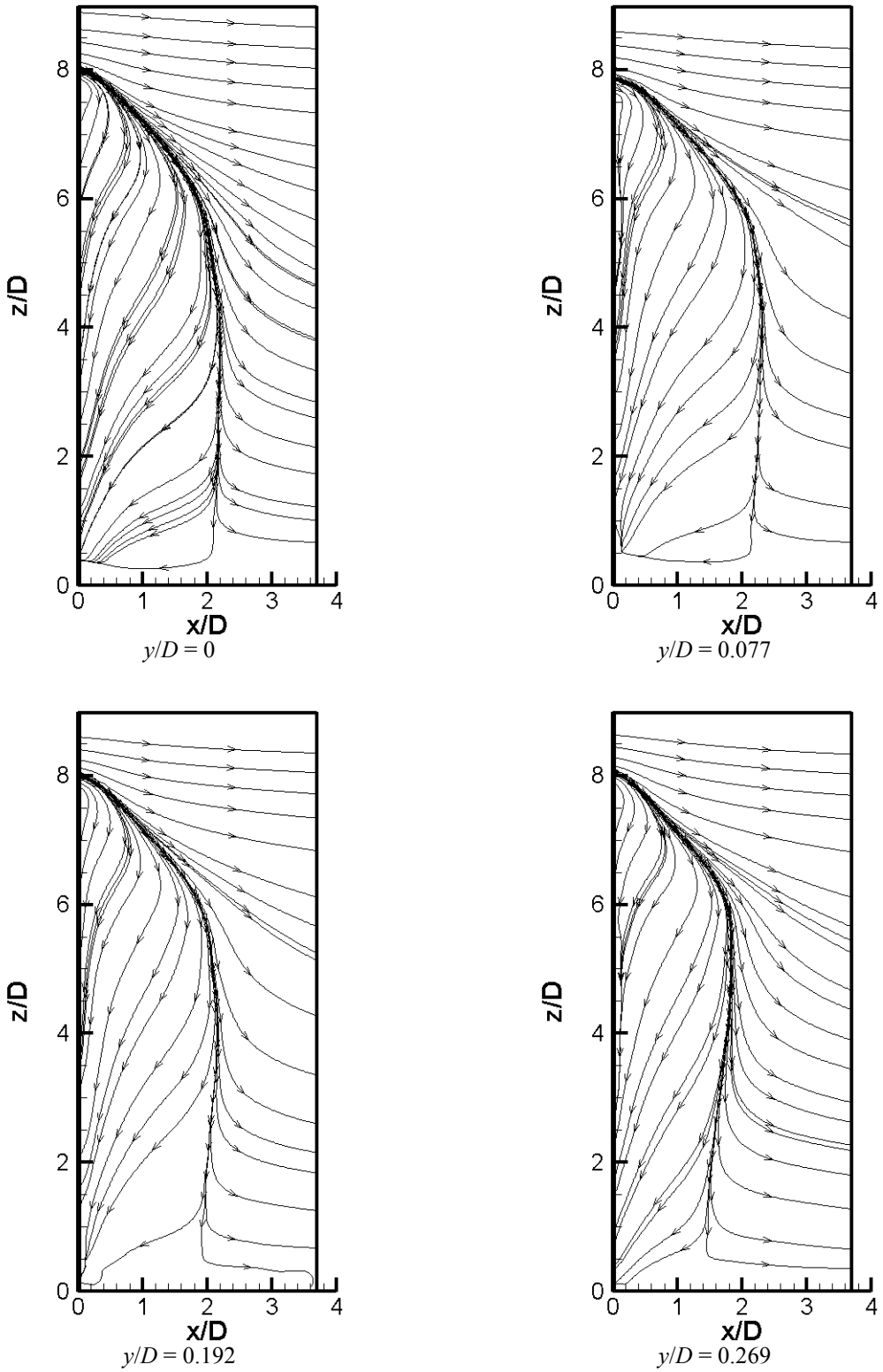

Fig. 5.30 Streamlines of the mean flow field in *xz*-planes relative to finite cylinder with AR=8.

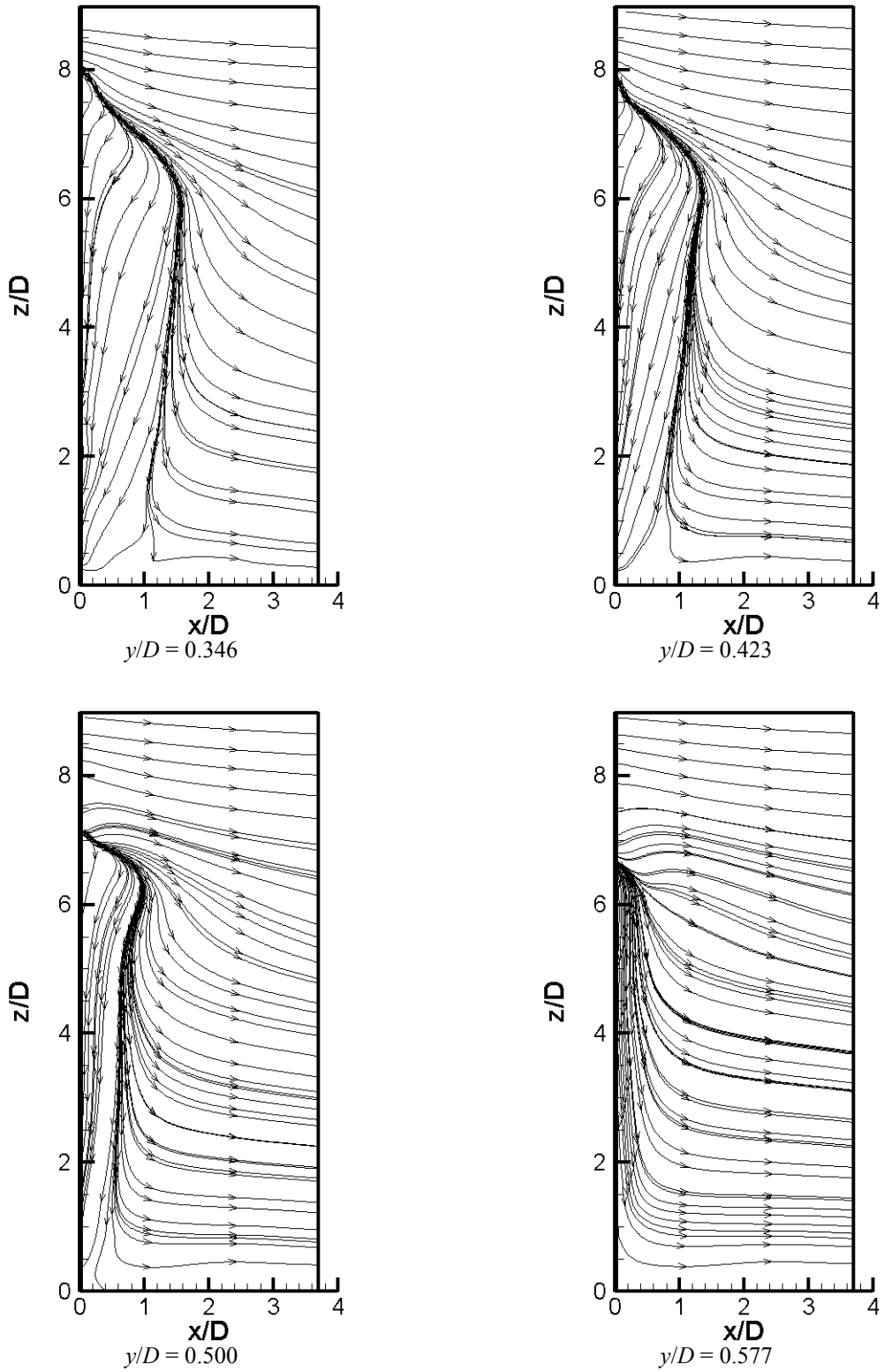

Fig. 5.31 Streamlines of the mean flow field in *xz*-planes relative to finite cylinder with AR=8.

5.6.2 Flow field in x-z plane relative to the cylinder with AR=2

In Tab. 5.3 all the measurement planes investigated are described. Also in this case, they are arranged along the positive *y*-axis: the last one is set at *y*/*D*=0.846. Also in this case, no measurement plane has been set at negative *y*-coordinate because the mean flow field is symmetric with respect to the *x*-axis.

Plane n.	*y* (*mm*)	*y*/*D*
1	0	0
2	2	0.077
3	4	0.154
4	6	0.231
5	8	0.308
6	10	0.385
7	12	0.462
8	14	0.538
9	16	0.615
10	18	0.692
11	20	0.769
12	22	0.846

Tab. 5.3 Measurement *xz*-planes investigated for the finite cylinder with AR=2.

The mean flow field streamlines maps are shown in Fig. 5.32 and Fig. 5.33. It's interesting to note that by decreasing the cylinder aspect ratio, the flow filed pattern changes drastically. Differently from the results obtained for AR=8, in this case a big recirculation region can be seen in the cylinder wake. Of course, this vortex decreases its dimension by approaching the planes set over the cylinder. The flow field pattern at *y*/*D*=0 is quite similar to the one shown by Fröhlich and Rodi (2004) and reported here in Fig. 2.46. Their measurements were for $Re=43\cdot10^3$ and AR=2.5.

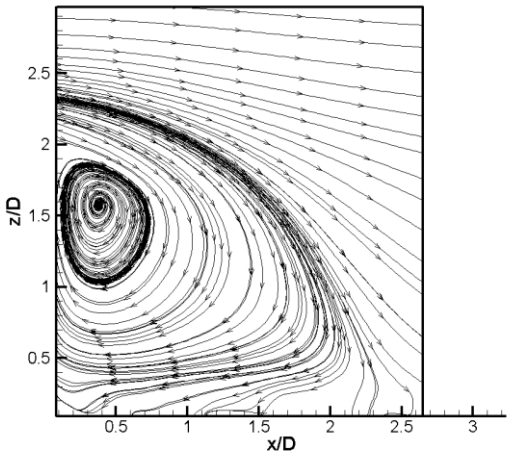

$y/D = 0$

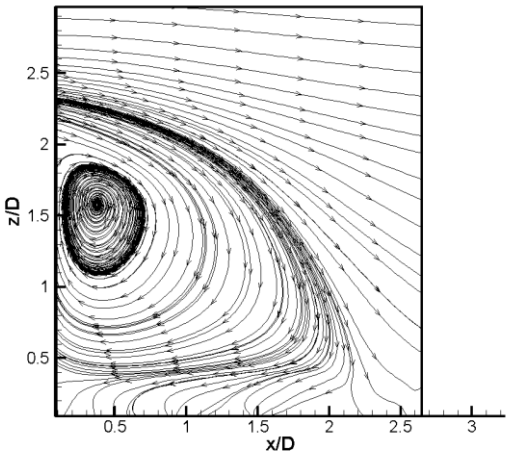

$y/D = 0.077$

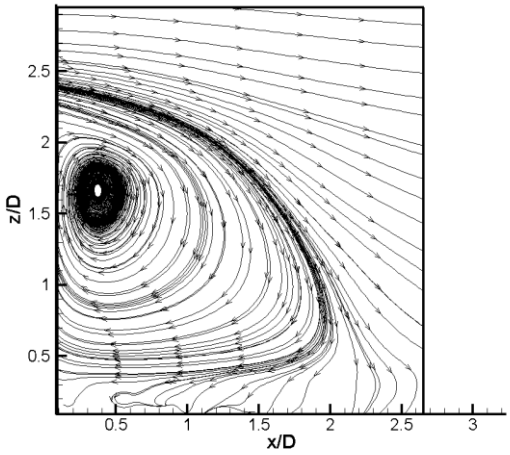

$y/D = 0.154$

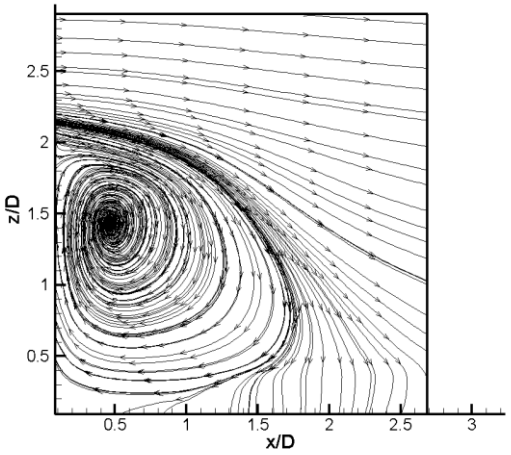

$y/D = 0.231$

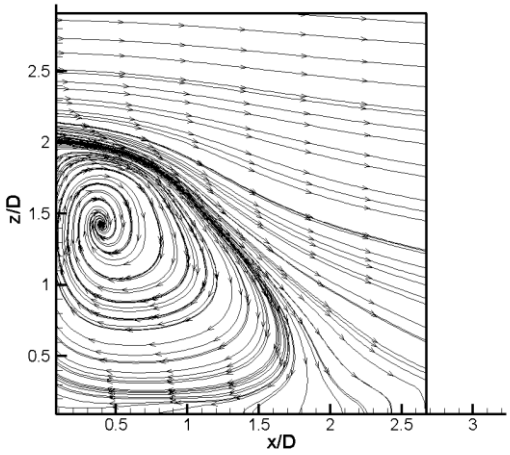

$y/D = 0.308$

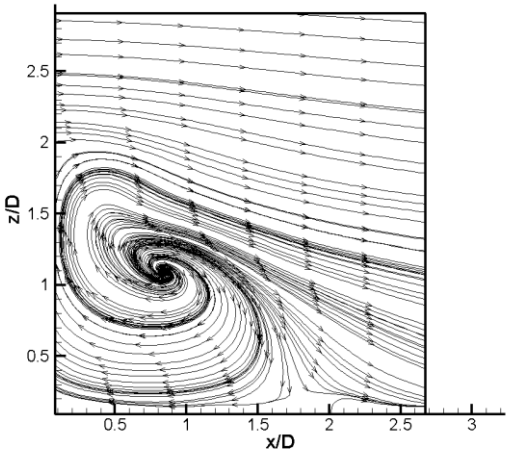

$y/D = 0.385$

Fig. 5.32 Streamlines of the mean flow field in *xz*-planes relative to finite cylinder with AR=2.

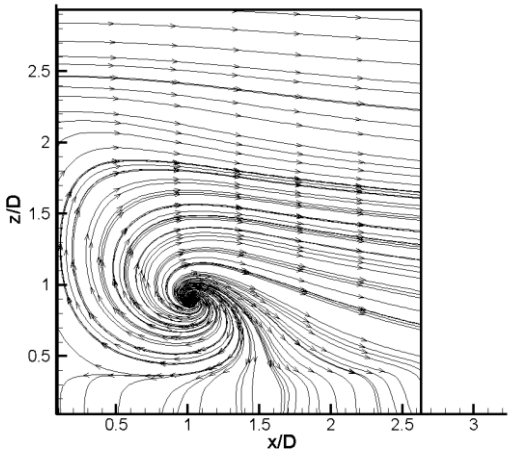

$y/D = 0.462$

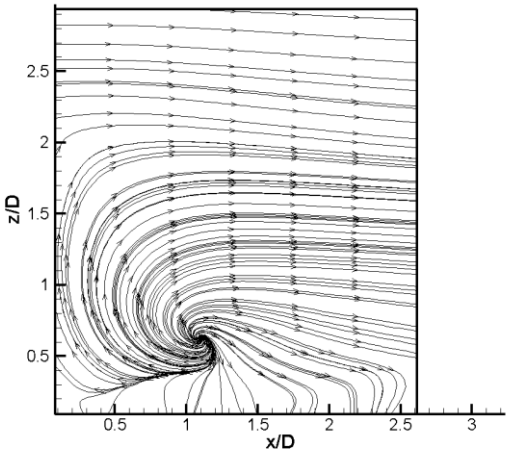

$y/D = 0.538$

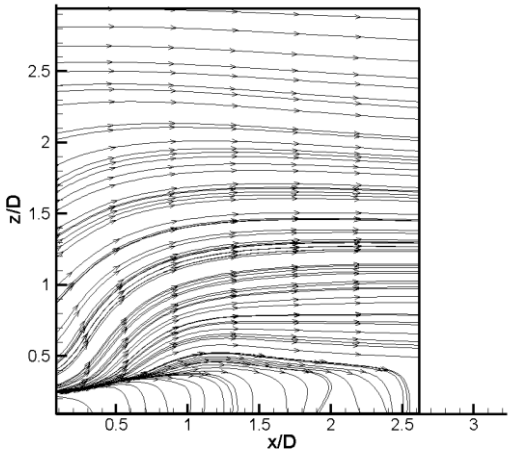

$y/D = 0.615$

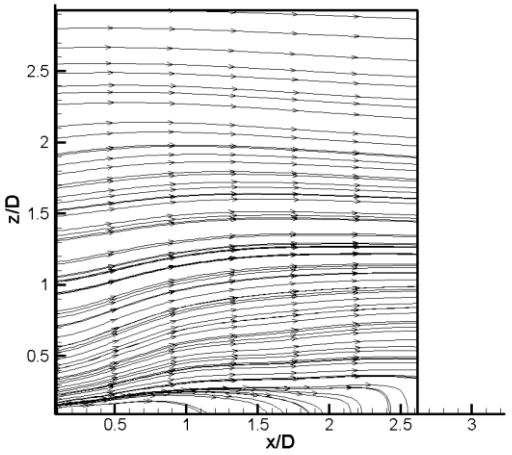

$y/D = 0.692$

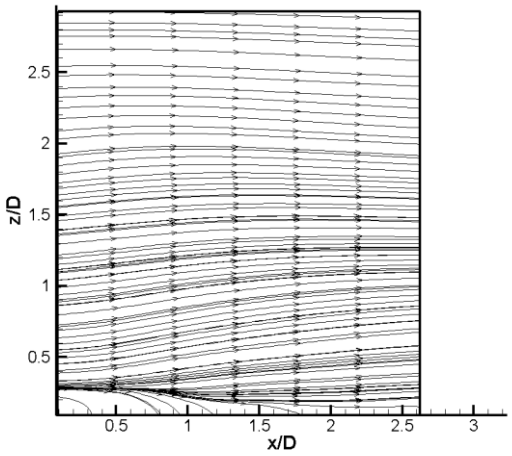

$y/D = 0.769$

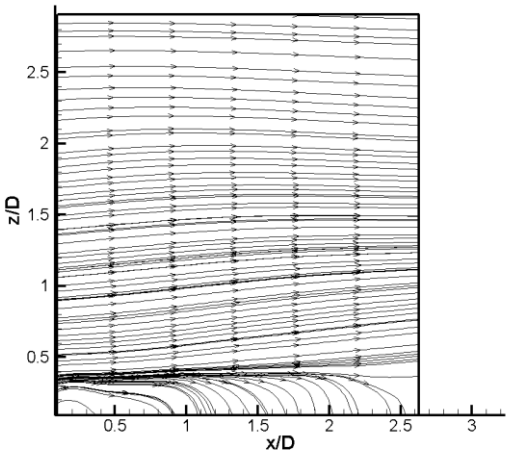

$y/D = 0.846$

Fig. 5.33 Streamlines of the mean flow field in *xz*-planes relative to finite cylinder with AR=2.

6 Conclusions

The Stereo PIV technique applied with both procedures proposed by Soloff et al. (1997) and Willert (1997) has been investigated by simulating non-uniform displacement fields. These consisted of a sinusoidal component with various wavelengths. This choice permitted to analyse the spatial resolution of the technique. Since the measured sine amplitude decreases with the reduction of the wavelength, the results have been showed in terms of Modulation Transfer Function (MTF) as a function of the normalised spatial wavelength. The theoretical analysis of the MTF associated to the Stereo PIV technique led to neglecting, for common configurations, the modulation relative to the 3C reconstruction for both approaches. The performance assessment, which has been conducted with synthetic images, showed a good agreement with the theoretical MTF.

The theoretical analysis has been extended in order to take into account a possible misalignment error between the calibration and measurement planes. The result of this analysis led to concluding that, depending on the stereoscopic set-up used, some wavelengths of the flow field can be dephased and modulated, even with a negative modulation modulus. The performance assessment has been conducted with synthetic images and, also in this case, showed a good agreement with the theoretical MTF.

Finally, in order to verify these analyses also in a real experiment, the images relative to a cylinder wake have been used. Since the cylinder was mounted in the first part of the tunnel test section, it wasn't possible to set the cameras in a symmetrical configuration. For this reason, the theoretical MTF curves relative to such a configuration have been computed and the experimental ones agreed with them.

With regard to the procedure proposed by Willert (1997), new formulas to compute the viewing angles have been proposed. These permit to compute the viewing angles without the necessity to measure any geometrical parameter of the experimental set-up and without further computations in addition to the unavoidable calibration of the stereoscopic configuration. The proposed method led to measurement accuracy comparable to that present in the literature.

Both PIV and Stereo PIV measurements have been done for both finite and infinite cylinders and compared. For the 2D cylinder the measurement section was in the middle of the cylinder length whereas, in order to study the flow evolution between the base and end plane of the finite cylinder, various sections along the cylinder length have been investigated.

The Reynolds numbers investigated are within the Shear-Layer Transition Regime suggested by Williamson (1996), which is characterized by vortex shedding.

The mean flow fields and Reynolds stress component maps have been obtained by averaging 5,000 images and showed the similarity between all the analysed sections. A substantial difference between the 2D and finite cylinders has been found in the vortex formation length. The analysis showed that the vortex formation length for the 2D cylinder is smaller than the ones of all the investigated sections of the finite cylinder.

The sampling frequency smaller than the von Kàrmàn one made an a posteriori phase averaging method needed. For this reason, the Proper Orthogonal Decomposition technique has been used to find the principal modes of the flow field and, by combining them to reconstruct the vortices evolution. With this method, the von Kàrmàn vortex shedding has been identified for the infinite cylinder as well as for the finite one, only for a small region near its base, accordingly with Kawamura et al. (1984). This region extends from $z/L \approx 0.14$ until $z/L \approx 0.43$, relatively to a finite cylinder with AR=8.

Finally, in order to investigate also the downwash flow, which characterizes the finite cylinder flow field as well, measurements in *xz*-planes have been performed. It has been evidenced that the flow fields in such planes are strongly dependent on the cylinder aspect ratio.

References

- Adaramola MS, Akinlade OG, Sumner D, Bergstrom DJ and Schenstead AJ (2006). Turbulent wake of a finite circular cylinder of small aspect ratio. J. Fluids Struct. 22: 919-928.
- Afgan I, Moulinec C, Prosser R and Laurence D (2007). Large eddy simulation of turbulent flow for wall mounted cantilever cylinders of aspect ratio 6 and 10. Int. J. Heat and Fluid Flow 28: 561–574.
- Astarita T (2006). Analysis of interpolation schemes for image deformation methods in PIV: effect of noise on the accuracy and spatial resolution. Exp Fluids 40: 977-987.
- Astarita T and Cardone G (2005). Analysis of interpolation schemes for image deformation methods in PIV. Exp Fluids 38: 233-243.
- Bearman PW (1965). Investigation of the flow behind a two-dimensional model with a blunt trailing edge and fitted with splitter plates. J. Fluid. Mech. 21: 241.
- Ben Chiekh M, Michard M, Grosjean N and Bèra J (2004). Reconstruction temporelle d'un champ aérodynamique instationnaire à partir de mesures PIV non résolues dans le temps. Proc 9e Congrès Francophone de Vélocimétrie Laser. Bruxelles, pp D.8.1-8.
- Bloor MS (1964). The transition to turbulence in the wake of a circular cylinder. J. Fluid. Mech. 19: 290.
- Bloor MG and Gerrard JH (1966). Measurements on turbulent vortices in a cylinder wake. Proc. of Royal Society of London A 294: 319-342.
- Braza M, Perrin R and Hoarau Y (2006). Turbulence properties in the cylinder wake at high Reynolds numbers. J. Fluids Struct. 22: 757-771.
- Cantwell B and Coles D (1983). An experimental study of entrainment and transport in the turbulent near wake of a circular cylinder. J. Fluid. Mech. 136: 321-374.
- Chyu C, Lin JC, Sheridan J and Rockwell D (1995). Karman vortex formation from a cylinder: Role of phase-locked Kelvin-Helmholtz vortices. Phys. Fluids 7 (9): 2288-2290.
- Cordier L and Bergmann M (2008). Proper Orthogonal Decomposition: an overview. In von Karman Institute Lecture Series: Post processing of numerical and experimental data. February 11-15, 2008.
- Coudert S and Schon JP (2001). Back-projection algorithm with misalignment corrections for 2D3C stereoscopic PIV. Meas Sci Technol 12:1371-1381.
- Coudert S and Westerweel J (2000). Comparison between warping and mapping methods on a Stereoscopic 2D3C DPIV system with Scheimpflug conditions. EuroMech 411 (Rouen).

- Etzold F and Fiedler H (1976). The near-wake structure of a cantilevered cylinder in a cross-flow. Z Flugwiss 24: 77–82.
- Fei R and Merzkirch W (2004). Investigation of the measurement accuracy of stereo particle image velocimetry. Exp Fluids 37:559-565.
- Foucaut JM, Carlier J and Stanislas M (2004). PIV optimization for the study of turbulent flow using spectral analysis. Meas Sci Technol 15:1046-1058.
- Fröhlich J and Rodi W (2004). LES of the flow around a circular cylinder of finite height. Int. J. Heat and Fluid Flow 25: 537–548.
- Gerrard JH (1966). The mechanism of the vortex formation region of vortices behind bluff bodies. J. Fluid. Mech. 25: 401.
- Giordano R and Astarita T (2009). Spatial resolution of the Stereo PIV technique. Exp Fluids DOI 10.1007/s00348-008-0589-y.
- Hain R, Käler CJ and Michaelis D (2007). Tomographic and time resolved PIV measurements on a finite cylinder mounted on a flat plate. In Proceeding of 7th International Symposium Particle Image Velocimetry, Rome (Italy).
- Hart DP (2000). Super-resolution PIV by recursive local-correlation. J Visual 3(2): 187–194.
- Huang HT, Fiedler HE and Wang JJ (1993). Limitation and improvement of PIV, part 2. Particle image distortion, a novel technique. Exp Fluids 15: 263–273.
- Jambunathan K, Ju XY, Dobbins BN and Ashforth-Frost S (1995). An improved cross correlation technique for particle image velocimetry. Meas Sci Technol 6: 507–514.
- Jeong J and Hussain AKMF (1995). On the identification of a vortex. J. Fluid. Mech. 285: 69-94.
- Kawamura T, Hiwada M, Hibino T, Mabuchi I and Kumada M (1984). Flow around a finite circular cylinder on a flat plate. Bull JSME 27: 2142–2151.
- Keane RD and Adrian RJ (1993). Theory of cross correlation analysis of PIV images. In: Nieuwstadt FTM (ed) Flow visualization and image analysis. pp 1–25.
- Konstantinidis E, Balabani S and Yianneskis M (2005). Conditional averaging of PIV plane wake data using a cross-correlation approach. Exp Fluids. Vol. 39, No. 1, pp 38-47.
- Kourta A, Boisson HC, Chassaing P and Ha Minh H (1987). Nonlinear interaction and the transition to turbulence in the wake of a circular cylinder. J. Fluid. Mech. 181: 141.
- Lawson N and Wu J (1997). Three-dimensional particle image velocimetry: experimental error analysis of digital angular stereoscopic system. Meas. Sci. Technol 8:1455–64.

- Lecordier B, Demare D, Vervisch LMJ, Rèveillon J and Trinitè M (2001). Estimation of the accuracy of PIV treatments for turbulent flow studies by direct numerical simulation of multi-phase flow. Meas Sci Technol 12: 1382–1391.
- Lecordier B and Westerweel J (2004). The EUROPIV synthetic image generator. In: Stanislas M, Westerweel J, Kompenhans J (eds) Particle image velocimetry: recent improvements. Springer, Heidelberg.
- Lin JC, Towfighi J and Rockwell D (1995a). Instantaneous structure of near-wake of a cylinder: on the effect of Reynolds number. J. Fluids Struct. 9: 409-418.
- Lin JC, Vorobieff P and Rockwell D (1995b). Three-dimensional patterns of streamwise vorticity in the turbulent near-wake of a cylinder. J. Fluids Struct. 9: 231-234.
- Lumley JL (1967). The structure of inhomogeneous turbulence. In Atmospheric Turbulence and Wave Propagation, ed. Yaglom AM and Tatarski VI, 166-178. Moscow: Nauka.
- Norberg C (1994). An experimental investigation of flow around a circular cylinder: influence of aspect ration. J. Fluid. Mech. 258: 287-316.
- Okamoto S and Sunabashiri Y (1992). Vortex shedding from a circular cylinder of finite length placed on a ground plane. J Fluid Eng T ASME 114: 512–521.
- Okamoto T and Yagita M (1973) The experimental investigation on the flow past a circular cylinder of finite length. B JSME 16: 805–814.
- Pattenden RJ, Turnock SR and Zhang X (2005). Measurements of the flow over a low-aspect-ratio cylinder mounted on a ground plane. Exp Fluids 39: 10–21.
- Park CW and Lee SJ (2000). Free end effects on the near wake flow structure behind a finite circular cylinder. J. Wind Eng. Ind. Aer. 88: 231-246.
- Perrin R, Braza M, Cid E, Cazin S, Barthet A, Sevrain A, Mockett A and Thiele F (2007a). Phase-averaged measurements of the turbulence properties in the near wake of a circular cylinder at high Reynolds number by 2C-PIV and 3C-PIV. Exp Fluids. 42,: 93-109.
- Perrin R, Braza M, Cid E, Cazin S, Barthet A, Sevrain A, Mockett A and Thiele F (2007b). Obtaining phase averaged turbulence properties in the near wake of a circular cylinder at high Reynolds number using POD. Exp Fluids 43:341-355.
- Perry AE, Chong MS and Lim TT (1982). The vortex shedding process behind two-dimensional bluff bodies. J. Fluid. Mech. 116: 77.
- Prasad A (2000). Stereoscopic particle image velocimetry. Exp Fluids 29:103-116.
- Prasad A and Jensen K (1995). Scheimpflug stereocamera for particle image velocimetry in liquid flows. Appl Opt 34:7092–7099.

- Raffel M, Willert C, Wereley S and Kompenhans J (2007). Particle Image Velocimetry. (ed. Springer Berlin Heidelberg), Germany, DOI 10.1007/978-3-540-72308-0.
- Rajagopalan S and Antonia RA (2005). Flow around a circular cylinder – structure of the near wake shear layer. Exp Fluids 38: 393-402.
- Roh S and Park S (2003). Vortical flow over the free end surface of a finite circular cylinder mounted on a flat plate. Exp Fluids 34:63–67
- Roshko A (1993). Perspectives on bluff body aerodynamics. J. Wind Eng. Ind. Aer. 49:79.
- Saad M, Lee L and Lee T (2007). Shear layers of a circular cylinder with rotary oscillation. Exp Fluids 43: 569-578.
- Sakamoto H and Arie M (1983). Vortex shedding from a rectangular prism and a circular cylinder placed vertically in a turbulent boundary layer. J Fluid Mech 126: 147–165.
- Said NM, Mhiri H, Bournot H and Le Palec G (2008). Experimental and numerical modelling of the three-dimensional incompressible flow behaviour in the near wake of circular cylinders. J. Wind Eng. Ind. Aer. 96: 471-502.
- Scarano F, David L, Bsibsi M and Calluaud D (2005). S-PIV comparative assessment: image dewarping + misalignment correction and pinhole + geometric projection. Exp Fluids 39:257-266.
- Scarano F, Elsinga GE, Bocci E and van Oudheusden BW (2006). Investigation of 3-D Coherent Structures in the Turbulent Cylinder Wake using Tomo-PIV. In Proceeding of 13th Int Symp on Applications of Laser Techniques to Fluid Mechanics Lisbon, Portugal.
- Scarano F and Riethmuller ML (1999). Iterative multigrid approach in PIV image processing with discrete window offset. Exp Fluids 26: 513– 523.
- Schiller L and Linke W (1933). Druck und Reibungswiderstand des Zylinders bei Reynoldsaachen Zahken 5000 bis 40000. Z. Flugtech. Motorluft. 24: 193.
- Soloff S, Adrian R and Liu Z (1997). Distortion compensation for generalized stereoscopic particle image velocimetry. Meas Sci Technol 8:1441-1454.
- Soria J (1996). An investigation of the near wake of a circular cylinder using a video-based digital cross-correlation particle image velocimetry technique. Exp Therm Fluid Sci 12: 221–233.
- Stanislas M, Okamoto K, Kähler CJ, Westerweel J and Scarano F (2008). Main results of the third international PIV Challenge. Exp Fluids DOI 10.1007/s00348-008-0462-z.
- Sumner D, Heseltine JL and Dansereau OJP (2004). Wake structure of a finite circular cylinder of small aspect ratio. Exp Fluids 37: 720–730.

- Szepessy S and Bearman PW (1992). Aspect ratio and end plate effects on vortex shedding from a circular cylinder. J. Fluid. Mech. 234: 191-217.
- Tanaka S and Murata S (1999). An investigation of the wake structure and aerodynamic characteristics of a finite circular cylinder. JSME Int. J. Ser. B Fluids Thermal Eng. 42, 178–187.
- Thompson MC and Hourigan K (2005). The shear-layer instability of a circular cylinder wake. Phys. Fluids 17: 021702.
- Tsai RY (1987). A Versatile Camera Calibration Technique for High-Accuracy 3D Machine Vision Metrology Using Off-the-Shelf TV Cameras and Lenses. IEEE Journal of Robotics and Automation 4: RA-3.
- Unal MF and Rockwell D (1988). On vortex formation from a cylinder. Part 1. The initial instability. J. Fluid. Mech. 190: 491-512.
- Utami T, Blackwelder RF and Ueno T (1991). A cross-correlation technique for velocity field extraction from particulate visualization. Exp Fluids 10: 213–223.
- van Oord J (1997). The design of a stereoscopic DPIV-system. Delft University of technology report MEAH-161, 17-18.
- van Oudheusden BW, Scarano F, van Hinsberg NP and Watt DW (2005). Phase resolved characterization of vortex shedding in the near wake of a square-section cylinder at incidence. Exp Fluids 39: 86-98.
- Wei T and Smith CR (1986). Secondary cortices in the wake of circular cylinders. J. Fluid. Mech. 169: 513.
- Wereley ST and Meinhart CD (2001). Second-order accurate particle image velocimetry. Exp Fluids 31: 258-268.
- Westerweel J (1993) Digital particle image velocimetry—theory and applications. PhD Thesis, Delft University of Technology, The Netherlands.
- Westerweel J (1997). Fundamentals of digital particle image velocimetry. Meas. Sci. Technol. 8: 1379–1392.
- Westerweel J, Dabiri D and Gharib M (1997). The effect of a discrete window offset on the accuracy of cross-correlation analysis of digital PIV recordings. Exp Fluids 23: 20–28.
- Wieneke B (2005). Stereo-PIV using self-calibration on particle images. Exp Fluids 39: 267-280.
- Willert C (1997). Stereoscopic digital particle image velocimetry for application in wind tunnel flows. Meas Sci Technol, 8: 1465-1479.

- Willert C (2006). Assessment of camera models for use in planar velocimetry calibration. Exp Fluids 41: 135-143.
- Willert CE and Gharib M (1991). Digital particle image velocimetry. Exp Fluids 10: 181–193.
- Williamson CHK (1996). Vortex dynamics in the cylinder wake. Annu. Rev. Fluid. Mech., 28: 477-539.
- Wu J, Sheridan J, Hourigan K and Soria J (1996). Shear Layer Vortices and Longitudinal Vortices in the Near Wake of a Circular Cylinder. Exp. Therm. Fluid. Sci. 12: 169-174.
- Wu J, Sheridan J, Welsh MC, Hourigan K and Thompson M (1994). Longitudinal vortex structures in a cylinder wake. Phys. Fluids. 6 (9): 2883-2885.
- Zdravkovich M (1997). Flow around circular cylinders, vol. 1. Oxford University Press, Oxford.